CONFINEMENT OF MULTIPLY CHARGED IONS IN AN ECRH MIRROR PLASMA

by

Clinton Craig Petty

B.S., University of Missouri (1983)
S.M., Massachusetts Institute of Technology (1986)

Submitted to the Department of Nuclear Engineering
in partial fulfillment of the requirements for the degree of

Doctor of Philosophy

at the

MASSACHUSETTS INSTITUTE OF TECHNOLOGY

August 1989

Signature of Author ....
Department of Nuclear Engineering
June 19, 1989

Certified by...
Donald K. Smith
Research Scientist, Plasma Fusion Center
Thesis Supervisor

Certified by...
Ian H. Hutchinson
Professor of Nuclear Engineering
Thesis Reader

Accepted by ....
Allan F. Henry
Chairman, Departmental Committee on Graduate Students

CONFINEMENT OF MULTIPLY CHARGED IONS IN AN ECRH MIRROR PLASMA

by

Clinton Craig Petty

Abstract

This thesis is an experimental study of multiply charged ions in the Constance B mirror experiment. By measuring the ion densities, end loss fluxes and ion temperatures, the parallel confinement times for the first five charge states of oxygen and neon plasmas are determined. The parallel ion confinement times increase with charge state and peak on axis, both indications of an ion-confining potential dip created by the hot electrons. The radial profile of ion end loss is usually hollow due to large ion radial transport ($\tau_{\|i} \approx \tau_{\perp i}$), with the peak fluxes occurring at the edge of the electron cyclotron resonance zone.

Several attempts are made to increase the end loss of selected ion species. Using minority ICRH, the end loss flux of resonant ions increases by 20% in cases when radial transport induced by ICRH is not too severe. A large antenna voltage can also extinguish the plasma. By adding helium to an oxygen plasma, the end loss of O^{6+} increases by 80% due to decreased ion radial transport.

An ion model is developed to predict the ion densities, end loss fluxes and confinement times in the plasma center using the ion particle balance equations, the quasineutrality condition and theoretical confinement time formulas. The model generally agrees with the experimental data for oxygen and neon plasmas to within experimental error. Under certain conditions spatial diffusion appears to determine the parallel ion confinement time of the highest charge states. For oxygen plasmas during ICRH, the measured parallel confinement time of the resonant ions is much shorter than their theoretical value, probably due to rf diffusion of the ions into the loss cone.

Acknowledgements

I would like to thank my thesis advisor, Dr. Donald Smith, for overseeing the work performed in this thesis. I have greatly benefited from his excellent teaching of the trade of scientific research. I also thank Dr. Donna Smatlak, the leader of the Constance group and an experienced experimentalist, for her advice and guidance. Dr. Smatlak is responsible for the excellent operation of Constance B as a plasma physics experiment. Dr. Barton Lane provided excellent suggestions in the area of plasma confinement. I also wish to thank Professor Ian Hutchinson for serving as my thesis reader.

My colleague and friend Daniel Goodman deserves special thanks. As the two graduate students studying ion physics on Constance B, we collaborated on certain experimental projects. I am also grateful to the other "mirror" graduate students: Xing Chen, Thomas Farish, Richard Garner, Gerald Gibson, Samuel Hokin, John Machuzak, Thomas Moran and John Zielinski for making the working environment both stimulating and enjoyable. I also wish to thank Nai-Chang Yeh for her unyielding support during this time.

Since this dissertation marks the end of my formal education, I would especially like to thank my parents, Clinton and Edye Petty, for showing me through example how to be a scholar and a gentleman.

Sojourned han thise merchantz in that toun
A certein tyme, as fil to hire plesance.
And so bifel that th'excellent renoun
Of the Emperoures doghter, dame Custance,
Reported was, with every circumstance,
Unto thise Surryen marchantz in swich wyse,
Fro day to day, as I shal yow devyse.

This was the commune voys of every man:
"Oure Emperour of Rome—God hym see!—
A doghter hath that, syn the world bigan,
To rekene as wel hir goodnesse as beautee,
Nas nevere swich another as is shee.
I prey to God in honour hire susteene,
And wolde she were of al Europe the queene.

"In hire is heigh beautee, withoute pride,
Yowthe, withoute grenehede or folye;
To alle hire werkes vertu is hir gyde;
Humblesse hath slayn in hire al tirannye.
She is mirour of alle curteisye;
Hir herte is verray chambre of hoolynesse,
Hir hand, ministre of fredam for almesse."

from "The Man of Law's Tale" in <u>The Canterbury Tales</u> by Geoffrey Chaucer.

Contents

List of Figures

10

List of Tables

Chapter 1

Introduction

1.1 Statement of problem

The motivation for this thesis is understanding the ion physics of electron cyclotron resonance (ECR) ion sources. These sources are minimum-B mirror plasmas which are created and maintained by electron cyclotron resonance heating (ECRH). They are usually fueled by a heavy gas or vaporized atoms from an oven. ECR ion sources produce high charge state ions which can be extracted from the open magnetic geometry for accelerators and atomic physics experiments. The ions in these sources are highly stripped due to the high electron temperature and long ion confinement time.

The coupling of ECR ion sources to cyclotrons has resulted in significant performance gains in energy, intensity, reliability and variety of ion species [Lyneis, 1986]. An ECR ion source installed on the injector of the CERN SPS synchrotron supplied fully stripped oxygen and sulphur which was accelerated up to relativistic energies to produce quark-gluon plasmas [Jacob, 1989]. A project is underway at Argonne National Laboratory to couple an ECR ion source to a superconducting heavy-ion linac [Pardo, *et al.*, 1989].

Although ECR ion sources have been used for the last decade with great success, the physics behind their operation is not well understood. Progress in source performance has mainly come experimentally by systematically changing the gas supply, ECR tuning, wall conditions, etc., on a trial and error basis. Understanding the

physics of ECR sources will help improve present sources without expensive systematic adjustments and will aid in the design of future sources. The goal of this thesis therefore is to determine the relevant physics of a multiple ion-species plasma in an ECRH minimum-B mirror.

This thesis concentrates on the ion physics of plasmas in the Constance B mirror experiment (electron physics was the subject of previous work on Constance B [Garner, *et al.*, 1987; Chen, *et al.*, 1989; Hokin, *et al.*, 1989]). Of particular importance are the parallel ion confinement times, which are determined by measuring the ion densities and end loss fluxes. The experimental results are compared to a theoretical ion model to determine the relevant ion physics. In addition, several methods of increasing the end loss of selected ions are tested. First, medium charge state ions in the plasma are heated by ion cyclotron resonance heating (ICRH). This should increase their end loss by "boiling" them out of the ion-confining potential dip. Second, gas mixing is investigated by adding helium to an oxygen plasma to increase the end loss of high charge states of oxygen.

1.2   Description of an ECR ion source

An elevation view of the ECR ion source operated at Lawrence Berkeley Laboratory is shown in Fig. 1-1 [Lyneis, 1987]. It is fairly typical of other ECR ion sources and will serve to point out their important features. The source is divided into two plasma stages and an extraction region. Gas and microwaves at 10.3 GHz are fed into the first stage to form a high pressure ECR discharge which produces a dense cold plasma. High field launch of the microwaves is needed to insure that they propagate to the ECR region. The plasma is guided by the solenoidal magnetic field into the second stage where it is trapped in a magnetic mirror and the electrons are heated by 6.4 GHz microwaves. A SmCo$_5$ sextupole in the second stage creates a minimum-B magnetic field configuration to stabilize the hot plasma against MHD modes. A large amount of differential pumping between the two stages keeps the neutral pressure low in the second stage. The low neutral pressure and energetic electrons of the
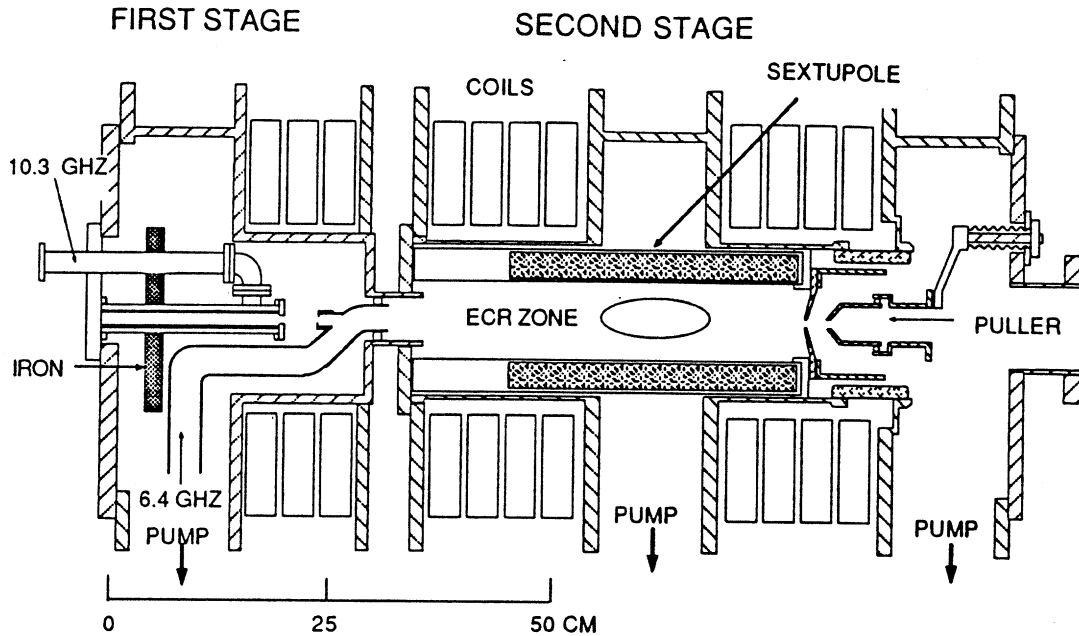
Figure 1-1: Elevation view of the ECR ion source at Lawrence Berkeley Laboratory.

second stage produce a high charge state plasma. The ion end loss from this plasma is then extracted into the beam line through the puller. Typical extraction voltages are 10–20 kV.

1.3 Ion confinement in a hot electron plasma

Charged particles are confined in a magnetic mirror due to conservation of their magnetic moment:

$$\mu = \frac{\frac{1}{2}mv_\perp^2}{B}.$$

(1.1)

Ignoring the effect of electrostatic fields for now, a charged particle moving into a region of increasing magnetic field parallel to the field line direction will be reflected provided that $\mu B_m > \varepsilon$, where B_m is the magnetic field maxima and ε is the total particle energy. Thus, there is a loss region in the particle's velocity space, with the loss cone angle given by

$$\theta = \sin^{-1}\sqrt{\frac{1}{R}},$$

(1.2)

where R is the mirror ratio.

For a classical mirror cell, the time it takes to knock a particle into the loss cone is on the order of its collision time. If the electrons and ions have approximately the same temperature, then the electrons will scatter out of the mirror much faster than the ions by virtue of their lighter mass. Thus, the plasma develops a positive potential which traps the electrons and expels the ions. The magnitude of the potential is determined by the need to balance the loss of positive and negative charge and therefore is called the ambipolar potential. The regions of confinement in velocity space for ions and electrons are shown in Fig. 1-2.

A positive ambipolar potential normally develops because electrons scatter into the loss cone faster than ions. If ions scatter into the loss cone faster because $T_i \ll T_e \sqrt[3]{m_e/m_i}$, then a negative ambipolar potential will develop to trap ions. A combination of these two situations occurs in ECRH mirror plasmas since the electron distribution splits into two components: a magnetically confined "hot" population and an electrostatically confined "cold" population. The hot electrons will be mainly trapped in the bottom of the magnetic well due to their temperature anisotropy $(\bar{E}_\perp > \bar{E}_\parallel)$ caused by the ECRH. The plasma potential is overall positive but dips in the region of the hot electrons creating the axial potential distribution shown in Fig. 1-3 [Baldwin, 1980]. The potential dip forms because the hot electrons require ions for charge neutralization, but the hot electrons do not contribute significantly to the ionization source. Thus, near the plasma center the hot electrons are magnetically confined and the ions are electrostatically confined by the potential dip $\Delta\phi_i = \phi_p - \phi_o$. Near the mirror throat the ions are magnetically confined and the cold electrons are electrostatically confined by the ambipolar potential $\Delta\phi_e = \phi_o - \phi_m$.

1.4   Previous work

Most of the experimental data to date for ECR ion sources consists of extracted ion currents. However, limited electron density and temperature data is available. Geller (1976) measured the electron density and temperature on SUPERMAFIOS using an interferometer and diamagnetic loop, and found $1 \times 10^{11} \text{cm}^{-3} < n_e < 3 \times 10^{11} \text{cm}^{-3}$
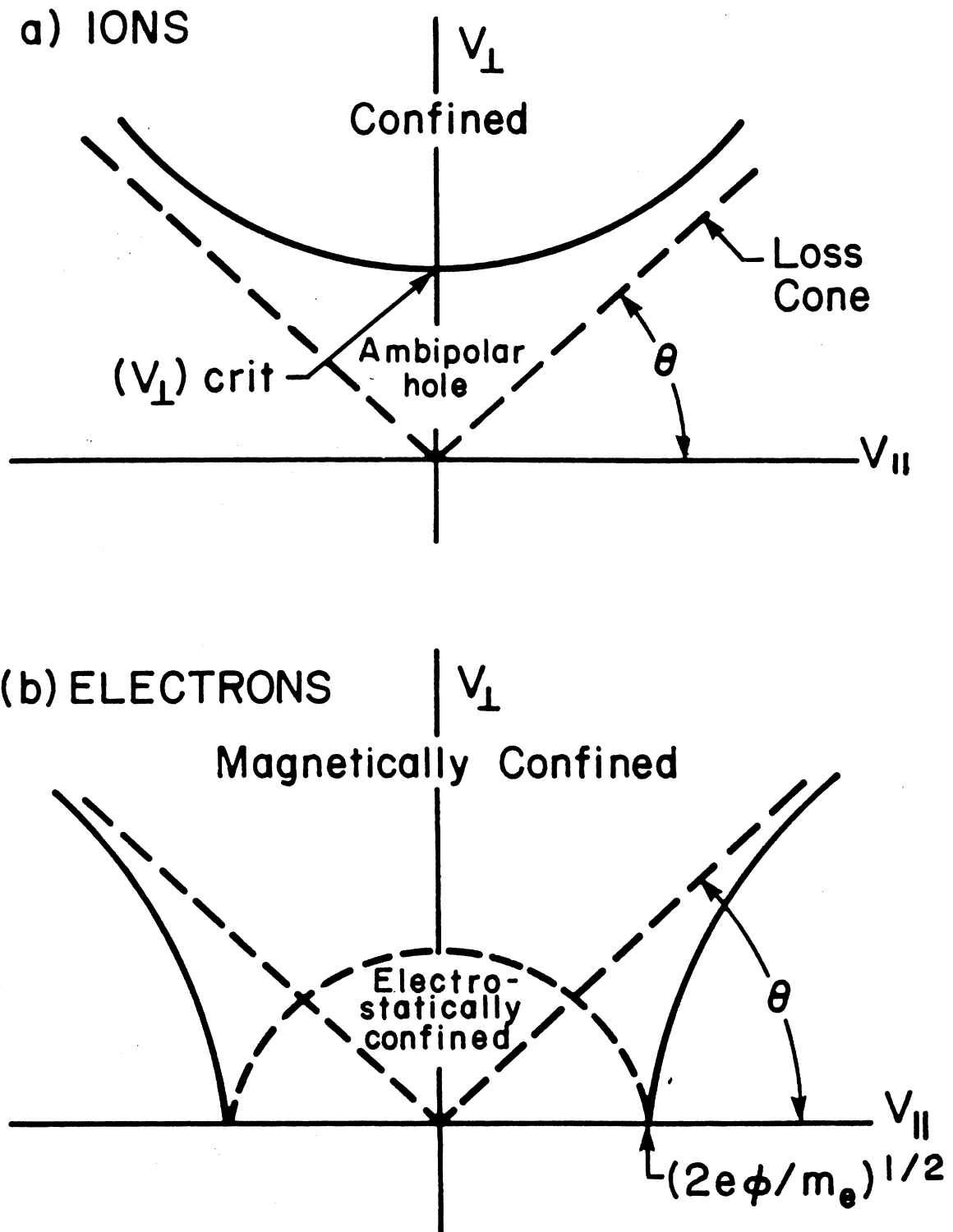
Figure 1-2: Regions of confinement in velocity space for (a) ions and (b) electrons. Dashed curves show purely magnetic confinement while solid curves indicate the loss boundary modification by the ambipolar potential.
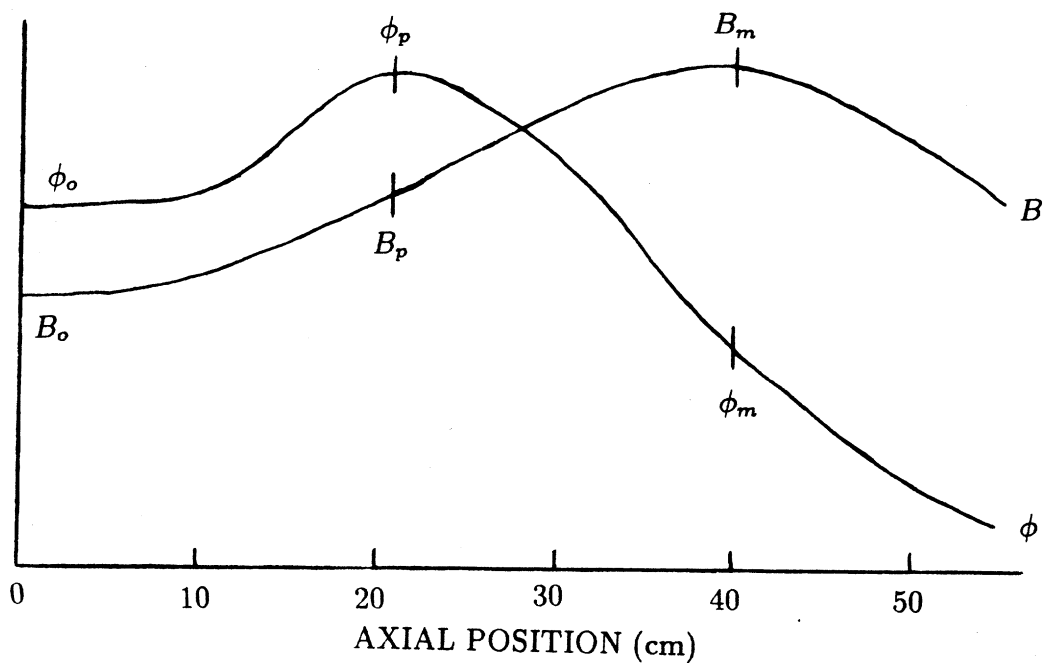
Figure 1-3: Axial potential and magnetic distribution for an ECRH mirror plasma.

and 7 keV $< T_e <$ 25 keV, depending upon ECRH power. Bernhardi and Wiesemann (1982) found a power law dependence for the electron distribution function measured on their simple ECRH mirror, with average electron energies of several hundred keV. Measurements on OCTOPUS using a Hall probe were consistent with a density of $3 \times 10^{11} \mathrm{cm}^{-3}$ at an energy of 4 keV [Lyneis, 1986]. The measured hot electron density in INTEREM was also $3 \times 10^{11} \mathrm{cm}^{-3}$ [Tamagawa, *et al.*, 1976]. The ion temperature has also been measured by several groups. Meyer (1986) found that ion temperatures in the ORNL ECR were $T_i/q_i \leq$ 5 eV. Köhler, *et al.*, (1987) measured the ion temperature using a double hemispherical energy analyzer and found that T_i varied between 1 and 3 eV and showed a slight increase for the higher charged ions.

Tandem mirrors have measured parallel confinement times for hydrogen ions which agree with theoretical electrostatic and magnetic confinement times [Cho, *et al.*, 1988]. Since tandem mirrors confine central cell ions parallel to the magnetic field lines using positive potential barriers developed in their plugs, their ion confinement physics is similar to that of ECR ion sources. Because tandem mirror data is for hydrogen plasmas, the scaling of parallel confinement time with ion charge state has not been

tested.

Several authors have developed models to determine the charge state distribution (CSD) of ions in an ECR ion source. Bliman and Chan-Tung (1981) proposed an ionization equilibrium model for multiply-charged argon plasmas with a single population of hot electrons. The ion densities were calculated from the ion particle balance equations by balancing single step ionization by electrons, charge exchange with neutrals and loss of confinement. This feature is common to all subsequent ion models; the differences are in how the ion confinement time is treated. Bliman and Chan-Tung treated the plasma as if it was unmagnetized and considered diffusional losses using an ambipolar diffusion coefficient. This resulted in ion confinement times that were two orders of magnitude too short, therefore the magnitude was arbitrarily adjusted to improve the fitting while the scaling with charge state was retained. Also Bliman and Chan-Tung compared their modeled CSD of the ion density to the experimental CSD of the extracted ion current. These two CSD's are not the same, however, unless all charge states have the same confinement time.

Jongen (1980) improved upon the model of Bliman and Chan-Tung by recognizing that their ambipolar diffusion equation neglected magnetic confinement of the hot electrons. Jongen calculated the confinement time of ions from the diffusion equation, neglecting mirror trapping of ions and ion radial transport. The ion trapping potential was found from the charge neutrality condition of electron and ion losses using the mirror confinement time of the hot electrons. This eliminated the need for a free parameter to improve the fitting. Jongen also calculated the CSD of the ion currents from the ion densities and confinement times, allowing an accurate comparison between the model and experimental results.

The model by West (1982) improved upon the physics of Jongen in several ways. First, to better approximate the electron distribution function West included populations of both cold and hot electrons. This changes the axial potential distribution considerably because the ambipolar potential, determined from the charge neutrality condition for electron and ion losses, was now positive. The ion trapping potential was determined by the need to balance creation and loss of ions (the global particle

balance equation). Instead of using the diffusional model of Jongen to calculate the ion confinement time, West used the Pastukhov and flow confinement times which take into account electrostatic and magnetic trapping. Ion radial transport was again neglected. With the addition of cold electrons, radiative recombination was included in the ion particle balance equations.

The limitations of these models fall into two categories: atomic physics and plasma physics. The atomic physics can be improved by including multiple step ionization and charge exchange, and dielectronic recombination. Better values for the single-step ionization cross-sections are also needed, especially for high charge state ions. This thesis does not attempt to improve the atomic physics of the model, but it does attempt to improve the plasma physics. Although West calculated the ion confinement time self consistently, he did not derive an explicit relation showing how the ion confinement time relates to the other plasma parameters. Previous models also neglected ion radial transport, which is included in this thesis since it is significant for Constance B. For parallel ion confinement, this thesis connects the Pastukhov-flow confinement of West (valid for low charge states) with the spatial diffusion confinement of Jongen (valid for high charge states).

1.5   Organization

This thesis is divided into five chapters. Chapter 1 gives an introduction to ECR ion sources and motivates this thesis work. The Constance B experiment and diagnostics are described in Chapter 2 along with an explanation of the experimental method. Chapter 3 develops a theoretical model for the ion densities, end loss fluxes and confinement times. In addition, electron confinement and particle and power balance is covered. The experimental results for both ions and electrons are presented in Chapter 4. Also the measured ion densities, end loss fluxes and confinement times are compared to the ion model for cases with and without minority ICRH. Finally, Chapter 5 summarizes the experimental and theoretical results of this thesis and applies them to ECR ion source issues.

Chapter 2

The Constance B Experiment

This chapter describes the Constance B mirror experiment, including magnetic geometry, plasma heating system, data acquisition, principle diagnostics and plasma parameter control. Constance B is a single cell quadrupole mirror in which hot electron plasmas are created and maintained with electron cyclotron resonance heating. The Constance B experiment started operation in October 1983 and is a continuation of the Constance I and Constance II magnetic mirror programs at MIT. The primary objective of the Constance program has been to examine the basic physics issues of ECRH plasmas in a minimum-B magnetic geometry in support of the tandem mirror fusion program. Previous subjects of doctoral research on Constance B were electron microinstabilities [Garner, 1986], electron velocity-space diffusion [Hokin, 1987], hot electron equilibrium and stability [Chen, 1988] and ion radial transport [Goodman, 1989]. An extensive description of the Constance B experiment and results is given by Smatlak, *et al.*, (1986).

2.1 Basic systems

2.1.1 magnetic field

The Constance B magnetic field is produced by a single copper magnet shaped like the seam of a baseball (see Fig. 2-1). It is located outside the vacuum chamber and
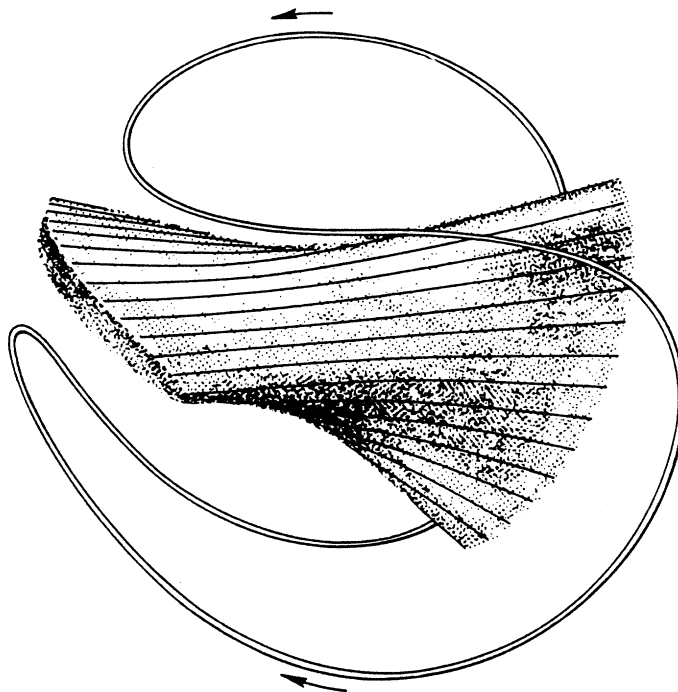
Figure 2-1: The Constance B magnet is wound in the shape of the seam of a baseball. The shape of the confined plasma is also shown.

is electrically isolated from the rest of the machine. During operation it consumes about 2 MW of electric power. The maximum flow rate of cooling water through the conductor limits the magnet pulse length to under 10 seconds and the pulse rate to 12 per hour. The maximum midplane magnetic-field strength is 3.8 kG.

The magnetic field lines and mod-B contours for the baseball magnet in the $y = 0$ plane are shown in Fig. 2-2. The magnetic field is minimum-B, has quadrupole symmetry and elliptical flux surfaces (the flux surfaces at the midplane are nearly circular, however). The mirror ratio on axis is 1.87 and the distance between mirror peaks is 80 cm. Both the mirror ratio and the distance between mirror peaks decrease off axis. The electron cyclotron resonance lies along a closed mod-B surface shaped like an egg.

2.1.2   vacuum system

The vacuum system consists of the vacuum chamber, pumping system and the gas control and monitoring system. The 5000 liter aluminum vacuum chamber consists
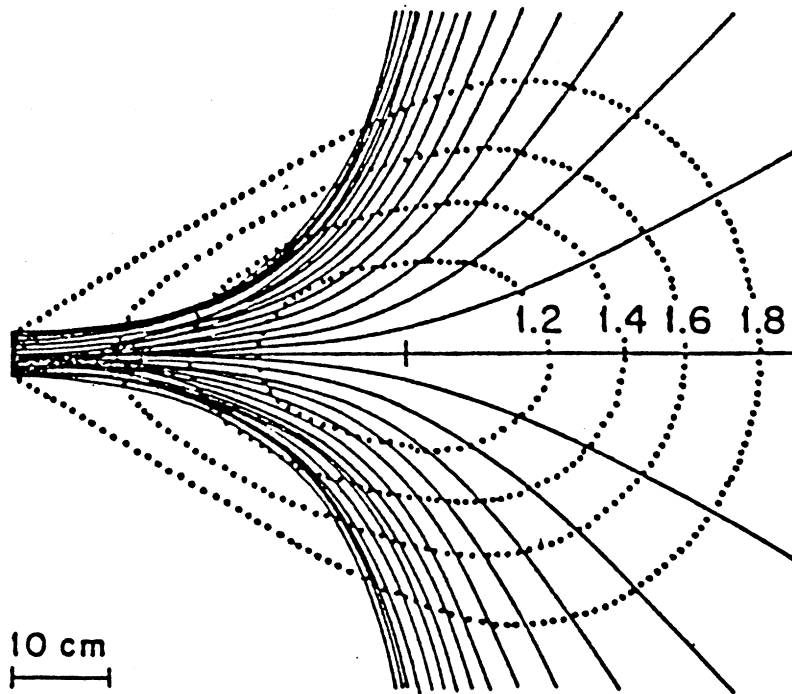
Figure 2-2: The Constance B magnetic field lines (solid lines) and mod-B contours (dotted lines) are shown. The mirror ratio for each mod-B contour is given.

of three sections and is specifically designed for the magnetic field geometry of the baseball magnet (see Fig. 2-3). The central chamber is made of two welded pieces which fit within the baseball magnet and contains the entire magnetic well. The plasma is accessible for diagnostic purposes from all sides. Plasma that escapes the magnetic well flows along magnetic field lines into one of two fan tanks located on either side of the central chamber. The fan tanks are rotated 90 degrees with respect to each other and are designed to accommodate the fanning of the quadrupole magnetic field. These large tanks minimize the electron cooling that results when secondary electrons from the walls stream back along field lines. This is in contrast to early INTEREM results where line tying to the nearby vacuum chamber end wall was important [Haste, *et al.*, 1968].

The vacuum is maintained by three separate pumping systems. A 250 l/s turbo-molecular pump (Airco 514) is located in the south fan tank and operates at pressures below 60 mTorr. A 1500 l/s cryogenic LHe pump (Leybold-Heraeus RPK-1500S2) is located in the north fan tank and is used at pressures below 2×10^{-5} Torr. Two
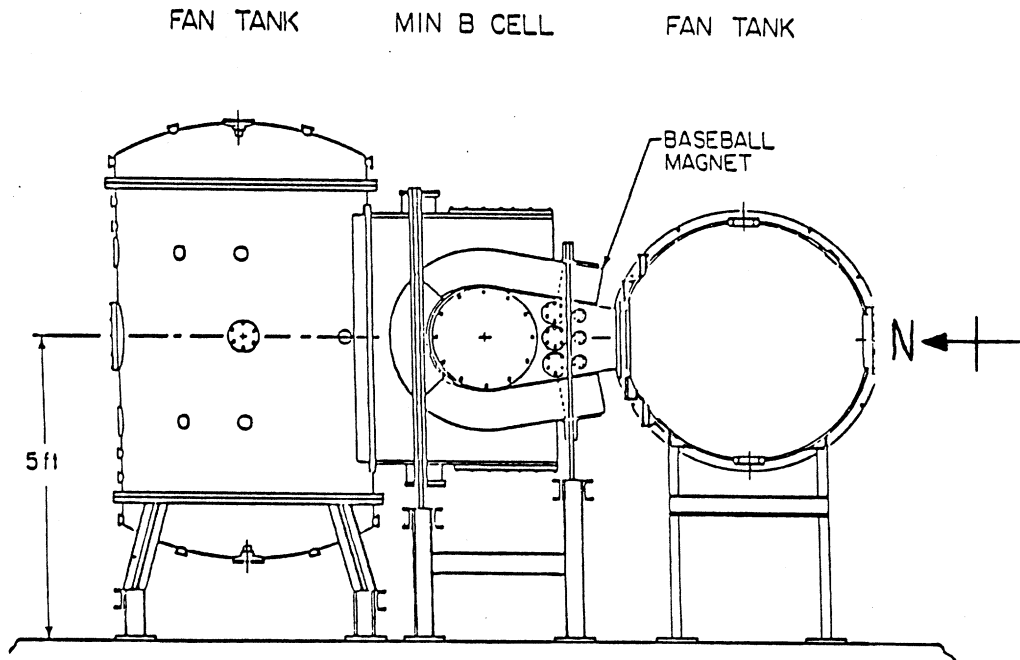
Figure 2-3: The Constance B vacuum chamber consists of a central chamber and two fan tanks. The fan tanks are rotated 90 degrees with respect to each other.

resistive titanium getters are located in each fan tank where the large surface area of the wall pumps reactive gasses such as hydrogen, nitrogen and oxygen. The machine base pressure is normally $1-2 \times 10^{-8}$ Torr.

The machine pressure is monitored by a fast Ratiomatic ionization gauge (Varian) located on top of the central chamber. The ionization gauge is magnetically shielded. Since the gauge is calibrated for nitrogen, the relative ionization gauge sensitivity (S/S_N) for various gasses is given in Table 2.1. To produce a plasma shot, the

Table 2.1: Relative ionization gauge sensitivity (compared to nitrogen).

Gas	S/S_N
Hydrogen	0.42
Helium	0.14
Oxygen	1.00
Neon	0.23
Argon	1.20
Krypton	1.70
Xenon	3.00

working gas is puffed into the machine through a piezo-electric gas valve located at the bottom of the central chamber after the magnetic field has been applied but before the ECRH pulse.

2.1.3 ECR heating system

The Constance B plasma is created and maintained with electron cyclotron resonance heating. Microwaves are produced by a Gunn diode and amplified by a klystron (Varian VA-911), which generates up to 5 kW of 10.5 GHz radiation with a bandwidth of 1 MHz. The forward and reflected powers are measured with thermistors connected to the output of the klystron by 40 dB directional couplers. XL band waveguide is used to direct the microwaves from the klystron to the central vacuum chamber. A 17 dB horn launches the microwaves perpendicular to the magnetic axis approximately 40 cm above the axis and 10 cm south of the midplane. The waves are primarily in X-mode polarization, which is accessible to the plasma center since it is launched from high magnetic field.

The density limit to X-mode accessibility occurs when the left hand cutoff frequency equals the cyclotron frequency, or $\omega_{pe} = \sqrt{2}\,\omega_{ce}$. Thus, X-mode launch has twice the density limit of O-mode launch. Previous experiments on Constance B have found that O-mode absorption by cold electrons is less than one-tenth that of X-mode absorption [Hokin, 1987], in agreement with slab model calculations. Since the vacuum chamber acts like a high Q microwave cavity ($Q \sim 10,000$), strong cavity heating effects (about one-third of the total amount) have been observed.

2.1.4 ICR heating system

Ion cyclotron resonance heating (ICRH) of minority ions in the plasma is used to alter the charge state distribution of the plasma end loss. A double half-turn antenna centered on the midplane launches the low frequency rf waves. Ground straps parallel to the magnetic axis add a parallel electric field to improve ion heating. The antenna diameter is 35.6 cm, with a typical plasma diameter being 20 cm. Since the plasma
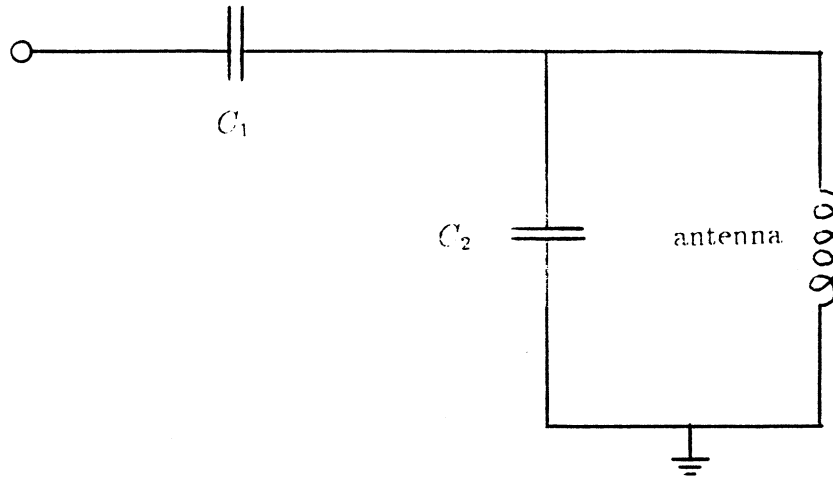
Figure 2-4: Antenna matching network for ICRH experiments.

volume is small (several liters), ion heating does not occur through wave propagation
and absorption. Instead, the near fields of the antenna directly interact with the ions
at the ICR layer. The situation is similar to that of ICRH in the Phaedrus tandem
mirror plugs [Smith, 1980].

The ICRH transmitter consists of a synthesizer/function generator (HP 3325A)
which feeds into a rf power pre-amp (ENI 2100L) and then into a high power rf
amplifier using an Eimac 4CW100,000E tube. The amplifier produces square output
pulses 150 ms long at 1.40 MHz, with power levels up to 10 kW. A directional coupler
measures the forward and reflected power to the antenna matchbox. The ratio of
forward to reflected power is typically 4:1. The antenna matching network is shown
in Fig. 2-4. There are two variable capacitors: the first (C_1) matches the antenna
network to the 50 Ω transmission line and the second (C_2) forms a LC resonant loop
with the antenna. The vacuum Q of the LC loop is approximately 200.

2.1.5 experimental control

There are three 'knobs' available to the experimenter to vary the plasma conditions for a given working gas: the ECRH power, gas pressure and magnetic field strength. For minority ion heating experiments, the ICRH power can also be varied. The ECRH power strongly affects the plasma density, while the gas pressure strongly affects the plasma confinement time. An industrial process controller (Gould 484) is used to control the timing sequences of the experiment and the magnetic field strength. Various safety interlocks are also connected to the process controller.

For a typical shot (see Fig. 2-5), the magnetic field is first ramped up to a pre-set value. The gas puff valve is also opened at this time to fill the machine to the desired background pressure. When the magnetic field is stabilized, a trigger is sent to the CAMAC data aquisition system. This time is labeled as $t = 0$ for all the experimental data. The ECR heating system is turned on at $t = 0.1$ s to break down the gas and form a plasma. The plasma reaches steady state in a few hundred milliseconds. The ICRH pulse is controlled by a CAMAC timer module (Jorway 221/222). The gas puff and ECRH are turned off at $t = 1.8$ s and the plasma is allowed to decay. The shot ends at $t = 2.0$ s when the magnet is ramped down.

2.1.6 data acquisition

A CAMAC-based data acquisition system (LeCroy) is used in the Constance B experiment in conjunction with a VAX 11/750 computer (Digital Equipment Corporation). It uses the VAX/VMS data aquisition software package MDS [Fredian and Stillerman, 1986] to set up and control the data system and to process the signals. Data processing occurs between shots while the magnet is cooling down.

A variety of waveform digitizers are used. Most of the data, such as the ionization gauge pressure and diamagnetic loop voltage, is sampled at 2 kHz over two seconds by a LeCroy 8212 digitizer. For the microwave interferometer, a phase digitizer (Jorway 1808) is used, and there are PHA modules (Lecroy 3512/3587/3588) for obtaining time resolved X-ray pulse-height spectra. The ion time-of-flight analyzer, charge-
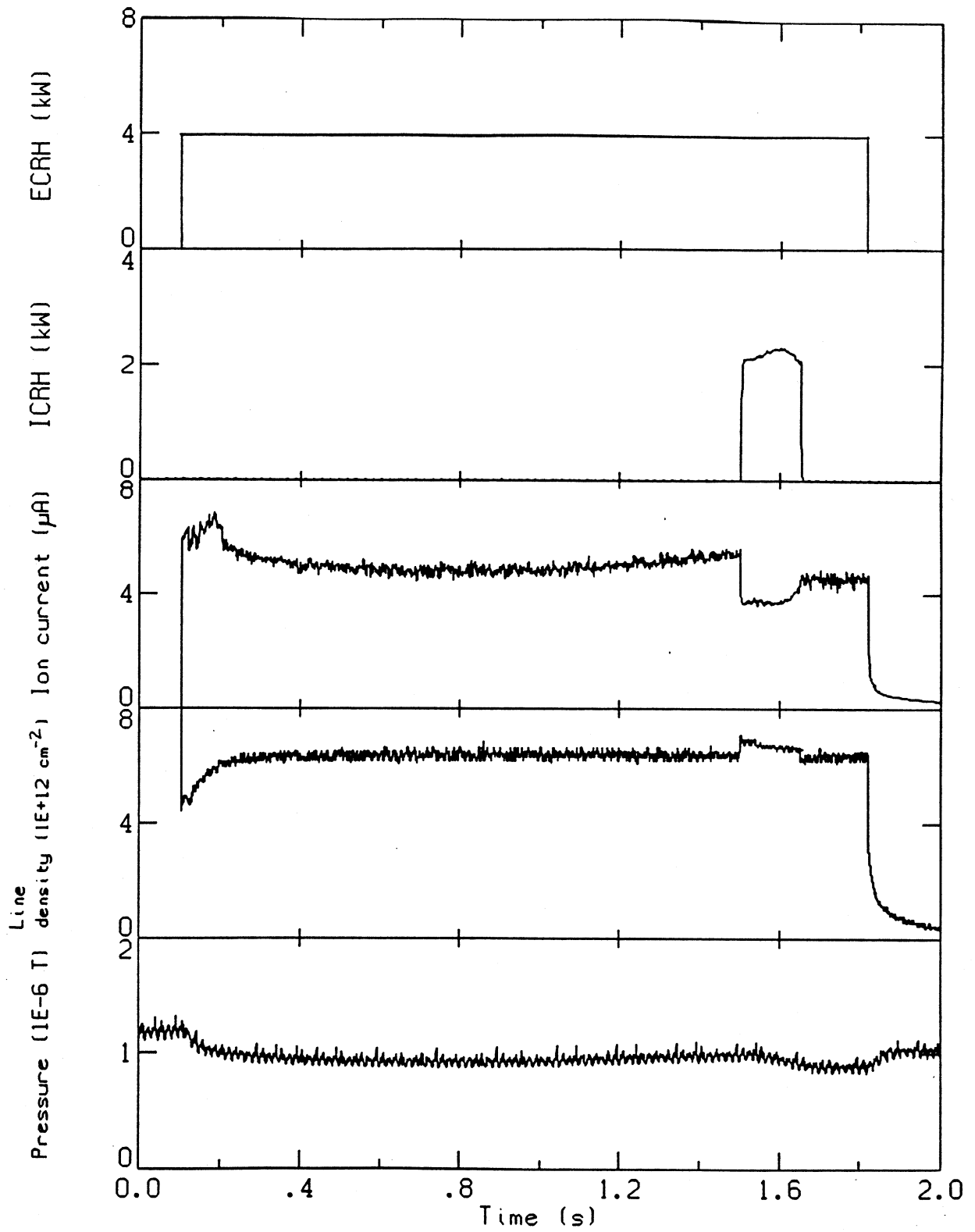
Figure 2-5: A typical shot for the Constance B mirror experiment.

coupled-device camera and spectrometers all require special CAMAC modules for data acquisition.

2.2 Diagnostics and experimental method

2.2.1 end loss analyzer

A gridded end-loss analyzer[1] (ELA) is located in the south fan tank. It can be used like an ELA to measure the maximum plasma potential and average ion temperature of the plasma, or like a Faraday cup to measure the ion and electron end-loss currents. The ELA has a one-eighth inch diameter entrance aperture followed by three grids and a collector. The outermost grid is grounded. The middle grid (ion repeller) is biased to repel ions with energies below its potential. The innermost grid (electron repeller) is biased to repel electrons with energies below its potential. The electron repeller grid also serves to suppress secondary electron emission from the collector since it is usually biased to -2000 V. In cases where the electron repeller grid is grounded, secondary electron emission from the collector is suppressed by biasing the collector to +180 V using a battery.

The ELA is located near the magnetic axis, 180.5 cm from the midplane. The magnetic field lines are parallel to the axis of the ELA and the magnetic flux surfaces are highly elliptical. One-dimensional radial scans of the plasma end loss can be made using a pair of deflecting magnets. The deflecting magnets move the mirror fan (in its "thin" direction) up and down relative to the position of the ELA. The amount of movement by the mirror fan for a given amount of current in the deflecting magnets is determined by the EFFI code [Sackett, 1978], which calculates the magnetic field generated by the baseball and deflecting magnets.

When operated as a Faraday cup, the ELA can measure the end loss currents for the ions and hot and cold electrons. The current collected by the ELA is passed through a resistor (R) and the resulting voltage drop (V) is related to the current

---

[1]This end loss analyzer was designed by Robert Klinkowstein for the TARA tandem mirror experiment.

density of particles in the loss cone at the midplane by

$$J_{\parallel} = \frac{2}{AT} \frac{B_o}{B_w} \frac{V}{R},$$ (2.1)

where A is the area of the entrance aperture, $T \, (= 0.26)$ is the grid transmission coefficient, B_o is the midplane magnetic field strength, B_w is the magnetic field strength at the ELA and the factor of two accounts for the fact that end loss on only one end of the machine is measured. Since hot electrons are collected along with ions, the hot electron current density must be subtracted to find the true ion current density.

The ELA can also measure the maximum plasma potential (ϕ_p) and average ion end-loss temperature (T_i) of the plasma by sweeping the ion repeller grid through a range of positive voltages while biasing the electron repeller grid to -2000 V. The ions are expelled from the plasma with typical energy $\varepsilon = q_i\phi_p + T_i$. As long as the voltage on the ion repeller grid (V_{rep}) is less than ϕ_p, all the ions are collected. When the repeller voltage exceeds ϕ_p, ions with energy less than $q_i V_{rep}$ are not collected and the ion current measured by the ELA will start to drop. The knee in the curve gives the maximum plasma potential and the rate of decline is inversely proportional to the ion temperature.

The shape of the ELA characteristic can be determined quantitatively in the limit that the ions are flow confined. Flow confinement assumes that the ions are sufficiently collisional so that their distribution function is Maxwellian, even in the loss cone. However, it also assumes that they are not so collisional that the ion's energy (ε) and magnetic moment (μ) are not conserved near the ion's turning point. Flow confinement is a valid approximation in Constance B since the ion mean-free-path is on the order of the plasma length. For a square well magnetic field where the maximum confining potential occurs at the mirror peak, the current density of ions in the loss cone with energies greater than $E = q_i V_{rep}$ is given by

$$
\begin{aligned}
\Gamma_{\parallel i}(E) &= \int_0^{2\pi} d\theta \int_E^{\infty} d\varepsilon \int_0^{(\varepsilon - q_i\phi_p)/B_p} v_{\parallel}\sqrt{\frac{2}{m_i^3}} \frac{B_o f(\varepsilon)}{(\varepsilon - q_i\phi_o - B_o\mu)^{1/2}} d\mu \\
&= n_i \frac{B_o}{B_p}\sqrt{\frac{2T_i}{\pi m_i}} \exp\left[\frac{-q_i(\phi_p - \phi_o)}{T_i}\right]\left(1 + \frac{E - q_i\phi_p}{T_i}\right)\exp\left[\frac{-(E - q_i\phi_p)}{T_i}\right]
\end{aligned}
$$ (2.2)

where ϕ_o and B_o are the potential and magnetic field at the midplane, ϕ_p and B_p

are the potential and magnetic field at the mirror peak and n_i is the ion density at the midplane. The lower energy bound for ions in the loss cone is $E = q_i \phi_p$ because ions with energy less than this cannot escape from the mirror. This equation is of importance for two reasons. First, it can be fitted to the ELA characteristic to determine the maximum plasma potential and ion temperature. Second, it can be used to determine the theoretical ion confinement time in the flow limit, as shown in section 3.2.1. An important feature of Eqn. 2.2 is that the ion-confining potential dip $(\phi_p - \phi_o)$ cannot be determined from the shape of the ELA characteristic, but only from its height.

Error in the end-loss current density measurement is due primarily to error in determining the AT product in Eqn. 2.1 (10%) and shot-to-shot variations in Constance B (5%). The error in the plasma potential determined from the knee in the ELA characteristic is about 10%. The ion temperature measured by the ELA is typically overestimated by a factor of two (compared to other diagnostics) due to the large RC time constant of the ELA (necessary to obtain an adequate signal-to-noise ratio) and therefore is not used.

2.2.2   ion time-of-flight analyzer

In order to determine the charge state distribution of the ion end-loss flux, a time-of-flight (TOF) analyzer was designed and constructed for this thesis [Petty, *et al.*, 1988]. Ion temperatures can also be determined for each ion species. An ion leaving the plasma as end loss has a total energy equal to its kinetic energy $(\mathcal{E})$ plus its potential energy $(q_i \phi_p)$. If the ion is then accelerated through an externally applied potential (ϕ_b), the time required for it to transverse a distance L is

$$t = L \sqrt{\frac{m_i}{2[q_i(\phi_p + \phi_b) + \mathcal{E}]}}. \tag{2.3}$$

The condition $\mathcal{E} \ll q_i(\phi_p + \phi_b)$ is always well satisfied, therefore

$$t \approx L \sqrt{\frac{m_i}{2q_i(\phi_p + \phi_b)}}. \tag{2.4}$$

Thus, the time-of-flight of an ion is proportional to the square root of its mass-to-charge ratio.

The ion flux ($\Gamma_{\parallel i}$) is proportional to the height of the output pulse for that ion species from the TOF analyzer. The absolute values of the ion fluxes are determined by scaling them according to the total ion (electric) current-density measured by the ELA:

$$\sum_i q_i \Gamma_{\parallel i} = J_{\parallel i}. \tag{2.5}$$

The TOF analyzer is located in the south fan tank near the magnetic axis and next to the ELA. One dimensional radial scans of the plasma end loss can be made using the deflecting magnets, as described in the previous section.

The temperature of each ion species can also be determined from the TOF data. The energy dependence of each ion species' flux can be found from the rise time of its pulse using Eqn. 2.3:

$$\varepsilon = q_i \phi_p + \mathcal{E} = \frac{m_i L^2}{2t^2} - q_i \phi_b. \tag{2.6}$$

This data is then fit to Eqn. 2.2 to determine the plasma potential and ion temperature. The finite rise time of the analyzer system (15 ns) leads to a minimum measurable ion temperature, which is given by

$$T_i(\text{eV}) = 1.12 \times 10^{-4} \sqrt{\frac{[z_i(\phi_p + \phi_b)]^3}{A_i}}, \tag{2.7}$$

where z_i is the ion charge state and A_i is the ion mass in amu. Thus, the higher the charge state the more difficult the measurement. In practice only ions up to $z_i = 5$ are analyzed.

There are four sections to the time-of-flight analyzer: (1) the accelerating/focusing lens, (2) the deflection plates, (3) the time-of-flight length and (4) the ion detector. A drawing of the the first two sections is shown in Fig. 2-6. For simplicity the analyzer is designed to be a line-of-sight device. If potential is measured relative to the plasma, then the entrance aperture is negative by the plasma potential (ϕ_p). The second aperture is biased at a high negative voltage (ϕ_b) to accelerate the ions to 2–3 kV. It is important that this bias voltage be much greater than the ion temperature, otherwise the TOF will depend more on temperature than on $\sqrt{m_i/q_i}$. These two accelerating apertures make up a convergent lens with a focal length approximately equal to three
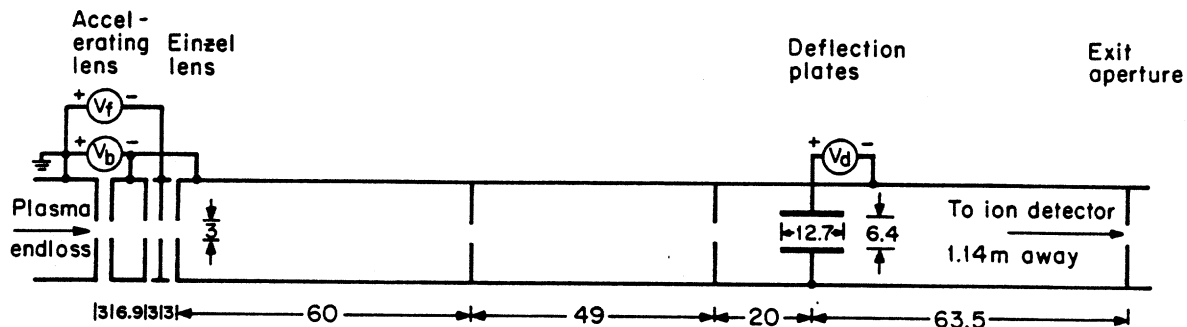
Figure 2-6: Diagram of accelerating/focusing lens, collimators and deflection plates. All dimensions are in mm.

times the distance between them [Harting and Read, 1976]. An einzel lens is placed after the accelerating lens in order to refocus the beam and therefore increase the amount of current reaching the ion detector. The einzel lens does not change the ion's energy because the entrance and exit apertures are at the same potential. The middle aperture is biased with a second power supply at a less negative potential (ϕ_f). The ions exit the accelerating/focusing lens with paths parallel to the axis when the sum of the midfocal lengths of the two lenses equals the distance between their reference planes. The current at the ion detector is typically increased by a factor of fifteen when the einzel lens is used.

After leaving the accelerating/focusing lens, the ion beam is collimated and passes between two electrostatic deflection plates. Normally, one plate is biased relative to the other, creating an electric field which deflects the ions. The angle of deflection (θ) is given by

$$\tan \theta = \frac{l\phi_d}{2d(\phi_p + \phi_b)},\tag{2.8}$$

where l is the deflection plate length, d is the separation between plates and ϕ_d
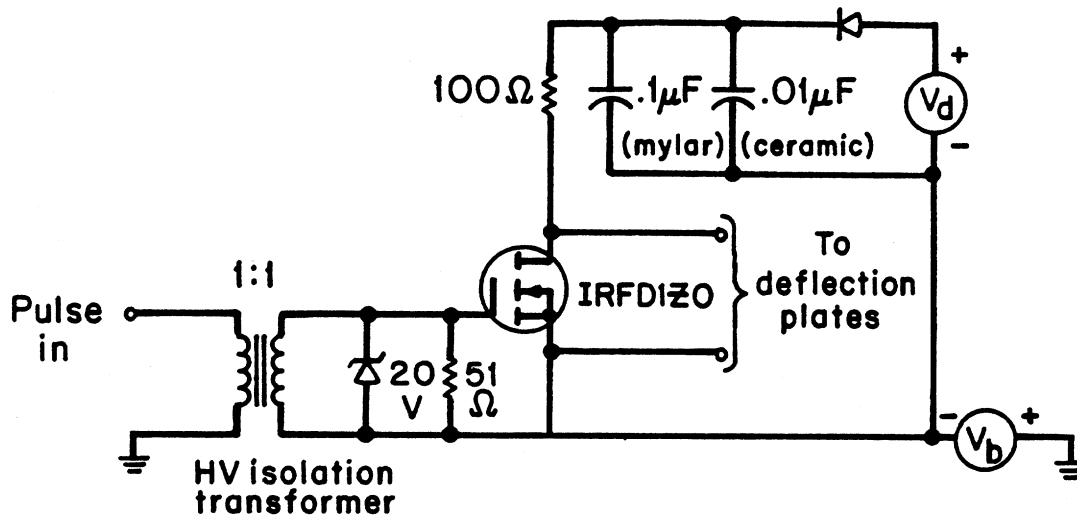
Figure 2-7: Fast switching circuit for deflection plates.

(= 100 V) is the potential difference between the plates. Note that the angle of deflection is independent of ion mass or charge. There is an exit aperture located 63.5 mm past the deflection plates which deflected ions cannot pass. In order to send a burst of ions through the exit aperture to the ion detector, the deflection plate voltage is pulsed to zero by the circuit shown in Fig. 2-7. Typical pulse lengths are 100–300 ns, with 7 ns rise and fall times. This fast rise time is necessary in order to determine the ion temperature from the analyzer output pulse. Because of fringing electric fields, the minimum required pulse length is actually twice as long as it takes the slowest ion to travel the length of the deflection plates (a too short pulse length will result in the lowest charge states being cut off).

After passing through the exit aperture, the ions travel down a long section of tubing. This serves as the time-of-flight length. In general, the longer the tube, the better the m_i/q_i resolution and the more accurate the ion temperature measurement. In this case, the maximum length was set by space limitations to be 1.20 m. This length gives typical time-of-flights of several microseconds.

At the end of the flight, an electron multiplier serves as the ion detector. A

Vacumetrics AEM-1000 multiplier is used which has a rise time of 3 ns and is small enough to fit inside a standard 1.375 inch diameter tube. The multiplier gain is 5×10^5 at 2 kV. The electron multiplier supply voltage is the same bias voltage used to accelerate the ions. Because large peak currents are drawn from the multiplier (typically 100 μA), a 300 pF vacuum compatible, glass capacitor is placed across the resistor from the last dynode to ground. The multiplier output is amplified by an EG&G PARC 115 wideband pre-amp with a gain of ten. All signal cables are terminated in 50 Ω. The total rise time of the analyzer system is determined from individual counts to be 15 ns.

The magnetic field lines from the Constance B baseball magnet are parallel to the axis of the TOF analyzer, with a typical field strength of 90 G at the entrance. The entire length of the analyzer is magnetically shielded to ensure that there are no ion gyroradius effects and to prevent gain loss of the electron multiplier. The magnetic shielding doubles as a high voltage shield since the analyzer floats at the bias voltage.

The TOF analyzer can produce an ion spectrum every 20 μs. Since the usual time scale of interest is several hundred milliseconds, data averaging is performed to improve the signal-to-noise ratio. On Constance B, the major source of noise is from hot electron end loss. Electrons with kinetic energy greater than about 40 keV will enter the analyzer and pass by the deflection plates unaffected, therefore reaching the electron multiplier. Summing many spectra averages these counts out to an offset current. Because the TOF analyzer is a line-of-sight instrument, a second source of noise is from photons which can pass through the apertures and strike the detector.

The primary method of signal averaging is to digitize the electron multiplier output at 100 MHz and then sum the spectra using a hardware signal averager. This setup consists of a Transiac 2001s transient digitizer linked to a Transiac 4001 signal averaging memory. Spectra 20.48 μs long can be summed at a rate of 1 kHz, with summation rate being inversely proportional to memory size. Thus, averaging over a period of one second gives a typical signal-to-noise ratio improvement of 32. A TOF spectrum for an argon plasma is shown in Fig. 2-8, demonstrating the resolution possible between high charge state ions. Plasma impurities are also evident, principally
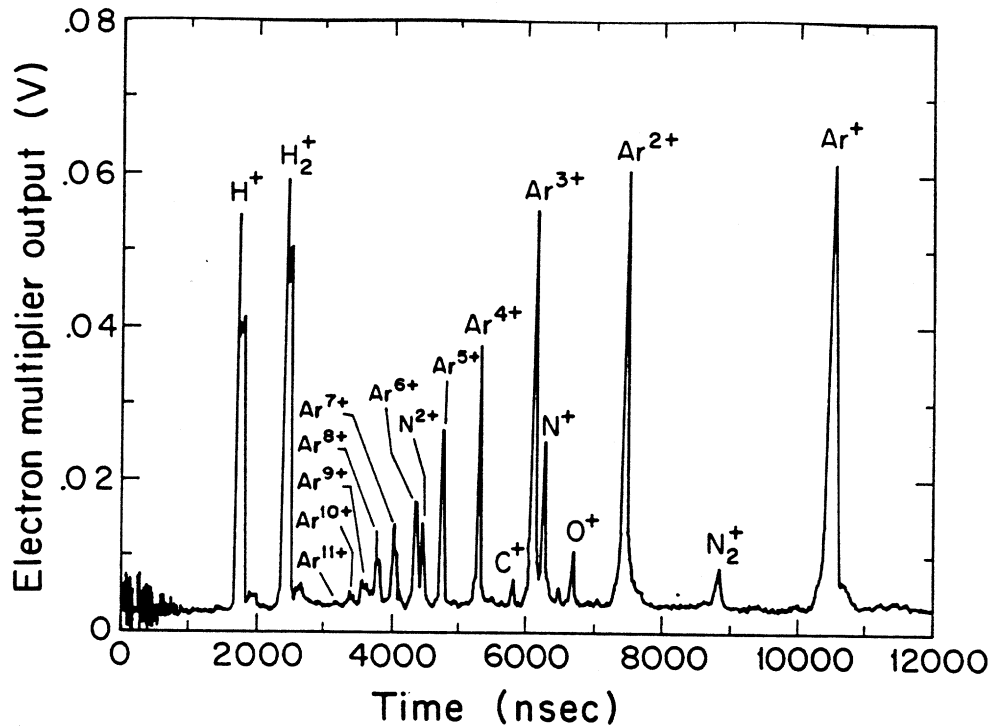
Figure 2-8: Time-of-flight spectrum for an argon plasma, the sum of 1000 spectra over one second.

atomic and molecular hydrogen. Hydrogen is the normal working gas of Constance B and is embedded in the gettered walls.

The main source of error in the charge state distribution measured by the TOF analyzer is in determining how the ion conversion efficiency of the electron multiplier differs for various ion masses and charge states. This in turn depends upon the electron yield for ion impact (γ) of the first dynode. An absolute calibration of γ is difficult, mainly because it is strongly affected by the surface condition of the dynode material [Brown, 1966; Flügge, 1955]. A relative calibration of γ is done by analyzing the height of individual counts from the electron multiplier corresponding to different ion species. The effect of ion mass on γ for singly charged ions can be seen in Fig. 2-9 and the effect of ion charge on γ for the first four charge states of argon can be seen in Fig. 2-10. No correlation between γ and ion mass or charge is found to within 10% for elements up to argon.

The main source of error in determining the maximum plasma potential from TOF analyzer data is the uncertainty in knowing the bias voltage of the analyzer
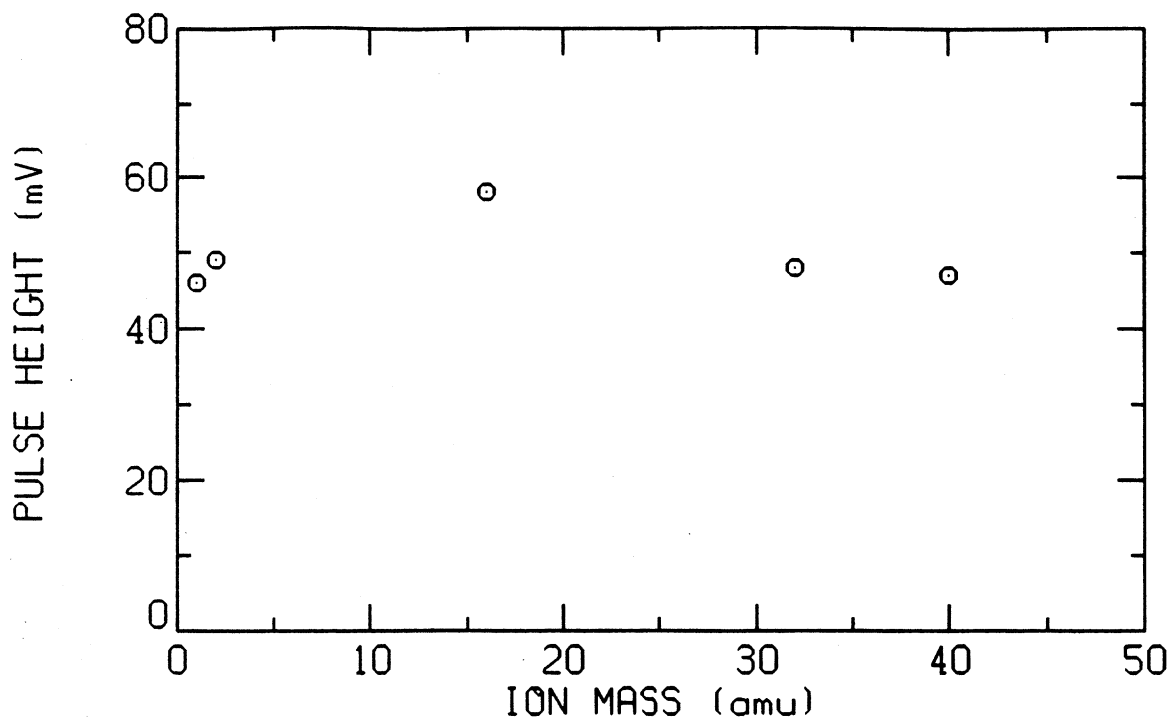
Figure 2-9: Count pulse height from the electron multiplier vs. ion mass for H^+, H_2^+, O^+, O_2^+ and Ar^+.
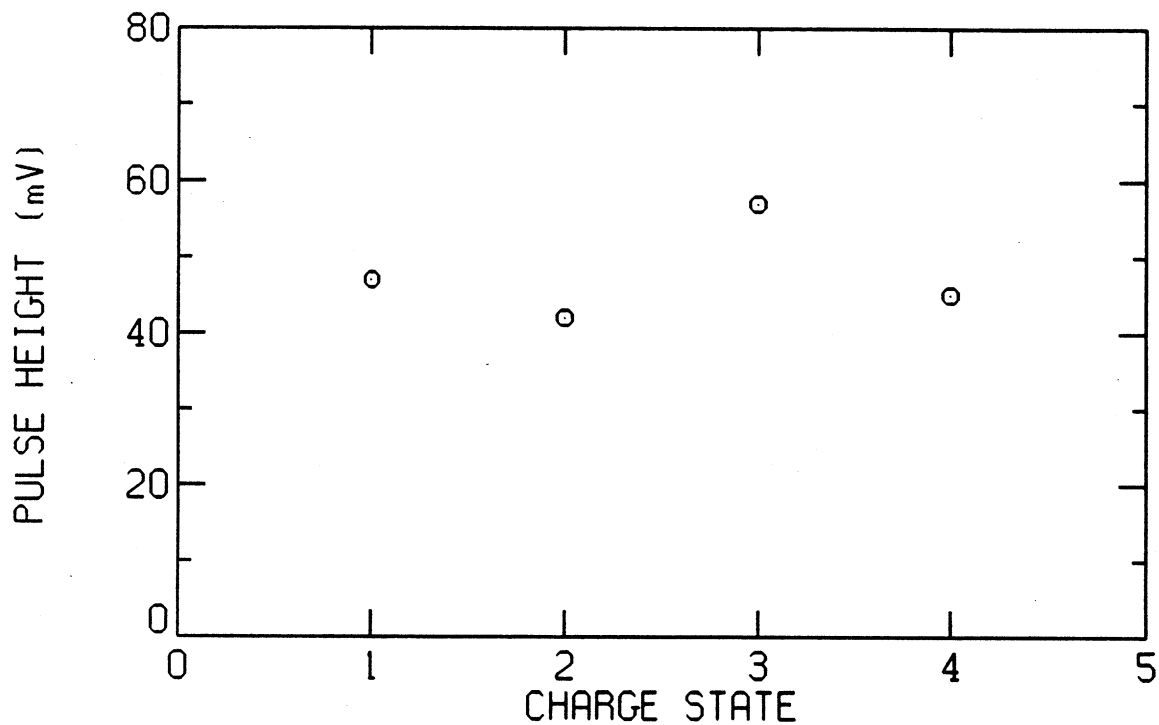
Figure 2-10: Count pulse height from the electron multiplier vs. ion charge state for argon.

(which adds linearly to the plasma potential), which gives a 5% error. Error in the plasma potential due to the finite digitization rate of the data can be greatly reduced by averaging over ion charge states. The ion temperature measurement has a 10% scatter due to fitting errors.

2.2.3   visible light spectrometers

Two visible light spectrometers are used to determine the ion temperature from Doppler broadening of ion emission lines. A 0.62 m spectrometer (Instruments SA HR640) on the west side of the central chamber views the plasma through a quartz window and lens. The spectrometer line-of-sight is perpendicular to the magnetic field lines. The spectrometer grating is ruled at 2400 grooves/mm and has a wavelength range between 2000 Å and 7000 Å. A microchannel-plate image-intensified photodiode array (Princeton Instruments IRY-512-N) serves as the photon detector. This optical multichannel analyzer (OMA) can record a complete spectrum approximately 50 Å wide in 17 ms. The photodiode array consists of 512 detectors whose response is digitized by a detector controller (Princeton Instruments ST-110). The instrumental resolution of the spectrometer and OMA is measured using a mercury vapor lamp with a quartz window. An ion line recorded by the spectrometer is fitted to a gaussian shape using a nonlinear least squares fitting routine to determine its width [Press, *et al.*, 1986]. The perpendicular ion temperature can then be determined from the Doppler broadening of the line by

$$T_{\perp i} = \frac{m_i c^2}{8 \ln 2} \frac{\Delta_d^2 - \Delta_i^2}{\lambda^2}, \tag{2.9}$$

where Δ_d is the FWHM of the line, Δ_i is the instrumental resolution and λ is the wavelength of the line.

A 0.5 m visible light spectrometer (Jarrell-Ash 82-049) next to the north fan tank measures the ion temperature approximately parallel to the magnetic field lines. It also views the plasma through a quartz window and lens. The spectrometer grating is ruled at 1200 grooves/mm and uses a photomultiplier tube (Hamamatsu R928P) as the photon detector. The photomultiplier is magnetically shielded and protected

from plasma X-rays by lead blocks. The photomultiplier signal is first sent to a fast pre-amp (Analog Devices 50J), then to a discriminator (Lecroy 623B) and is recorded by a scaler (Lecroy 8590). Line spectra are obtained by changing the spectrometer wavelength setting between plasma shots.

The error in determining the ion temperature from Doppler broadening is due to two sources. First, the error in measuring the instrumental resolution is about 10%. Second, the shot-to-shot scatter in the ion temperature is about 10% due to the small amount of Doppler broadening relative to the instrumental resolution. The total error in the ion temperature is therefore around 15%.

2.2.4   VUV spectrometer

A vacuum ultraviolet (VUV) spectrometer located on the east side of the central chamber measures the brightnesses of ion emission lines in order to determine the ion densities. It is a 0.2 m normal incidence spectrometer (Minuteman 302-VM) with a 1200 grooves/mm iridium grating and has a wavelength range between 450 Å and 2500 Å. A sodium salicytate phosphor converts VUV photons into visible light, which is then detected by a matched photomultiplier (Hamamatsu R1527). The photomultiplier is shielded from magnetic fields and plasma X-rays. The photomultiplier output first goes to a wide-band pre-amp (EG&G PARC 115) and then to a discriminator and scaler.

In order to determine the ion densities, photons from $\Delta n = 0$ transitions to the ground state are measured. The brightness of these spectral lines is related to the ion density by

$$B_{ij} = \frac{1}{4\pi} \left(\frac{A_{ij}}{\sum_k A_{ik}} \right) \int n_i n_e \langle \sigma v \rangle^{ce} dl, \qquad (2.10)$$

where A_{ij} is the Einstein coefficient for spontaneous emission, n_i is the density of ions in the ground state (or low metastable state), n_e is the electron density and $\langle \sigma v \rangle^{ce}$ is the excitation rate parameter for electron impact. All ion species are assumed to have the same radial profile since no spatial resolution by the VUV spectrometer is possible. The ion density is therefore proportional to the line brightness divided by

the (average) excitation rate parameter. For oxygen, excitation rate parameters from Itikawa, *et al.*, (1985) are used, while for neon the gaunt method [Gabriel and Jordan, 1971] is used. The relative ion densities measured by the VUV spectrometer are scaled according to the electron density profile measured by the microwave interferometer and CCD camera (see next two sections) using the quasineutrality condition:

$$\sum_i z_i n_i = n_e. \tag{2.11}$$

A significant fraction of the ions are experimentally found to be in metastable states and their contribution is included in calculating the total ion density.

The error in determining the relative ion densities is dominated by the uncertainty in the excitation rate parameters, which for most lines is 20%. Using O IV and Ne V line ratios, the VUV spectrometer response is found to be independent of wavelength to within 5% between 480 Å and 790 Å, the region where the majority of data is taken. When two lines are located close to each other (the instrumental resolution is 6.8 Å), additional error in deconvoluting their peaks can occur.

2.2.5   microwave interferometer

A single channel 24 GHz microwave interferometer[2] measures the electron line density at the midplane. The interferometer is oriented at 45 degrees with respect to the symmetry plane and launches microwaves perpendicular to the magnetic axis. The index of refraction for these O-mode waves is approximately [Mauel, 1985]

$$N_\perp^2 = 1 - \frac{\omega_{pe}^2}{\omega^2} \langle \frac{1}{\gamma} \rangle, \tag{2.12}$$

where

$$\langle \frac{1}{\gamma} \rangle = \frac{K_1(mc^2/T_{eh})}{K_2(mc^2/T_{eh})} \tag{2.13}$$

is a relativistic correction to the cold plasma dielectric caused by the relativistic mass shift. The relativistic correction implies that hot electrons are more transparent to waves than cold electrons because they cause a smaller phase shift.

---

[2]The interferometer hardware was set up by Donna Smatlak and software to interpret the data was written by Evelio Sevillano.
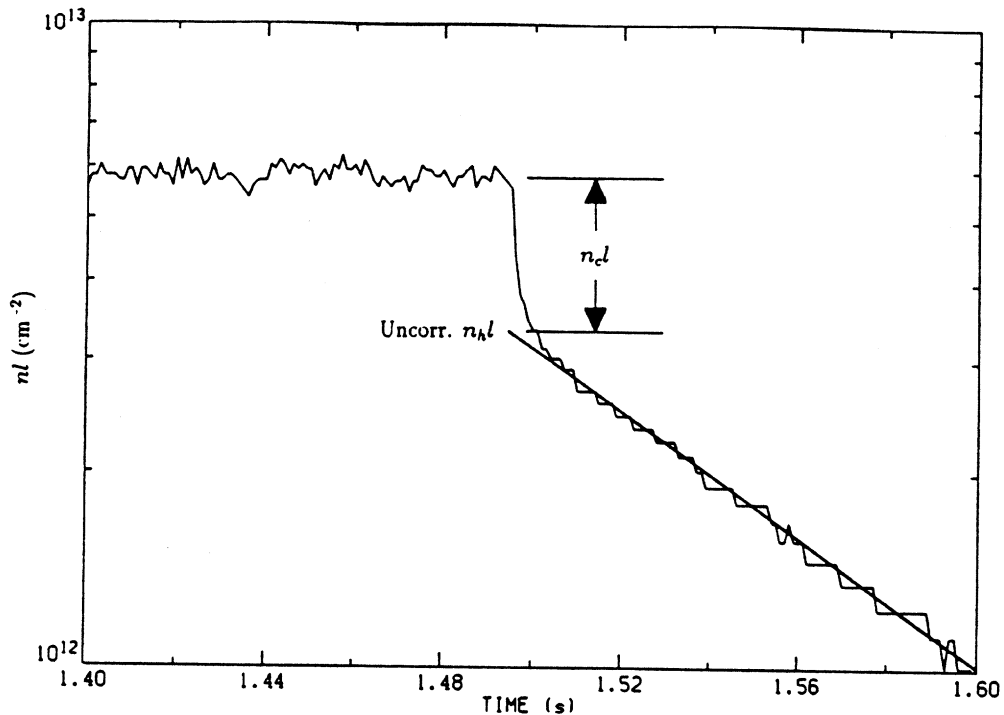
Figure 2-11: The technique used to divide the electrons into their hot and cold components from the microwave interferometer decay is shown.

From the decay of the interferometer when the ECRH is turned off, the electron density is divided into "hot" and "cold" components. The cold electrons, which have a temperature of around 100 eV, scatter quickly into the loss cone and leave the mirror in a few hundred microseconds. The hot electrons, which have a temperature of around 300 keV, decay on a time scale of seconds. Thus, the long-time decay of the total line density is extrapolated back to the ECRH turnoff time to divide the electrons into their hot and cold components (see Fig. 2-11). Knowing the hot electron temperature, the hot electron line density can be corrected for relativistic effects by dividing it by $\langle 1/\gamma \rangle$.

2.2.6 CCD camera

A camera system[3] consisting of a charge-coupled-device (CCD) light-integrating camera (EG&G Reticon MC9128) controlled by a CAMAC module (Data Design Corp.

---

[3]The camera system was set up and software to interpret the data was written by Daniel Goodman.

AC100) is used to measure the spatial distribution of the electron density. The charge sensitive detectors are mounted in a square 128×128 array. Frame integration times can be set from 3 ms to several seconds. In order to amplify small light signals, a microchannel-plate image intensifier (Electrophysics 9100) is mounted in front of the CCD camera.

The CCD camera records the emission of a single atomic transition using optical bandpass filters (10 Å FWHM). The CCD camera is located in the north fan tank and views the plasma approximately parallel to the magnetic field lines. The brightness of an emission line from a neutral atom is given by

$$B(r) = \frac{1}{4\pi} \int n_o n_e \langle \sigma v \rangle^{ce} dz, \qquad (2.14)$$

where n_o is the neutral density and dz is the line-of-sight path element for the CCD camera. In order to determine the cold electron density profile, the 4^1D (4922 Å) He I line for a helium plasma is used. The contribution of hot electrons to the overall line brightness is small. The neutral density is calculated to be uniform across the plasma diameter for helium discharges and the cold electron temperature is measured as a function of radius as described in section 2.2.9. Thus, the cold electron density integrated along a magnetic field line can be found from the brightness profile by

$$\int n_{ec} \, ds = \frac{4\pi B_c(r)}{n_o \langle \sigma v \rangle_c^{ce}} \times \frac{\int n \, ds}{\int n \, dz}, \qquad (2.15)$$

where the last term is a geometrical correction to compensate for the difference between a line-of-sight integration and a field line integration. The geometrical correction is calculated using the 3-D equilibrium plasma-pressure profile for Constance B [Chen, 1989] and is shown in Fig. 2-12. The ten free parameters in the model profile are adjusted until the shape and diameter of the experimental camera picture agree with the model simulated picture.

Although two-dimensional profiles of the electron density are measured, they are azimuthally averaged over flux surface in order to use them in conjunction with other radial profile data. Also instead of using a calibrated brightness profile to determine the absolute magnitude of the cold electron density, the average density profile is
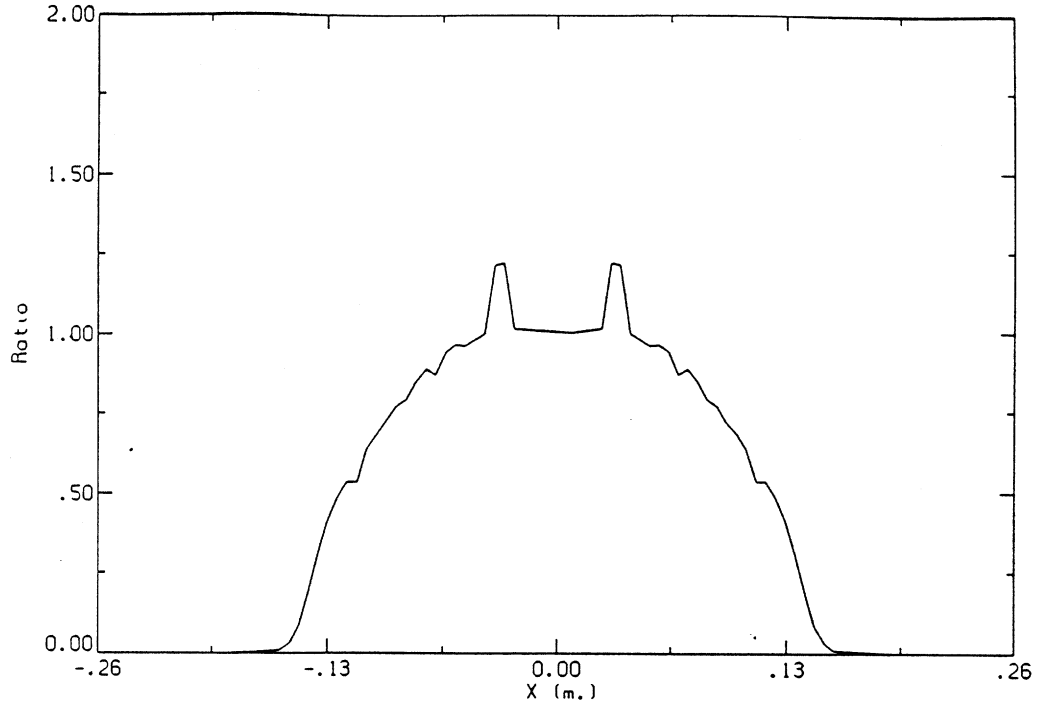
Figure 2-12: The geometrical correction $\int n\, ds / \int n\, dz$ is shown for the best fit plasma model.

radially integrated and set equal to the cold electron line density measured by the microwave interferometer:

$$\int \left(\frac{\int n_{ec}\, ds}{L_p} \right) dl = \langle n_c l \rangle, \qquad (2.16)$$

where L_p is the plasma length. From the CCD camera pictures it is determined that the plasma is approximately confined within the $R = 1.37$ mod-B surface, which gives a plasma length of $L_p(cm) = 41.0 - 1.45r$. The integrated cold electron density profile is determined in this way with and without ICRH.

The hot electron density profile is determined in the afterglow of a hydrogen plasma. After the ECRH is turned off, the cold electrons quickly scatter into the mirror loss cone, leaving behind a hot electron plasma. Since the decay time of the hot electrons is on the order of seconds, their spatial profile can easily be measured in the afterglow. Since the excitation rate parameter of atomic and molecular hydrogen is nearly independent of electron energy in the 100–1000 keV range, only the geometrical corrective factor from Eqn. 2.15 is needed to determine the integrated hot electron profile. The absolute magnitude is determined from the hot electron line

density measured by the microwave interferometer, just as for the cold electrons. The hot electron profile should not change during ICRH since the hot electrons are not expected to interact with low frequency rf.

Although the electron density profile depends upon several subsidiary measurements and models, only two have an important effect on the error. They are error in $\langle\sigma v\rangle^{ce}$ (for the cold electrons) and error in the geometrical correction factor. Because of the weak dependence of $\langle\sigma v\rangle^{ce}$ on electron temperature for the 4922 Å He I line, the error in this term is only about 10%. The geometrical correction term is equal to 1 on axis, and deviates substantially from 1 only at the plasma edge. Thus, the error in this term is much smaller near the plasma center (10%) than at extreme radii (factor of two). The overall error in the density profile is therefore about 15% for the plasma region of interest. Also the cold electron density profile measured for an argon plasma was found to be nearly identical with the density profile for a helium plasma [Goodman, 1989]. Thus, the helium profile is used for all gases since it is the most accurate.

2.2.7 · X-ray spectroscopy

X-ray spectra have been taken over a range of photon energies[4] from 1 keV to 1.5 MeV using three detectors: a NaI(Tl) detector (0.03–1.5 MeV), a high purity Ge detector (2–150 keV) and a Si(Li) detector (1–12 keV). The NaI(Tl) detector is the standard diagnostic used to determine the (chord averaged) hot electron temperature from X-ray bremsstrahlung. It was found that the X-ray intensity spectrum can be adequately modeled by a Maxwellian distribution, which is much simpler to use than a mirror distribution. Although diamagnetic loop temperatures are used in this thesis (see next section), it is important to note that they have been confirmed by X-ray spectroscopy.

---

[4]The X-ray spectroscopic measurement was conducted by Sam Hokin.

2.2.8 diamagnetic loop

An elliptical diamagnetic loop[5] measures the stored energy of the plasma, from which the plasma beta and hot electron temperature can be determined. The 20 turn pickup loop is wound inside a one-half inch diameter stainless-steel tubing (0.01 inch wall thickness) and is installed inside the vacuum chamber four inches from the midplane. The loop surrounds the plasma and is large enough to avoid limiting the plasma size. In order to obtain the magnetic flux inside the loop due to plasma currents, the diamagnetic loop signal is integrated by a gated electronic integrator (Evans 4031). Using the 3-D equilibrium plasma-pressure profile for Constance B [Chen, 1989], the total stored energy of the plasma can be found from the measured magnetic flux. Knowing the volume of the hot electrons (1000 cm^3 for 3.5 kG), the plasma beta can also be found.

The hot electron temperature is related to the total stored energy (W) by

$$T_{eh}\langle\gamma\rangle = \frac{W}{\langle n_h l\rangle A},\qquad(2.17)$$

where $\langle n_h l\rangle$ is the hot electron line density from the microwave interferometer (uncorrected for relativistic effects) and A ($= 58$ cm^2 for 3.5 kG) is an effective area which depends upon the hot electron radial profile and volume. The left hand side of this equation is a function only of temperature and therefore the hot electron temperature can be determined using Eqn 2.13.

The error in calculating the stored energy and plasma beta from the diamagnetic loop signal is estimated to be 10%. The hot electron temperature has the additional error of the hot electron density profile, so its error is about 15%.

2.2.9 line ratios

The brightness ratio of a He I singlet (4911 Å) and triplet (4713 Å) line is used to determine the cold electron temperature. The measured line ratio is inverted to find T_{ec} using knowledge of the temperature-dependent excitation rate parameters for

---

[5]The diamagnetic loop was constructed and calibrated by Xing Chen.

population of the excited atomic states as well as the branching ratios for depopulation of the states. A power law fit to this inversion which is accurate to within 8% of the analytical result over the temperature range 15–500 eV is [Goodman, 1989]

$$T_{ec}(\text{eV}) = 26 \left(\frac{B(4922\text{Å})}{B(4713\text{Å})} \right)^{1.15}. \tag{2.18}$$

The line ratio can be measured with the CCD camera using bandpass filters to obtain 2-dimensional temperature profiles. For non-helium plasmas, a small amount of helium impurity is introduced in order to make the measurement. In these cases, the visible light spectrometer with the OMA is used to determine the ratio since it has a better signal-to-noise ratio than the CCD camera.

The error in T_{ec} is about 40% due to differences between the theoretical and experimental cross sections for electron impact excitation of the helium singlet-triplet lines.

Chapter 3

Plasma Modeling

In this chapter, a self consistent model is developed for the ion densities, end loss fluxes and confinement times, which are related by

$$\tau_{\|i} = \frac{L_p n_i}{\Gamma_{\|i}},\tag{3.1}$$

where $\Gamma_{\|i}$ is the end loss flux out both ends of the mirror. Only the plasma center is considered, since that is the region of extraction for ECR ion sources. This model is similar to one by West (1982), the main differences being that spatial diffusion confinement of high charge state ions is added along with ion radial transport. In addition, a model by West for the cold electron density is omitted in favor of experimental data. The electron particle and power balance equations are also examined to see how electron density, temperature and confinement time should scale with ECRH power density and neutral pressure. The model results will be compared to experimental results from Constance B in Chapter 4.

3.1 Ion particle balance

The ion densities are found from the ion particle balance equations. The density of each ion charge state is determined by balancing ionization, charge exchange, radiative recombination and loss of confinement:

$$\frac{dn_i}{dt} = (n_{eh}\langle\sigma v\rangle_{i-1,i}^{ion,h} + n_{ec}\langle\sigma v\rangle_{i-1,i}^{ion,c})n_{i-1} - (n_{eh}\langle\sigma v\rangle_{i,i+1}^{ion,h} + n_{ec}\langle\sigma v\rangle_{i,i+1}^{ion,c}$$

$$+n_o\langle\sigma v\rangle^{ex}_{i,i-1} + n_{ec}\langle\sigma v\rangle^{rr}_{i,i-1} + \frac{1}{\tau_i})n_i + (n_o\langle\sigma v\rangle^{ex}_{i+1,i} + n_{ec}\langle\sigma v\rangle^{rr}_{i+1,i})n_{i+1}$$

$$= 0, \tag{3.2}$$

where $\langle\sigma v\rangle^{ion}$ is the ionization rate parameter for the hot (h) and cold (c) electrons, $\langle\sigma v\rangle^{ex}$ is the charge exchange rate parameter, $\langle\sigma v\rangle^{rr}$ is the radiative recombination rate parameter and τ_i is the ion confinement time. Only single step ionization and charge exchange have been included and dielectronic recombination has been ignored. All rate parameters are averaged over Maxwellian distributions.

A general formula for the ionization rate parameter for electron impact is given by Lotz (1968):

$$\langle\sigma v\rangle^{ion}_{i,i+1}(\text{cm}^3\text{s}^{-1}) = 6.7 \times 10^{-7} \sum_{j=1}^{N} \frac{a_{ij}q_{ij}}{T_e^{3/2}} \left[\frac{\text{Ei}(P_{ij}/T_e)}{P_{ij}/T_e} - \frac{b_{ij}\exp c_{ij}}{P_{ij}/T_e + c_{ij}}\text{Ei}(\frac{P_{ij}}{T_e} + c_{ij}) \right], \tag{3.3}$$

where a_{ij}, b_{ij} and c_{ij} are constants tabulated for various ions by Lotz, T_e is in eV, P_{i1} is the ionization potential in eV for the outer shell, P_{i2} is the binding energy in eV for the first inner subshell, etc., q_{ij} is the number of electrons in the respective shells and the summation runs over N shells. An empirical formula which fits the experimental ionization cross-section data for argon of Müller, et al., (1980) to within 20% is

$$\langle\sigma v\rangle^{ion}_{i,i+1}(\text{cm}^3\text{s}^{-1}) = 9.37 \times 10^{-6} \frac{\text{Ei}(P_{i1}/T_e)}{P_{i1}T_e^{1/2}}, \tag{3.4}$$

where T_e and P_{i1} are in eV. The charge exchange rate parameter is calculated from [Müller and Salzborn, 1977]

$$\langle\sigma v\rangle^{ex}_{i,i-1}(\text{cm}^3\text{s}^{-1}) = 3.15 \times 10^{-6} z_i^{1.17} P_{i1}^{-2.75} \sqrt{\frac{T_i}{A_i}}, \tag{3.5}$$

where P_{i1} is in eV, T_i is the ion temperature in eV and A_i is the ion mass in amu. A formula for the radiative recombination rate parameter valid for $P_{i1} < T_{ec}$ is [Hutchinson, 1987]

$$\langle\sigma v\rangle^{rr}_{i+1,i}(\text{cm}^3\text{s}^{-1}) = 5.2 \times 10^{-14} z_i \left(\frac{P_{i1}}{T_{ec}}\right)^{\frac{3}{2}} \exp\left(\frac{P_{i1}}{T_{ec}}\right) \text{Ei}\left(\frac{P_{i1}}{T_{ec}}\right). \tag{3.6}$$

Radiative recombination is important only for very high charge states (it surpasses charge exchange around $z_i \sim 20$). It is included here only to be consistent with the work by West (1982).

In solving the ion particle balance equations, experimental values for the hot and cold electron density, electron temperature and neutral density are used in order to concentrate on the ion physics. The density of neutrals in the plasma is reduced from that outside the plasma (measured by the ionization gauge) due to burn up by ionization and charge exchange. The reduction factor is given by [West, 1982]

$$R = \frac{v_o S/2V}{v_o S/2V + n_{eh}\langle\sigma v\rangle_{0,1}^{ion,h} + n_{ec}\langle\sigma v\rangle_{0,1}^{ion,c} + \sum_{i=2} n_i \langle\sigma v\rangle_{i,i-1}^{ex}}, \qquad (3.7)$$

where v_o is the neutral velocity, S is the surface area of the plasma and V is the volume of the plasma. The charge exchange summation starts at $i = 2$ because

$$n_o + n_1 \rightarrow n_1 + n_o$$

does not change the neutral or ion density (ignoring charge exchange pumping of the neutrals). The neutrals are assumed to be at room temperature when calculating their velocity.

An ion particle balance equation given by Eqn. 3.2 can be written for each ion charge state. However, it is convenient to replace the ion particle balance equation for the first charge state with the quasineutrality condition:

$$\sum_i z_i n_i = n_{eh} + n_{ec}, \qquad (3.8)$$

which ensures that charge balance is satisfied. The ion confinement times still need to be found before the ion densities can be determined from these equations.

3.2 Ion confinement

The ion confinement time is uniquely determined by the need to balance creation and loss of ions and therefore is not an independent variable. Since the ion particle balance equation for the first charge state is not used to find the ion densities, it is an independent condition that can be used to determine the average ion confinement time. For a monatomic gas, the ion particle balance equation for the lowest charge

state is

$$\frac{dn_1}{dt} = (n_{eh}\langle\sigma v\rangle_{0,1}^{ion,h} + n_{ec}\langle\sigma v\rangle_{0,1}^{ion,c})n_o - (n_{eh}\langle\sigma v\rangle_{1,2}^{ion,h} + n_{ec}\langle\sigma v\rangle_{1,2}^{ion,c} + \frac{1}{\tau_1})n_1$$

$$+(n_o\langle\sigma v\rangle_{2,1}^{ex} + n_{ec}\langle\sigma v\rangle_{2,1}^{rr})n_2 + \sum_{i=2} n_o\langle\sigma v\rangle_{i,i-1}^{ex}n_i + \frac{\Gamma_{ext}}{L_p}$$

$$= 0, \tag{3.9}$$

where loss of n_1 due to radiative recombination has been neglected and Γ_{ext} is an externally supplied flux of singly ionized plasma from a pre-ionizer. Including an external flux allows two-stage ECR ion sources to be modeled. For modeling Constance B, which is a one stage ion source, external fluxes are neglected. Summing the ion particle balance equations over all charge states results in the global particle balance equation:

$$(n_{eh}\langle\sigma v\rangle_{0,1}^{ion,h} + n_{ec}\langle\sigma v\rangle_{0,1}^{ion,c})n_o + \sum_{i=2} n_o\langle\sigma v\rangle_{i,i-1}^{ex}n_i + \frac{\Gamma_{ext}}{L_p} = \frac{\sum n_i}{\langle\tau_i\rangle}, \tag{3.10}$$

where

$$\langle\tau_i\rangle = \frac{\sum n_i}{\sum n_i/\tau_i} \tag{3.11}$$

is the average ion confinement time. Defining the source function as

$$S_o = (n_{eh}\langle\sigma v\rangle_{0,1}^{ion,h} + n_{ec}\langle\sigma v\rangle_{0,1}^{ion,c})n_o L_p + \sum_{i=2} n_o\langle\sigma v\rangle_{i,i-1}^{ex}n_i L_p + \Gamma_{ext} \tag{3.12}$$

(the middle term is small compared to the first) allows the average ion confinement time be written as

$$\langle\tau_i\rangle = \frac{L_p \sum n_i}{S_o}. \tag{3.13}$$

This equation gives the relationship between the ion confinement time and the ion density. The ion confinement time for each individual charge state still needs to be found. Ions can be lost either parallel or perpendicular to the magnetic field lines, with the total ion confinement time given by

$$\frac{1}{\tau_i} = \frac{1}{\tau_{\|i}} + \frac{1}{\tau_{\perp i}}. \tag{3.14}$$

3.2.1 parallel ion confinement

Parallel ion confinement is dependent upon the axial profiles of the magnetic field and plasma potential. Since the axial potential profile is not measured, the potential trap model (shown in Fig. 1-3) is proposed based on the following reasons:

1. Since the electrostatically trapped cold electrons follow a Boltzmann distribution between the midplane and the mirror peak, with the electron density at the midplane being significantly larger, the potential must decrease from the midplane to the mirror peak according to the relation

$$\frac{n_{ec,m}}{n_{ec,o}} = \exp[-(\phi_o - \phi_m)/T_{ec}], \tag{3.15}$$

   where "o" refers to the midplane value and "m" refers to the mirror peak value.

2. The potential should dip in the region of the magnetically confined hot electrons. This is because the hot electrons require ions for charge neutralization, but the hot electrons do not contribute significantly to the ionization source.

3. The measured parallel confinement time for ions is much greater than the calculated ion collision time, which strongly implies electrostatic confinement.

The different regions of particle confinement in (ε, μ) space for the potential trap model are shown in Fig. 3-1, where ε is the total particle energy and μ is the particle's magnetic moment. The unconfined regions for ions are I and II, while the confined regions are III and IV. Particles with energy less than $\varepsilon = \mu B_o + q\phi_o$ are classically forbidden in the plasma. Region II is the ambipolar hole, a common feature of all mirror plasmas (because electrons scatter out faster than ions). The ions in region III are either mirror confined or Yushmanov trapped (a special class of ions caught between a mirror peak and a central positive potential hill). The majority of ions are confined in the region IV, the area of the potential dip. This is supported experimentally because no cold ions are observed in the end loss, as there would be if there were an ambipolar hole in the ion distribution function. The axial extent of the potential dip is determined by the axial extent of the magnetically confined hot electrons.
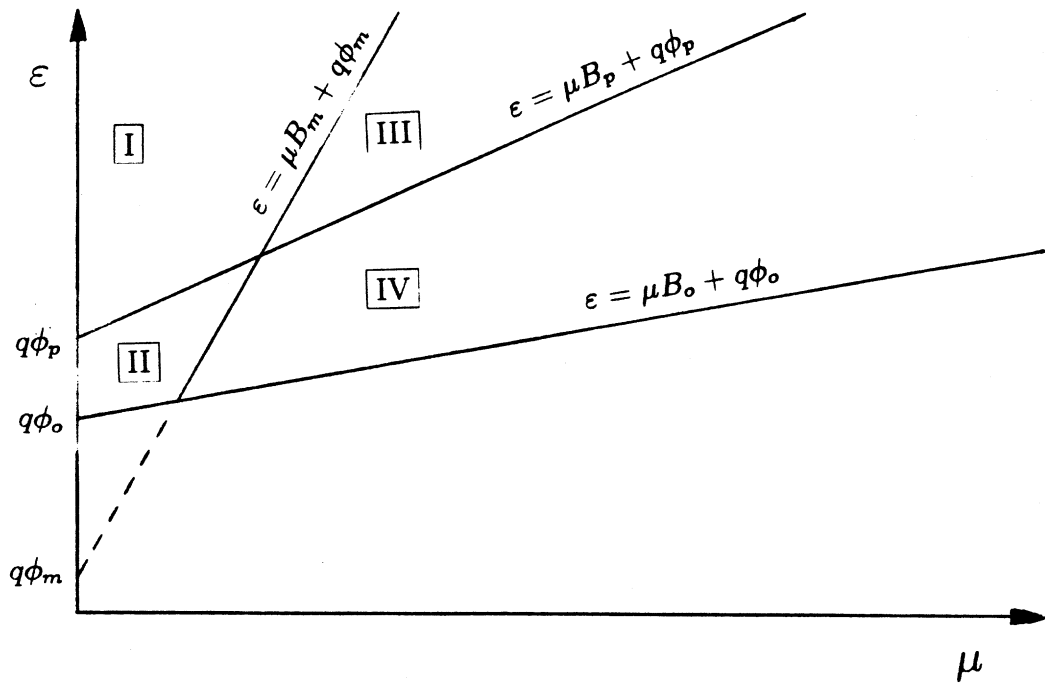
Figure 3-1: Regions of particle confinement in (ε, μ) space for the potential trap model (not to scale).

Fig. 3-2 shows the axial hot electron density determined from X-rays [Hokin, *et al.*, 1989] and the axial plasma pressure determined from magnetic measurements [Chen, *et al.*, 1989]. Since the hot electrons are deeply trapped in the magnetic well, and since the ions charge neutralize the hot electrons, the plasma length is much shorter than the distance between mirror peaks (80 cm).

The physics which determines the parallel ion confinement time depends upon the collisionality of the ions. Since all ions have nearly the same ion temperature (without ICRH), the main factor in determining the ion collisionality is the ion charge state. Ions with low collisionality are lost through velocity space diffusion, while highly collisional ions are lost through real space diffusion. A problem occurs in calculating confinement times due to velocity space diffusion because the maximum confining potential does not occur at the mirror peak. In these cases, only confinement in region IV is considered. While this ignores the confinement in region III, it is a good approximation since that region is not substantially populated.
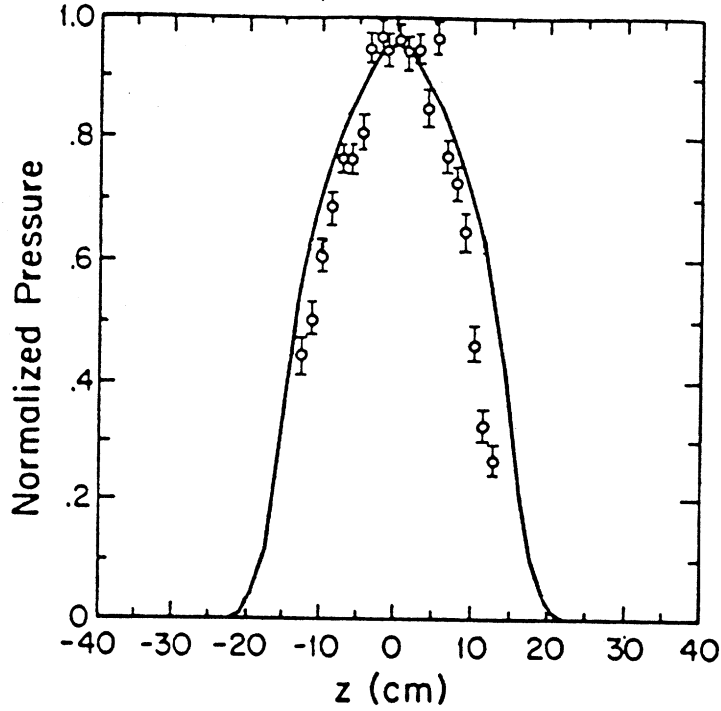
Figure 3-2: Axial profile of hot electron density (hollow points) and plasma pressure (solid line).

Long mean-free-path regime ($\lambda \geq R_p L_p$). The parallel ion confinement time in this case is determined by velocity space diffusion of ions into the loss cone. This time is approximated by the Pastukhov formula [Pastukhov, 1974; Cohen, et al., 1978]:

$$\tau_p = \frac{\sqrt{\pi}}{4} \frac{1}{Z_i} \tau_c \left(\frac{q_i \Delta\phi_i}{T_i} \right) \exp\left(\frac{q_i \Delta\phi_i}{T_i} \right) \frac{G(R_p Z_i)}{I(T_i/q_i \Delta\phi_i)}, \qquad (3.16)$$

where $\Delta\phi_i$ is the potential dip and

$$Z_i = \frac{1}{2} \frac{\sum_j n_j z_j^2 \lambda_{ij}}{\sum_j n_j z_j^2 \lambda_{ij}(T_j/T_i)(m_i/m_j)} \qquad (3.17)$$

$$\frac{1}{\tau_c} = 4\pi e^4 \sum_j \frac{n_j z_i^2 z_j^2 \lambda_{ij}}{m_i m_j v_i^3} \frac{T_j}{T_i} \qquad (3.18)$$

$$G(x) = \sqrt{1 + x^{-1}} \ln\left(\frac{\sqrt{1 + x^{-1}} + 1}{\sqrt{1 + x^{-1}} - 1} \right) \qquad (3.19)$$

$$I(x) = \frac{1 + x/2}{1 + x^2/4}. \qquad (3.20)$$

Eqn. 3.20 is modified from the Pastukhov form in order to reproduce classical mirror confinement [Post, 1987],

$$\tau_m = \tau_{ii} \frac{R_p - 1}{R_p + 1.5} \tag{3.21}$$

(where $\tau_{ii} = 1.88\tau_c$ is the ion-ion collision time), in the limit $\Delta\phi_i/T_i \rightarrow 0$ [Cohen, 1979].

Recently, new Pastukhov-like confinement times have been derived for mirror systems with improved boundary conditions and more accurate representations than those previously used by Pastukhov [Najmabadi, et al., 1984]. However, these new relationships diverge for small trapping potentials and therefore are not as robust as the modified Pastukhov expression. For large trapping potentials, the Pastukhov and Najmabadi confinement times give nearly identical fits to the experimental data, therefore the Pastukhov result is exclusively used.

Short mean-free-path regime ($\lambda \leq R_p L_p$). This is the regime of flow confinement that was previously discussed in section 2.2.1. In this case, collisions are strong enough to fill the loss cone with ions except within approximately a mean free path of the mirror peak. Using Eqn. 2.2 with $E = q_i \phi_p$, the ion end-loss flux for a flow confined plasma is

$$\Gamma_{\|i} = n_i \frac{B_o}{B_p} \sqrt{\frac{2T_i}{\pi m_i}} \exp\left[-\frac{q_i(\phi_p - \phi_o)}{T_i} \right]. \tag{3.22}$$

Inserting this into Eqn. 3.1 gives the flow confinement time:

$$\tau_f = R_p L_p \sqrt{\frac{\pi m_i}{2T_i}} \exp\left(\frac{q_i \Delta\phi_i}{T_i} \right), \tag{3.23}$$

where the potential dip is defined as $\Delta\phi_i = \phi_p - \phi_o$. It has been shown using a Monte Carlo code that a smooth transition occurs between the long-mean-free path and short-mean-free path regimes and that the two regimes are complementary [Rognlien and Cutler, 1980]. Thus, a reasonable expression for the composite confinement time is

$$\tau_{\|i} = \tau_p + \tau_f. \tag{3.24}$$

Spatial diffusion regime ($\lambda \ll R_p L_p$). In the limit that the ions are highly collisional, their flux parallel to the magnetic field is governed by the diffusion equation:

$$\Gamma_{\|i} = \mu_i n_i E_{\|} - D_i \nabla_{\|} n_i, \tag{3.25}$$

58

where the ion mobility (μ_i) and diffusion coefficient (D_i) are connected by the Einstein relation:

$$\mu_i = \frac{q_i D_i}{T_i}.$$
(3.26)

The ion diffusion coefficient is given by

$$D_i = \frac{T_i \tau_{ij}}{m_i},$$
(3.27)

where τ_{ij} is the unlike ion-ion collision time. Like ion-ion collisions are not included because they do not result in real space diffusion (although they do result in velocity space diffusion). Assuming that the potential dip and ion density have similar parallel gradients, and using the Einstein relation, the spatial diffusion confinement time is found to be

$$\tau_{sd} = \frac{L_p^2 m_i}{K_\parallel \tau_{ij} T_i} \exp\left(\frac{q_i \Delta \phi_i}{T_i}\right),$$
(3.28)

where $K_\parallel$ is a "shape factor" that depends upon the axial plasma profile. So far a slab model of the plasma has been used in the axial direction which would give $K_\parallel = 0$, clearly an unphysical result. At the other extreme is a quasi-triangular profile, for which $K_\parallel = 4$. The real value will lie somewhere in between these two cases. The transition from the Pastukhov-flow regime to the spatial diffusion regime with increasing ion charge state is assumed to be smooth, with the point of transition occurring when the two confinement times are equal. Thus, low to medium charge state ions have a parallel confinement time given by Eqn. 3.24, while high charge state ions have a parallel confinement time given by Eqn. 3.28. The particular charge state where this transition occurs is dependent upon the value of $K_\parallel$.

3.2.2   perpendicular ion confinement

The flux of ions perpendicular to a magnetic field is given by

$$\Gamma_{\perp i} = \mu_{\perp i} n_i E_\perp - D_{\perp i} \nabla_\perp n_i.$$
(3.29)

The effect of the ion mobility is to replace the diffusion coefficient with an effective diffusion coefficient given by

$$D_{\text{eff}} = D_{\perp i} \left[1 + \frac{q_i L_n E_\perp}{T_i}\right],$$
(3.30)

where

$$\frac{1}{L_n} = -\nabla_\perp \ln n_i \qquad (3.31)$$

is the scale length of the radial density profile. Since previous experimental data for an argon plasma in Constance B showed that ion mobility effects are small [Goodman, 1989], they is suppressed for the remainder of this chapter.

The average perpendicular confinement time is given by

$$\langle \tau_{\perp i} \rangle = \frac{L_p \sum n_i}{S_o - \sum \Gamma_{\parallel i}}. \qquad (3.32)$$

Note that $S_o - \sum \Gamma_{\parallel i} \neq \sum \Gamma_{\perp i}$, because the left hand side is a current divided by a cross sectional area while the right hand side is a current divided by a surface area. For cylindrical geometry, the relationship is

$$\pi r^2 \times (S_o - \sum \Gamma_{\parallel i}) = 2\pi r L_p \times \sum \Gamma_{\perp i}, \qquad (3.33)$$

therefore Eqn. 3.32 can be written as

$$\langle \tau_{\perp i} \rangle = \frac{r \sum n_i}{2 \sum \Gamma_{\perp i}}. \qquad (3.34)$$

Using Eqn. 3.29 and assuming that all ions have the same density radial profile (necessary since no spatial information by charge state is available) allows the average perpendicular confinement time to be written in the general form

$$\langle \tau_{\perp i} \rangle = \frac{a^2}{K_\perp \langle D_{\perp i} \rangle}, \qquad (3.35)$$

where a is the plasma radius,

$$\langle D_{\perp i} \rangle = \frac{\sum D_{\perp i} n_i}{\sum n_i}, \qquad (3.36)$$

and $K_\perp$ is a "shape factor" that is equal to 4 for a parabolic profile. The perpendicular confinement time for an individual charge state can be shown to be

$$\tau_{\perp i} = \frac{a^2}{K_\perp D_{\perp i}}. \qquad (3.37)$$

The processes that determine the ion diffusion coefficient include classical and neoclassical transport, turbulent transport and convection. The relative importance

of each process depends upon the device and parameter regime. The importance of each of these processes is discussed below for Constance B.

Classical ion transport across magnetic field lines occurs because of unlike coulomb collisions. Because the Constance B plasma has multiple ion species, unlike ion-ion collisions dominate over ion-electron and ion-neutral collisions. The classical diffusion coefficient is given by [Chen, 1974]

$$D_{cl} = \frac{D_i}{1 + (\omega_{ci}\tau_{ij})^2}, \qquad (3.38)$$

where ω_{ci} is the ion cyclotron frequency.

Neoclassical transport occurs in all non-axisymmetric systems due to particles drifting off flux surfaces. Calculations for Constance B show that neoclassical transport is smaller than classical transport near the plasma center [Goodman, 1989] and therefore will be neglected.

Previous studies of ion radial transport on Constance B measured diffusion coefficients that were an order of magnitude larger than the classical and neoclassical contributions [Goodman, 1989]. One potential explanation of this is turbulent diffusion due to low frequency fluctuations. The Constance B experiment is driven unstable to the whistler wave by warm (2 keV) electrons [Garner, et al., 1987]. The instability comes in bursts at a rate of 1–100 kHz, depending upon plasma conditions. The instability is associated with fluctuations in the plasma potential, which can excite waves and lead to enhanced transport. The diffusion coefficient for strong turbulence is [Dupree, 1967]

$$D_{tur} \approx \frac{c\tilde{E}_{\perp}}{k_{\perp}B}. \qquad (3.39)$$

This result was obtained for a specific mode, namely drift waves due to electron drift. However, the nonlinear mechanism producing such a diffusion coefficient, namely effects associated with perturbed particle orbits in a turbulent plasma, may be quite general [Porkolab and Kino, 1968]. Note that the diffusion coefficient is independent of charge or mass, as is the usual case for $\mathbf{E} \times \mathbf{B}$ drifts. Since the magnitude of the fluctuating electric field ($\tilde{E}_{\perp}$) cannot be modeled, an additional piece of experimental data is needed in order to determine D_{tur}. The turbulent contribution to ion radial

transport can be determined from the perpendicular ion flux by

$$D_{tur} + \langle D_{cl} \rangle = \frac{L_n \sum \Gamma_{\perp i}}{\sum n_i}. \tag{3.40}$$

Since the perpendicular ion flux is not directly measured, it is determined from Eqn. 3.33 using the total ion flux ($\sum \Gamma_{\parallel i}$) measured by the TOF analyzer. Thus, the turbulent diffusion coefficient can be found from

$$D_{tur} + \langle D_{cl} \rangle = \frac{a^2}{K_\perp} \frac{S_o - \sum \Gamma_{\parallel i}}{L_p \sum n_i}. \tag{3.41}$$

It is somewhat unfortunate that the measured total ion flux is included in the calculation, since ideally it should be modeled.

Besides plasma turbulence, convection can also lead to anomalous radial losses. Since the plasma drifts along equipotential surfaces, asymmetric potential profiles will lead to transport across magnetic field lines. Convection can therefore transport ions to large radii where they are lost due to poor parallel confinement. Such asymmetries in the potential profile are not normally expected because the heating and fueling of the plasma should be azimuthally uniform due to the low plasma density and substantial cavity microwave heating.

Asymmetries in the potential profile have been measured during ICRH, however. They arise because the antenna electric field is stronger at the bottom of the antenna than at the top. Experimentally, enhanced ion radial transport is observed during ICRH, most likely due to convection. Assuming that the enhanced radial transport is strictly due to the $\mathbf{E} \times \mathbf{B}$ drift, the perpendicular confinement time is approximately

$$\tau_{\perp i} \approx \frac{a^2 B}{\Delta \phi}, \tag{3.42}$$

where $\Delta \phi$ is the potential difference on opposite sides of the plasma surface. Like turbulent diffusion, convective losses are independent of ion charge or mass.

3.3 Ion power balance

Ideally, the ion temperatures can be determined self consistently using the ion power balance equations,

$$
\begin{aligned}
\frac{d}{dt}(n_i T_i) &= \left(\frac{T_{eh} - T_i}{\tau_{i,h}^{eq}} + \frac{T_{ec} - T_i}{\tau_{i,c}^{eq}} + \sum_{i \neq j} \frac{T_j - T_i}{\tau_{i,j}^{eq}} \right) n_i + (n_{eh} \langle \sigma v \rangle_{i-1,i}^{ion,h} + \\
&\quad n_{ec} \langle \sigma v \rangle_{i-1,i}^{ion,c}) n_{i-1} T_{i-1} - (n_{eh} \langle \sigma v \rangle_{i,i+1}^{ion,h} + n_{ec} \langle \sigma v \rangle_{i,i+1}^{ion,c} + \\
&\quad n_o \langle \sigma v \rangle_{i,i-1}^{ex} + \frac{1 + q_i \Delta \phi_i / T_i}{\tau_i}) n_i T_i + n_o \langle \sigma v \rangle_{i+1,i}^{ex} n_{i+1} T_{i+1} \\
&= 0, \tag{3.43}
\end{aligned}
$$

where

$$
\tau_{i,j}^{eq} = \frac{1}{4\sqrt{2\pi}} \frac{m_i m_j}{n_j z_i^2 z_j^2 e^4 \lambda_{ij}} \left[\frac{T_i}{m_i} + \frac{T_j}{m_j} \right]^{\frac{3}{2}} \tag{3.44}
$$

is the equilibration time. Experimental measurements of the ion temperature (see section 4.1), however, give results which are an order of magnitude greater than that predicted by these equations. Thus, the ions are anomalously heated.

Possible anomalous heating mechanisms include radial transport down a potential hill and turbulent heating. Radial transport can lead to ion heating if the plasma potential is peaked on axis. The heating rate per unit volume is given by

$$
\mathcal{P}_{\nabla \phi} = -q_i E_\perp \Gamma_{\perp i}. \tag{3.45}
$$

There are two problems with this explanation for the anomalous ion heating. First, the measured radial potential usually appears slightly hollow and not peaked [Goodman, 1989]. Second, if ion heating is caused by radial transport, then the ions at larger radii should be hotter than ions in the plasma center, whereas the measured radial profile of ion temperature is flat (see section 4.3).

A more plausible explanation for the anomalous ion temperatures is turbulent heating due to low frequency fluctuations. As mentioned in the previous section, Constance B is driven unstable to the whistler wave by warm (2 keV) electrons. The instability is associated with fluctuations in the plasma potential, which can excite waves and lead to ion heating by Landau damping or cyclotron harmonic resonances. A general analysis of velocity space diffusion from weak plasma turbulence

in a magnetic field shows that resonant particles with velocities much larger than typical phase velocities in the turbulent spectrum are scattered primarily in pitch angle about the magnetic field [Kennel and Engelmann, 1966]. Only particles with velocities on the order of the phase velocities or less are scattered in energy at a rate comparable with their pitch angle scattering rate. For example, if the ions gain energy by Landau diffusion and the maximum phase velocity of the turbulent spectrum is $|\omega/k_{\parallel}|_{max}$, then the ions can heat up to a maximum temperature given by

$$T_i \approx \frac{m_i}{2} \left| \frac{\omega}{k_{\parallel}} \right|_{max}^2 . \tag{3.46}$$

The ion temperature can equilibrate in the parallel and perpendicular directions through collisions. Note that the ion temperature for heating by Landau diffusion is independent of charge state and increases with mass.

Since modeling the ion temperature by velocity space diffusion from weak plasma turbulence requires knowledge of the turbulent spectrum, a self-consistent ion temperature is not used in the ion model. Instead, the measured ion temperatures are used.

3.4 Solving the ion model

Using the ion physics developed so far in this chapter, the ion densities, end loss fluxes and confinement times can now be determined self consistently. For N charge states, there are $2N + 1$ unknowns (N ion densities, N confinement times and the potential dip). To solve for these, there are N particle balance equations, N confinement time relations and the quasineutrality condition, which constitute $2N + 1$ equations. Inputs to the model are the hot and cold electron density and temperature, the neutral pressure outside the plasma, information about the magnetic geometry (mirror ratio, plasma length and diameter, mod-B, etc.), the ion temperature and the total ion flux. The ion temperature is not modeled by the ion power balance equations because of anomalous ion heating. The total ion flux is needed for cases of anomalous radial transport to divide the ion confinement time into its parallel and perpendicular

components.

The equations for the ion model are solved iteratively, as shown in the flow chart in Fig. 3-3. Initially, all the ion densities are assumed to be equal. The iterative process starts with calculating the ion confinement times and the potential dip. The value of the potential dip is determined by the need to satisfy Eqn. 3.13. The ion model can give results for cases of (1) no radial transport, (2) classical radial transport, or (3) anomalous radial transport ($\sum \Gamma_{\|i}$ is needed in this case). For each case the potential dip is determined in a different way. If there is no perpendicular diffusion, due to a strong inward radial electric field perhaps, then the potential dip is determined from the relation

$$L_p \sum_i \frac{n_i}{\tau_{\|i}} = S_o. \tag{3.47}$$

When classical radial transport exists, the potential dip is determined from the relation

$$L_p \sum_i \frac{n_i}{\tau_{\|i}} = S_o - \frac{K_\perp L_p}{a^2} \sum_i D_{cl} n_i. \tag{3.48}$$

If the radial transport is anomalous so that the measured total ion flux has been used, then the above equation becomes

$$L_p \sum_i \frac{n_i}{\tau_{\|i}} = \sum_i \Gamma_{\|i}. \tag{3.49}$$

Once the ion confinement times are known, they are used to solve for the ion densities from the ion particle balance equations. The ion confinement times are then recalculated until the results converge, usually in five to ten passes.

3.5   Electron confinement

The electron distribution is divided into "hot" and "cold" components which obey different confinement physics. The electron confinement time is determined experimentally from its end loss:

$$\tau_e = \frac{e L_p n_e}{J_e}. \tag{3.50}$$
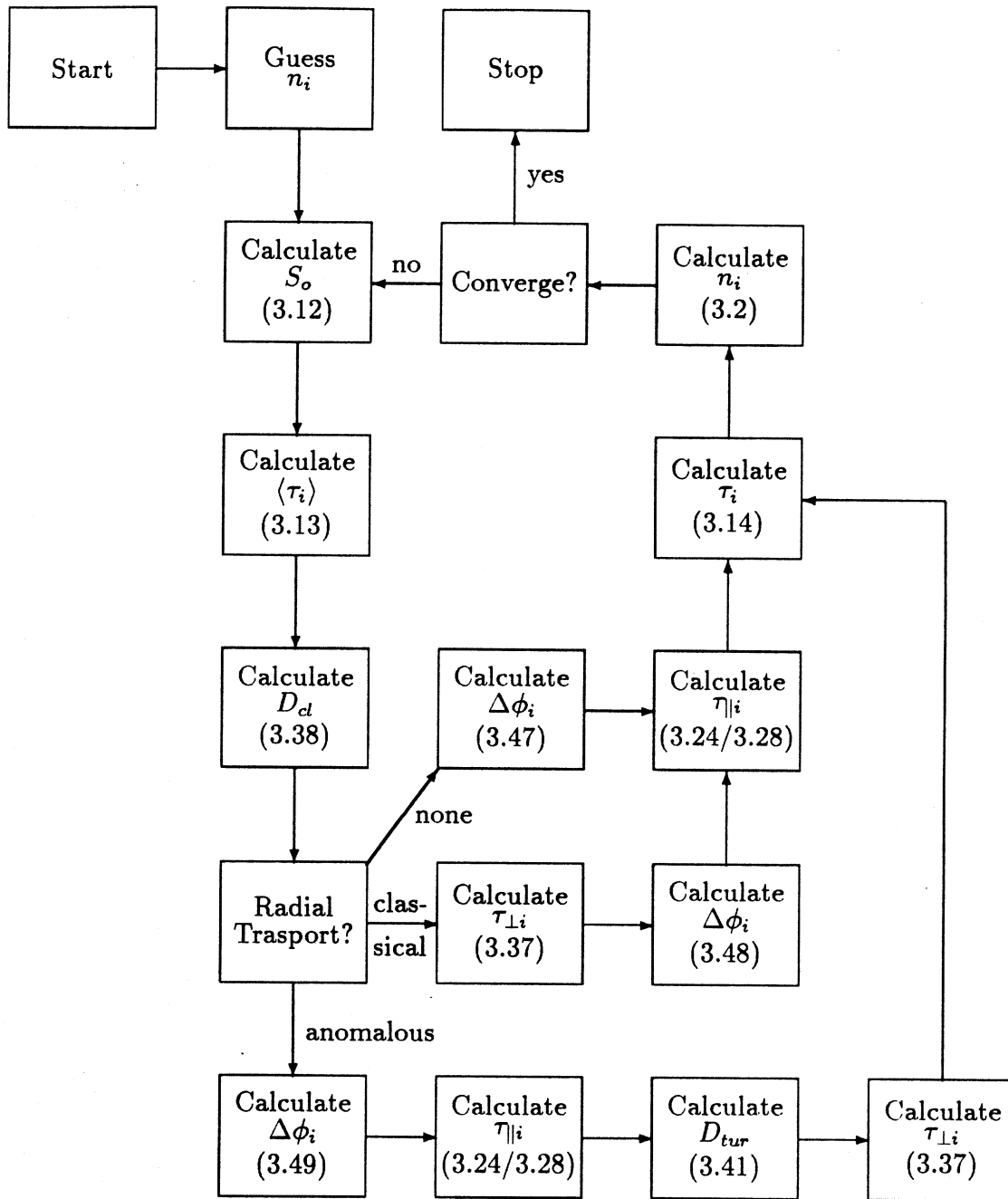
Figure 3-3: Flow chart for determining the ion densities, confinement times and potential dip from the ion model equations (in parenthesis).

The electrons are not required to transport radially with the ions because ion losses at the plasma edge can be balanced by electron losses in the plasma center, with the vacuum vessel wall completing the circuit.

The cold electrons are primary trapped by the positive ambipolar potential of the plasma. Referring to Fig. 3-1, the loss cone for cold electrons is region I. The electrons are electrostatically trapped in region II, magnetically trapped in region III and Yushmanov trapped in region IV. The theoretical confinement time for the cold electrons is given by [Pastukhov, 1974]:

$$\tau_p = \frac{\sqrt{\pi}}{4} \frac{1}{Z_e} \tau_c \left(\frac{e\Delta\phi_e}{T_{ec}} \right) \exp\left(\frac{e\Delta\phi_e}{T_{ec}} \right) \frac{G(R_m Z_e)}{I(T_{ec}/e\Delta\phi_e)}, \tag{3.51}$$

where

$$Z_e = \frac{1}{2} \left(1 + \frac{\sum z_i^2 n_i \lambda_{ci}}{n_{ec} \lambda_{cc}} \right) \tag{3.52}$$

$$\frac{1}{\tau_c} = \frac{4\pi e^4 n_{ec} \lambda_{cc}}{m_e^2 v_{ec}^3} \tag{3.53}$$

and $\Delta\phi_e = \phi_o - \phi_m$ is the ambipolar potential. Note that the cold electrons do not scatter off the hot electrons.

The experimental hot-electron confinement time can be compared to the classical mirror confinement time [Post, 1987]:

$$\tau_m = \tau_{hh} \frac{R_m - 1}{R_m + 1.5}, \tag{3.54}$$

where R_m is the maximum mirror ratio and

$$\frac{1}{\tau_{hh}} = \frac{8\sqrt{\pi}}{3} \frac{e^4}{m_e^2 v_{eh}^3} \left(n_{eh} \lambda_{hh} + n_{ec} \lambda_{hc} + \sum n_i z_i^2 \lambda_{hi} \right) \tag{3.55}$$

is the hot electron collision time. Previous work on Constance B showed that the measured hot-electron confinement time is over an order of magnitude shorter than the classical mirror confinement time [Hokin, et al., 1989]. This is because during ECRH the confinement time of the hot electrons is determined by rf diffusion and not collisions.

3.6 Electron particle and power balance

Besides the magnetic geometry, the experimenter has two "knobs" to control the plasma: the ECRH power and the neutral pressure. The purpose of this section is to predict how the hot and cold electrons are affected by changes in the ECRH power density and neutral pressure. (The theoretical results derived in this section are not used in the ion model because it uses only experimental inputs for electrons.)

In principle, the electron density, temperature and confinement time can be modeled by the electron particle and power balance equations, mirror confinement physics and ECRH theory. In order to concentrate on the electron physics, an "average ion" model is used where the ions are replaced with a single ion species of charge z_p and ionization potential P_p. The electron particle balance equations are therefore

$$
\begin{aligned}
\frac{dn_{ec}}{dt} &= \frac{z_p \Gamma_{ext}}{L_p} + z_p(n_{ec}\langle\sigma v\rangle^{ion,c} + n_{eh}\langle\sigma v\rangle^{ion,h})n_o - \frac{n_{ec}}{\tau_{ec}} - \frac{n_{ec}}{\tau_{c\to h}} \\
&= 0, \tag{3.56} \\
\frac{dn_{eh}}{dt} &= \frac{n_{ec}}{\tau_{c\to h}} - \frac{n_{eh}}{\tau_{eh}} \\
&= 0, \tag{3.57}
\end{aligned}
$$

where $\tau_{c\to h}$ is the cold electron heating time and $z_p\Gamma_{ext}$ is an externally supplied electron flux from a pre-ionizer or from secondary electron emission from a surface. Such external fluxes are negligible for Constance B but can be important for ECR ion sources. The electron power balance equations are

$$
\begin{aligned}
\frac{d}{dt}(n_{ec}T_{ec}) &= \eta_c \mathcal{P}_{ech} - \frac{n_{ec}T_{ec}}{\tau_{c\to h}} - P_p n_o\langle\sigma v\rangle^{ion,c} n_{ec} - \frac{T_{ec}-T_i}{\tau_{c,i}^{eq}}n_{ec} - \frac{n_{ec}(T_{ec}+e\Delta\phi_e)}{\tau_{ec}} \\
&= 0, \tag{3.58} \\
\frac{d}{dt}(n_{eh}T_{eh}) &= \eta_h \mathcal{P}_{ech} + \frac{n_{ec}T_{ec}}{\tau_{c\to h}} - P_p n_o\langle\sigma v\rangle^{ion,h} n_{eh} - \frac{T_{eh}-T_i}{\tau_{h,i}^{eq}}n_{eh} - \frac{n_{eh}T_{eh}}{\tau_{eh}} \\
&= 0, \tag{3.59}
\end{aligned}
$$

where $\mathcal{P}_{ech}$ is the applied microwave power per unit volume and η is the absorption efficiency. Power loss from microinstability rf has been ignored. The particle confinement times have been used in the power balance equations along with the average energy lost per particle lost [Pastukhov, 1974; Hokin, *et al.*, 1989].

The cold electron absorption coefficient for X-mode launch in the limit of low parallel wavenumber and low density is given by [Antonsen and Manheimer, 1978]

$$\eta_c \approx 1.8 \times 10^{-6} L_\perp f T_{ec} N_\parallel^2 \frac{\omega_{ce}^2}{\omega_{pe}^2}, \tag{3.60}$$

where the perpendicular magnetic scale length $L_\perp$ is in cm, f is in GHz and T_{ec} is in eV. The hot electron absorption efficiency has been measured to be $\eta_h \approx 0.9$ [Hokin, et al., 1989]. Thus, there are six equations but nine unknowns (the densities, temperatures, confinement times, absorption efficiencies and $\tau_{c \rightarrow h}$). Still, some important relations can be drawn.

From Eqn. 3.57, the cold electron heating time is

$$\tau_{c \rightarrow h} = \frac{n_{ec}}{n_{eh}} \tau_{eh}. \tag{3.61}$$

Using this relationship in Eqn. 3.56 and solving for the cold electron confinement time gives

$$\frac{1}{\tau_{ec}} = z_p n_o \langle \sigma v \rangle^{ion,c} \left(1 + \frac{n_{eh}}{n_{ec}} \frac{\langle \sigma v \rangle^{ion,h}}{\langle \sigma v \rangle^{ion,c}} \right) + \frac{z_p \Gamma_{ext}}{L_p n_{ec}} - \frac{n_{eh}}{n_{ec}} \frac{1}{\tau_{eh}}, \tag{3.62}$$

where the last term is small since $\tau_{eh} \gg \tau_{ec}$. Thus, the cold electron confinement time is inversely proportional to the neutral density and only weakly dependent on electron temperature and density. This formula for τ_{ec} is the same as that obtained using the charge neutrality condition for plasma losses:

$$\frac{n_{ec}}{\tau_{ec}} + \frac{n_{eh}}{\tau_{eh}} = \frac{z_p n_i}{\tau_i}. \tag{3.63}$$

If the cold electrons do not transport radially, then Eqns. 3.51 and 3.62 can be used to determine the ambipolar potential of the plasma from the cold electron density and temperature.

Eqn. 3.58 relates the cold electron density and temperature to the absorbed microwave power. Neglecting ion drag on the electrons, this relation is approximately

$$\frac{n_{ec}(T_{ec} + e\Delta\phi_e + P_p/z_p)}{\tau_{ec}} \approx \eta_c \mathcal{P}_{ech}, \tag{3.64}$$

where equations for the cold electron confinement time and ambipolar potential have already been given. Using Eqn. 3.60 for η_c gives the following predicted scaling of the

69

cold electron confinement time and density:

$$\tau_{ec} \quad \propto \quad \frac{1}{z_p n_o \langle \sigma v \rangle^{ion,c}} \tag{3.65}$$

$$n_{ec} \quad \propto \quad \sqrt{\frac{P_{ech}}{z_p n_o \langle \sigma v \rangle^{ion,c}}}. \tag{3.66}$$

There is still a weak temperature dependence in the ionization rate parameter.

West (1982) models n_{ec} by assuming that the cold electron density in the mirror throat is charge neutralized by ion end loss flowing out at its thermal velocity:

$$n_{ec,m} = \frac{J_{\parallel i} R_m}{e} \sqrt{\frac{\pi m_i}{2 T_i}}. \tag{3.67}$$

The midplane cold electron density is then found from the Boltzmann relation (see Eqn. 3.15). The problem with this model is that it was developed for the anchor of a tandem mirror [Baldwin, 1980], which has a different axial potential structure than an ECR ion source. In a conventional tandem mirror, no separate ambipolar potential develops for the anchor because it is connected to the plug or central cell (or both). However, for an ECR ion source, the ambipolar potential which develops to confine cold electrons accelerates ions out of the mirror not at their thermal velocity, but at the much faster ion acoustic velocity. Also Eqn. 3.67 ignores the charge negation by mirror trapped ions. Thus, this model is probably not correct for an ECR ion source and will not be used.

For the hot electrons, Eqn. 3.59 reduces to

$$\frac{n_{eh} T_{eh}}{\tau_{eh}} \approx \eta_h P_{ech} \tag{3.68}$$

for $T_{eh} \gg T_{ec}, P_p$. Thus, the global hot-electron confinement time can be determined experimentally from

$$\langle \tau_{eh} \rangle \approx \frac{W}{\eta_h P_{ech}}, \tag{3.69}$$

where W is the total stored energy and P_{ech} is the total applied microwave power. Additional relations for T_{eh} from super-adiabatic theory and for τ_{eh} from classical mirror confinement can be used to get scaling laws for the hot electron density, temperature and confinement time. (However, for Constance B super-adiabatic theory

and classical mirror confinement do not apply [Hokin, *et al.*, 1989], so experimental results must be used.)

From super-adiabatic theory, the hot electron temperature boundary is

$$T_{eh} \propto \omega_{ce}^{1/2} \mathcal{E}_{\perp}^{3/4} \propto \omega_{ce}^{1/2} \mathcal{P}_{ech}^{3/8}, \tag{3.70}$$

where plasma shielding of the electric field has been neglected. The ω_{ce} dependence has been included for use in section 5.2 when frequency scaling is discussed. If the hot electrons are classically mirror confined, then

$$\tau_{eh} \propto \frac{T_{eh}^{3/2}}{n_{eh} + n_{ec}}. \tag{3.71}$$

Combining these two relations with Eqn. 3.68 gives the following scalings for the hot electron confinement time and density:

$$\tau_{eh} \propto \omega_{ce}^{5/8} \mathcal{P}_{ech}^{-1/32} \tag{3.72}$$

$$n_{eh} \propto \omega_{ce}^{1/8} \mathcal{P}_{ech}^{19/32}. \tag{3.73}$$

Thus, increasing $\mathcal{P}_{ech}$ increases both the density and temperature such that the confinement time stays nearly the same.

Finally, the total power lost from the plasma per unit volume is given by

$$\mathcal{P}_{lost} \approx \frac{n_{eh} T_{eh}}{\tau_{eh}} + \frac{n_{ec}(T_{ec} + e\Delta\phi_e + P_p/z_p)}{\tau_{ec}} + \frac{n_i(T_i + z_p e \Delta\phi_i)}{\tau_i}, \tag{3.74}$$

where the first term dominates. This is the power density which must be supplied by the ECRH system.

Chapter 4

Experimental Results

In this chapter, the experimental results for Constance B are presented and compared to the plasma model developed in the previous chapter. The first two sections cover oxygen and neon plasmas in detail, showing measured ion densities, end loss fluxes, confinement times and temperatures. The third section covers the other noble gases in lesser detail. The fourth section shows the results of minority ion heating experiments for oxygen and neon plasmas. The phenomenon of gas mixing (helium and oxygen) is studied in the fifth section and the last section covers electron measurements.

4.1   Oxygen

The ion densities and fluxes as a function of charge state are measured for three different oxygen plasmas in order to determine the parallel ion confinement times using Eqn. 3.1. The electron densities, electron temperatures and ion temperatures are also measured for use in the ion model developed in the previous chapter. After the experimental results are presented, they are compared to results from the ion model.

The three oxygen plasmas studied in this section differ in applied ECRH power and neutral pressure, as shown in Table 4.1. The electron density and plasma beta values given in this table are for the plasma center. All plasmas have the same magnetic geometry. An example of the radial profile of hot and cold electron density for the

Table 4.1: Parameters for the three oxygen plasmas studied in this section.

ECRH power	1 kW	1 kW	3.4 kW
Neutral pressure	5×10^{-7}Torr	1×10^{-6}Torr	1×10^{-6}Torr
Magnetic field	3.5 kG	3.5 kG	3.5 kG
Hot electron density	2.8×10^{11}cm^{-3}	2.2×10^{11}cm^{-3}	4.3×10^{11}cm^{-3}
Hot electron temperature	320 keV	260 keV	290 keV
Plasma beta	0.17	0.12	0.25
Cold electron density	1.1×10^{11}cm^{-3}	1.1×10^{11}cm^{-3}	3.8×10^{11}cm^{-3}
Cold electron temperature	180 eV	130 eV	230 eV
Plasma potential	140 V	90 V	200 V

1 kW, 5×10^{-7}Torr oxygen plasma is shown in Fig. 4-1. The cold electrons peak on axis, while the hot electrons have a 10% hollow profile. The electron density radial profile is used to determine the radial profile of ions. The radial profile of the plasma beta for the same oxygen plasma is shown in Fig. 4-2. The plasma pressure profile used to calculate the beta profile is from Chen, et al., (1989). The beta profile is used to calculate the midplane magnetic field, which is needed to calculate the midplane current density of plasma end loss.

The measured ion densities in the plasma center are shown in Fig. 4-3 for the three oxygen plasmas. Only the first five charge states can be measured due to the wavelength range of the VUV spectrometer. This figure shows that increasing the neutral pressure lowers the average charge state of the ions, while increasing the ECRH power raises the average charge state of the ions.

The ion fluxes for the three oxygen plasmas are shown in Figs. 4-4—4-6. These one-dimensional radial scans are fairly symmetric about the plasma center and are hollow, with the hollowness increasing with charge state. The peak flux occurs on the outer-most field line that is resonant with the ECR frequency (6 cm radius). The ion flux decreases with increasing ion charge state.

The parallel ion confinement times can now be found from the ion densities and fluxes using Eqn. 3.1. The parallel confinement times for the three oxygen plasmas are shown in Figs. 4-7—4-9. Any asymmetry in the parallel ion confinement times is due to asymmetry in the fluxes since the ion density radial profile is assumed to be symmetric. The parallel confinement times increase with charge state (except for
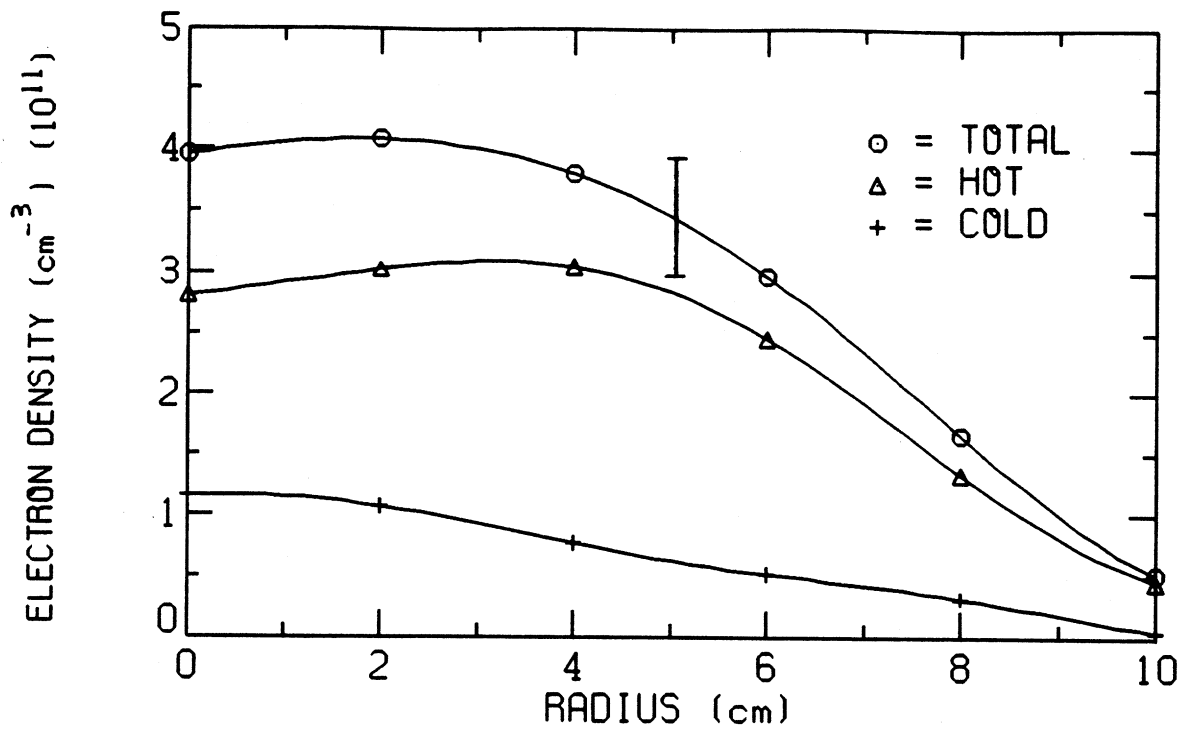
Figure 4-1: Radial profile of hot and cold electron density for the 1 kW, 5×10^{-7} Torr oxygen plasma.
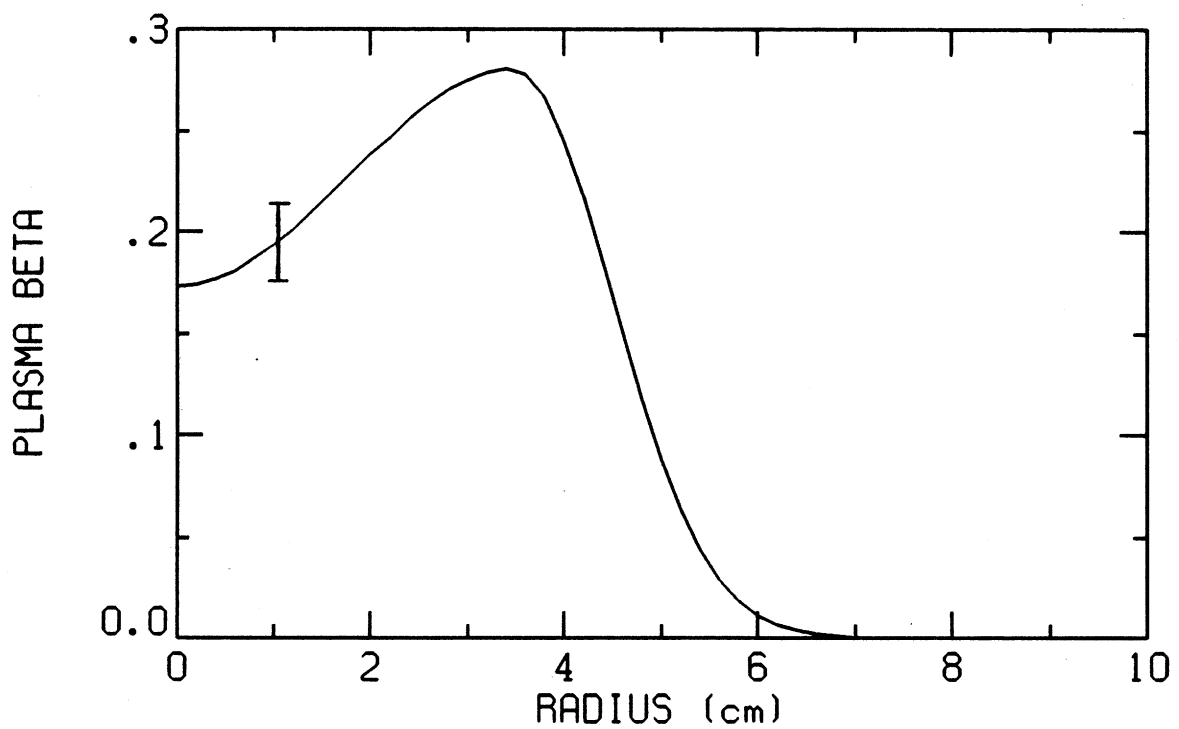
Figure 4-2: Radial profile of plasma beta for the 1 kW, 5×10^{-7} Torr oxygen plasma.
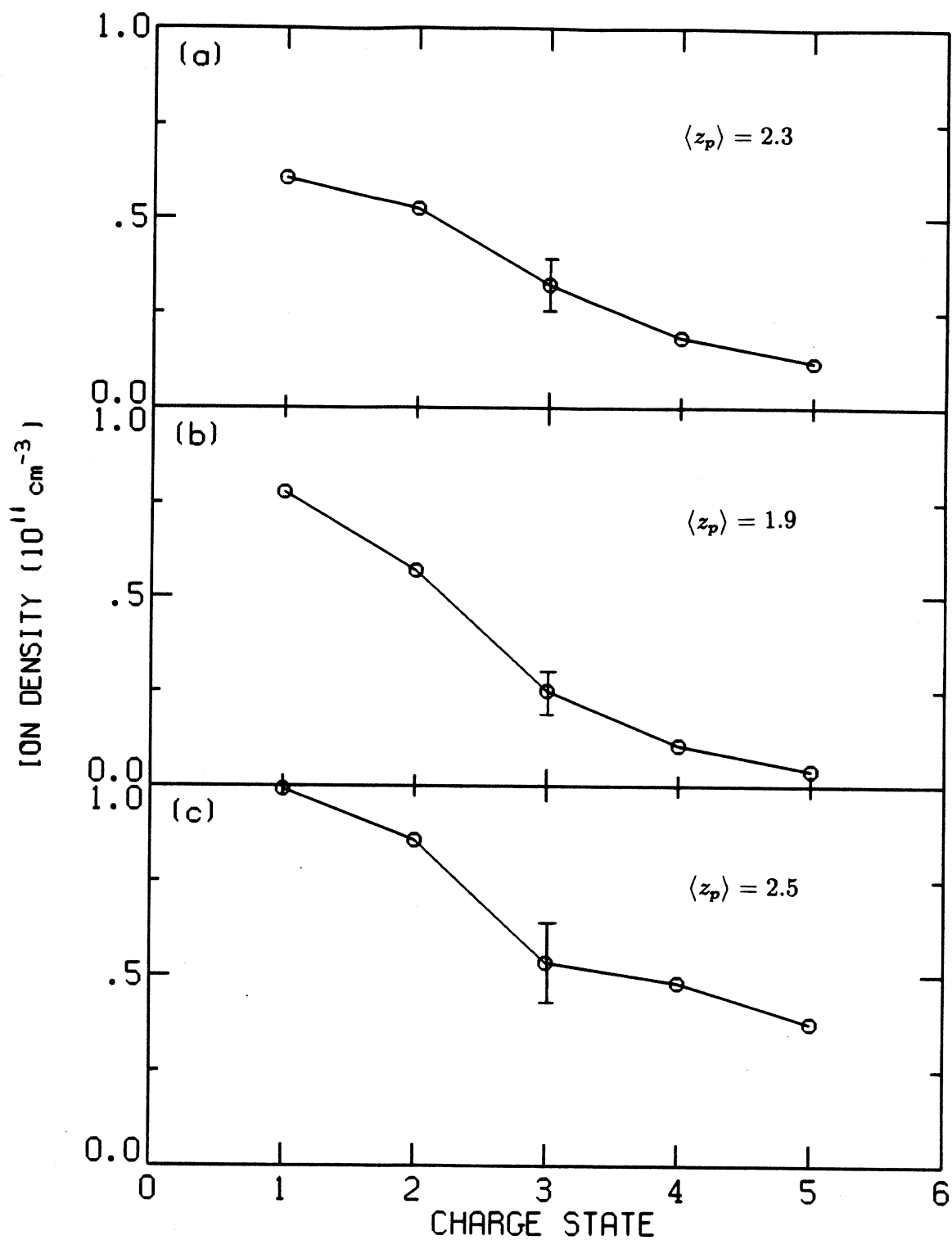
Figure 4-3: Ion densities in the plasma center for the (a) 1 kW, 5×10^{-7} Torr, (b) 1 kW, 1×10^{-6} Torr and (c) 3.4 kW, 1×10^{-6} Torr oxygen plasmas.
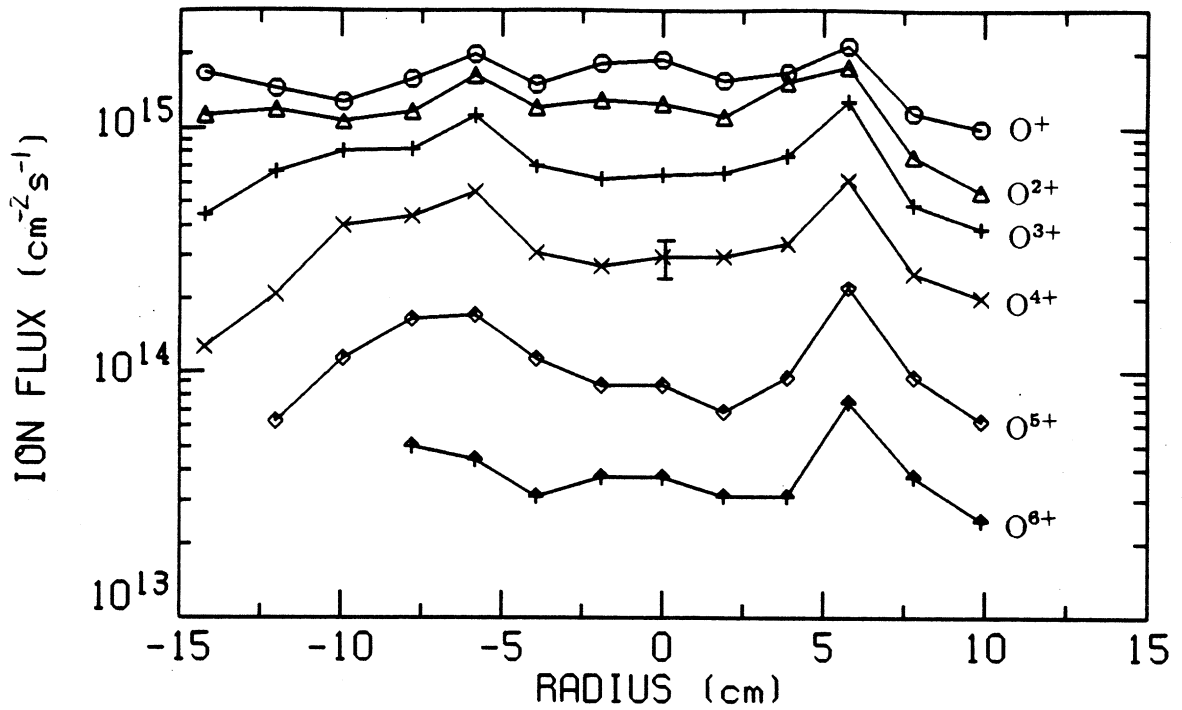
Figure 4-4: Ion fluxes mapped to the magnetic midplane for the 1 kW, 5×10^{-7}Torr oxygen plasma.
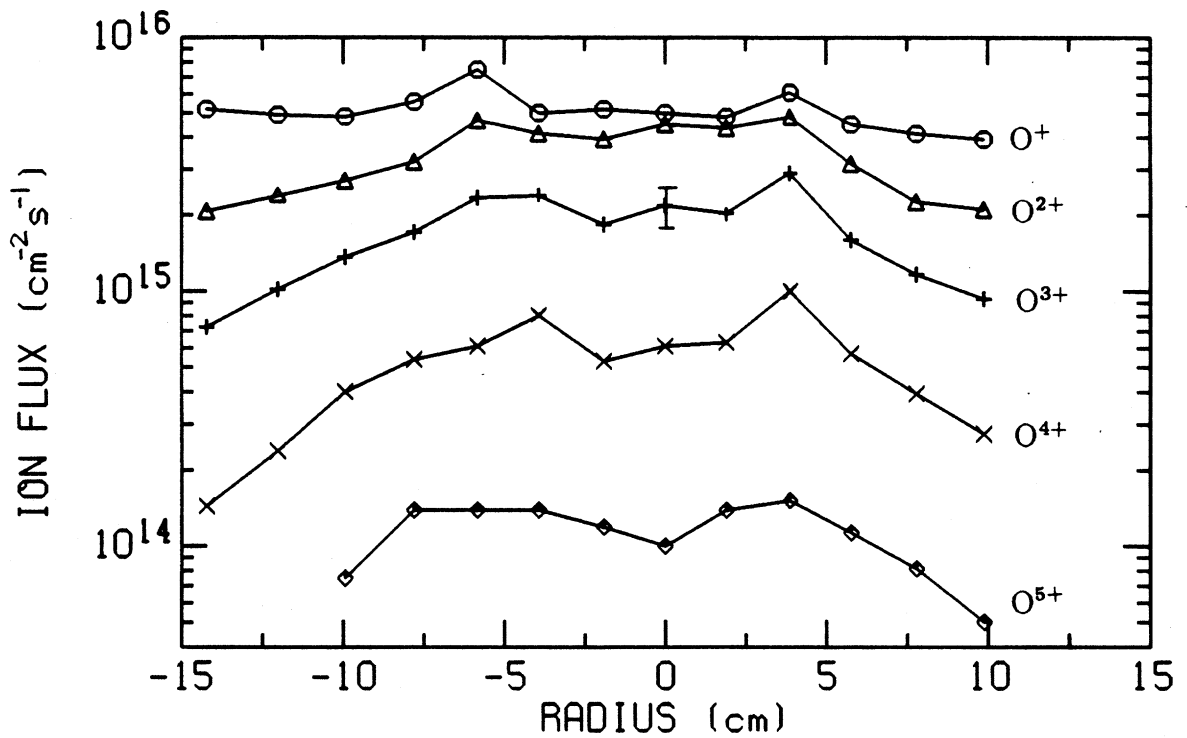
Figure 4-5: Ion fluxes mapped to the magnetic midplane for the 1 kW, 1×10^{-6}Torr oxygen plasma.
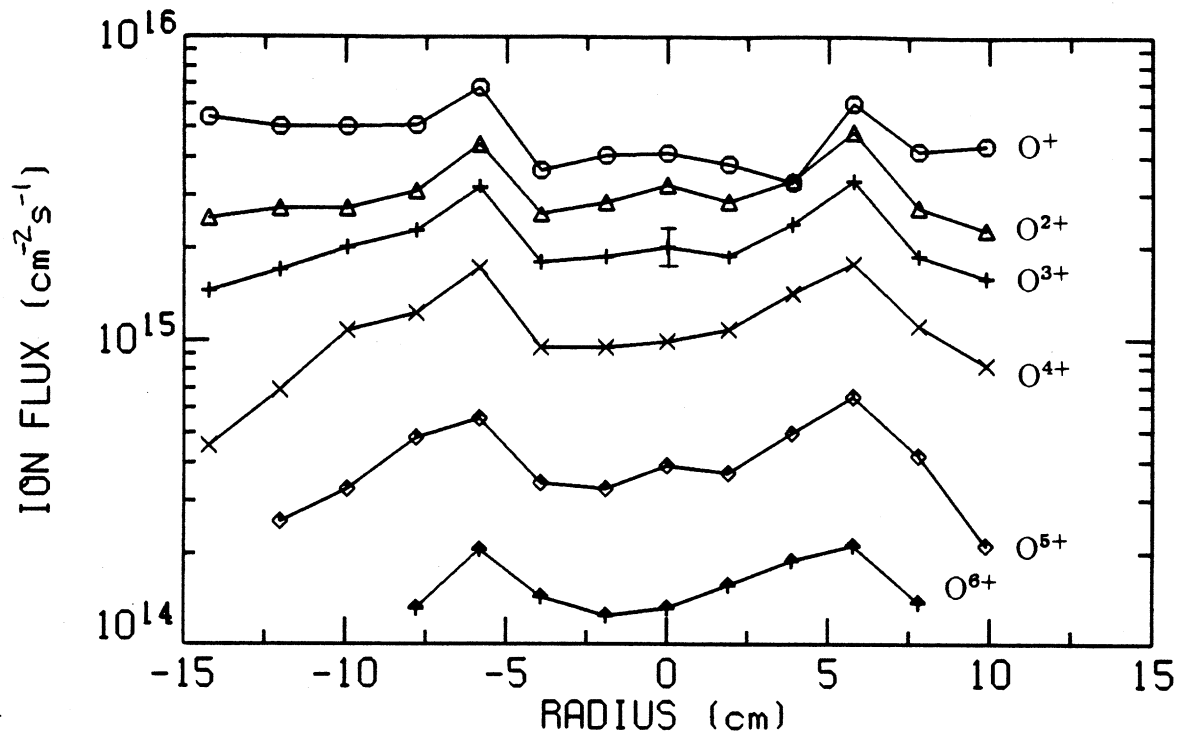
Figure 4-6: Ion fluxes mapped to the magnetic midplane for the 3.4 kW, 1×10^{-6} Torr oxygen plasma.
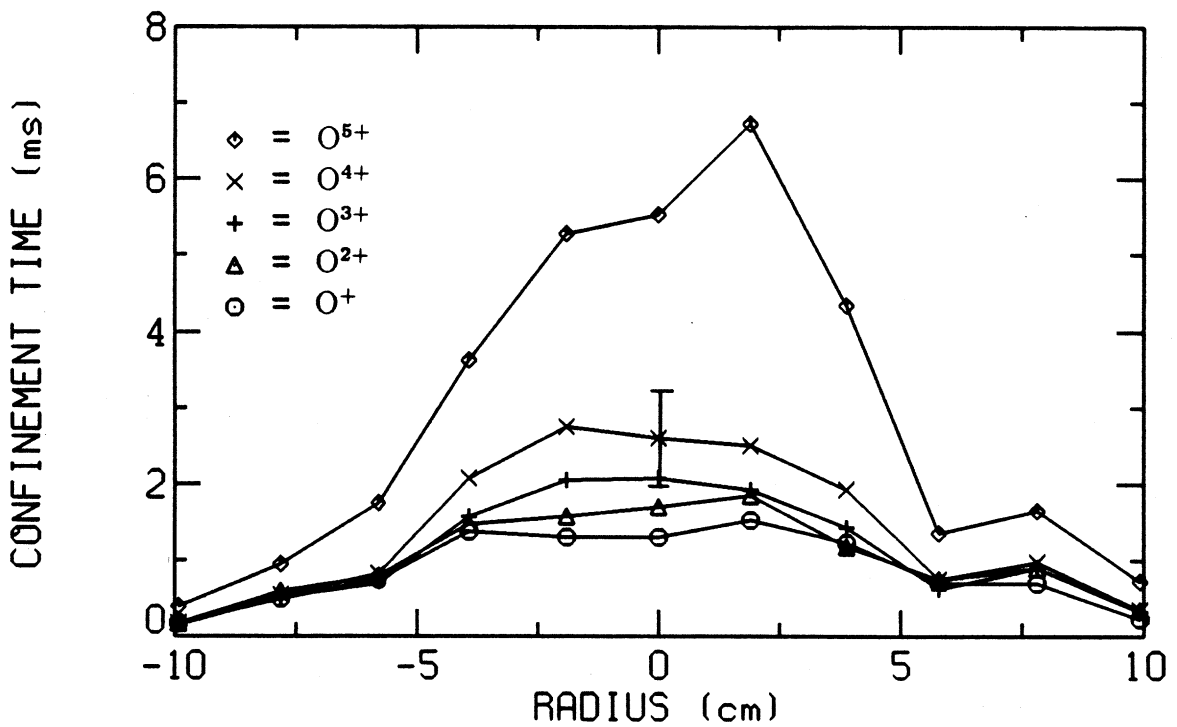
Figure 4-7: Parallel ion confinement times for the 1 kW, 5×10^{-7} Torr oxygen plasma.
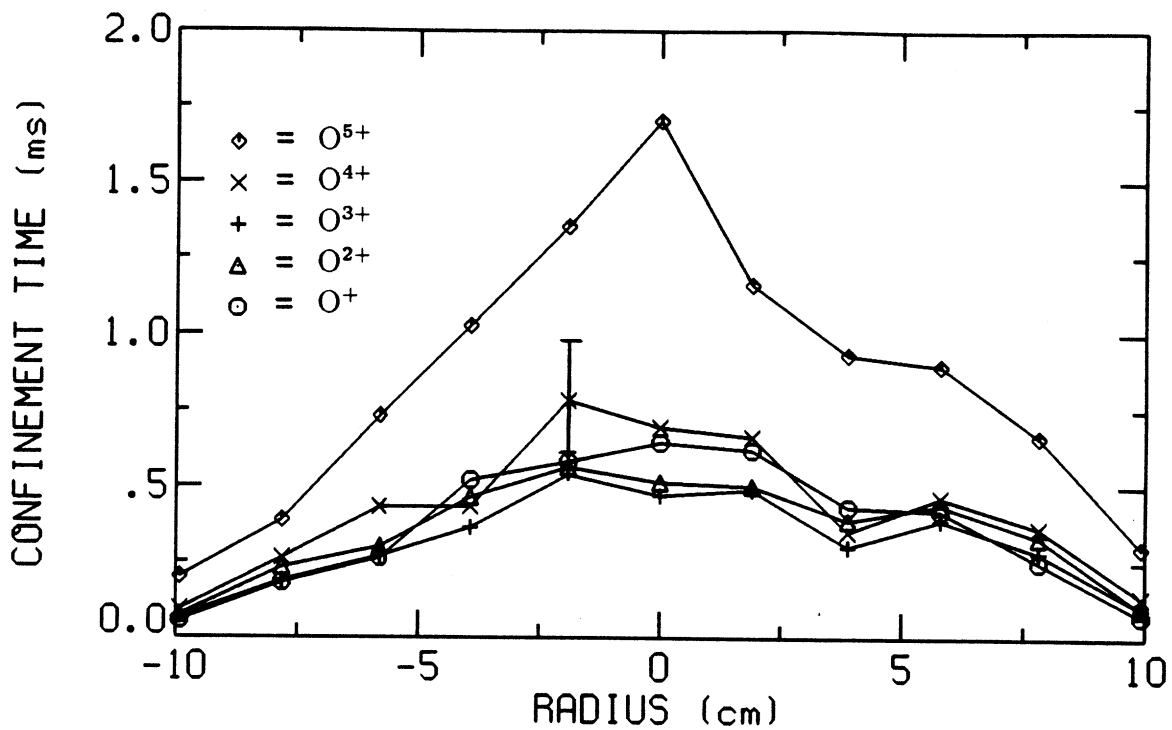
Figure 4-8: Parallel ion confinement times for the 1 kW, 1×10^{-6} Torr oxygen plasma.
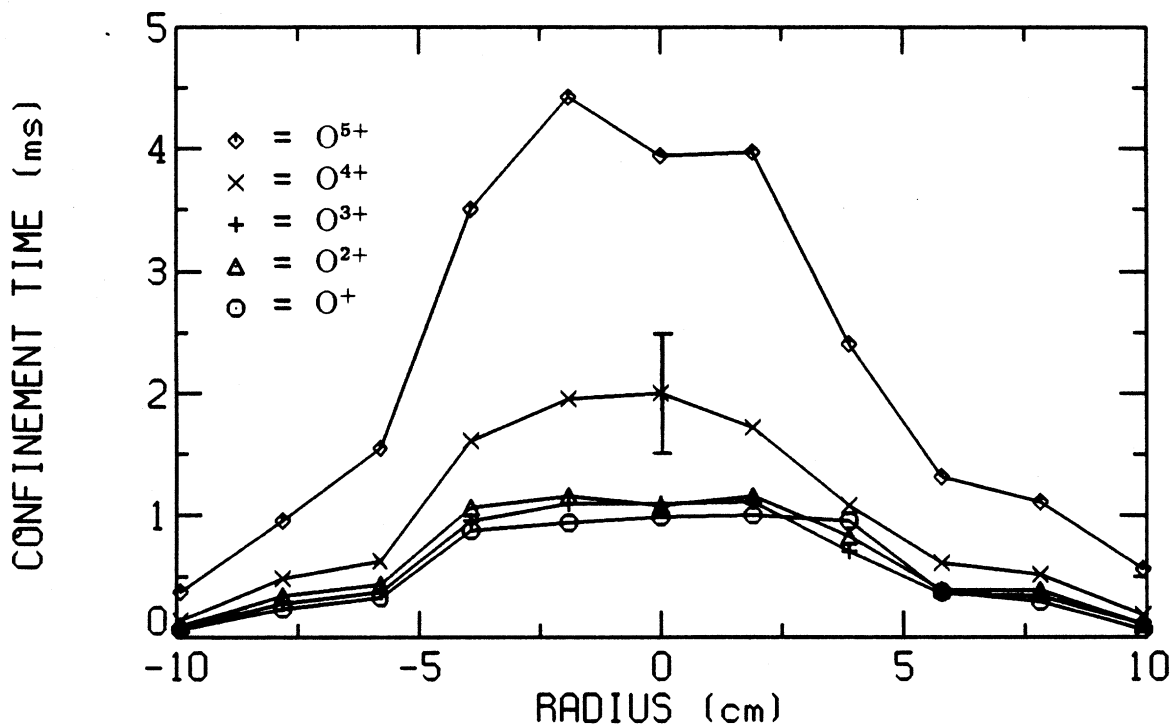
Figure 4-9: Parallel ion confinement times for the 3.4 kW, 1×10^{-6} Torr oxygen plasma.

low charge states of Fig. 4-8). This is a strong indication of electrostatic trapping because the scattering times decrease with charge state. The experimental parallel confinement time is also an order of magnitude longer than the calculated collision time. In addition, the parallel ion confinement times peak in the plasma center and fall off outside the ECR zone (this rapid decrease in parallel confinement at the edge of the ECR zone accounts for the hollow ion fluxes). All of these observations support the parallel confinement of ions by a potential dip caused by the hot electrons.

The ion temperatures for the first four charge states of oxygen, measured by Doppler broadening, are shown in Fig. 4-10. These ion temperatures are an order of magnitude greater than can be explained by electron drag heating alone. The measured parallel and perpendicular ion temperatures are the same to within experimental error, except possibly for the first charge state. The first charge state has the largest ratio of magnetic to electrostatic confinement and therefore its distribution function may be stretched in the parallel direction. The ion temperatures also show a slight increase with charge state.

The ion temperatures determined from the time-of-flight analyzer for the 1 kW, 5×10^{-7}Torr oxygen plasma are shown in Fig. 4-11. These temperatures are much larger than the ion temperatures measured by Doppler broadening and have a strong linear increase with charge state. The TOF ion temperatures are likely incorrect due to fluctuations in the plasma potential, as discussed in the next section on neon plasmas.

Next the results of the ion model developed in the previous chapter are compared to experiment. The model calculates the ion densities, fluxes and confinement times in the plasma center given the electron density and temperature, the neutral pressure outside the plasma, information about the magnetic geometry, the ion temperature and the total ion flux. The last experimental measurement is needed to divide the ion confinement time into its parallel and perpendicular components. The ion particle balance equations for oxygen take into account ionization of molecular oxygen by the following two step process:

$$O_2 + e \quad \rightarrow \quad O_2^+ + 2e$$
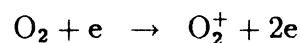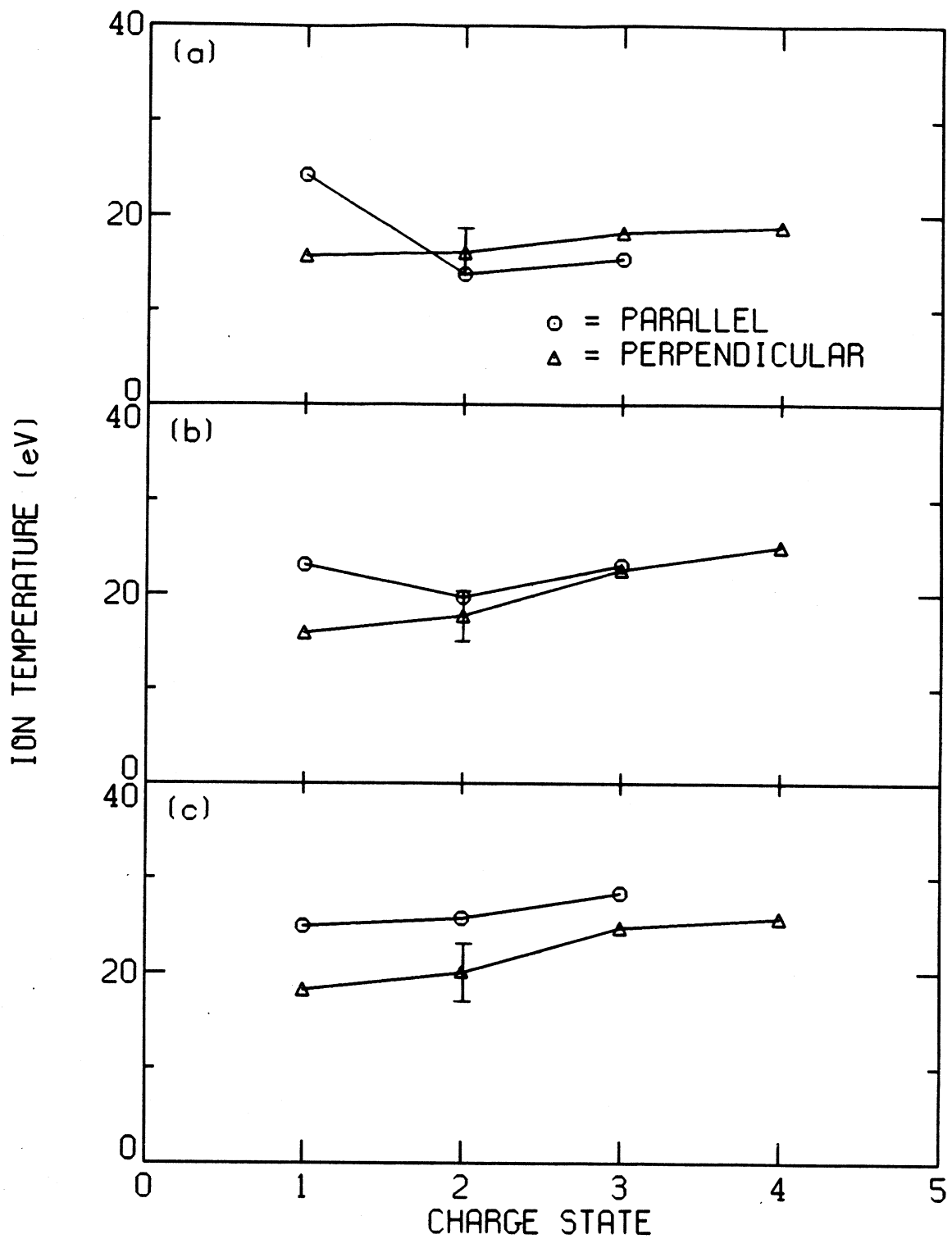
Figure 4-10: Ion temperatures parallel and perpendicular to the magnetic field, measured by Doppler broadening, for the (a) 1 kW, 5×10^{-7}Torr, (b) 1 kW, 1×10^{-6}Torr and (c) 3.4 kW, 1×10^{-6}Torr oxygen plasmas.
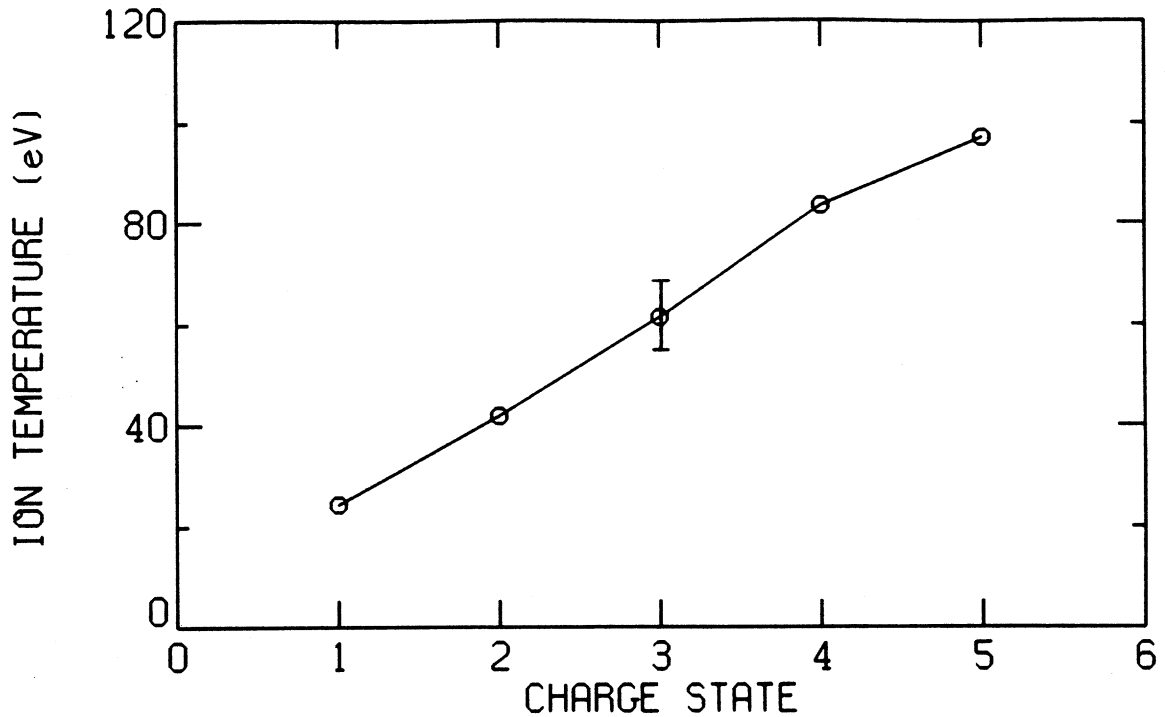
Figure 4-11: Ion temperatures from the time-of-flight analyzer for the 1 kW, 5 × 10^{-7}Torr oxygen plasma.

$$O_2^+ + e \quad \rightarrow \quad O + O^+ + e,$$
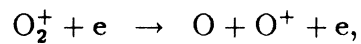
where the atomic oxygen is lost to the plasma. Note that each oxygen molecule contributes only one ion to the plasma.

Table 4.2 compares the experimental average charge state of the plasma and end loss and the average parallel confinement time to the ion model. The average perpendicular confinement time from the ion model is also shown. Although the ion model tends to overestimate the average charge state of the confined ions, it does follow the

Table 4.2: Comparison of ion model results to experiment for oxygen plasmas.

ECRH power Neutral pressure Magnetic field	1 kW 5×10^{-7}Torr 3.5 kG		1 kW 1×10^{-6}Torr 3.5 kG		3.4 kW 1×10^{-6}Torr 3.5 kG	
	Exper.	Model	Exper.	Model	Exper.	Model
$\langle z \rangle$ of plasma	2.3	2.6	1.9	1.8	2.5	3.0
$\langle z \rangle$ of end loss	2.0	1.9	1.8	1.9	2.1	2.3
$\langle \tau_\parallel \rangle$	1.8 ms	1.6 ms	0.5 ms	0.6 ms	1.2 ms	1.0 ms
$\langle \tau_\perp \rangle$		1.8 ms		6.3 ms		0.9 ms
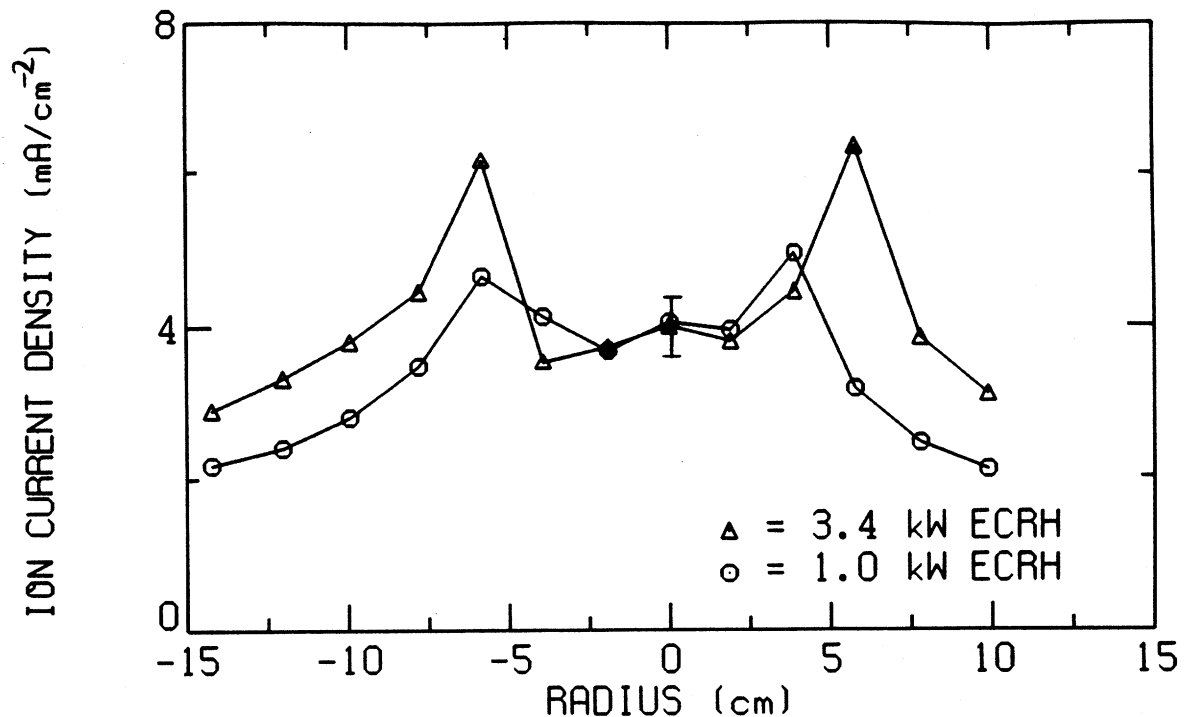
Figure 4-12: Ion current density mapped to the magnetic midplane for two oxygen plasmas. The neutral pressure in both cases is $n_o = 1 \times 10^{-6}$ Torr.

experimental value as the neutral pressure and ECRH power are varied. Also the ion model predicts that radial transport is an important loss mechanism for the ions, especially at low neutral pressure and high ECRH power. This agrees with previous measurements of ion radial transport on Constance B [Goodman, 1989].

Fig. 4-12 shows the radial profile of the ion current density for two oxygen plasmas with the same neutral pressure but different ECRH powers. From Table 4.2, the two plasmas have nearly the same total ion confinement time; however, the 3.4 kW plasma has 2.5 times the electron density of the 1 kW plasma. This extra density does not show up as end loss within the ECR zone and therefore is lost radially. Once outside the ECR zone, the parallel confinement time drops quickly (see Fig. 4-9) and the extra density now shows up as an increase in the end loss. Thus, the radial profile hollowness of ion end loss increases with increasing ion radial transport.

A more detailed comparison between the experiment and ion model is shown in Figs. 4-13—4-15, where the parallel confinement times, densities and fluxes for the first five charge states are shown for the three oxygen plasmas. In these figures, O_2^+
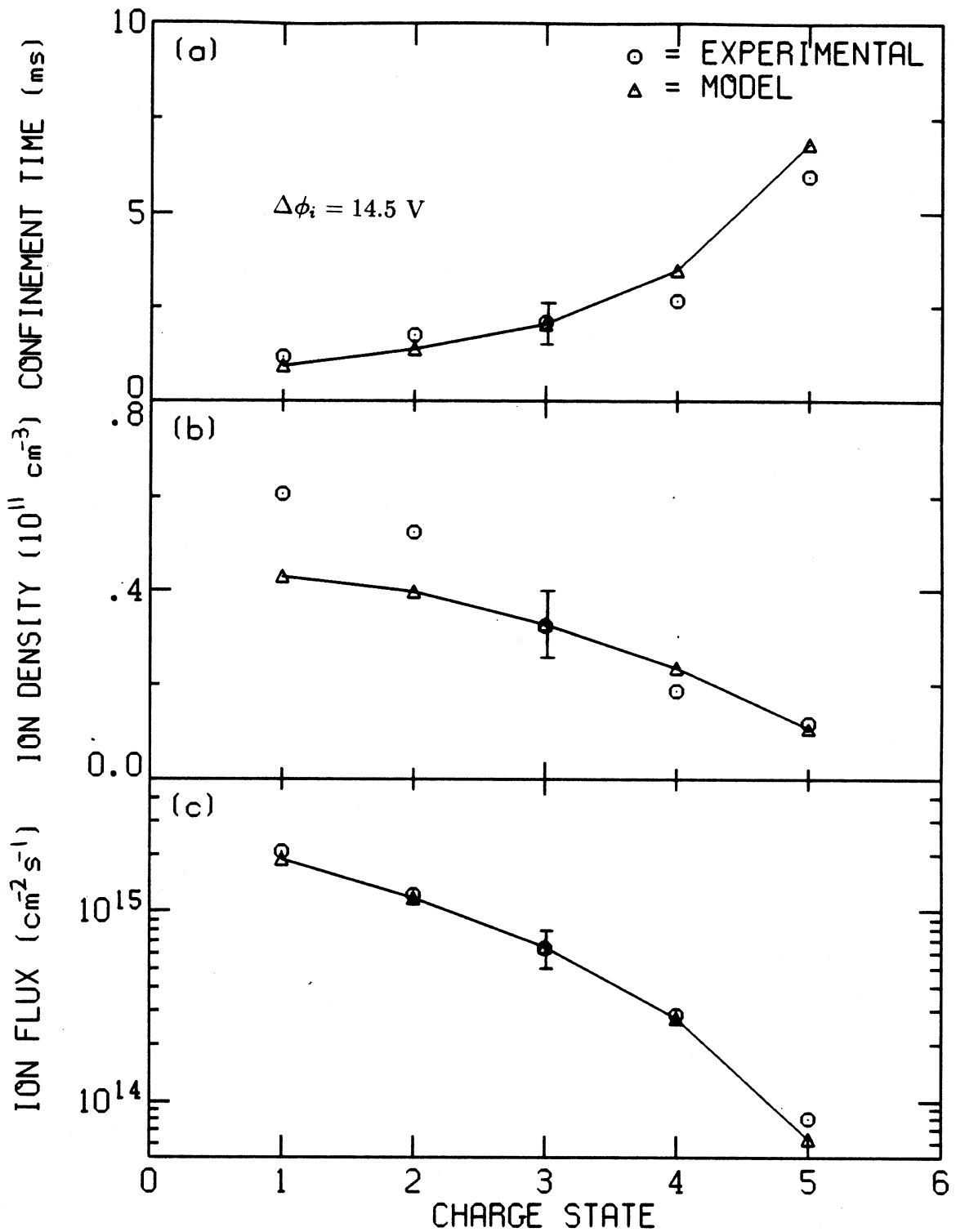
Figure 4-13: Comparison of experimental and model results: (a) parallel ion confinement times, (b) ion densities and (c) ion fluxes for the 1 kW, 5×10^{-7} Torr oxygen plasma.
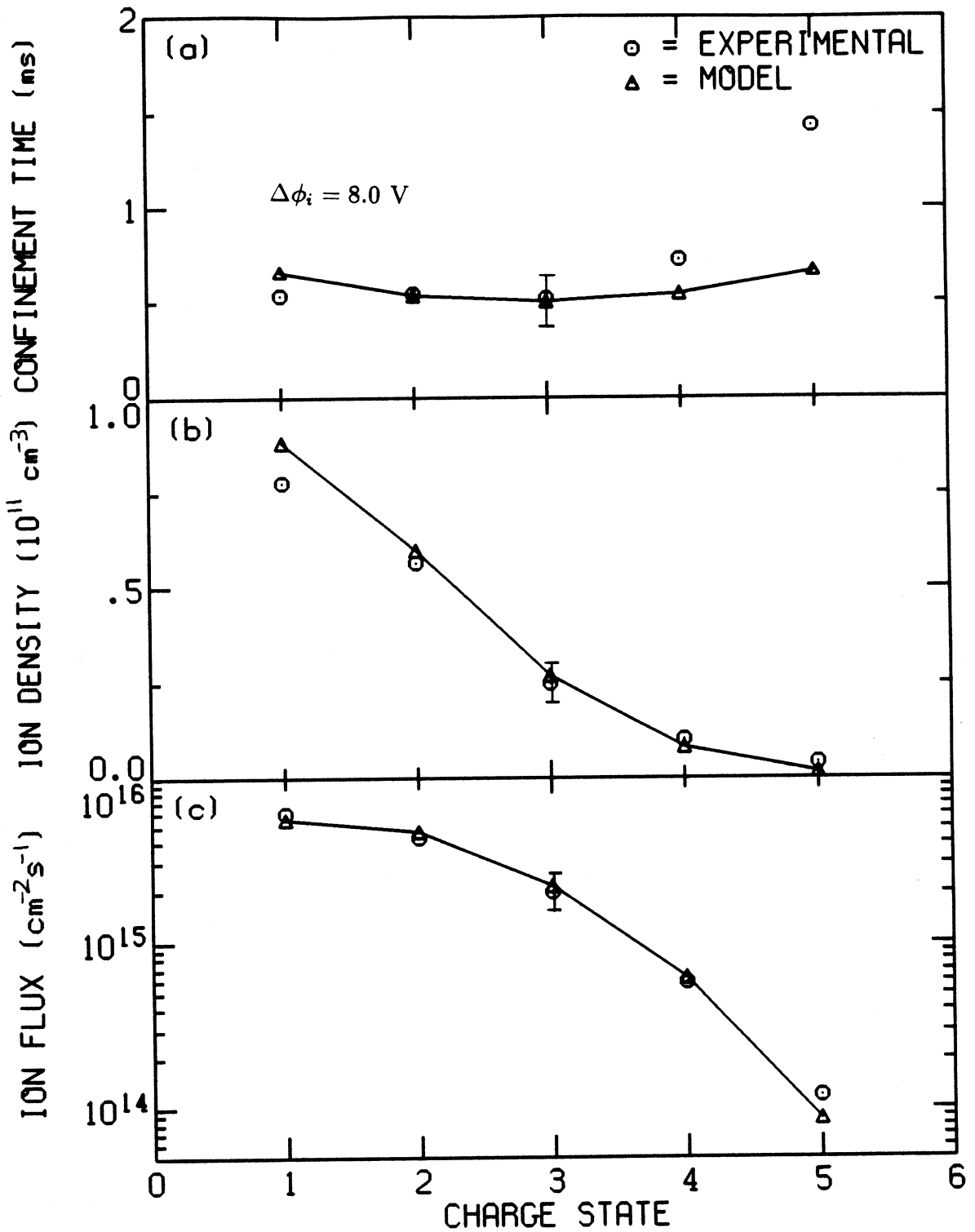
Figure 4-14: Comparison of experimental and model results: (a) parallel ion confinement times, (b) ion densities and (c) ion fluxes for the 1 kW, 1×10^{-6} Torr oxygen plasma.
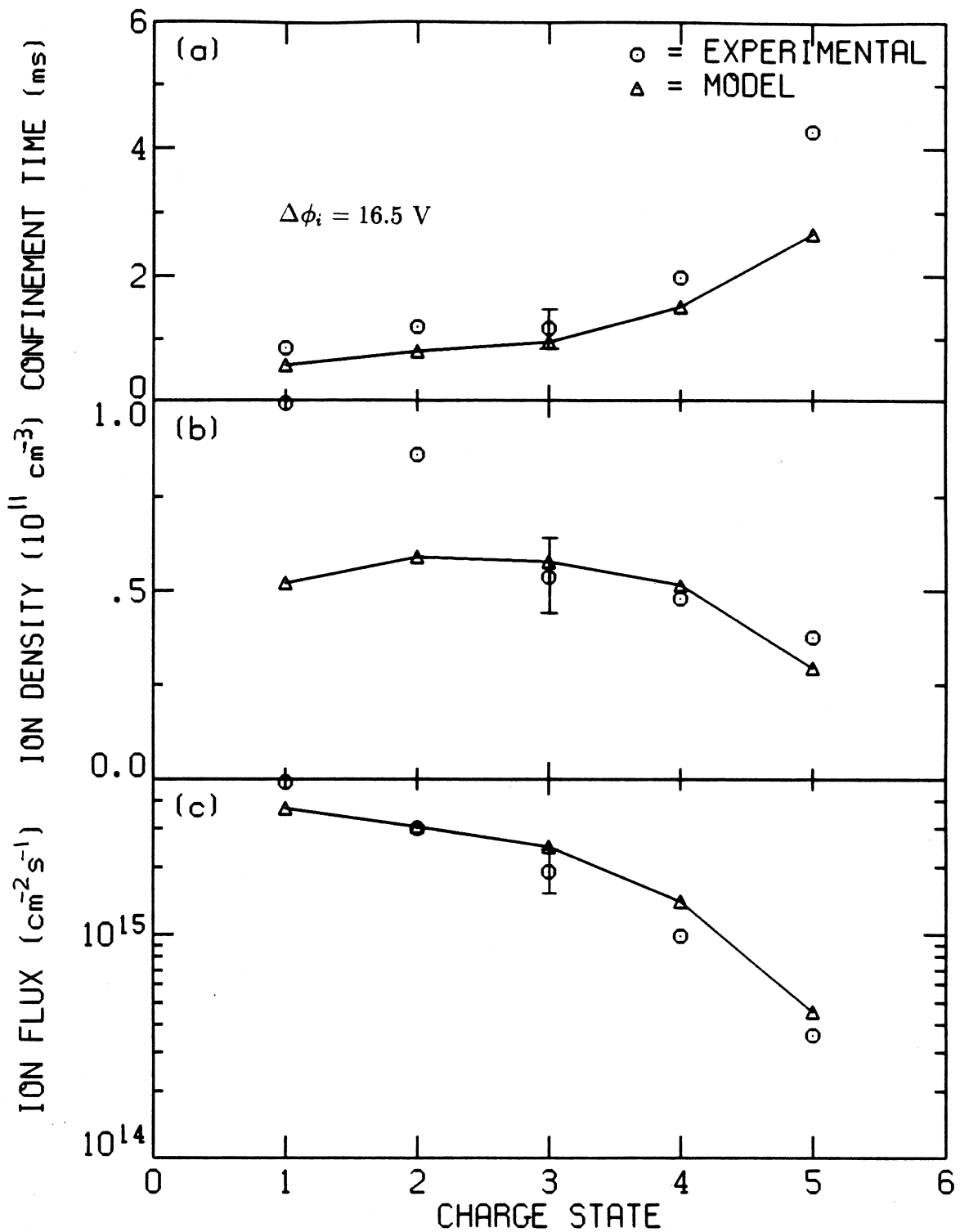
Figure 4-15: Comparison of experimental and model results: (a) parallel ion confinement times, (b) ion densities and (c) ion fluxes for the 3.4 kW, 1×10^{-6} Torr oxygen plasma.

and O^+ are lumped together under the heading "charge state 1". In calculating the spatial diffusion confinement time, a value of $K_{\parallel} = 1.9$ for a B-compressed parabolic profile is tried. As a result, the crossover from Pastukhov-flow confinement to spatial diffusion occurs around $z_i = 8$ and therefore only the Pastukhov-flow confinement times are important. The model parallel confinement times generally follow the experimental ones with increasing charge state, except for $z_i = 5$ in Fig. 4-14 where the model confinement time is much too short. It is possible that this charge state is in the spatial diffusion regime instead of the Pastukhov-flow regime. A more thorough discussion of this possibility is given in the next section on neon plasmas.

The model ion densities generally follow the experimental results, but the densities of the lower charge states tend to be underestimated. In calculating the ionization rates, the Müller rate parameters are used instead of Lotz since Lotz published no results for molecular oxygen. The over estimating of the average charge state of the confined ions leads directly to the underestimating of the parallel ion confinement times by underestimating the potential dip. This effect is most evident in Fig. 4-15.

The model ion fluxes tend to fit the experimental results better than either the parallel confinement times or the densities. This is because an underestimated ion confinement time leads to an underestimated ion density and therefore their ratio, proportional to the ion flux, is not very sensitive to errors. This is a fortunate result, since model predictions of ion fluxes are in the most demand.

The sensitivity of the ion model results to the model inputs is now examined. For this purpose, the sensitivity is defined to be the change in the model $\langle z \rangle$ of the confined ions divided by the change in a particular input. The ion model sensitivity to the model inputs is shown in Table 4.3 for a typical oxygen plasma. The ion model is fairly sensitive to changes in the neutral pressure and electron density. Changes in the total ion flux, ion temperature or cold electron temperature have a weaker effect on the ion model results. Changes in the hot electron temperature has almost no effect on the ion model results.

Using the experimental radial profiles of ion density and flux, the radial profile of the potential dip can be deduced from the Pastukhov-flow model. An example for

Table 4.3: Sensitivity of model $\langle z_p \rangle$ to model inputs.

Input parameter	Sensitivity
n_o	.27
n_{eh}	.26
n_{ec}	.10
$\Gamma_{\|i}$	.05
T_{ec}	.05
T_i	.03
T_{eh}	.00

the 1 kW, 5×10^{-7}Torr oxygen plasma is shown in Fig. 4-16, where the potential dip is chosen to give the measured *average* parallel confinement time. The deduced potential dip is relatively flat throughout the ECR zone and falls rapidly outside it where there are few hot electrons. The deduced potential dip reaches zero at 10 cm, which is the plasma radius.

4.2   Neon

The ion densities and fluxes as a function of charge state are measured for three different neon plasmas in order to determine the parallel ion confinement times. The electron densities, electron temperatures and ion temperatures are also measured for use in the ion model. After the experimental results are presented, they are compared to results from the ion model.

As with the oxygen plasmas, the three neon plasmas differed in applied ECRH power and neutral pressure, as shown in Table 4.4. The electron density and plasma beta values given in this table are for the plasma center. The neutral pressure values are gauge pressures. All plasmas have the same magnetic geometry. In these experiments, the isotope Ne_{22} is used instead of natural neon in order to avoid m_i/q_i overlaps in the time-of-flight spectrum with impurities such as hydrogen and helium.

The ion densities in the plasma center are shown in Fig. 4-17 for the three neon plasmas. As with oxygen, increasing the neutral pressure for neon plasmas lowers the average charge state of the ions, while increasing the ECRH power raises the
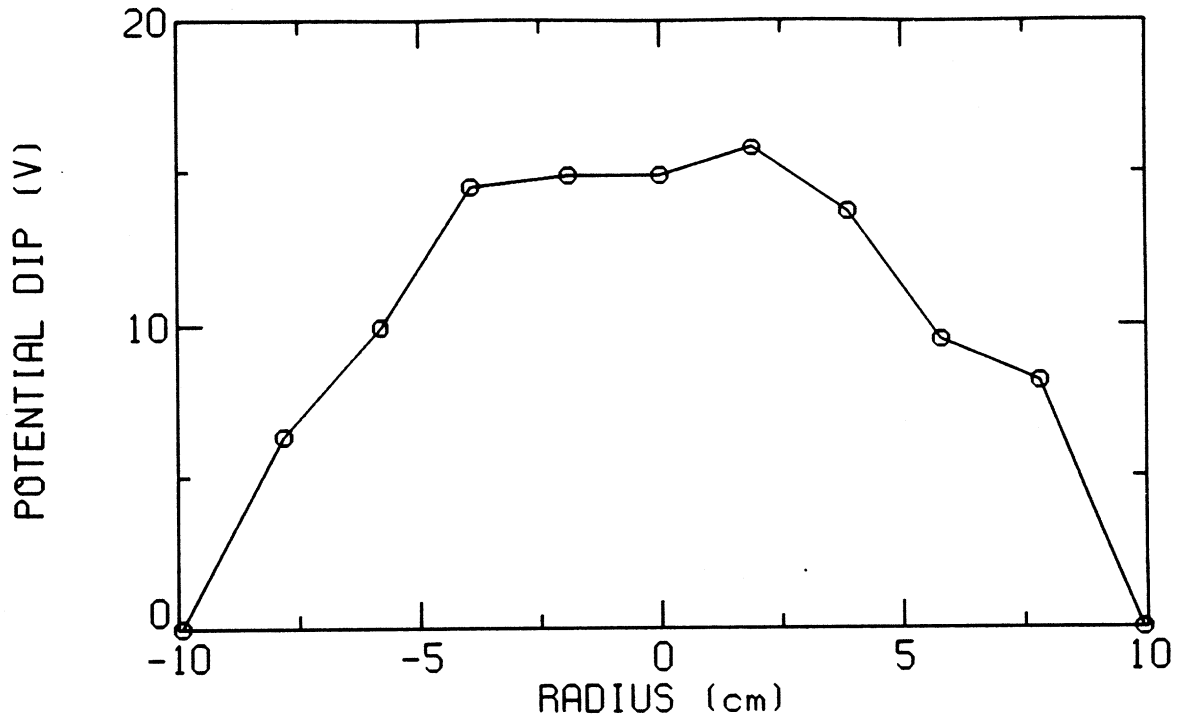
Figure 4-16: Deduced potential dip from the Pastukhov-flow model for the 1 kW, 5×10^{-7}Torr oxygen plasma.

Table 4.4: Parameters for the three neon plasmas studied in this section.

ECRH power	1 kW	4 kW	4 kW
Neutral pressure	5×10^{-7}Torr	5×10^{-7}Torr	1×10^{-6}Torr
Magnetic field	3.5 kG	3.5 kG	3.5 kG
Hot electron density	1.5×10^{11}cm^{-3}	5.1×10^{11}cm^{-3}	3.9×10^{11}cm^{-3}
Hot electron temperature	300 keV	320 keV	370 keV
Plasma beta	0.08	0.32	0.28
Cold electron density	1.4×10^{11}cm^{-3}	2.5×10^{11}cm^{-3}	2.7×10^{11}cm^{-3}
Cold electron temperature	100 eV	100 eV	60 eV
Plasma potential	110 V	220 V	140 V
Ion temperature	12 eV	18 eV	19 eV
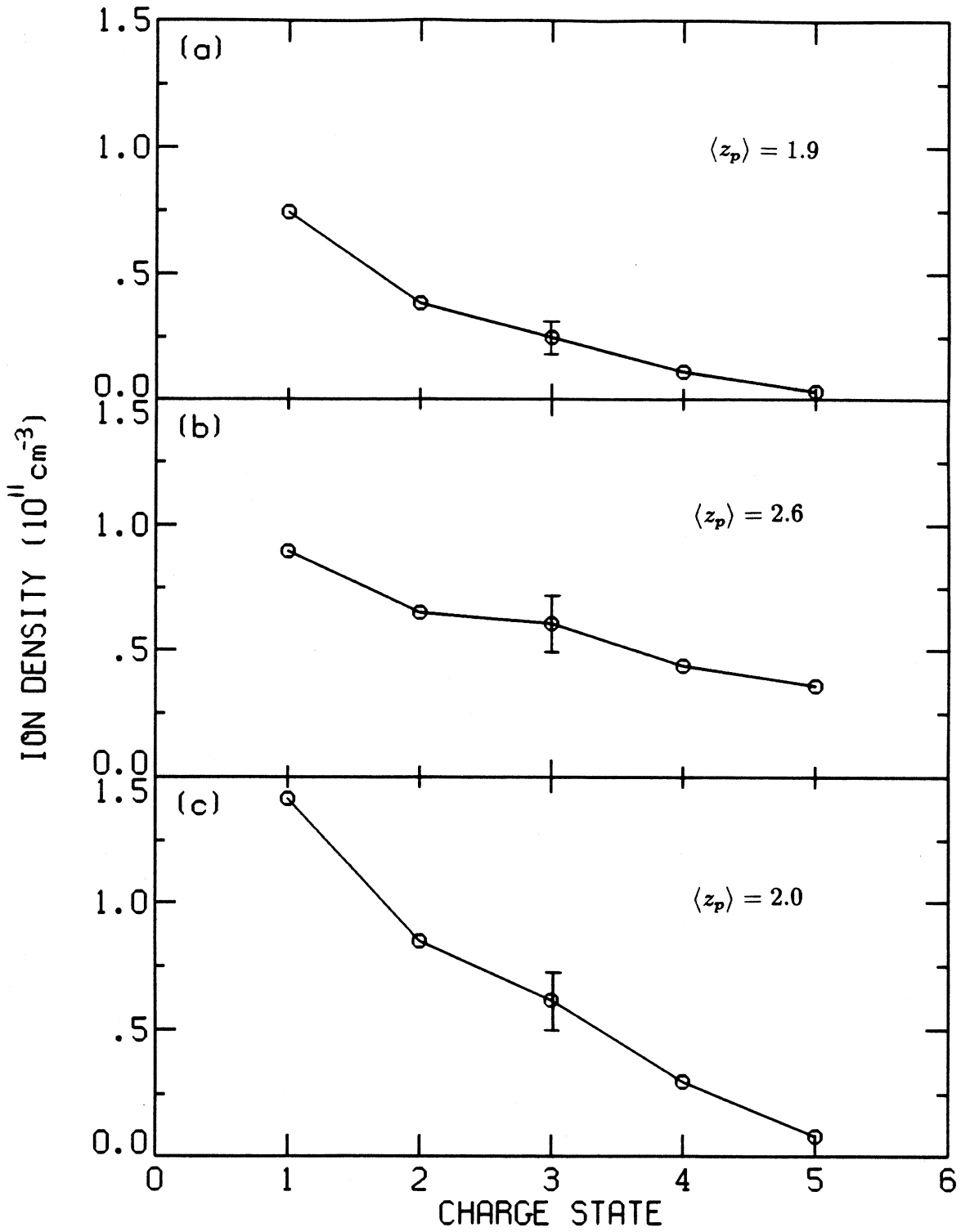
Figure 4-17: Ion densities in the plasma center for (a) 1 kW, 5×10^{-7}Torr, (b) 4 kW, 5×10^{-7}Torr and (c) 4 kW, 1×10^{-6}Torr neon plasmas.
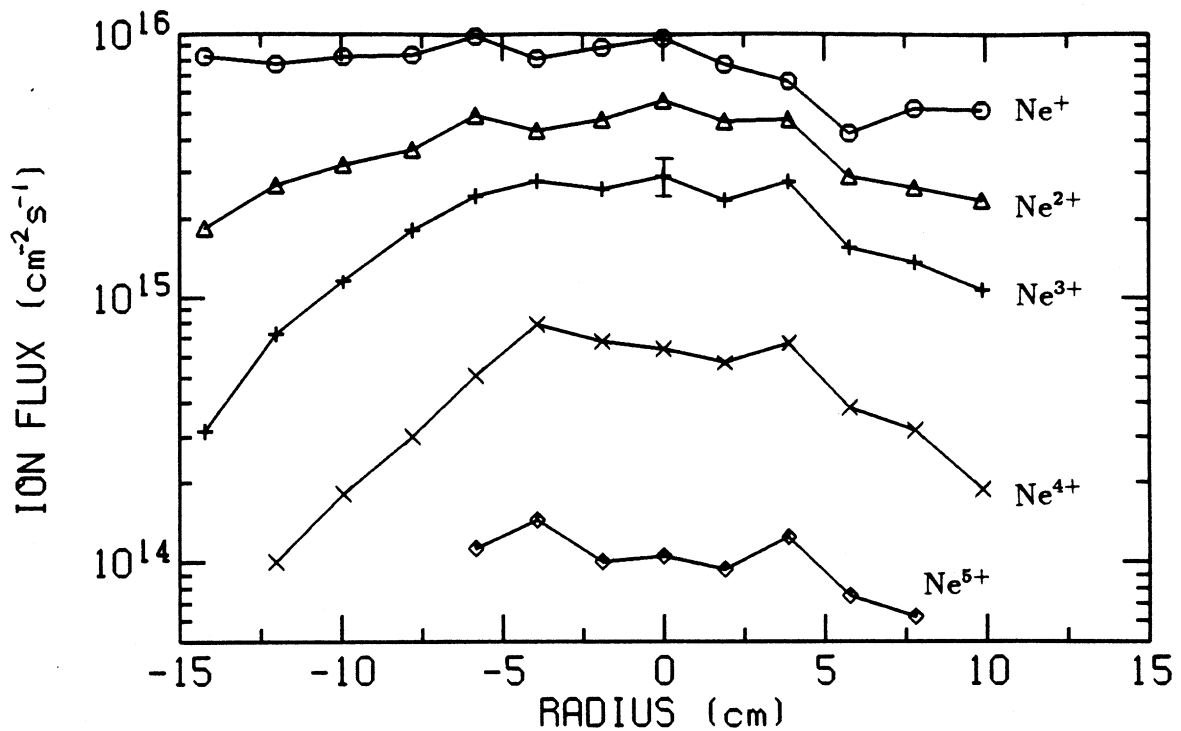
Figure 4-18: Ion fluxes mapped to the magnetic midplane for the 1 kW, 5×10^{-7} Torr neon plasma.

average charge state of the ions. The ion model predicts that increasing the neutral pressure lowers the average charge state because the ion confinement time decreases and charge exchange increases, while increasing the ECRH power raises the average charge state because the ionization time decreases due to a higher electron density.

The ion fluxes for the three neon plasmas are shown in Figs. 4-18—4-20. They are similar to the results for oxygen in that the ion fluxes decrease with charge state and the radial profiles are hollow. The parallel ion confinement times determined from the ion densities and fluxes are shown in Figs. 4-21—4-23 for the three neon plasmas. The parallel ion confinement times increase with charge state and peak in the plasma center.

The ion temperatures for the first three charge states of neon are measured by Doppler broadening. However, the quality of the data is poor compared to oxygen because the lines are weaker and the amount of Doppler broadening is smaller due to the greater mass of Ne_{22}. This makes it difficult to determine the absolute ion temperature, although relative changes in ion temperatures as conditions vary can
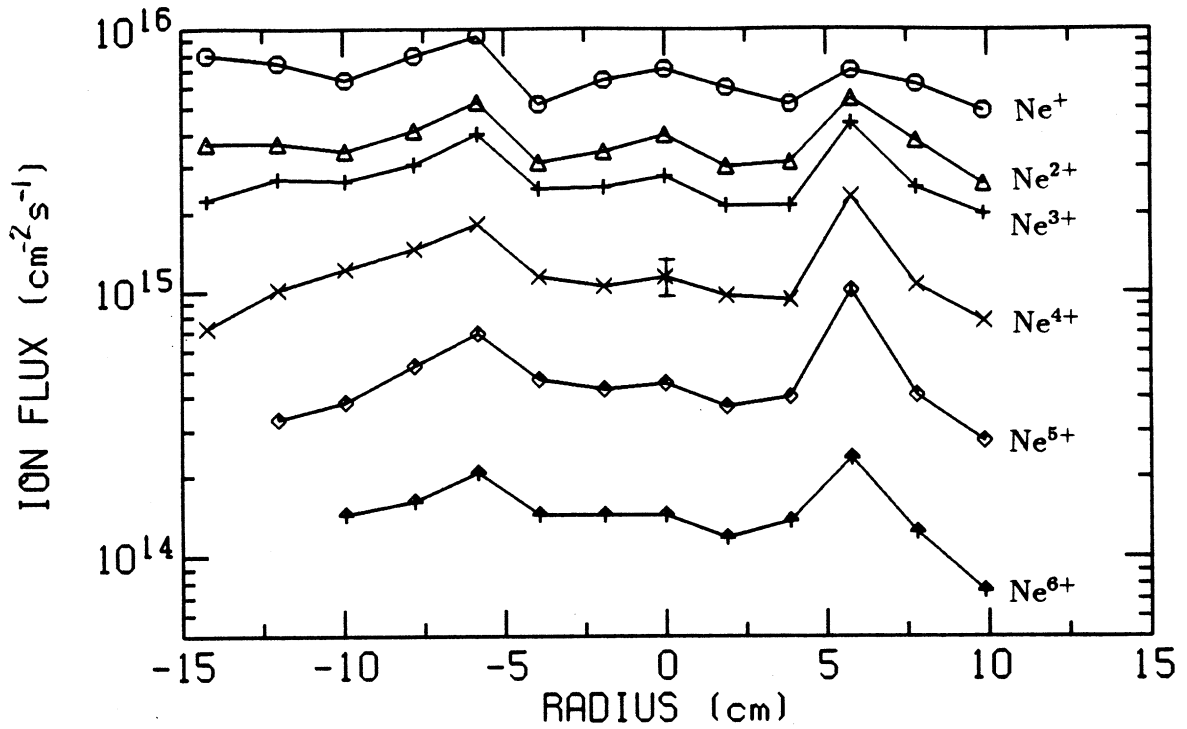
Figure 4-19: Ion fluxes mapped to the magnetic midplane for the 4 kW, 5×10^{-7}Torr neon plasma.
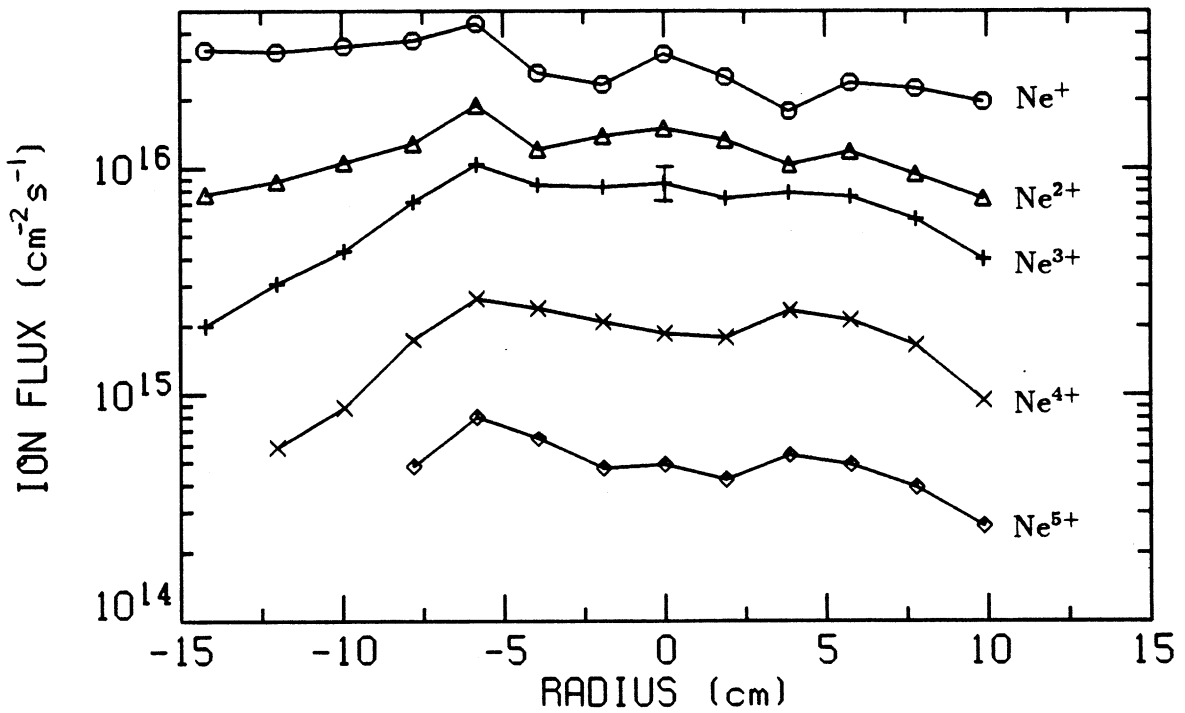
Figure 4-20: Ion fluxes mapped to the magnetic midplane for the 4 kW, 1×10^{-6}Torr neon plasma.
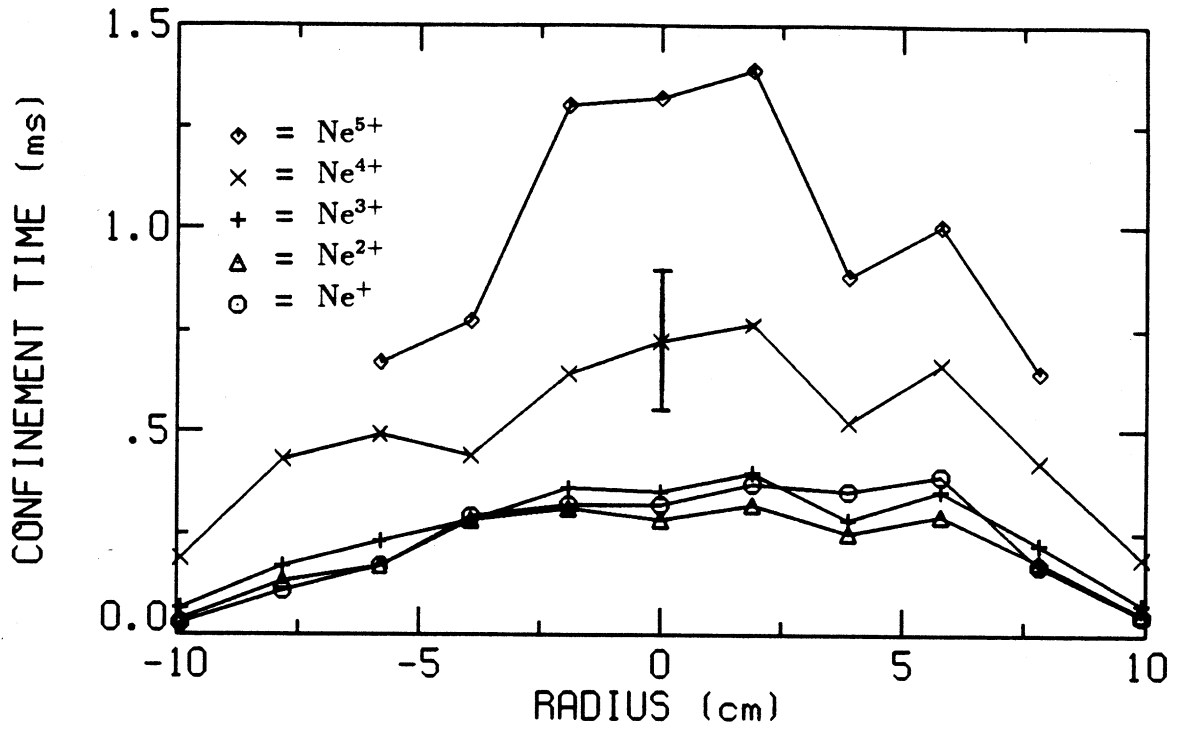
Figure 4-21: Parallel ion confinement times for the 1 kW, 5×10^{-7}Torr neon plasma.
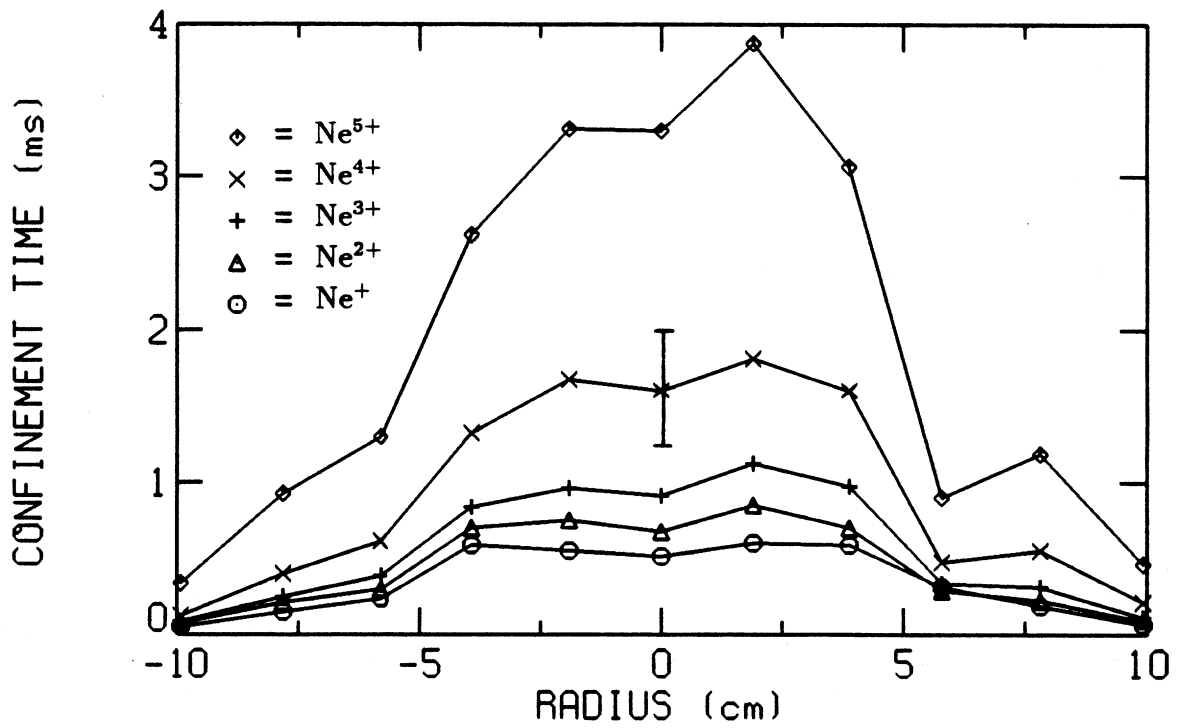
Figure 4-22: Parallel ion confinement times for the 4 kW, 5×10^{-7}Torr neon plasma.
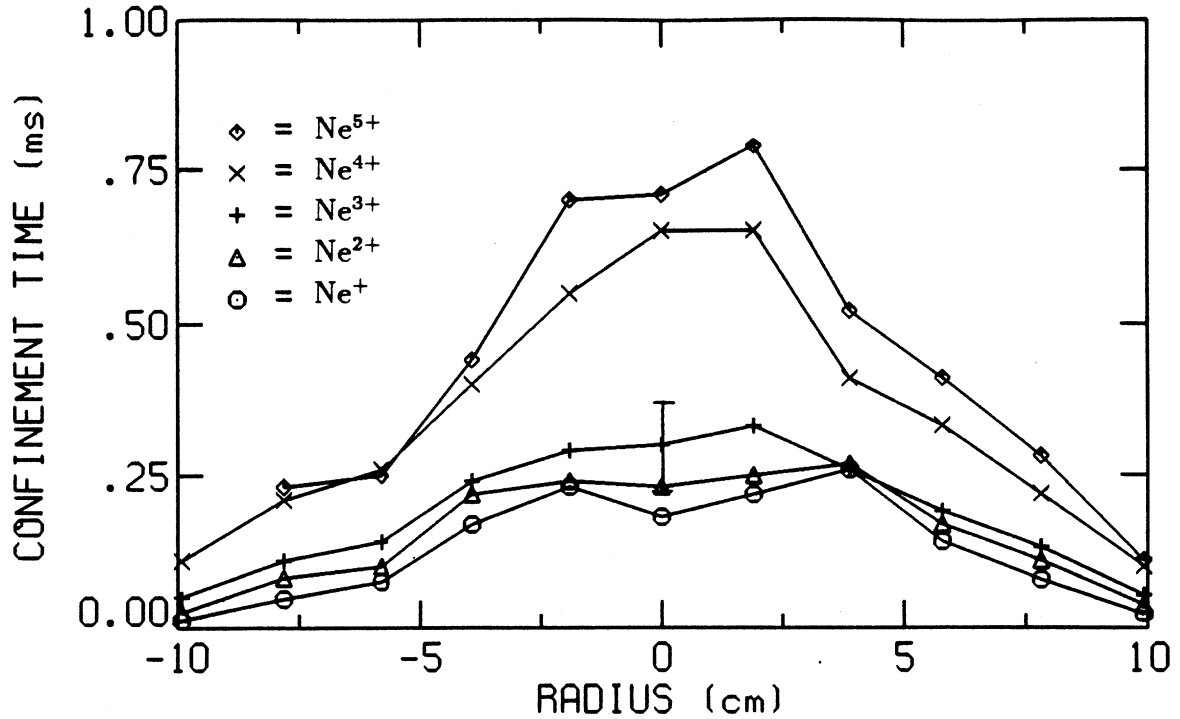
Figure 4-23: Parallel ion confinement times for the 4 kW, 1×10^{-6}Torr neon plasma.

still be determined. Since neon and oxygen are close in atomic mass, they should have similar ion temperatures. The average neon ion temperature is therefore assumed to be the same as the average oxygen ion temperature. Also, all neon charge states are assumed to have the same temperature. The neon ion temperatures are given in Table 4.4.

As mentioned in the last section, the TOF analyzer ion temperatures strongly increase with charge state and are much larger than the ion temperatures measured by Doppler broadening. Fig. 4-24 shows that the TOF ion temperature for Ne^+ strongly correlates with the plasma potential, where the plasma potential is scanned by varying the ECRH power, neutral pressure and magnetic field strength. A likely explanation is that fluctuations in the plasma potential ($\tilde{\phi}$) distort the measured energy dependence of the ion flux, which gives rise to a pseudo-temperature for the end loss. For the condition $q_i\tilde{\phi} \gg T_i$, numerical simulations of this effect give a pseudo-temperature equal to $q_i\tilde{\phi}$. This can explain the TOF analyzer results if $\tilde{\phi}/\phi_p$ is constant. The large ion temperature measured by the TOF analyzer is not due to ionization along a potential gradient because the TOF analyzer temperature is

93
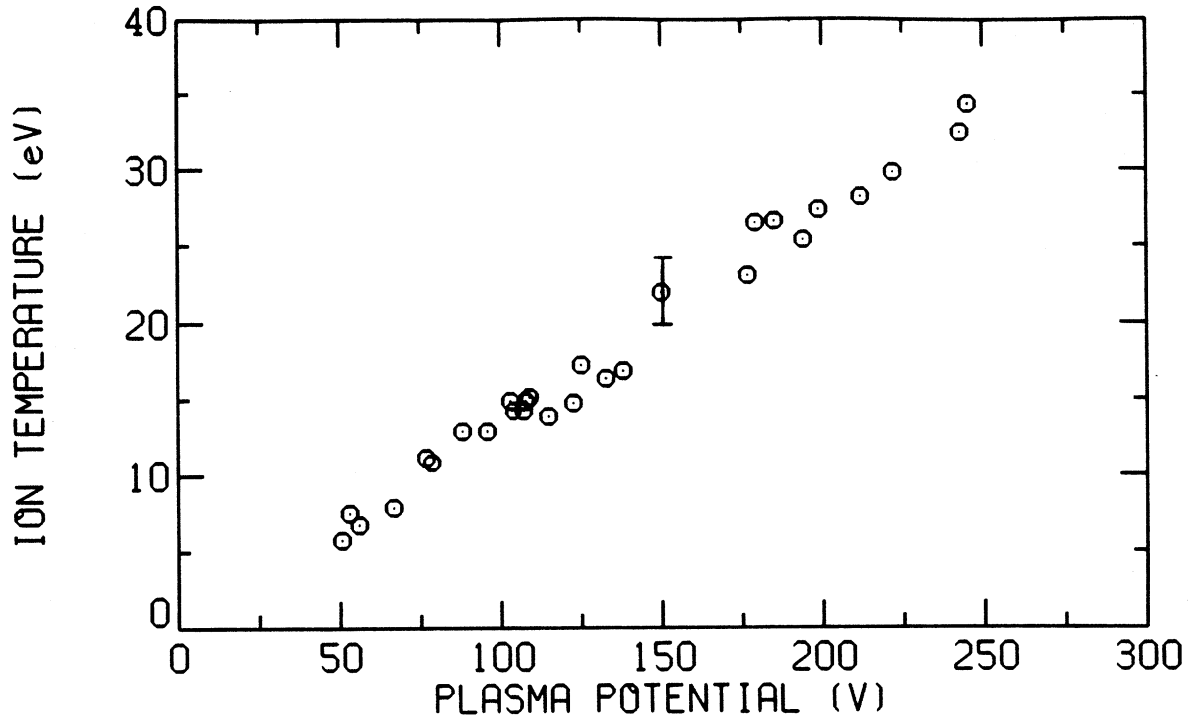
Figure 4-24: Time-of-flight analyzer ion temperature for Ne^+ as a function of the plasma potential for a neon plasma.

determined from the energy spectrum of ions which all have energy greater than the maximum plasma potential.

Next the results of the ion model are compared to experiment. Table 4.5 compares the experimental average charge state of the plasma and end loss and the average parallel confinement time to the ion model. The average perpendicular confinement time from the ion model is also shown. The model $\langle z \rangle$ of the plasma fits the experimental data for neon better than for oxygen.

Table 4.5: Comparison of ion model results to experiment for neon plasmas.

ECRH power Neutral pressure Magnetic field	1 kW 5×10^{-7}Torr 3.5 kG		4 kW 5×10^{-7}Torr 3.5 kG		4 kW 1×10^{-6}Torr 3.5 kG	
	Exper.	Model	Exper.	Model	Exper.	Model
$\langle z \rangle$ of plasma	1.9	1.7	2.6	2.6	2.0	1.8
$\langle z \rangle$ of end loss	1.7	1.8	2.0	1.9	1.7	1.9
$\langle \tau_\| \rangle$	0.4 ms	0.4 ms	0.9 ms	0.9 ms	0.3 ms	0.3 ms
$\langle \tau_\perp \rangle$		7.2 ms		0.7 ms		3.1 ms

A more detailed comparison between the experiment and ion model is shown in Figs. 4-25—4-27, where the parallel confinement times, densities and fluxes for the first five charge states are shown for the three neon plasmas. The Lotz rate parameters are used to determine the electron ionization rates. The ion densities and fluxes predicted by the model follow the experimental results fairly well.

In calculating the spatial diffusion confinement time, a value of $K_{\parallel} = 1.9$ for a B-compressed parabolic profile is tried. As a result, the crossover from Pastukhov-flow confinement to spatial diffusion occurs around $z_i = 7$ and therefore only the Pastukhov-flow confinement times are important. This seems satisfactory except for $z_i = 4, 5$ for Figs. 4-25 and 4-27, where the model confinement times are too short. These two cases plus the one case for oxygen (Fig. 4-14) all have small potential dips in common. It is possible that in these cases the ions are more shallowly trapped in the magnetic well and therefore have a flatter axial plasma profile. This is in qualitative agreement with previous experimental observations on Constance B that the axial plasma profile peaks up as the ECRH power is increased or the neutral pressure is decreased. A flatter axial plasma profile means that $K_{\parallel}$ is smaller, therefore resulting in longer spatial diffusion confinement times and a transition from the Pastukhov-flow regime to the spatial diffusion regime at a lower ion charge state. The model parallel confinement times using $K_{\parallel} = 0.4$ are compared to experiment in Fig. 4-28 for the 1 kW, 5×10^{-7}Torr neon plasma. For this case, the transition from Pastukhov-flow confinement to spatial diffusion occurs at $z_i = 4$ and the model more closely follows the experimental results.

To summarize the oxygen and neon experimental results, increasing the neutral pressure lowers the average charge state of the ions, while increasing the ECRH power raises the average charge state of the ions. The radial profile of ion end loss is hollow. The parallel ion confinement times increase with charge state and peak on axis. The parallel and perpendicular ion temperatures are the same to within experimental error. The average difference between the experimental and ion model densities, fluxes and parallel confinement times is 20% for oxygen and neon plasmas. This is close to the experimental error in these quantities, therefore the ion model
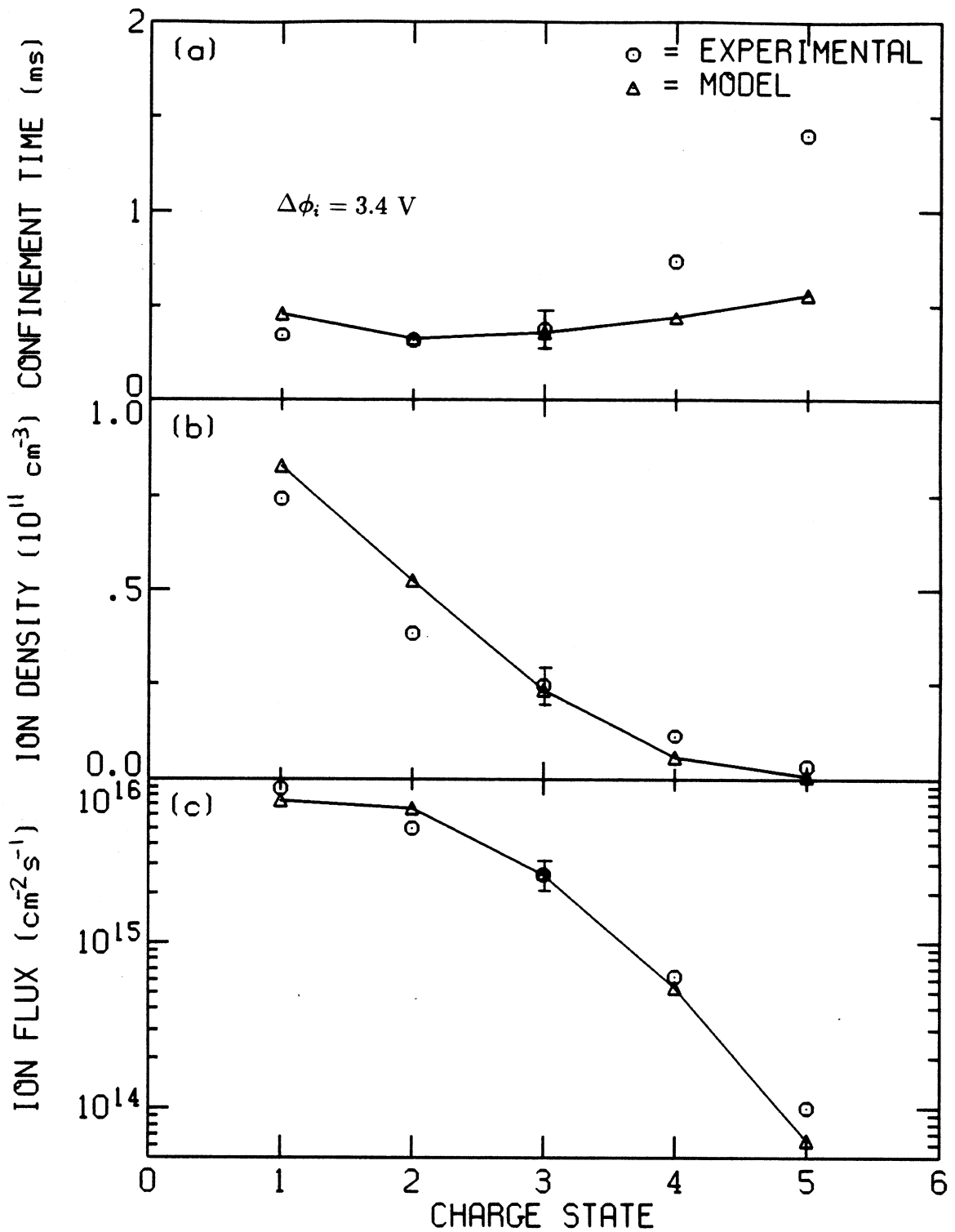
Figure 4-25: Comparison of experimental and model results: (a) parallel ion confinement times, (b) ion densities and (c) ion fluxes for the 1 kW, 5×10^{-7}Torr neon plasma.
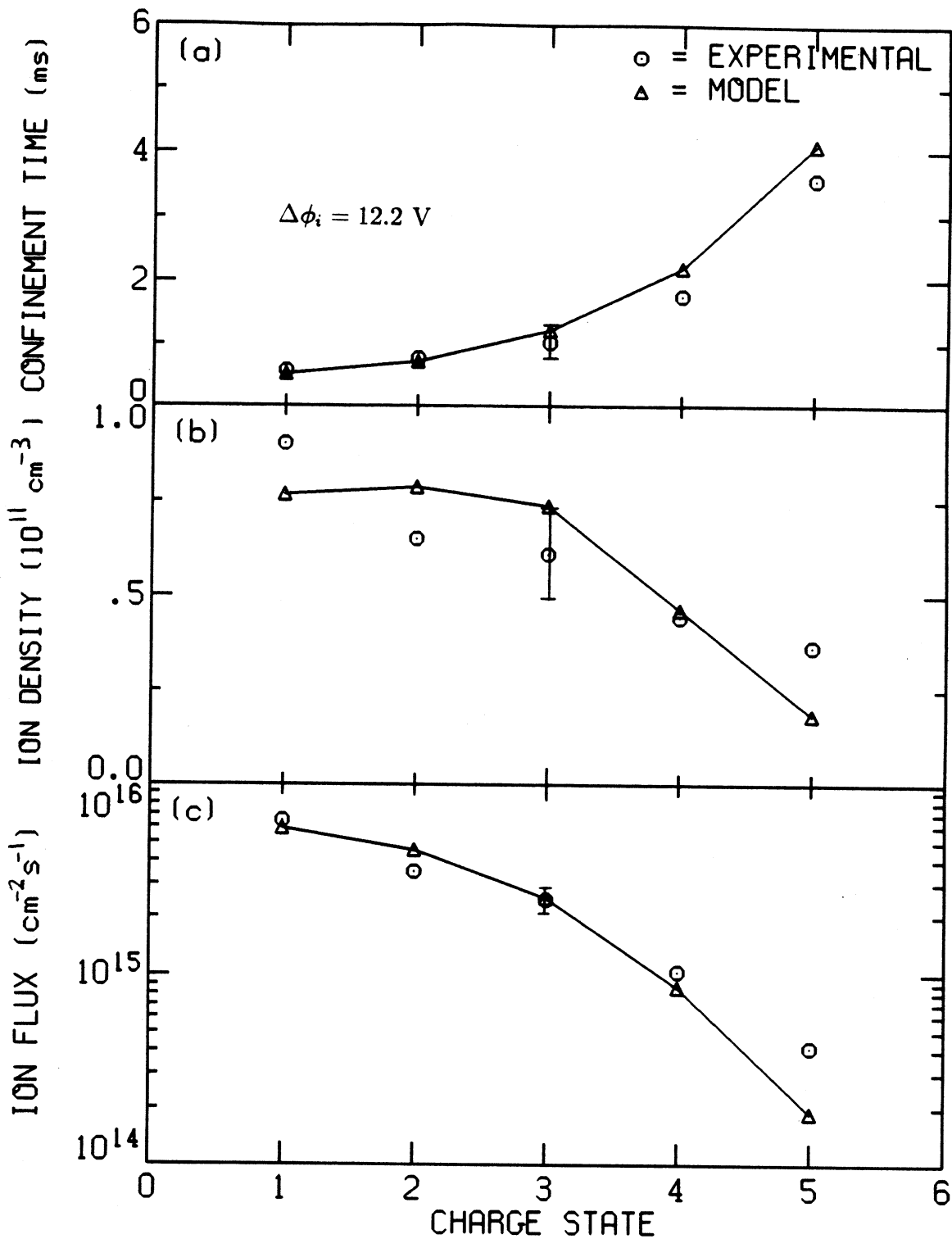
Figure 4-26: Comparison of experimental and model results: (a) parallel ion confinement times, (b) ion densities and (c) ion fluxes for the 4 kW, 5×10^{-7} Torr neon plasma.
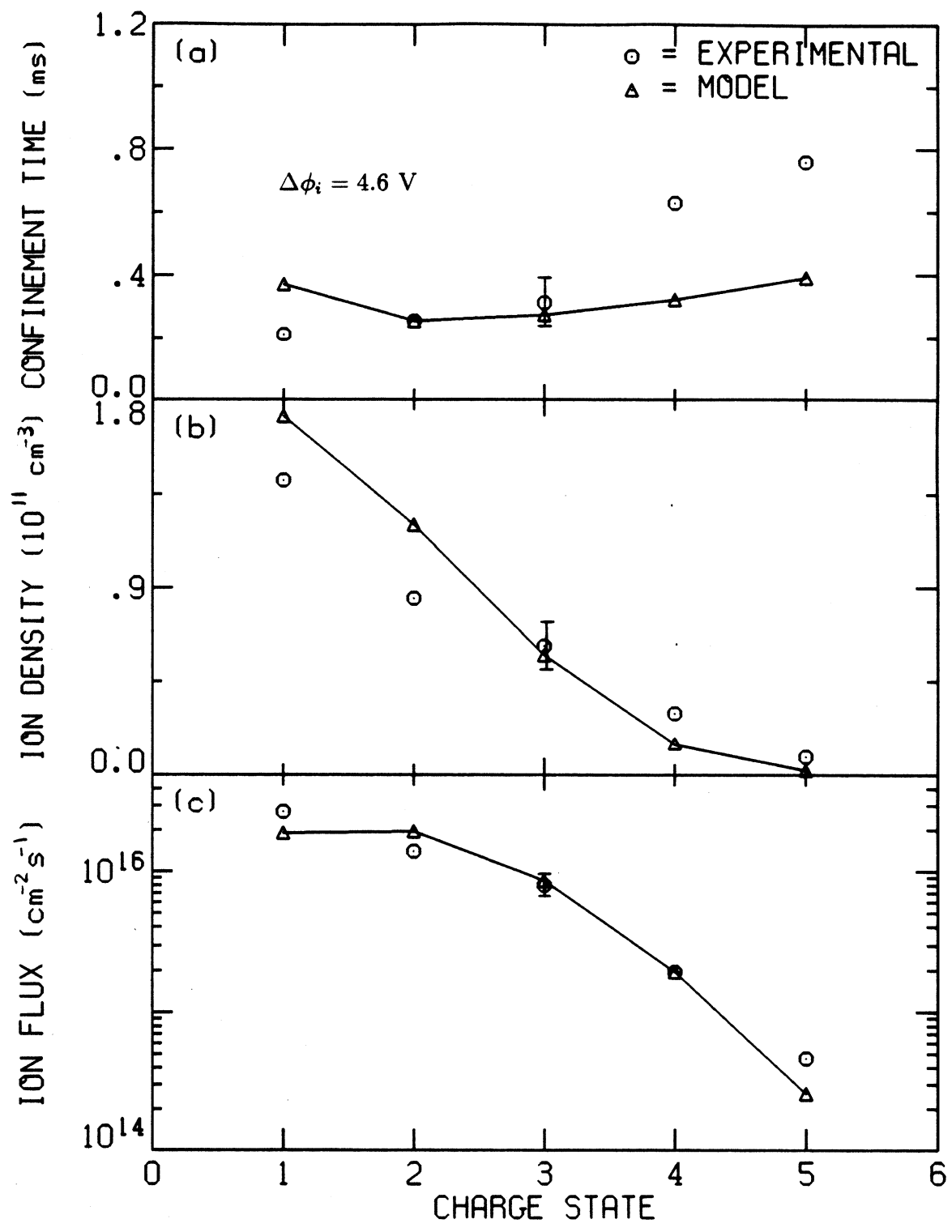
Figure 4-27: Comparison of experimental and model results: (a) parallel ion confinement times, (b) ion densities and (c) ion fluxes for the 4 kW, 1×10^{-6} Torr neon plasma.

Table 4.6: Electron parameters for the noble gas plasmas studied in this section.

Gas	helium	argon	krypton	xenon
Hot electron density (10^{11}cm^{-3})	6.5	3.8	3.5	3.5
Hot electron temperature (keV)	340	440	480	420
Plasma beta	0.43	0.33	0.32	0.27
Cold electron density (10^{11}cm^{-3})	2.8	2.5	1.6	0.9
Cold electron temperature (eV)	90			
Plasma potential (V)	120	330	350	330

and experimental results generally agree to within experimental error.

4.3 Other gases

This section presents experimental ion temperatures and ion fluxes for the noble gases up to xenon, except for neon which was covered in the previous section. The electron density and temperature are also measured for use in the ion model. After the experimental results are presented, the experimental and ion model fluxes are compared.

The conditions for all plasmas in this section are the same: 4 kW ECRH power, 1×10^{-6}Torr gauge pressure and 3.5 kG magnetic field strength. The variation in electron density and temperature with gas is shown in Table 4.6. The electron density and plasma beta values given in this table are for the plasma center. The electron density decreases with increasing ion mass.

The ion temperature measured by Doppler broadening for helium through xenon is shown in Fig. 4-29. The ion temperature increases linearly with mass up to krypton. Thus, the assumption in the last section that neon has the same average temperature as oxygen is a slight underestimate. The linear increase of ion temperature with mass and the weak dependence of ion temperature on charge state (Fig. 4-10) are both consistent with the turbulent heating model (Eqn. 3.46). A radial scan of the ion temperature at the magnetic midplane[1] is shown in Fig. 4-30 for a helium plasma. To within the experimental error, the radial profile is flat.

---

[1]This data was taken by Daniel Goodman.

a shift in the parallel confinement physics from primarily electrostatic to primarily magnetic caused by ion heating. The parallel confinement time for cold ions, which are primarily trapped by the potential dip, rapidly decreases outside the ECR zone (6 cm radius) since there are few hot electrons out there to depress the plasma potential. The parallel confinement time for hot ions, which are primarily trapped by the mirror geometry, only slowly decreases with increasing radii due to the slowly decreasing mirror ratio. The second difference is that the parallel confinement times no longer increase with charge state. In fact, there is no clear order except that the resonant ions have the shortest confinement times. This is also probably due to primarily magnetic confinement caused by ion heating.

Before the experimental results can be compared to the ion model, the theoretical parallel confinement times have to be modified to take into account the ion temperature anisotropy. Experimentally $T_\perp = T_\parallel$ without ICRH, but during ICRH $T_\perp > T_\parallel$ since ICRH mainly increases the ion's energy perpendicular to the magnetic field. The average ion temperature (used to calculate the ion-ion collision time) for this case is

$$T_i = \frac{1}{3}(T_\parallel + 2T_\perp). \tag{4.1}$$

The Pastukhov confinement time becomes

$$\tau_p = \frac{\sqrt{\pi}}{4} \frac{1}{Z_i} \tau_c \left(\frac{q_i \Delta \phi_i}{T_\parallel}\right) \exp\left(\frac{q_i \Delta \phi_i}{T_\parallel}\right) \frac{G(R_p Z_i)}{I(T_\parallel / q_i \Delta \phi_i)}, \tag{4.2}$$

while the flow confinement time becomes

$$\tau_f = \left[1 + \frac{T_\perp}{T_\parallel}(R_p - 1)\right] L_p \sqrt{\frac{\pi m_i}{2 T_\parallel}} \exp\left(\frac{q_i \Delta \phi_i}{T_\parallel}\right). \tag{4.3}$$

The confinement time for spatial diffusion is

$$\tau_{sd} = \frac{L_p^2 m_i}{K_\parallel \tau_{ij} T_\parallel} \exp\left(\frac{q_i \Delta \phi_i}{T_\parallel}\right), \tag{4.4}$$

although during ICRH spatial diffusion is not an important process since the ions are fairly collisionless.

Table 4.9 compares the experimental average charge state of the plasma and end loss and the average parallel confinement time to the ion model during ICRH. The

114

Table 4.9: Comparison of ion model results to experiment during ICRH for oxygen plasmas.

ECRH power Neutral pressure Magnetic field	1 kW 5×10^{-7} Torr 3.5 kG		1 kW 1×10^{-6} Torr 3.5 kG		3.4 kW 1×10^{-6} Torr 3.5 kG	
	Exper.	Model	Exper.	Model	Exper.	Model
$\langle z \rangle$ of plasma	1.9	2.2	1.6	1.7	2.1	2.3
$\langle z \rangle$ of end loss	2.0	1.9	1.7	1.7	2.2	2.4
$\langle \tau_{\parallel} \rangle$	2.4 ms	2.0 ms	1.5 ms	1.4 ms	1.3 ms	1.2 ms
$\langle \tau_{\perp} \rangle$		1.5 ms		0.9 ms		1.0 ms

average perpendicular confinement time from the ion model is also shown. Although the ion model still overestimates the average charge state of the confined ions, it does predict that the average charge state decreases with ICRH, in agreement with the experimental results. Also the model predicts that ion radial transport increases during ICRH, in agreement with previous work on Constance B [Goodman, 1989]. This increase in the perpendicular losses is believed to be responsible for the sudden loss of plasma equilibrium at high ICRH powers, which is discussed in section 4.4.3.

A more detailed comparison between the experiment and ion model during ICRH is shown in Figs. 4-46—4-48, where the parallel confinement times, densities and fluxes are shown for the three oxygen plasmas. (Since the temperature of O^{5+} is not measured, its value is chosen so that the theoretical confinement time agrees with the experimental value.) Note that the theoretical parallel confinement time for O^{4+}, and to a lesser degree O^{3+}, is much larger than the measured confinement time. Since O^{4+} is resonant with the applied ICRH in the plasma (O^{3+} is resonant outside the plasma), its parallel confinement may be degraded by rf diffusion. Fig. 4-49 shows typical rf diffusion paths for a resonant ion in a magnetic mirror. Since the hot resonant ions are mainly mirror trapped, they have an almost empty loss cone. Ions near the loss cone boundary are therefore primarily diffused down in energy and into the loss cone. This results in a parallel confinement time shorter than the classical mirror confinement time. Collisions are still important because they move ions near the loss cone boundary where the rf diffusion paths point downward in energy. In the limit of strong rf diffusion, all ions resonant with the ICRH are lost in a single transit,
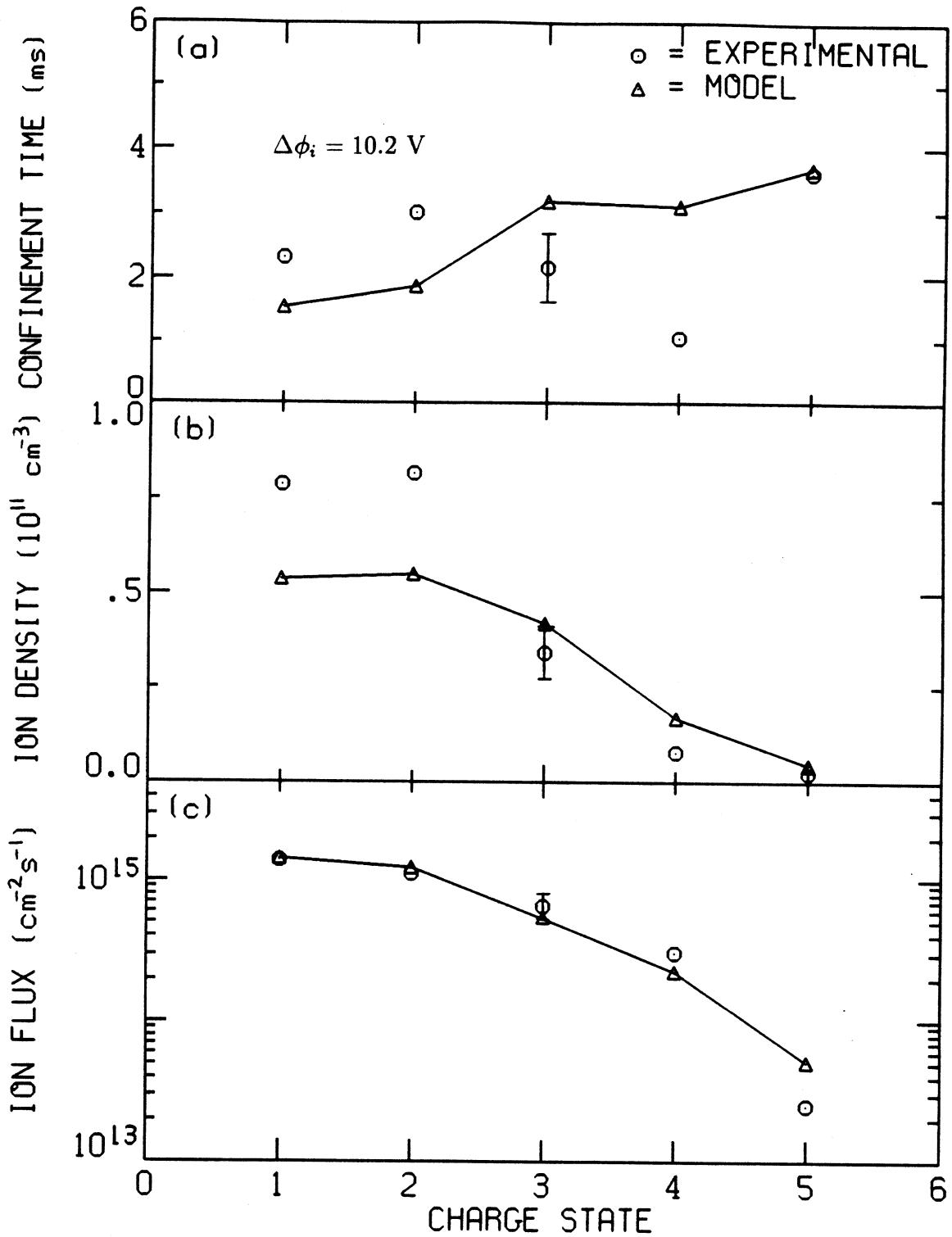
Figure 4-46: Comparison of experimental and model results during ICRH: (a) parallel ion confinement times, (b) ion densities and (c) ion fluxes for the 1 kW, 5×10^{-7} Torr oxygen plasma.
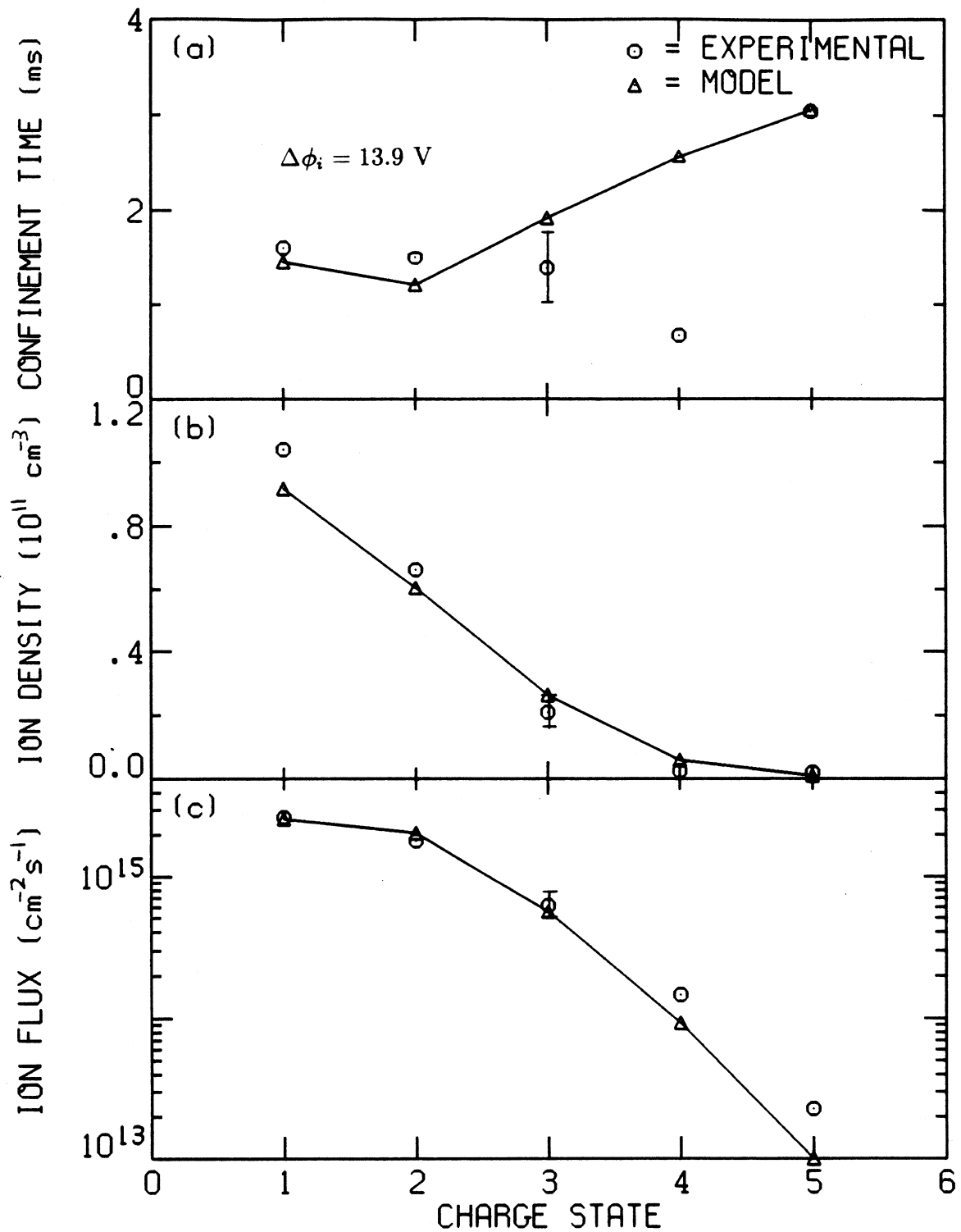
Figure 4-47: Comparison of experimental and model results during ICRH: (a) parallel ion confinement times, (b) ion densities and (c) ion fluxes for the 1 kW, 1×10^{-6} Torr oxygen plasma.
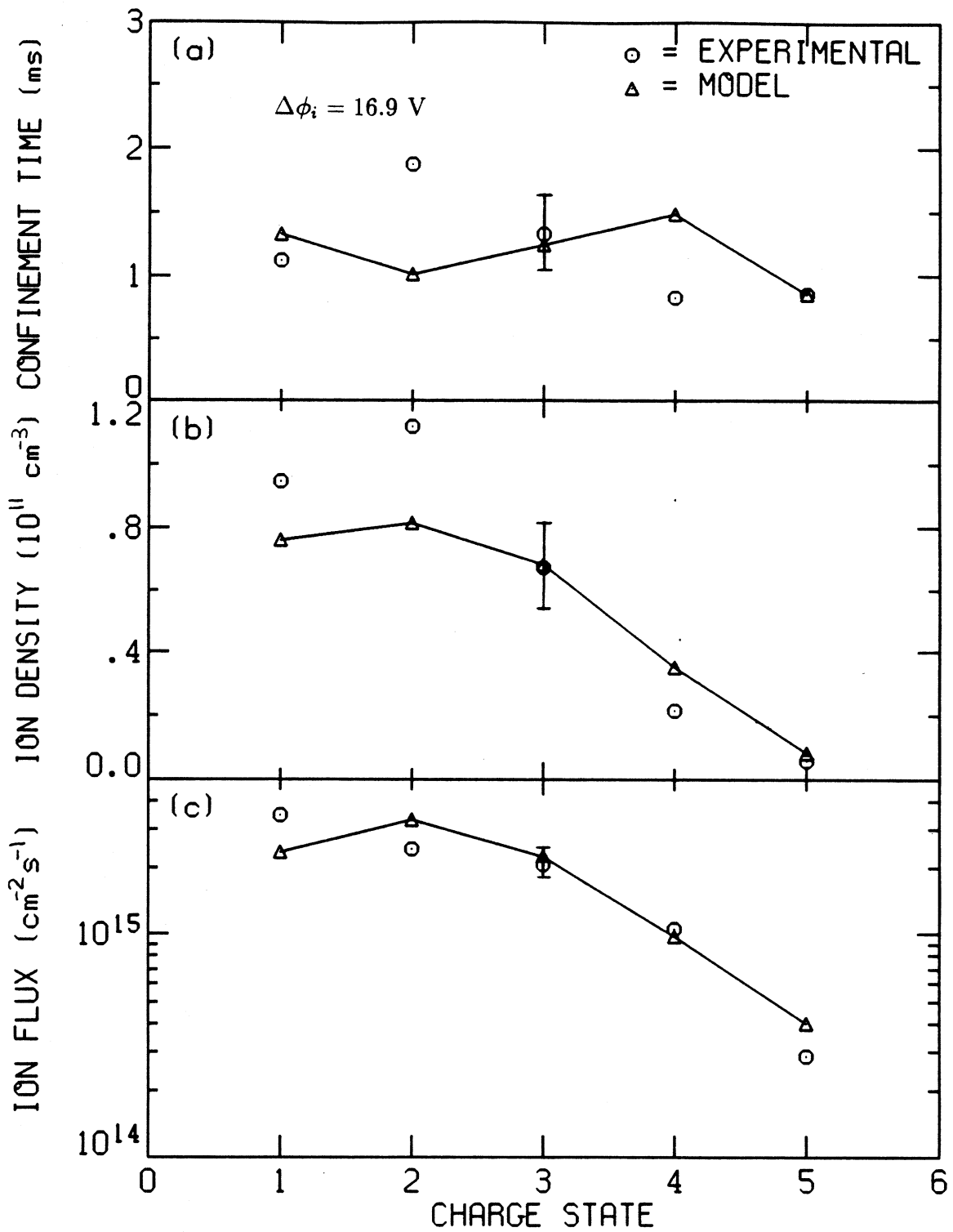
Figure 4-48: Comparison of experimental and model results during ICRH: (a) parallel ion confinement times, (b) ion densities and (c) ion fluxes for the 3.4 kW, 1×10^{-6} Torr oxygen plasma.
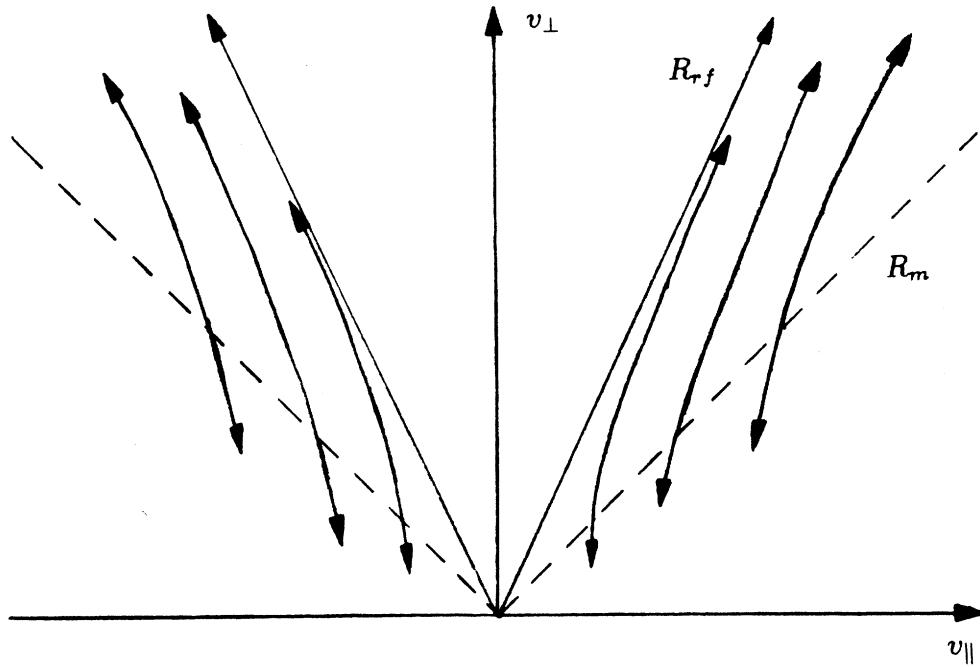
Figure 4-49: Typical rf diffusion paths for the case when the resonance occurs off the magnetic midplane.

Table 4.10: Comparison of measured parallel confinement time for O^{4+} during ICRH with various theoretical values for oxygen plasmas.

ECRH power	1 kW	1 kW	3.4 kW
Neutral pressure	5×10^{-7}Torr	1×10^{-6}Torr	1×10^{-6}Torr
Magnetic field	3.5 kG	3.5 kG	3.5 kG
Pastukhov	3.1 ms	2.6 ms	1.5 ms
rf diffusion	0.5 ms	0.3 ms	0.3 ms
Experimental	1.0 ms	0.7 ms	0.8 ms

leading to an effective loss cone boundary at the resonant mirror ratio instead of the maximum mirror ratio. The parallel confinement time in this limit is therefore

$$\tau_{rf} = \tau_{ii} \frac{R_{rf} - 1}{R_{rf} + 1.5},$$ (4.5)

where R_{rf} is the mirror ratio at which the ICRH is resonant. Table 4.10 compares the measured parallel confinement time for O^{4+} with the theoretical Pastukhov and rf diffusion confinement times for the three oxygen plasmas. In all cases the experimental value lies between the Pastukhov and rf diffusion limits. Thus, a reasonable conclusion is that rf diffusion degrades the parallel confinement time of O^{4+}, typically by a factor
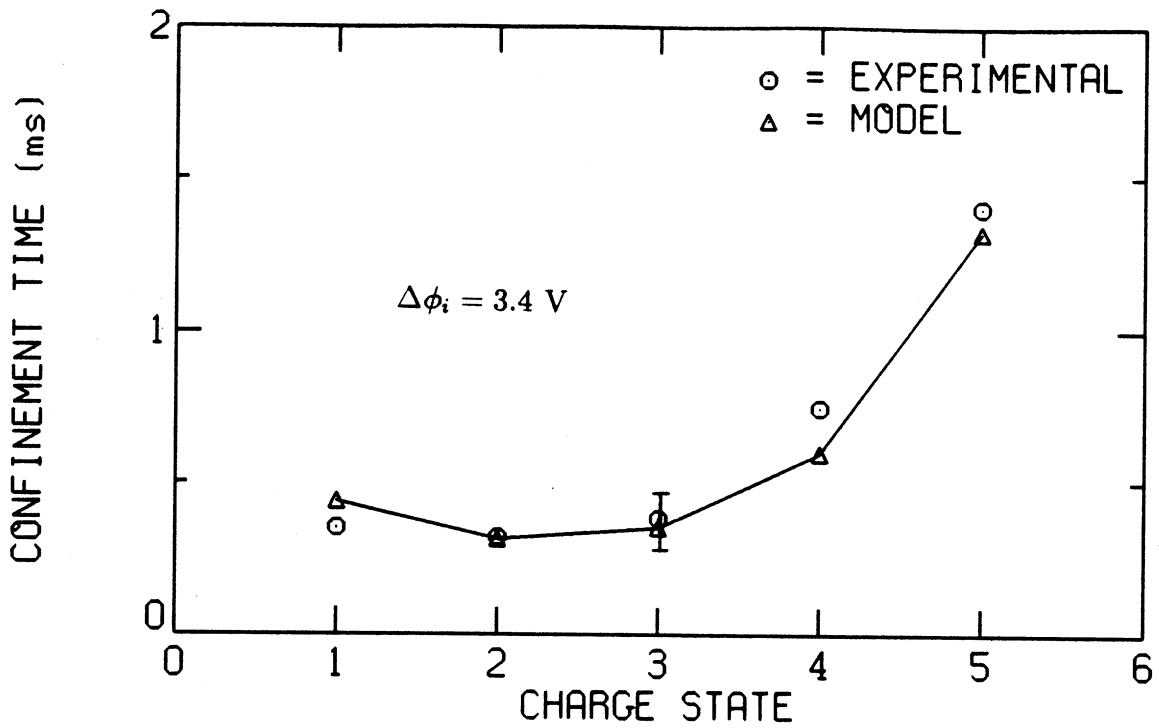
Figure 4-28: Comparison of experimental and model parallel confinement times using $K_\parallel = 0.4$ for the 1 kW, 5×10^{-7}Torr neon plasma.
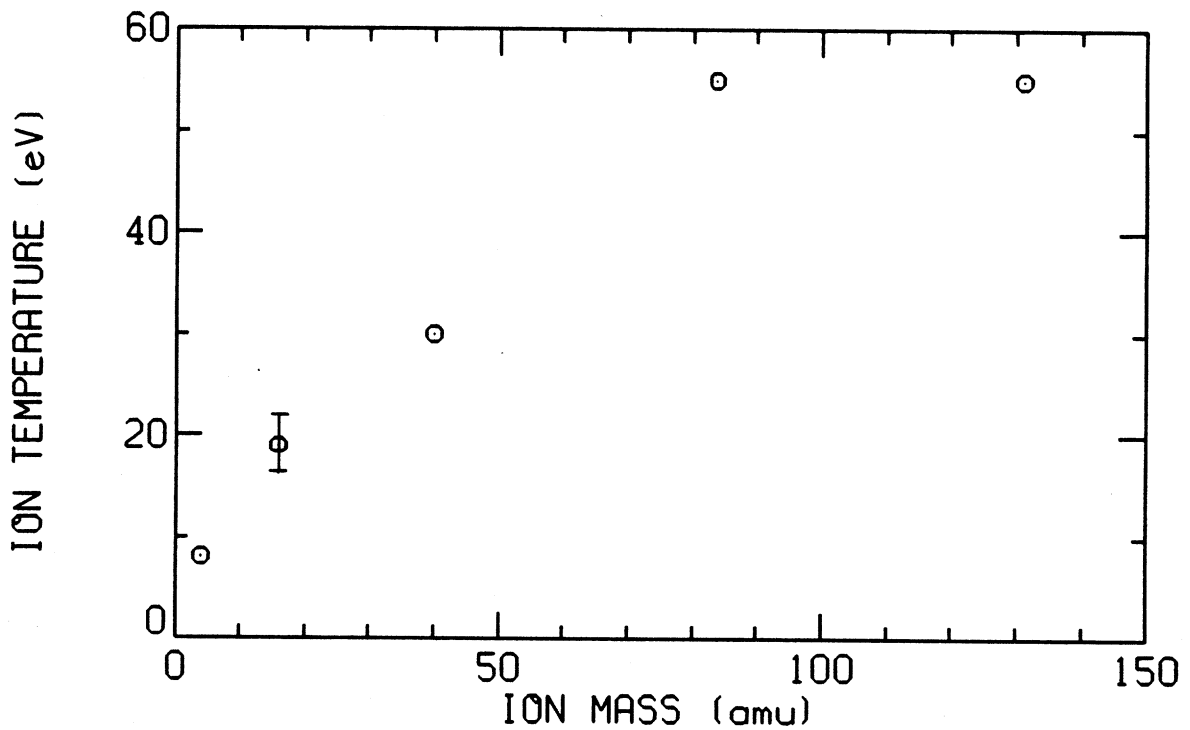
Figure 4-29: Ion temperature of lowest charge state (measured by Doppler broadening) for helium, oxygen, argon, krypton and xenon plasmas.
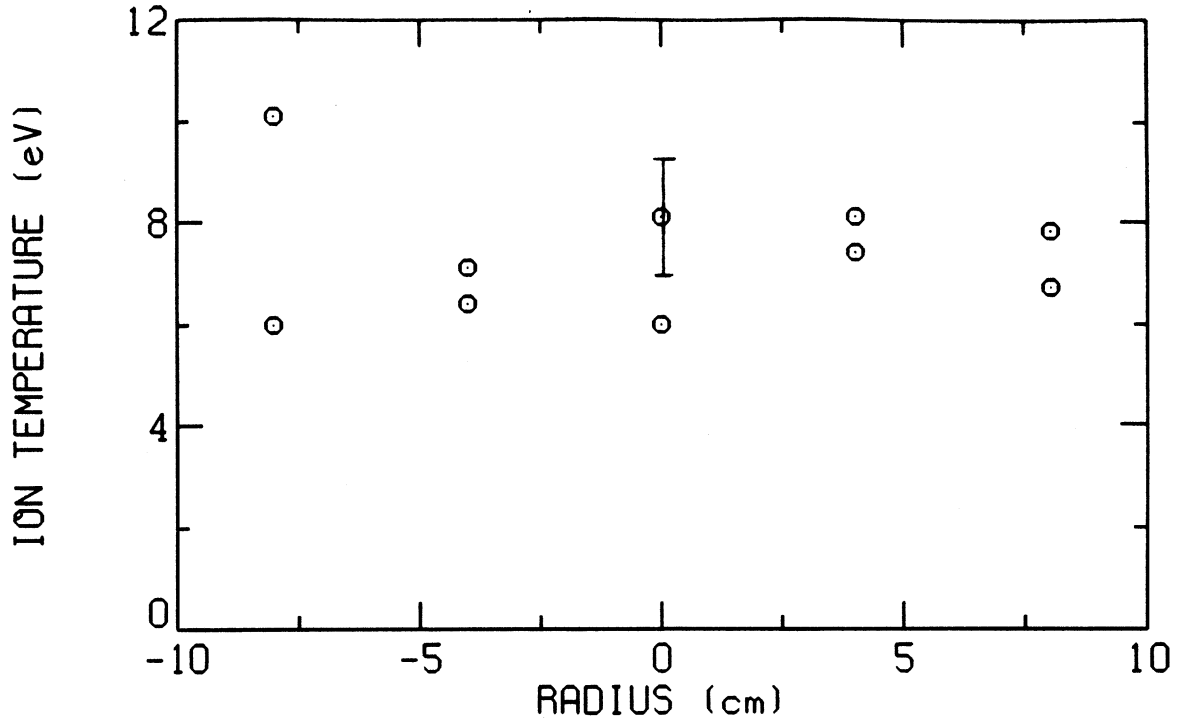
Figure 4-30: Radial scan of He^+ temperature at the magnetic midplane, determined from Doppler broadening.

The ion fluxes in the plasma center for argon, krypton and xenon plasmas are shown in Fig. 4-31. This figure shows how the charge state distribution of the ion end loss flattens with increasing ion mass. Previous work on ion radial transport on Constance B showed that the perpendicular diffusion coefficients increase with ion mass [Goodman, 1989], which may explain why the total ion flux decreases with increasing ion mass.

Next the experimental results are compared to the ion model for the noble gases. Since the ion densities and confinement times are not measured, only results for the ion fluxes are shown. Fig. 4-32 compares the experimental and model ion fluxes for helium. Agreement is excellent, as may be expected for this simple two-species plasma. The results for argon are shown in Fig. 4-33, where the cold electron temperature is estimated from the plasma potential. There is good agreement up to $z_i = 6$, but after that the model results fall off too quickly. The presence of a radial electric field, which up to now has been ignored, can account for this discrepancy. Radial electric fields can develop due to radial variation in the ion or cold-electron parallel confine-
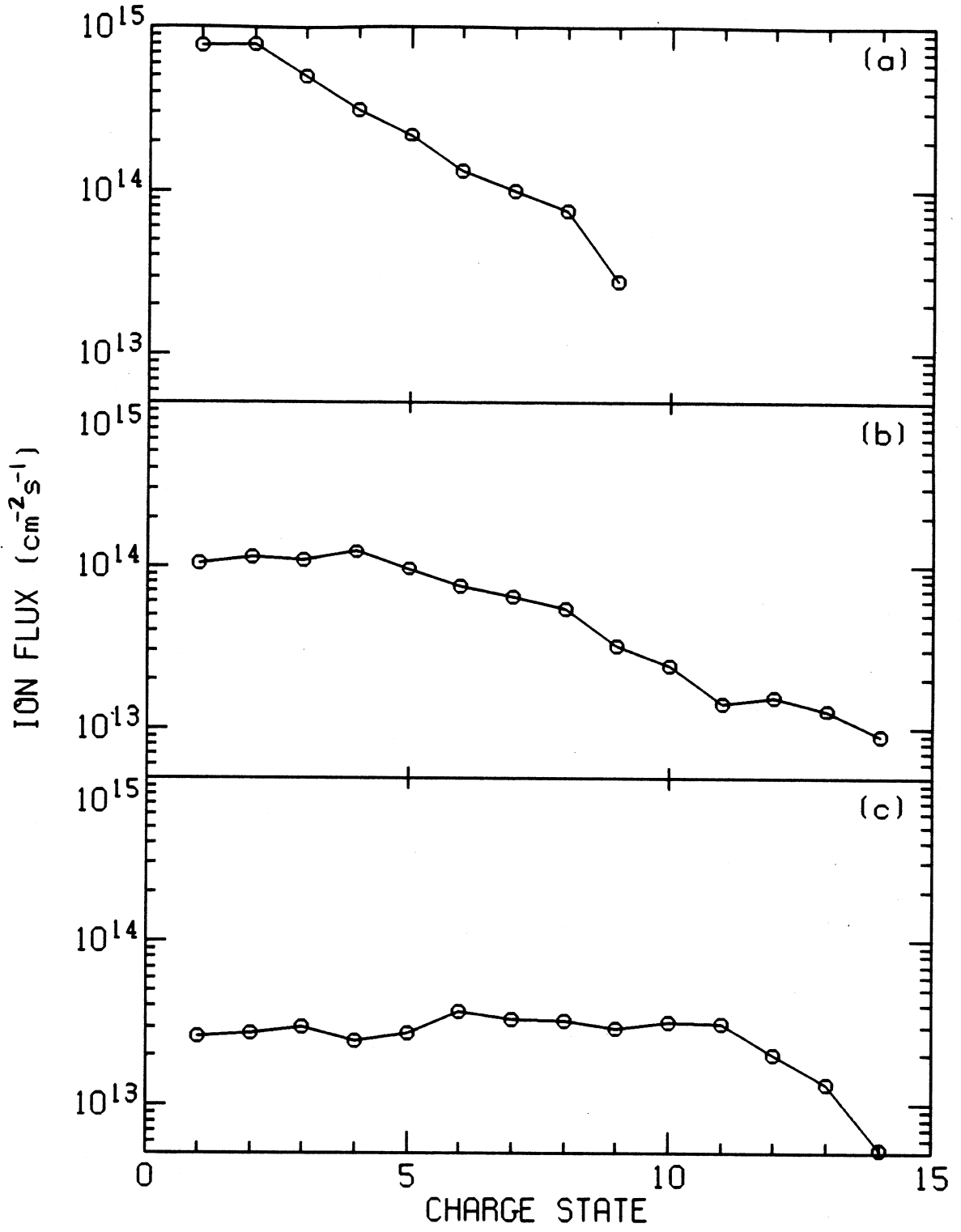
Figure 4-31: Ion fluxes for (a) argon, (b) krypton and (c) xenon plasmas under identical conditions.
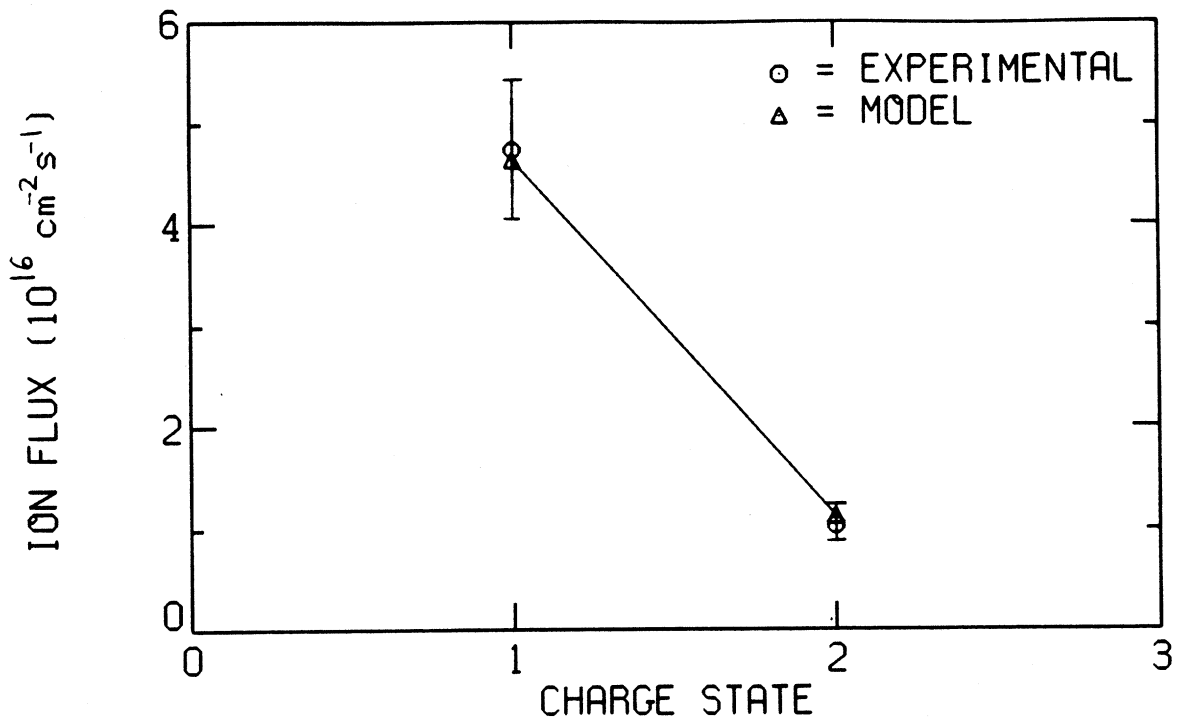
Figure 4-32: Comparison of experimental and model ion fluxes for helium.
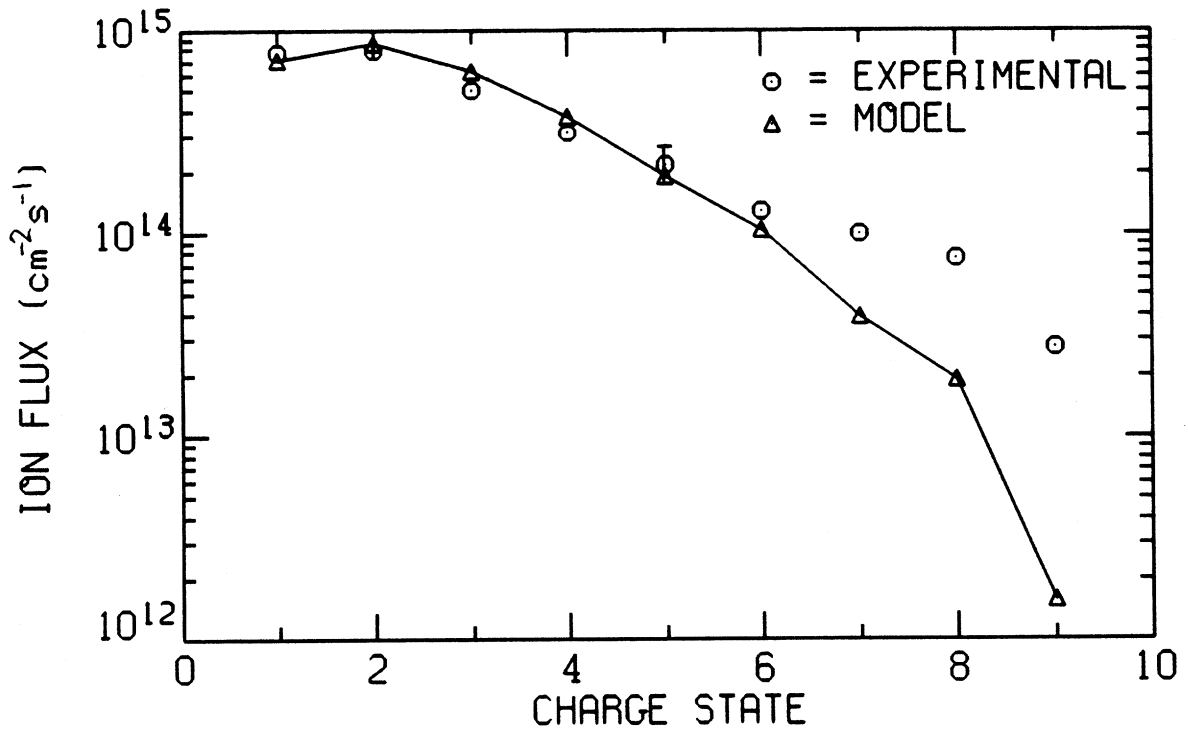
Figure 4-33: Comparison of experimental and model ion fluxes for argon.
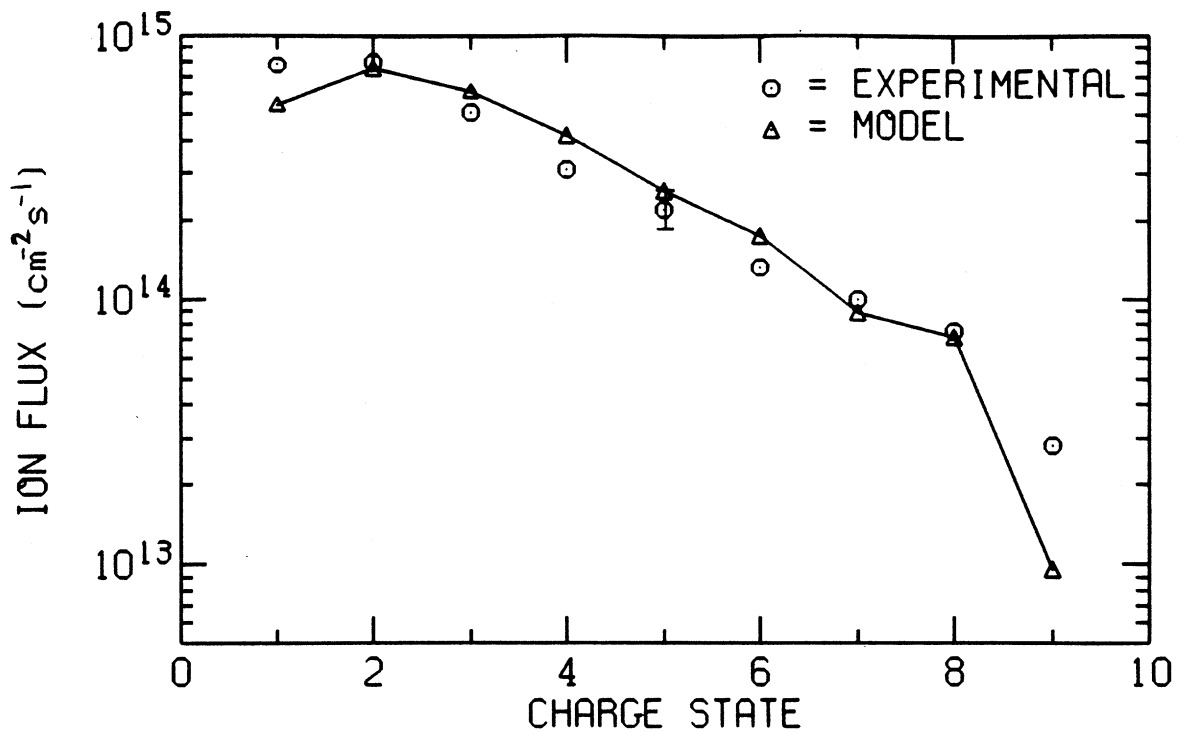
Figure 4-34: Comparison of experimental and model ion fluxes for argon using $E_\perp = -0.20$ V/cm.

ment times. An inward radial electric field which confines ions primarily increases the perpendicular confinement time of high charge state ions. This allows them to build up to a larger density and therefore increase their flux. Fig. 4-34 compares the experimental argon fluxes with the ion model using $E_\perp = -0.20$ V/cm. The ion model now shows agreement with experiment up to $z_i = 8$. Thus, it is seen that a small radial electric field may increase the flux of high charge state ions.

The experimental and ion model fluxes are compared in Fig. 4-35 for krypton and in Fig. 4-36 for xenon (with no radial electric field). In these cases the agreement between model and experiment is poor. Since the ion densities are not measured, it is not known whether the failure of the ion model is due to an error in calculating the ion densities or the ion confinement times. Error in the confinement times can be due to both the wrong scaling with charge state (if the modeled potential dip is wrong) or the wrong perpendicular losses. Error in the ion densities can be due to both the wrong confinement times or the wrong ionization rate parameters. Since no Lotz rate parameters are available for elements above zinc, the Müller rate parameters are used,
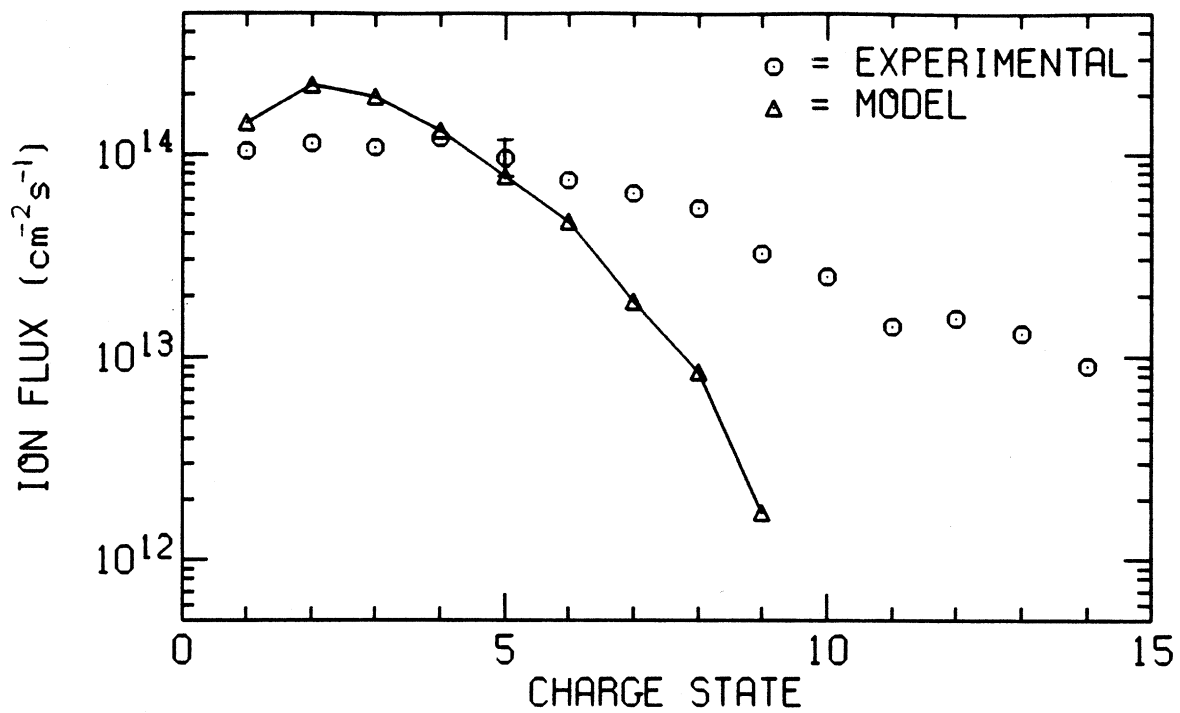
Figure 4-35: Comparison of experimental and model ion fluxes for krypton.
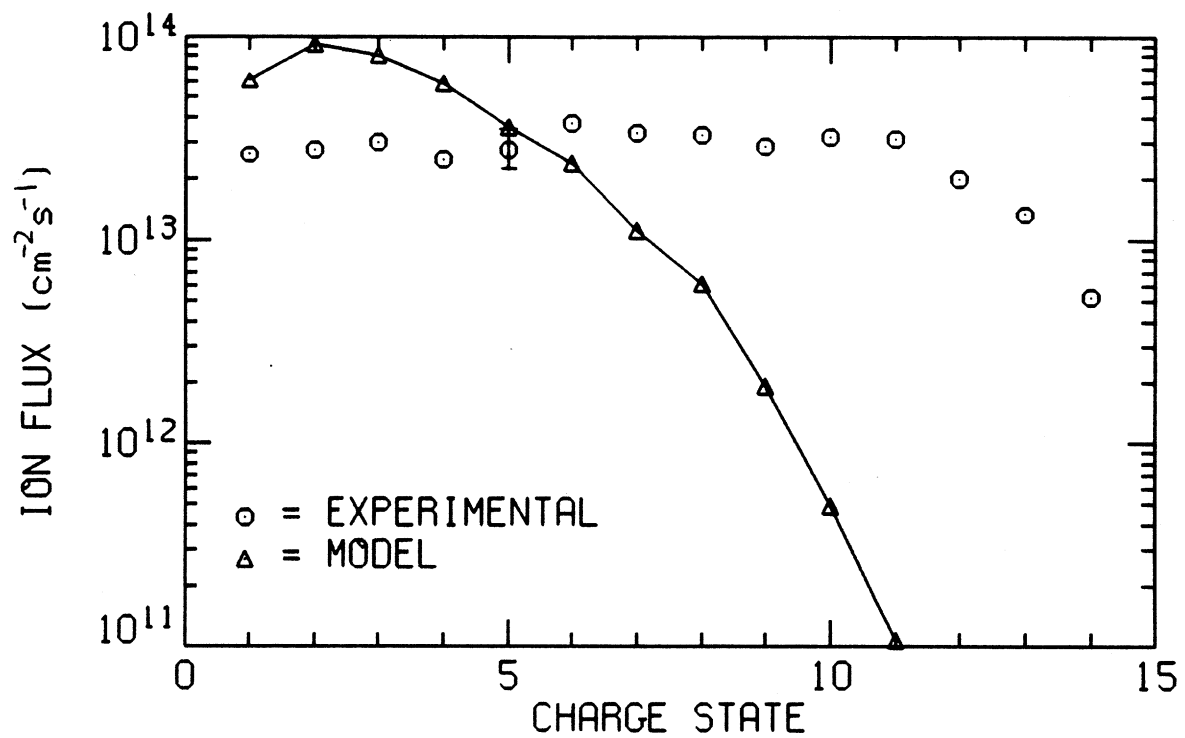
Figure 4-36: Comparison of experimental and model ion fluxes for xenon.

which may not be very accurate.

4.4 Minority ion heating

In this section, results of experiments using ion cyclotron resonance heating (ICRH) are presented. The purpose of these experiments is to selectively heat a medium charge state ion to decrease its parallel confinement time and increase its extracted flux [Smith and Petty, 1986]. For an electrostatically trapped ion, the parallel confinement time decreases as the temperature increases. The ion model predicts that selectively raising the temperature of a medium charge state ion by 100 eV can increase its flux by two to three times. The ICRH transmitter produces a 2 kW pulse at 1.4 MHz, which heats primarily O^{4+} in an oxygen plasma and $Ne^{4,5+}$ in a neon plasma for the standard 3.5 kG midplane magnetic field.

4.4.1 oxygen

The ion densities and fluxes as a function of charge state are measured for three different oxygen plasmas during ICRH in order to determine the parallel ion confinement times using Eqn. 3.1. The electron densities, electron temperatures and ion temperatures are also measured for use in the ion model developed in the previous chapter. After the experimental results are presented, they are compared to results from the ion model.

The ion temperatures for the three oxygen plasmas during ICRH are shown in Fig. 4-37. The resonant ions are strongly heated by ICRH, with the temperature of O^{4+} increasing by several hundred eV. Most of the absorbed power goes into increasing the perpendicular energy of the resonant ions. Because the plasma density is low, little energy is thermalized into the parallel direction. The other ions collide with the resonant ions and gain primarily perpendicular energy since the coefficient of dynamical friction is a vector quantity. Due to the small anisotropy index ($\gamma = \bar{E}_{\parallel}/\bar{E}_{\perp}$), the ions remain deeply trapped in the magnetic well during ICRH. The mirror ratio at which the ions are magnetically reflected is given by $R = 1 + \gamma$,
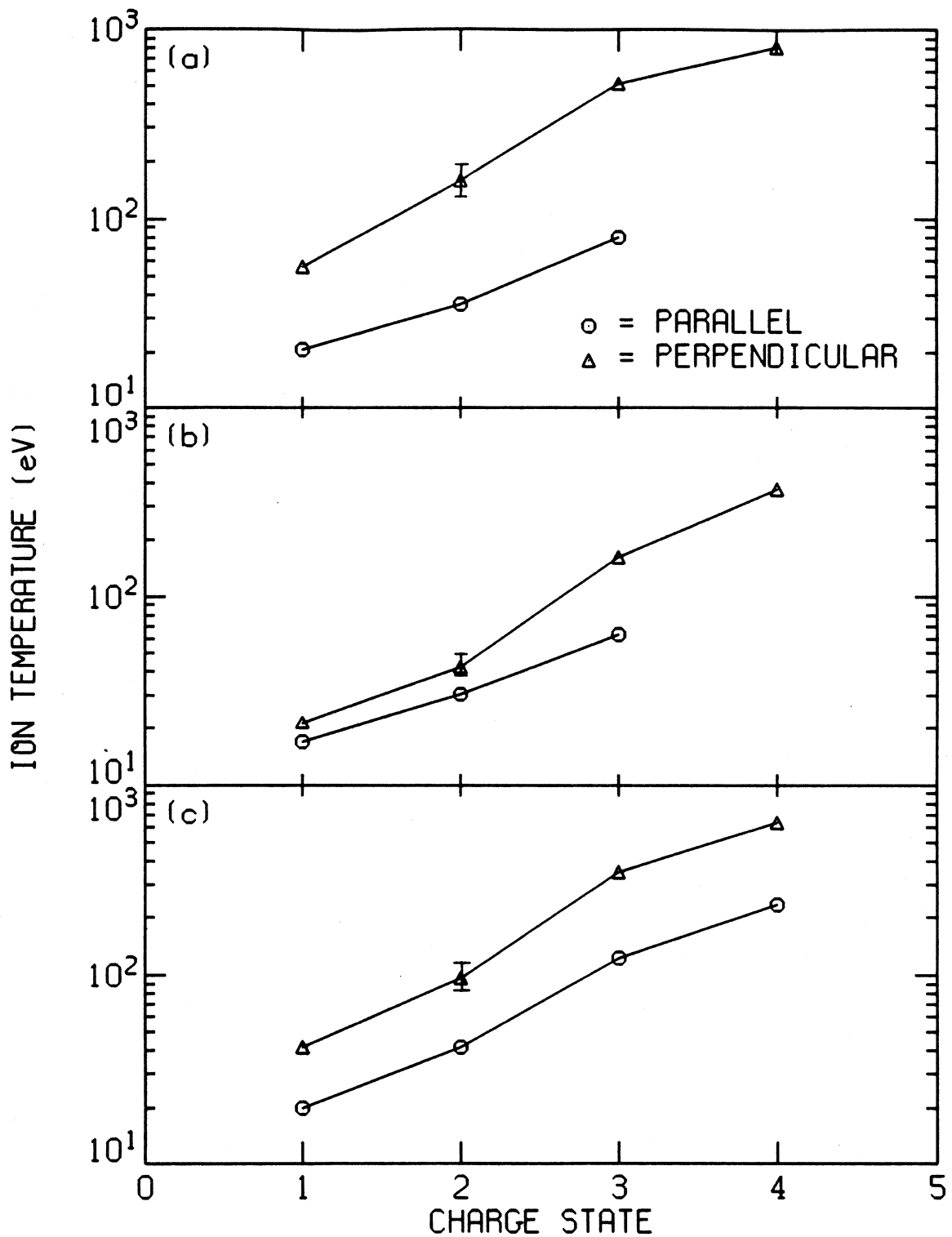
Figure 4-37: Ion temperatures parallel and perpendicular to the magnetic field during ICRH for (a) 1 kW, 5×10^{-7}Torr, (b) 1 kW, 1×10^{-6}Torr and (c) 3.4 kW, 1×10^{-6}Torr oxygen plasmas.

Table 4.7: Cold electron parameters during ICRH for oxygen plasmas.

ECRH power	1 kW	1 kW	3.4 kW
Neutral pressure	5×10^{-7}Torr	1×10^{-6}Torr	1×10^{-6}Torr
Magnetic field	3.5 kG	3.5 kG	3.5 kG
Cold electron density	1.0×10^{11}cm^{-3}	1.0×10^{11}cm^{-3}	2.0×10^{11}cm^{-3}
Cold electron temperature	120 eV	90 eV	160 eV
Plasma potential	330 V	310 V	430 V

so O^{4+} which has a parallel temperature one third its perpendicular temperature is confined inside the $R = 1.33$ flux surface.

The effect of ICRH on the cold electron density and temperature in shown in Table 4.7. ICRH decreases the cold electron density for these cases. By turning off the ECRH and ICRH simultaneously and observing the interferometer decay, it is determined that the hot electron density does not change during ICRH. The ion densities in the plasma center with and without ICRH is shown in Fig. 4-38. The application of minority ICRH increases the density of low charge state ions and decreases the density of high charge state ions.

The ion fluxes during ICRH for the three oxygen plasmas are shown in Figs. 4-39—4-41. In contrast to the normally hollow radial profiles for end loss, the radial profiles during ICRH are more peaked on axis. The change in end loss profile from hollow to peaked is shown in Fig. 4-42 for O^{4+}, which is resonant with the ICRH. Although the total end loss of O^{4+} decreases, in the plasma center the flux increases by 20%. Since ECR ion sources extract from the plasma center, the decrease in flux off center is not important. The change in the ion fluxes in the plasma center during ICRH is summarized in Table 4.8 for the three oxygen plasmas. For the first and third cases, the fluxes of O^{3+} and O^{4+} rise by about 20% during ICRH. For the second case, all the ion fluxes fall during ICRH, probably due to increased ion radial transport.

The parallel ion confinement times determined from the ion densities and fluxes during ICRH are shown in Figs. 4-43—4-45 for the three oxygen plasmas. There are two important differences between the parallel confinement times before and during ICRH. First, the radial profiles are broader during ICRH than before ICRH (which causes the radial profile of ion end loss to be more peaked). This is probably due to
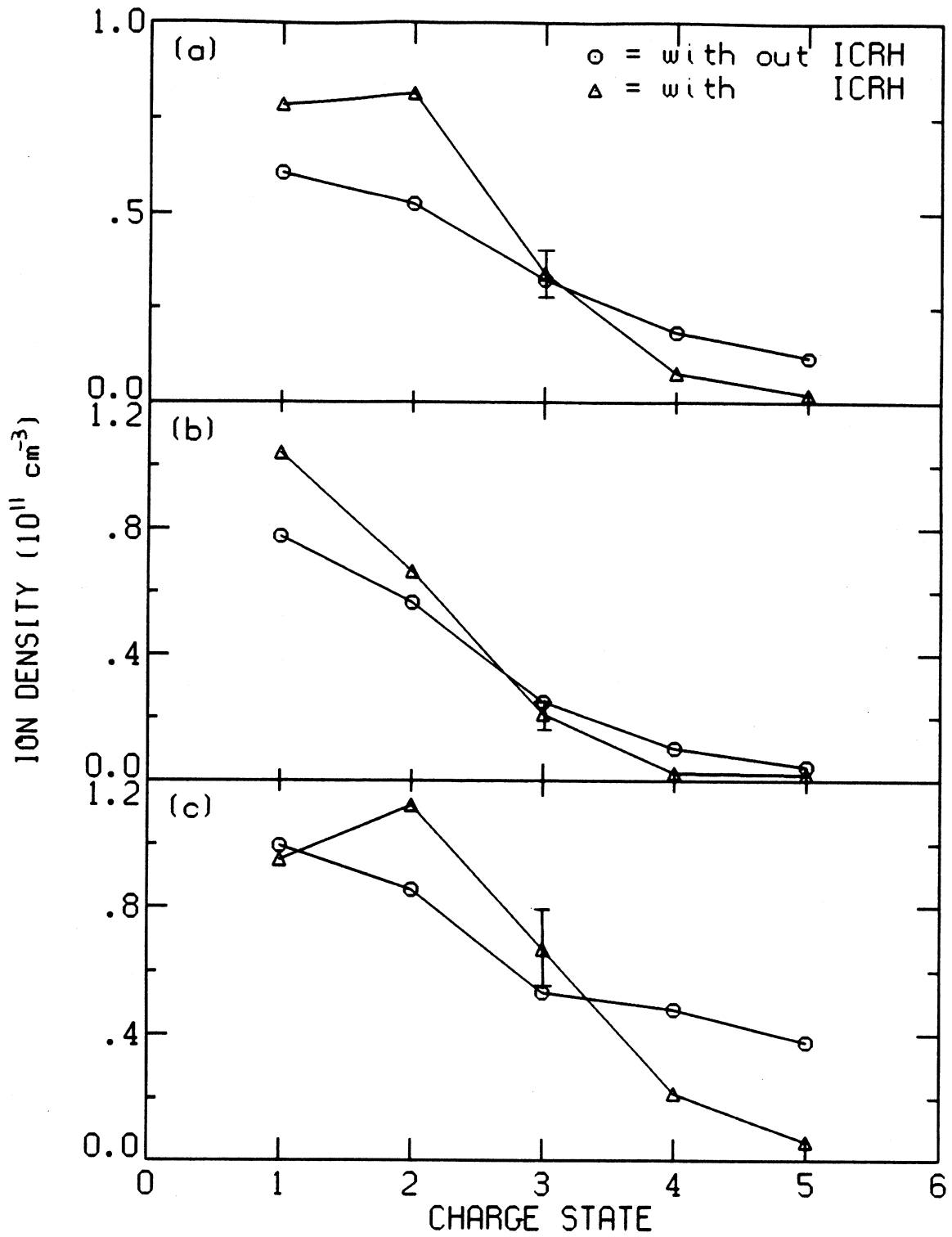
Figure 4-38: Ion densities with and without ICRH for the (a) 1 kW, 5×10^{-7} Torr, (b) 1 kW, 1×10^{-6} Torr and (c) 3.4 kW, 1×10^{-6} Torr oxygen plasmas.
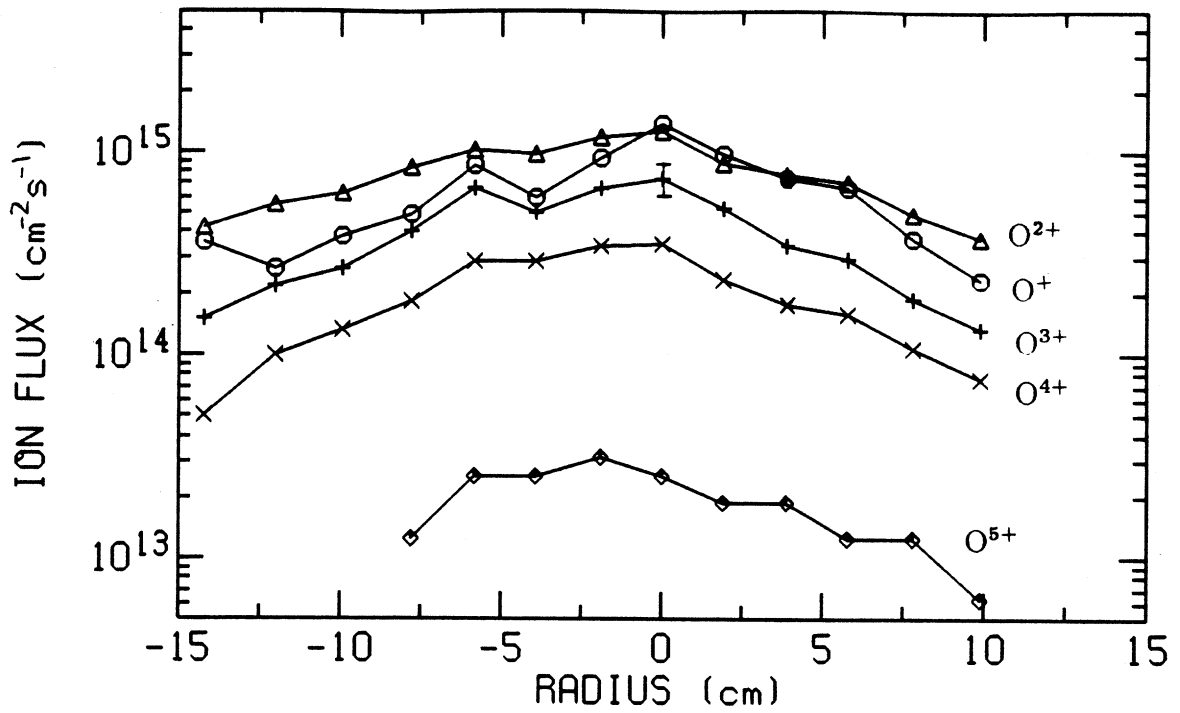
Figure 4-39: Ion fluxes mapped to the magnetic midplane during ICRH for the 1 kW, 5×10^{-7} Torr oxygen plasma.
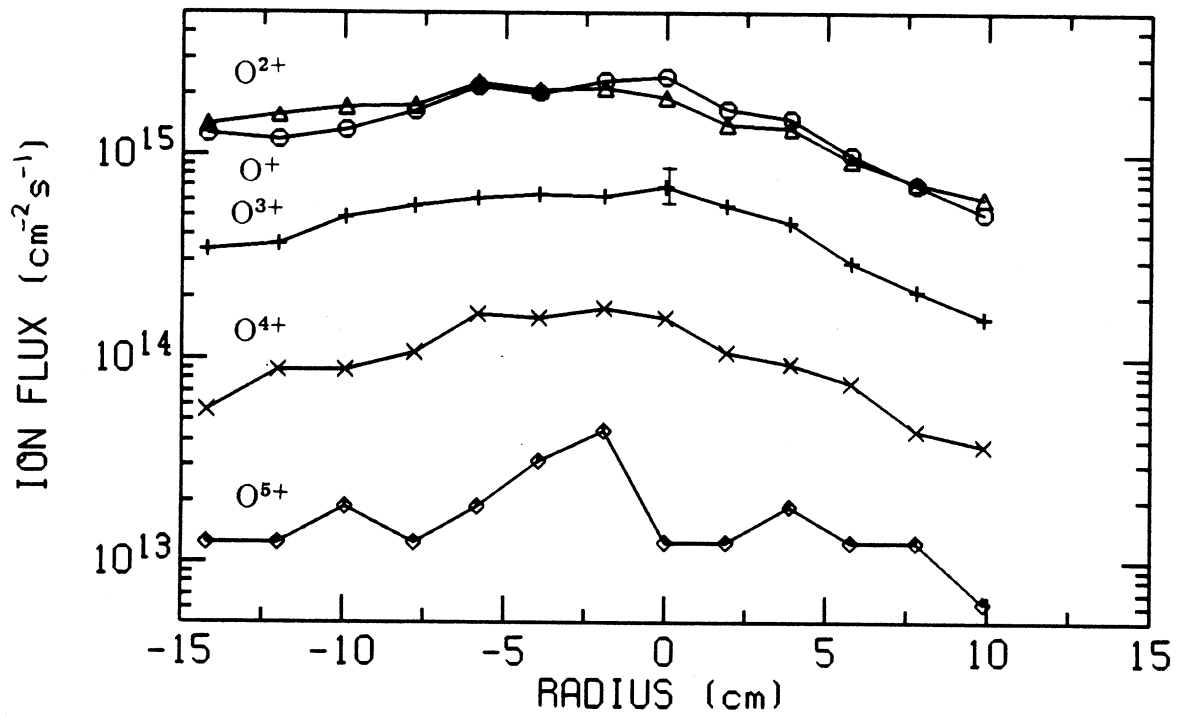
Figure 4-40: Ion fluxes mapped to the magnetic midplane during ICRH for the 1 kW, 1×10^{-6} Torr oxygen plasma.
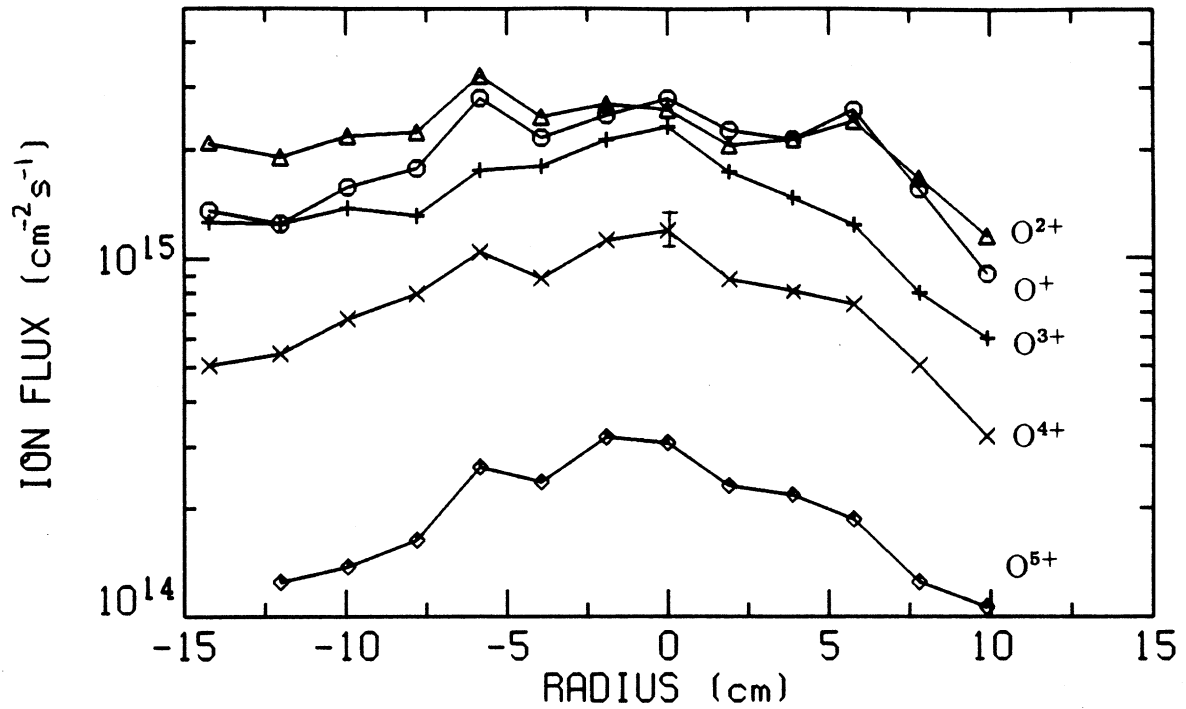
Figure 4-41: Ion fluxes mapped to the magnetic midplane during ICRH for the 3.4 kW, 1×10^{-6} Torr oxygen plasma.
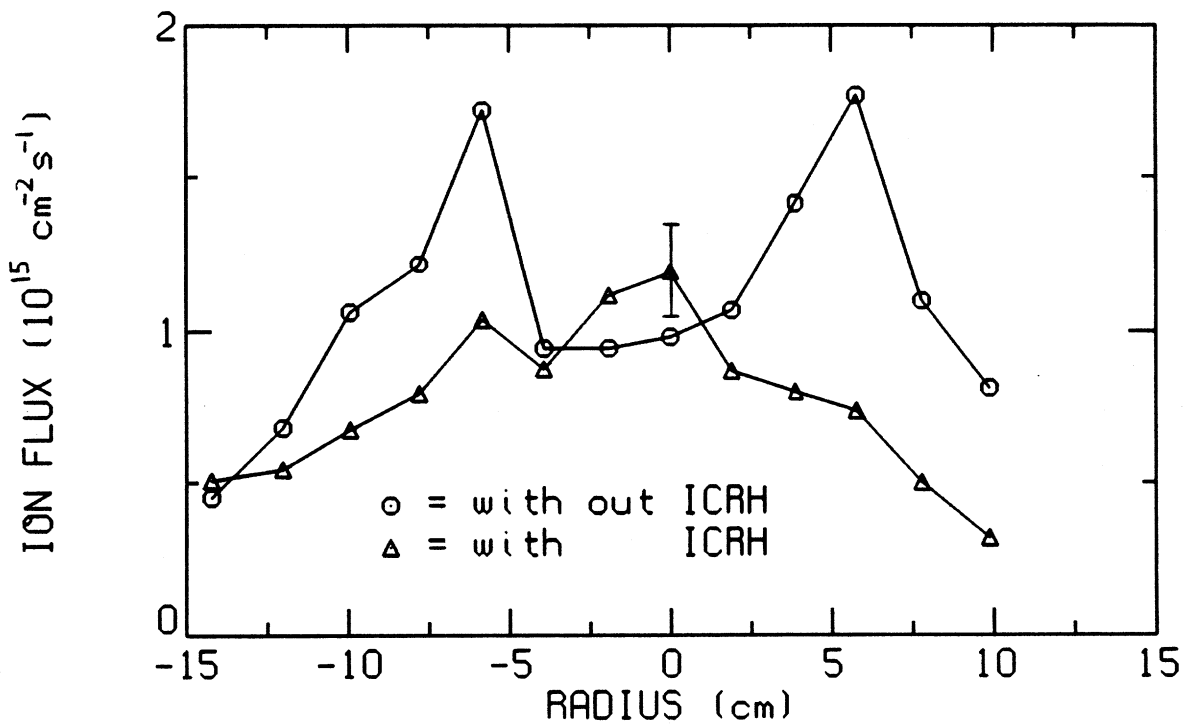
Figure 4-42: Flux of O^{4+} mapped to the magnetic midplane with and without ICRH for the 3.4 kW, 1×10^{-6} Torr oxygen plasma.

Table 4.8: Ion fluxes $(cm^{-2}s^{-1})$ in the plasma center before and during ICRH for oxygen plasmas.

ECRH Pressure B field	1 kW 5×10^{-7}Torr 3.5 kG		1 kW 1×10^{-6}Torr 3.5 kG		3.4 kW 1×10^{-6}Torr 3.5 kG	
	Before	During	Before	During	Before	During
O^+	1.9×10^{15}	1.4×10^{15}	5.0×10^{15}	2.4×10^{15}	4.1×10^{15}	2.8×10^{15}
O^{2+}	1.3×10^{15}	1.3×10^{15}	4.5×10^{15}	1.9×10^{15}	3.2×10^{15}	2.6×10^{15}
O^{3+}	6.4×10^{14}	7.4×10^{14}	2.2×10^{15}	6.9×10^{14}	2.0×10^{15}	2.3×10^{15}
O^{4+}	2.9×10^{14}	3.5×10^{14}	6.1×10^{14}	1.6×10^{14}	9.8×10^{14}	1.2×10^{15}
O^{5+}	8.8×10^{13}	2.5×10^{13}	1.0×10^{14}	1.2×10^{13}	3.9×10^{14}	3.1×10^{14}
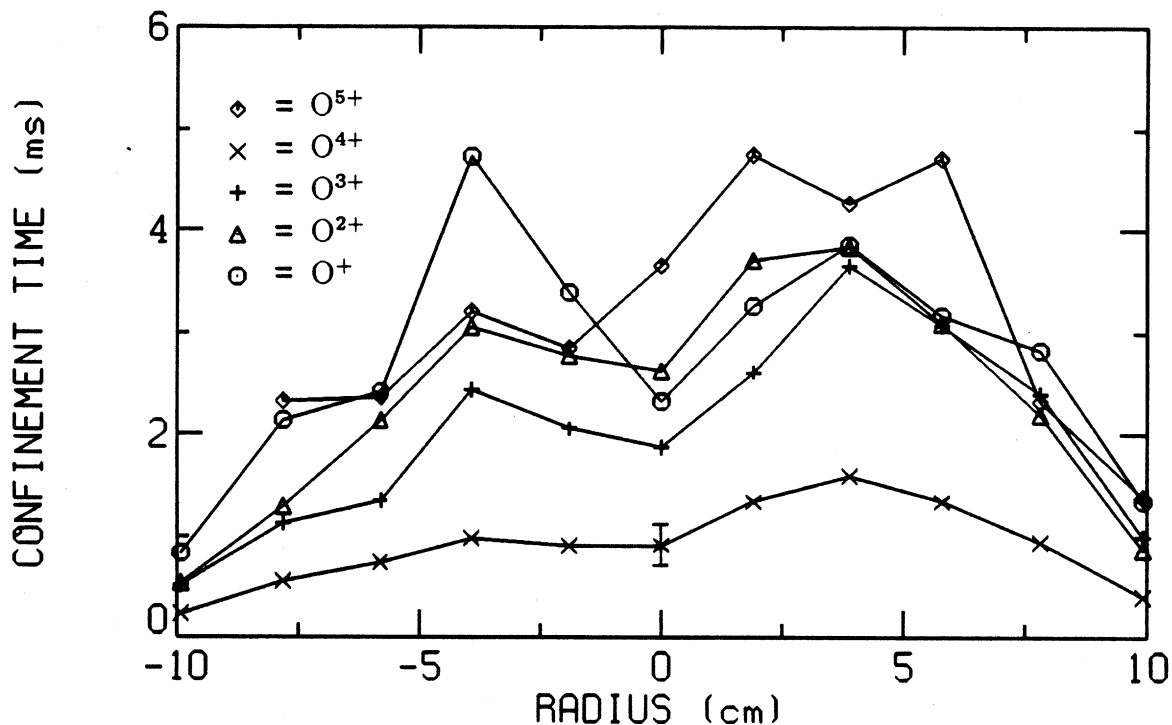
Figure 4-43: Parallel ion confinement times during ICRH for the 1 kW, 5×10^{-7}Torr oxygen plasma.
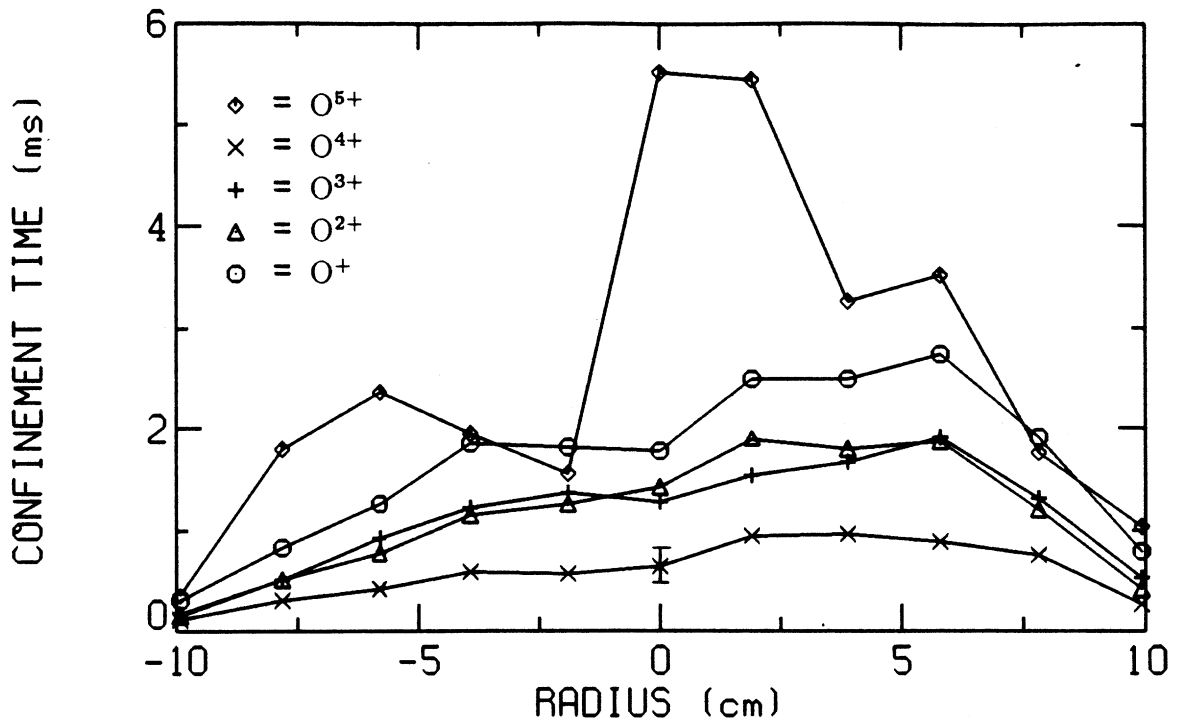
Figure 4-44: Parallel ion confinement times during ICRH for the 1 kW, 1×10^{-6} Torr oxygen plasma.
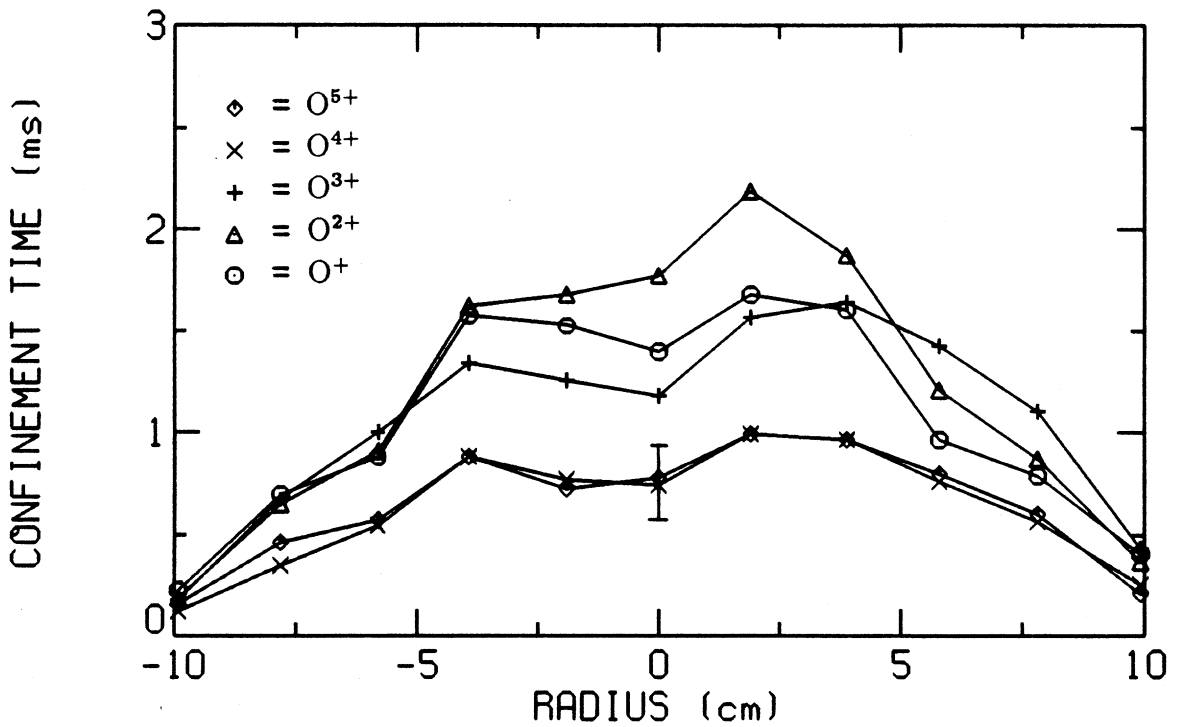
Figure 4-45: Parallel ion confinement times during ICRH for the 3.4 kW, 1×10^{-6} Torr oxygen plasma.

of three.

Since O^{3+} is also resonant with the applied ICRH, it too apparently suffers some degradation in parallel confinement time, most evident in Fig. 4-46 where it is heated the strongest. However, since it is resonant only at large mirror ratios, rf diffusion covers a much smaller region of phase space and therefore has a smaller effect. For O^+ and O^{2+}, the Pastukhov expression provides a good description of the parallel confinement times. The apparent discrepancy in Fig. 4-46 for the first two charge states is an artifact of incorrectly modeling the O^{3+} and O^{4+} confinement times. Making adjustments for rf diffusion raises the model potential dip from 10.2 V to 13.6 V, bringing the Pastukhov confinement time into agreement with the measured confinement times for O^+ and O^{2+}.

The ion model densities and fluxes are somewhat thrown off by the error in the parallel confinement times caused by neglecting rf diffusion. However, the ion model still predicts that the densities of O^+ and O^{2+} increase during ICRH while the densities of O^{4+} and O^{5+} decrease, in agreement with the experimental results.

Using the experimental radial profiles of ion density and flux, the radial profile of the potential dip during ICRH can be deduced from the Pastukhov-flow model. An example is shown in Fig. 4-50 for the 1 kW, 5×10^{-7}Torr oxygen plasma. The magnitude of the deduced potential dip increases during ICRH because the ion model needs to increase the parallel ion confinement time to offset the increase in ion radial transport.

4.4.2   neon

The ion densities and fluxes as a function of charge state are measured for three different neon plasmas during ICRH in order to determine the parallel ion confinement times. The electron densities, electron temperatures and ion temperatures are also measured for use in the ion model. After the experimental results are presented, they are compared to results from the ion model.

The ion temperatures for the three neon plasmas during ICRH are shown in Fig. 4-51. The neon ion temperature with ICRH can be measured more accurately than
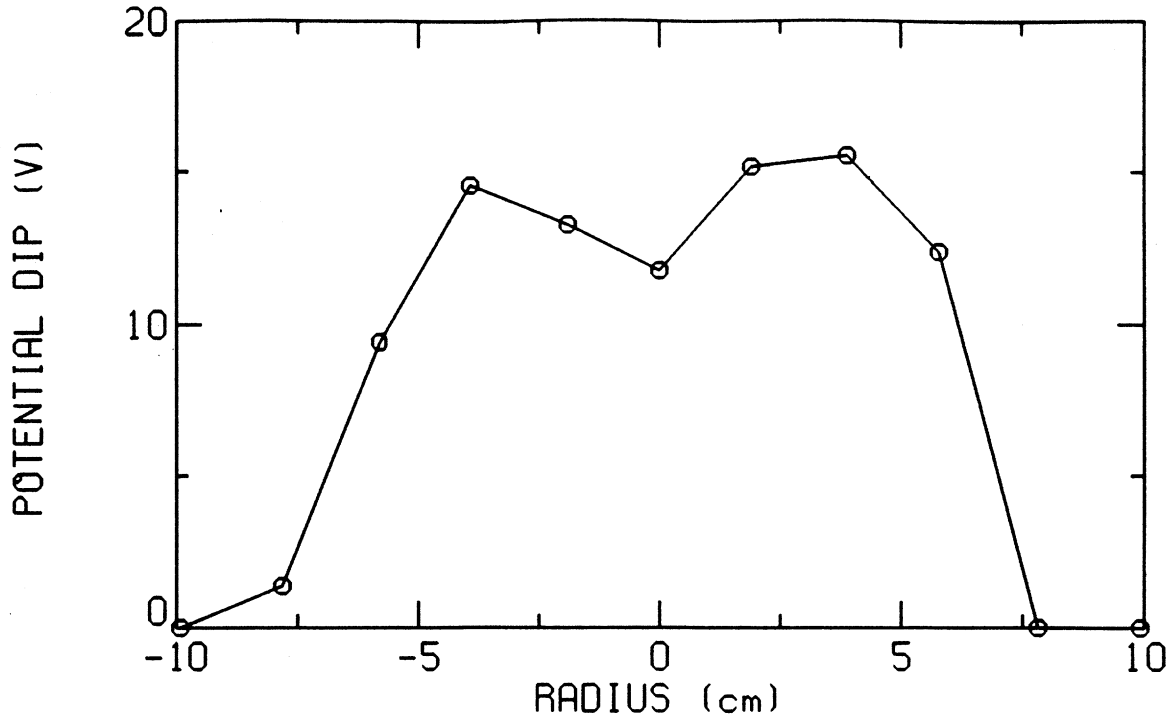
Figure 4-50: Deduced potential dip during ICRH for the 1 kW, 5×10^{-7}Torr oxygen plasma.

Table 4.11: Cold electron parameters during ICRH for neon plasmas.

ECRH power	1 kW	4 kW	4 kW
Neutral pressure	5×10^{-7}Torr	5×10^{-7}Torr	1×10^{-6}Torr
Magnetic field	3.5 kG	3.5 kG	3.5 kG
Cold electron density	1.2×10^{11}cm^{-3}	1.6×10^{11}cm^{-3}	2.8×10^{11}cm^{-3}
Cold electron temperature	110 eV	90 eV	60 eV
Plasma potential	360 V	350 V	310 V

without ICRH since the amount of Doppler broadening is much greater. Like oxygen, most of the absorbed ICRH power for neon goes into increasing the perpendicular energy. However, the amount of heating is smaller for neon than for oxygen plasmas. The temperatures of Ne$^{4,5+}$, which are resonant with the ICRH in the plasma, can be estimated by extrapolating the data in Fig. 4-51 (as suggested by the more complete oxygen data).

The effect of the ICRH on the cold electron density and temperature in shown in Table 4.11. For the first two cases the cold electron density decreases during ICRH, but for the third case it increases. The hot electron density does not change during
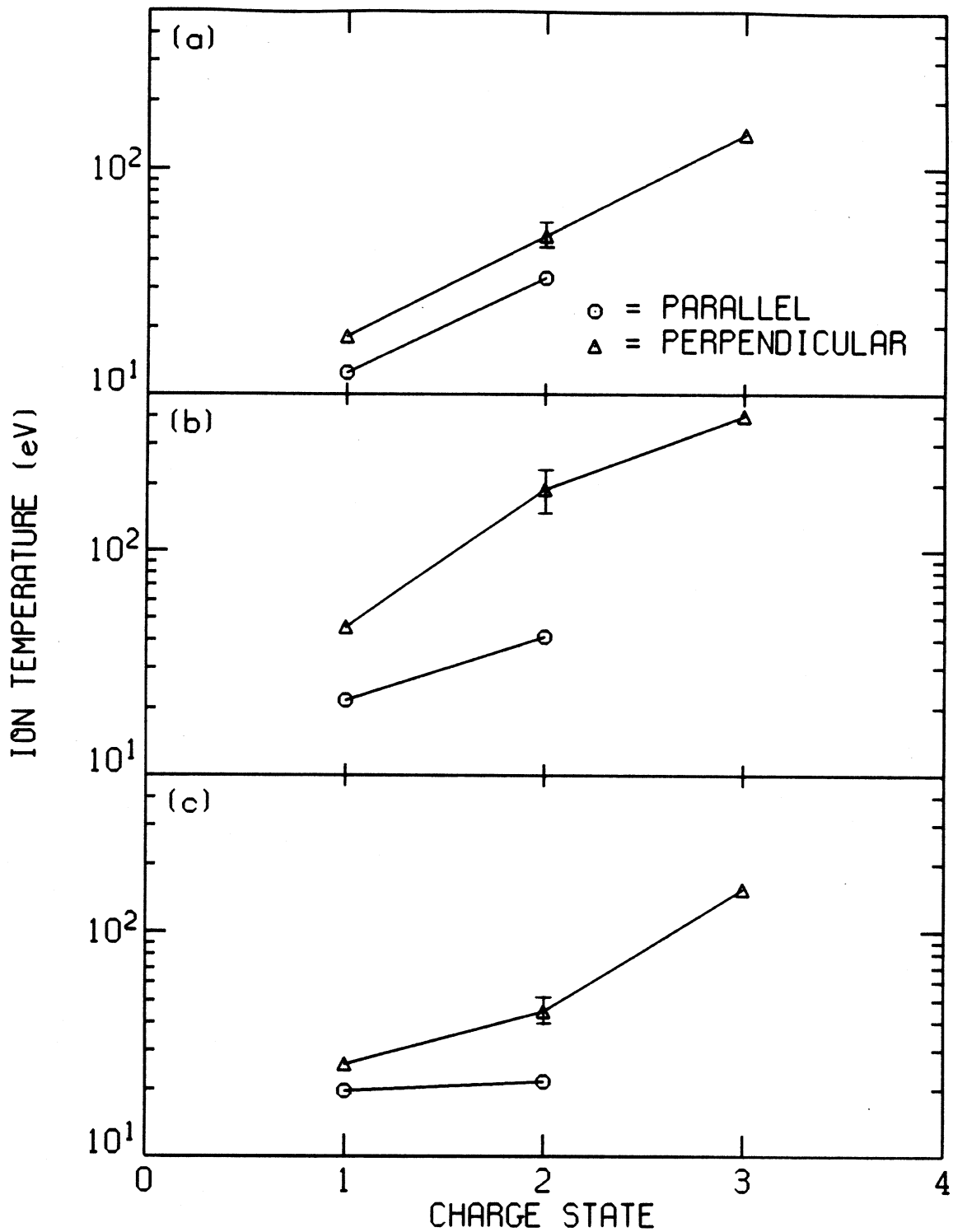
Figure 4-51: Ion temperatures parallel and perpendicular to the magnetic field during ICRH for (a) 1 kW, 5×10^{-7}Torr, (b) 4 kW, 5×10^{-7}Torr and (c) 4 kW, 1×10^{-6}Torr neon plasmas.

Table 4.12: Ion fluxes ($cm^{-2}s^{-1}$) in the plasma center before and during ICRH for neon plasmas.

ECRH Pressure B field	1 kW 5×10^{-7}Torr 3.5 kG		4 kW 5×10^{-7}Torr 3.5 kG		4 kW 1×10^{-6}Torr 3.5 kG	
	Before	During	Before	During	Before	During
Ne$^+$	8.9×10^{15}	6.0×10^{15}	7.1×10^{15}	6.1×10^{15}	3.2×10^{16}	1.8×10^{16}
Ne^{2+}	4.8×10^{15}	2.9×10^{15}	3.9×10^{15}	4.2×10^{15}	1.5×10^{16}	9.4×10^{15}
Ne^{3+}	2.6×10^{15}	2.0×10^{15}	2.8×10^{15}	4.0×10^{15}	8.5×10^{15}	6.8×10^{15}
Ne^{4+}	6.8×10^{14}	3.4×10^{14}	1.1×10^{15}	1.3×10^{15}	1.9×10^{15}	1.5×10^{15}
Ne^{5+}	1.0×10^{14}		4.5×10^{14}	2.7×10^{14}	4.9×10^{14}	

ICRH.

The ion densities in the plasma center with and without ICRH are shown in Fig. 4-52. Minority ICRH increases the density of low charge state ions and decreases the density of high charge state ions, but the effect is weaker for neon than oxygen. The only strong change for neon occurs in Fig. 4-52b, which also has the greatest amount of ion heating. Thus, the lowering of the average charge state of the confined ions seems to be related to the amount of ion heating. The ion model predicts that this occurs because strong ion heating lowers the parallel confinement times of the high charge state ions and also increases ion radial transport and charge exchange losses.

The ion fluxes during ICRH for the three neon plasmas are shown in Figs. 4-53—4-55. As with oxygen, the radial profiles of ion flux for neon are more peaked on axis during ICRH. The change in the ion fluxes in the plasma center during ICRH is summarized in Table 4.12 for the three neon plasmas. For the first and third cases, the fluxes of all the ions fall during ICRH, probably due to increased in ion radial transport. For the middle case, only a small increase (about 15%) in Ne^{4+} is found, while the flux of Ne^{5+} drops by a factor of two. The flux of Ne^{3+} increases by 45% in this case, however.

The parallel ion confinement times during ICRH are shown in Figs. 4-56—4-58 for the three neon plasmas. The first three charge states of neon all have nearly the same parallel confinement times during ICRH, while Ne^{4+} (and Ne^{5+} where measurable) have the longest confinement times. The radial confinement times of the resonant
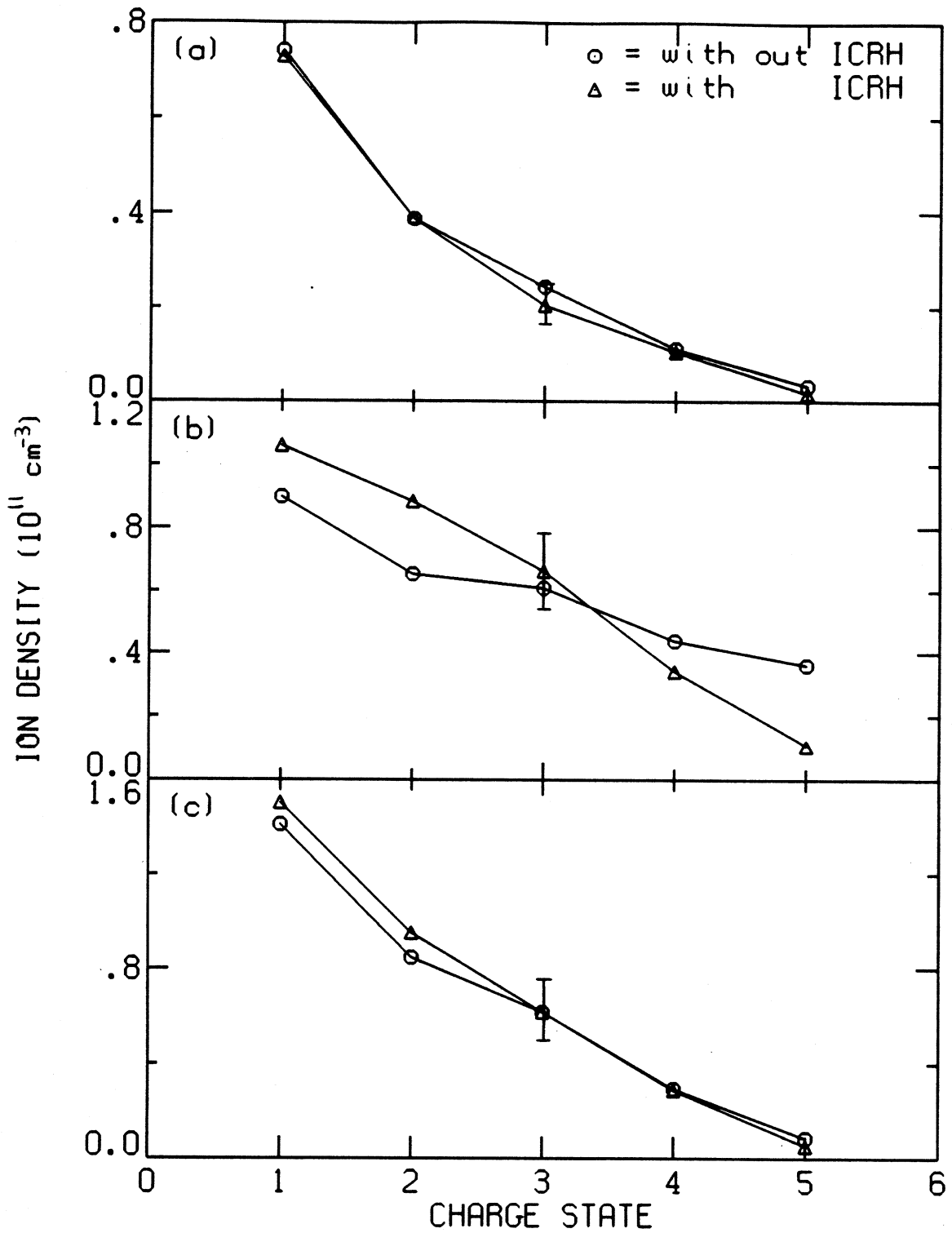
Figure 4-52: Ion densities with and without ICRH for (a) 1 kW, 5×10^{-7}Torr, (b) 4 kW, 5×10^{-7}Torr and (c) 4 kW, 1×10^{-6}Torr neon plasmas.
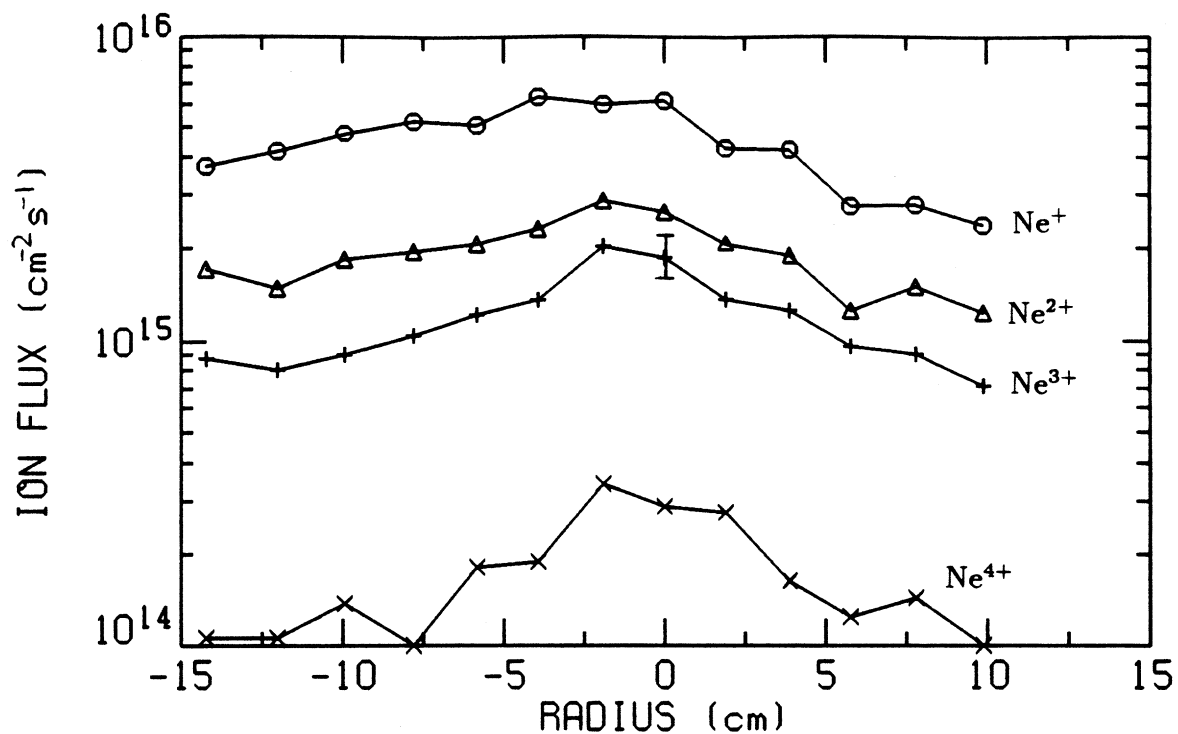
Figure 4-53: Ion fluxes mapped to the magnetic midplane during ICRH for the 1 kW, 5×10^{-7} Torr neon plasma.
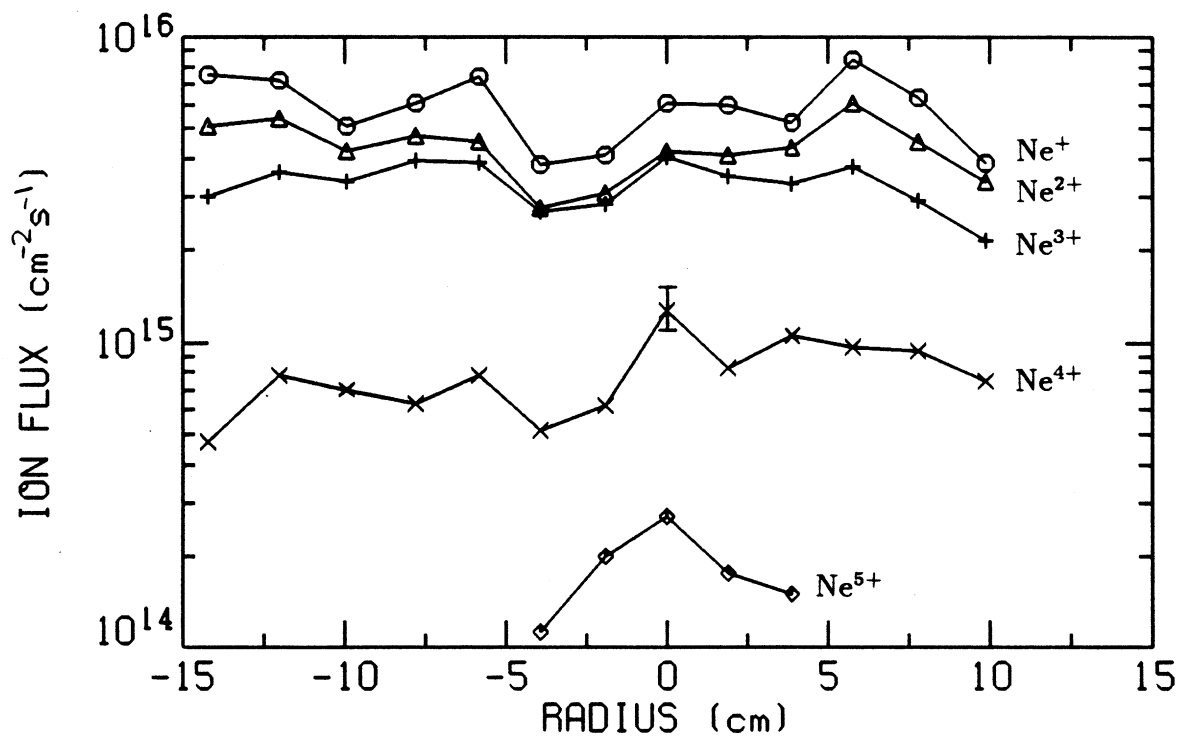
Figure 4-54: Ion fluxes mapped to the magnetic midplane during ICRH for the 4 kW, 5×10^{-7} Torr neon plasma.
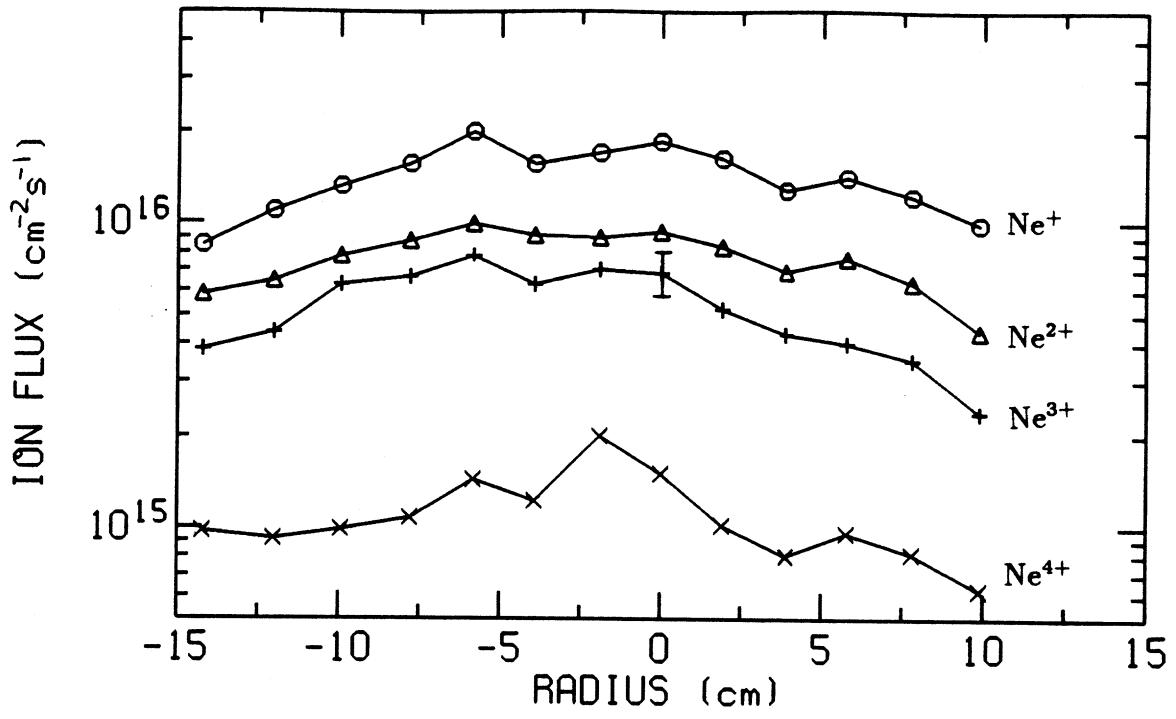
Figure 4-55: Ion fluxes mapped to the magnetic midplane during ICRH for the 4 kW, 1×10^{-6} Torr neon plasma.
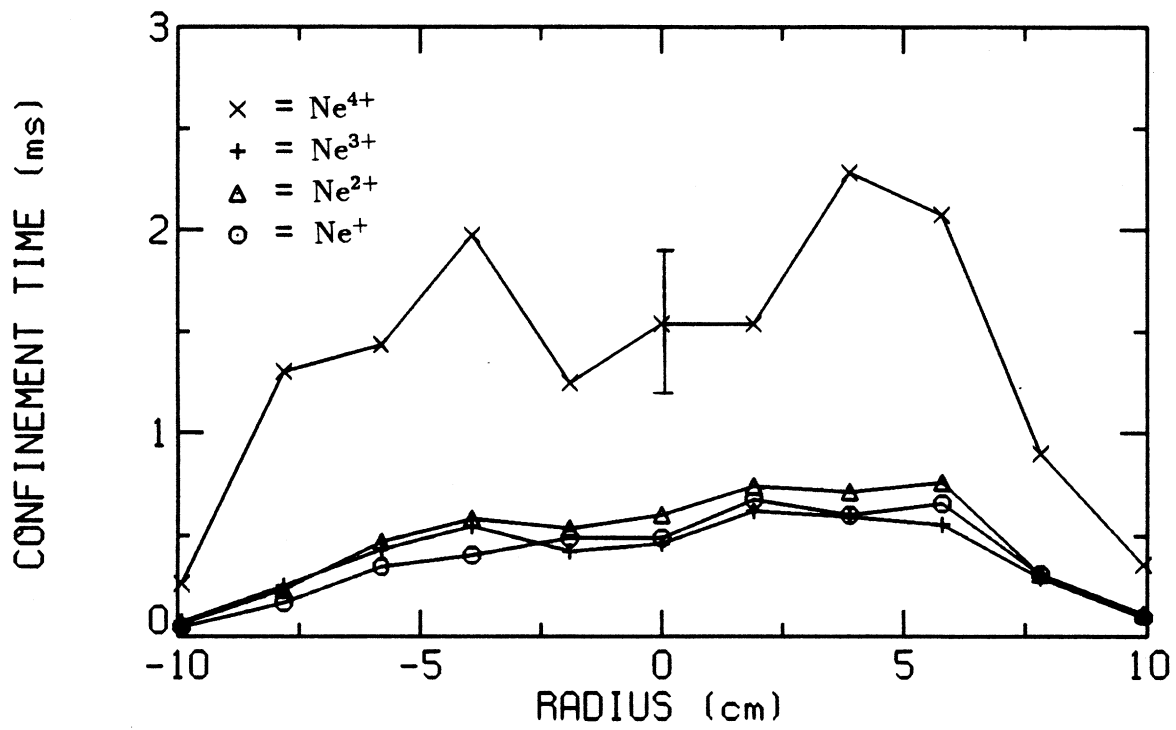
Figure 4-56: Parallel ion confinement times during ICRH for the 1 kW, 5×10^{-7} Torr neon plasma.
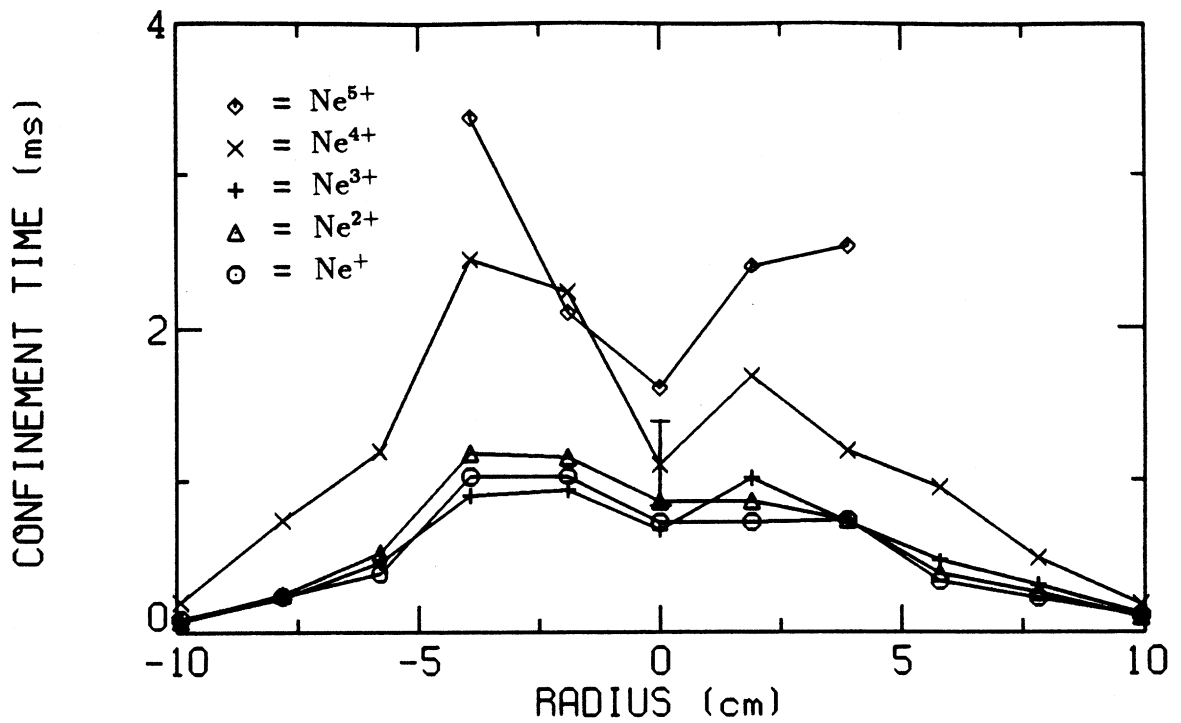
Figure 4-57: Parallel ion confinement times during ICRH for the 4 kW, 5×10^{-7}Torr neon plasma.
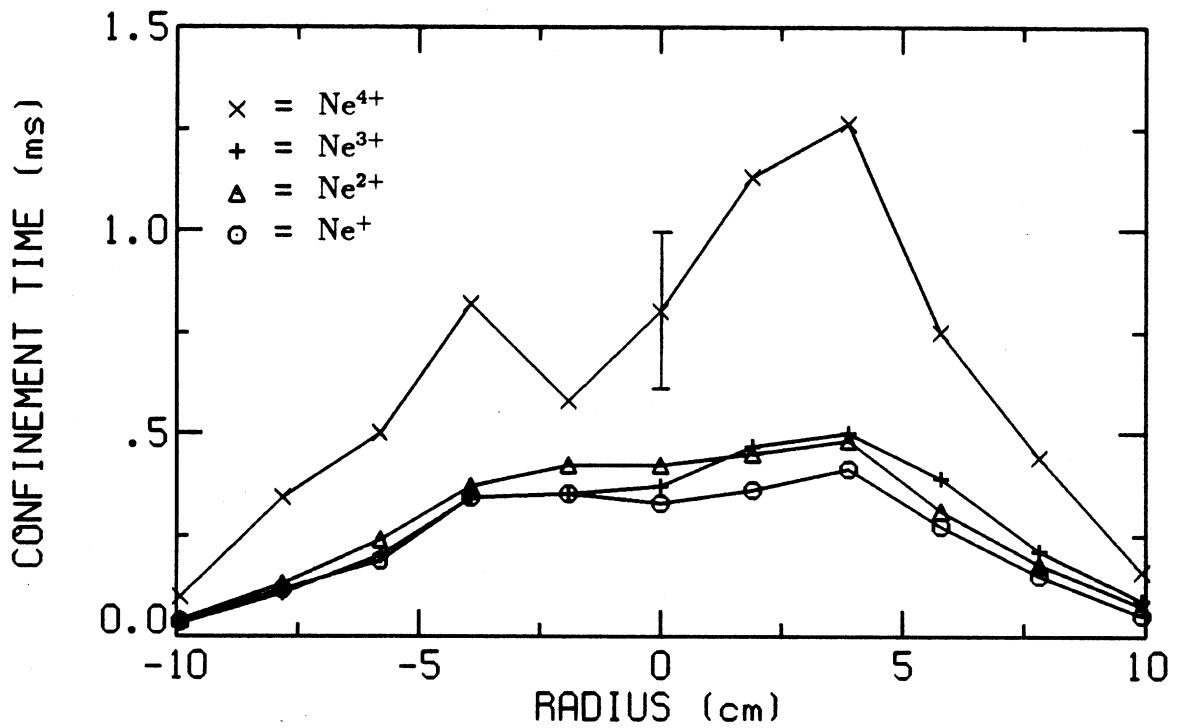
Figure 4-58: Parallel ion confinement times during ICRH for the 4 kW, 1×10^{-6}Torr neon plasma.

Table 4.13: Comparison of ion model results to experiment during ICRH for neon plasmas.

ECRH power Neutral pressure Magnetic field	1 kW 5×10^{-7}Torr 3.5 kG		4 kW 5×10^{-7}Torr 3.5 kG		4 kW 1×10^{-6}Torr 3.5 kG	
	Exper.	Model	Exper.	Model	Exper.	Model
$\langle z \rangle$ of plasma	1.8	1.8	2.2	2.4	2.0	1.9
$\langle z \rangle$ of end loss	1.7	1.6	2.0	1.9	1.8	1.8
$\langle \tau_{\parallel} \rangle$	0.6 ms	0.6 ms	0.9 ms	0.8 ms	0.4 ms	0.4 ms
$\langle \tau_{\perp} \rangle$		0.8 ms		0.9 ms		0.7 ms

ions are also hollow, which may be due to better ion heating at the edge of the ICRH zone (4 cm radius).

Table 4.13 compares the experimental average charge state of the plasma and end loss and the average parallel confinement time to the ion model during ICRH. The average perpendicular confinement time from the ion model is also shown. Generally there is good agreement between model and experiment in all categories. As with oxygen, the ion model predicts that ICRH increases ion radial transport. A large increase in perpendicular losses may explain why ICRH fails to increase the resonant ion flux in many cases.

A more detailed comparison between the experiment and ion model during ICRH is shown in Figs. 4-59—4-61, where the parallel confinement times, densities and fluxes are shown for the three neon plasmas. In contrast to oxygen, for neon the Pastukhov confinement times agree with the experimental results for all charge states, including the resonant ones, with the exception of $Ne^{3,4+}$ in Fig. 4-59. Thus, rf diffusion of the resonant ions does not appear to degrade their parallel confinement much. This is probably related to the weaker ion heating observed for neon compared to oxygen, but uncertainties in the actual $Ne^{4,5+}$ temperatures make the theoretical confinement times uncertain. The ion densities and fluxes also show good agreement between model and experiment.

To summarize the oxygen and neon experimental results during ICRH, the ion heating is primarily in the perpendicular direction. Minority ICRH increases the density of low charge state ions and decreases the density of high charge state ions.
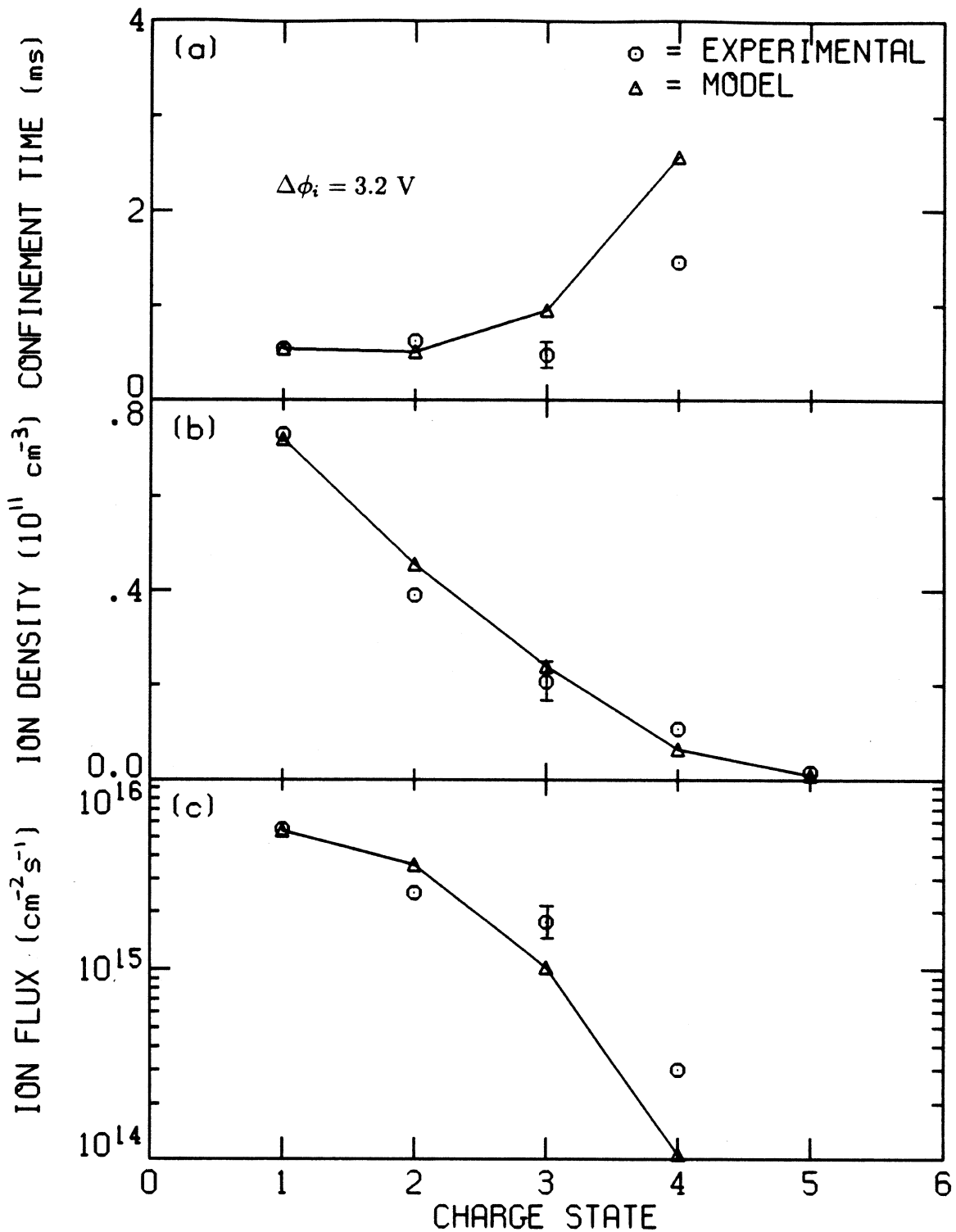
Figure 4-59: Comparison of experimental and model results during ICRH: (a) parallel ion confinement times, (b) ion densities and (c) ion fluxes for the 1 kW, 5×10^{-7} Torr neon plasma.
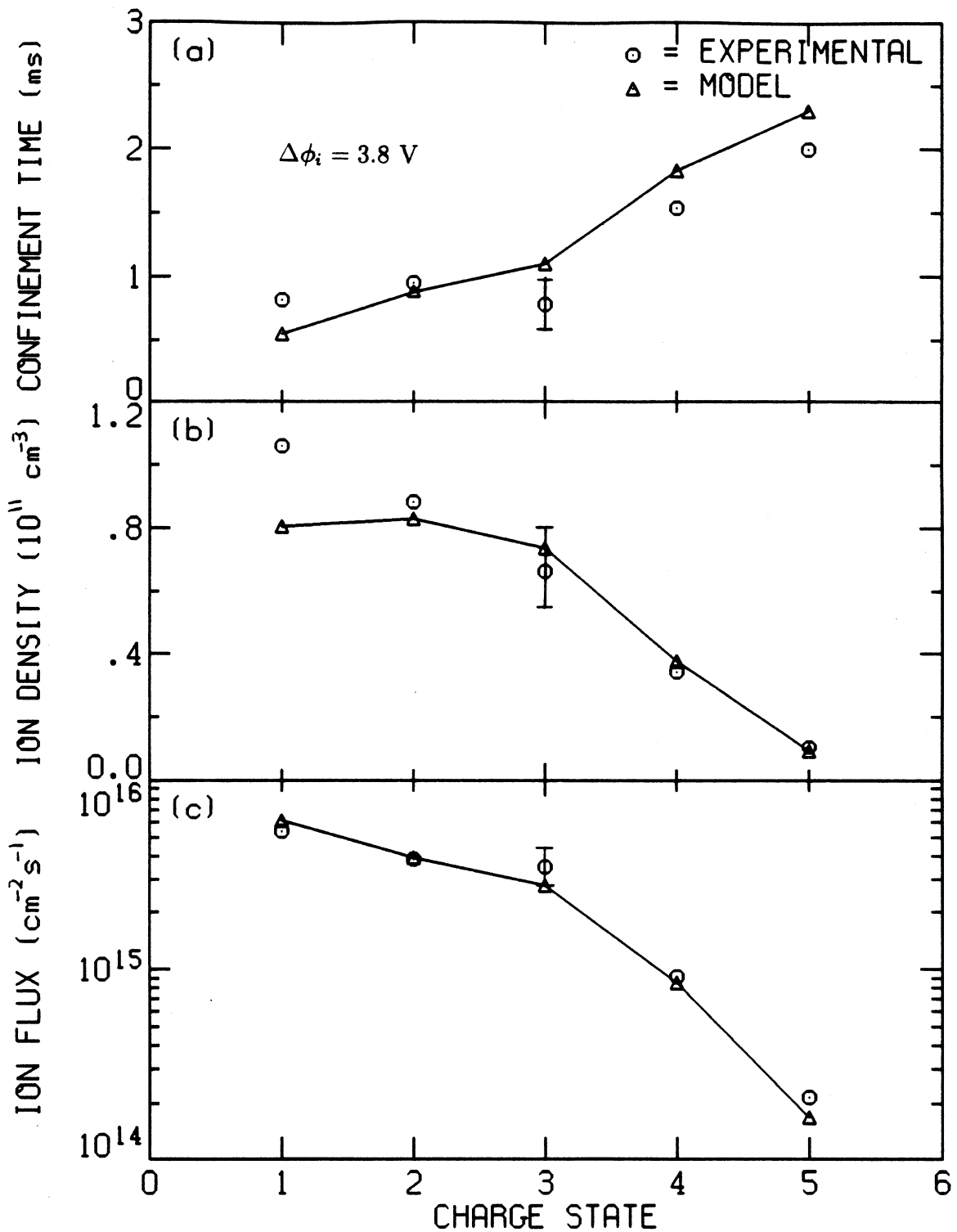
Figure 4-60: Comparison of experimental and model results during ICRH: (a) parallel ion confinement times, (b) ion densities and (c) ion fluxes for the 4 kW, 5×10^{-7} Torr neon plasma.
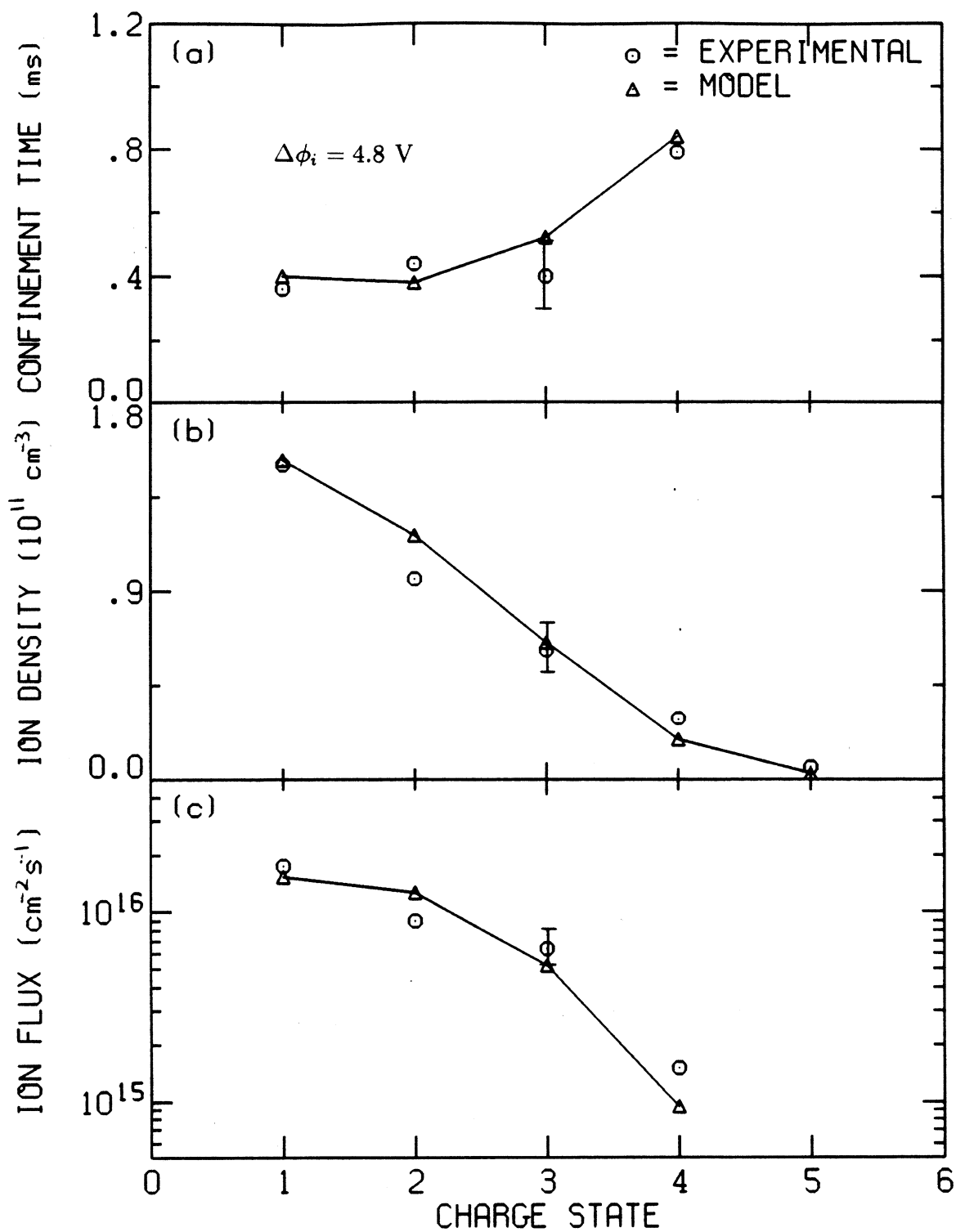
Figure 4-61: Comparison of experimental and model results during ICRH: (a) parallel ion confinement times, (b) ion densities and (c) ion fluxes for the 4 kW, 1×10^{-6} Torr neon plasma.

The radial profile of ion end loss becomes more peaked on axis. The measured parallel confinement time of resonant oxygen ions is much shorter than their theoretical value, probably due to rf diffusion of the ions into the loss cone. Even in the best cases only a small increase in flux (20%) during ICRH is observed for the resonant ions of oxygen and neon. The beneficial effects of ICRH appear to be limited by enhanced ion radial transport, enhanced charge exchange losses and drag heating of non-resonant ions.

4.4.3 candle effect

This section attempts to explain the sudden loss of plasma equilibrium during high power ICRH. After an example is shown, a candle effect model is developed based upon ICRH-driven ion radial transport. This model is then compared to experiment.

When the voltage on the ICRH antenna exceeds a threshold value, which is pressure dependent, a large portion of the plasma is lost. Such a case is shown in Fig. 4-62 for a helium plasma, where a 5 kW pulse of ICRH (tuned to He^+) is applied half way through the shot. At the onset of ICRH, the electron line density rapidly drops as the cold electrons are lost. This removes the particle source for the hot electrons, so the hot electron density decays (as observed from the drop in the stored energy). Without the cold electrons, which provide most of the ionization source, the neutral pressure rises because the plasma no longer "pumps" on it. After the ICRH is turned off, the plasma recovers. This phenomenon is termed the "candle effect" because the sudden loss of plasma seems analogous to extinguishing the flame of a candle.

The candle effect is probably a result of one other effect of ICRH: an increase in ion radial transport. This in turn may be related to the large increase in the plasma potential during ICRH. The rise in the plasma potential is due to an interaction between the rf electric field and the cold electrons [Parks, 1987]. The parallel electric field generated by the antenna pulls out the cold electron distribution function in the parallel direction. This causes an increase in the plasma potential in order to maintain electrostatic confinement of the cold electrons. The theoretical model of this process developed by Parks has been experimentally verified on Constance B [Goodman, 1989].
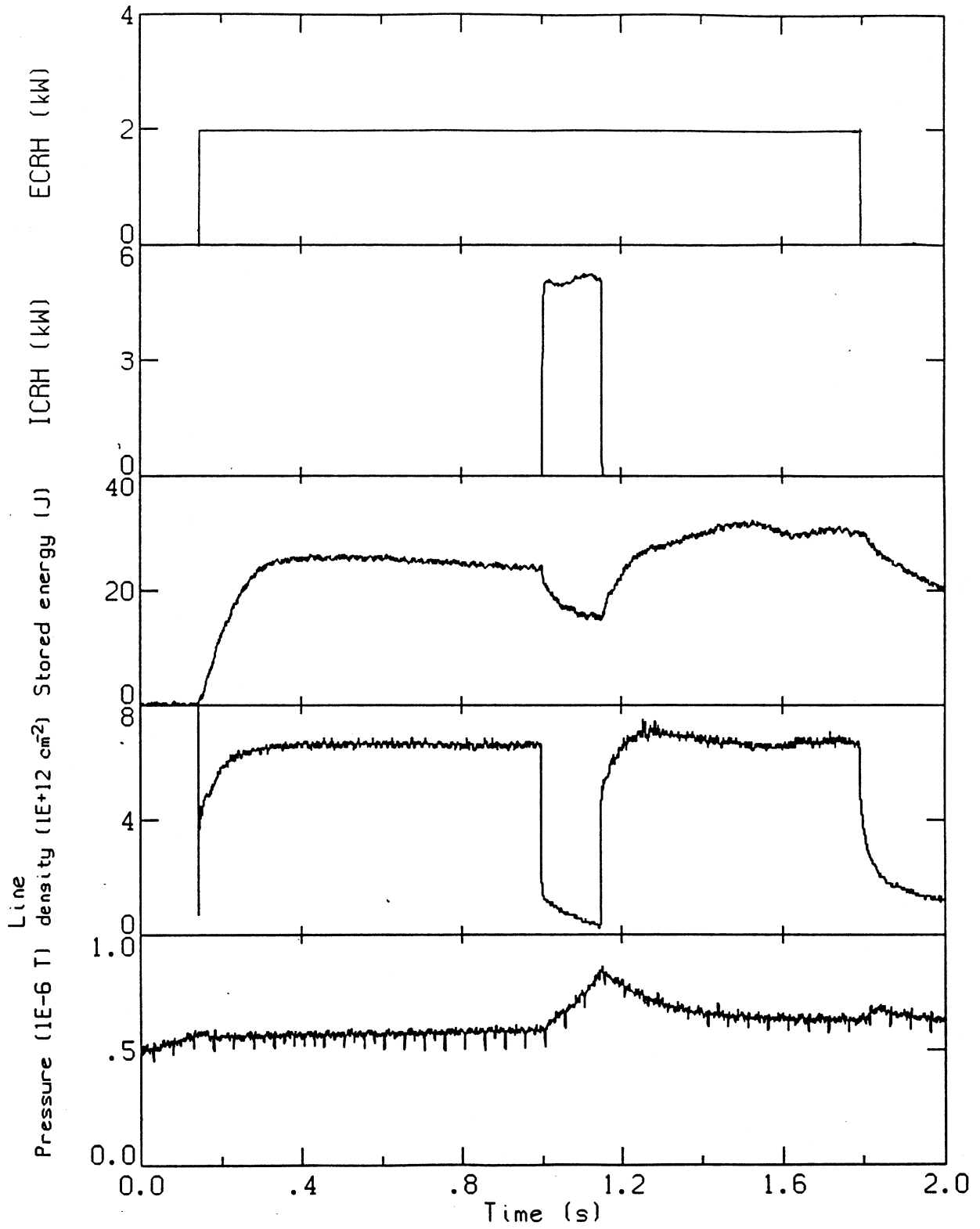
Figure 4-62: A candle effect shot for a helium plasma. The plasma equilibrium is lost during the high power ICRH pulse.
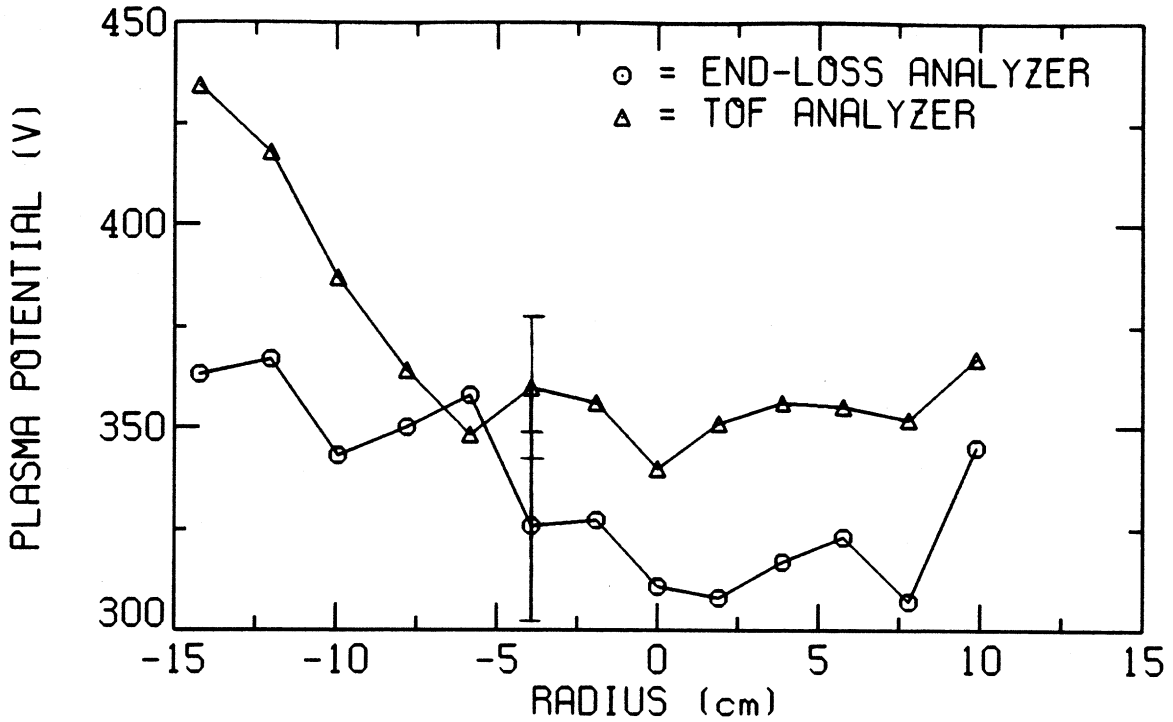
Figure 4-63: Maximum plasma potential during ICRH for the 1 kW, 5×10^{-7}Torr oxygen plasma.

Since the ICRH antenna is bottom fed, the electric field at the bottom of the antenna is larger than at the top. This causes the distortion in the parallel electron distribution function to be greater at the bottom than at the top, which in turn leads to a higher plasma potential near the bottom of the antenna. Experimentally this asymmetry in the plasma potential is seen during ICRH, as shown in Fig. 4-63 for an oxygen plasma. This asymmetry can give rise to convective loss of the plasma and therefore ion radial transport increases during ICRH. Increased ion radial transport during ICRH due to convection has been seen in other mirror experiments [Kuthi, *et al.*, 1988; Brau, *et al.*, 1988].

A simple model for the candle effect is now proposed. In equilibrium, the creation and loss of ions from the plasma must be balanced:

$$\frac{1}{\langle \tau_{\|i} \rangle} + \frac{1}{\langle \tau_{\perp i} \rangle} = \frac{S_o}{L_p \sum n_i}, \tag{4.6}$$

where S_o is the source function. During ICRH, convective loss of ions causes a decrease in $\langle \tau_{\perp i} \rangle$, therefore $\langle \tau_{\|i} \rangle$ must increase to maintain particle balance. As the antenna voltage is increased, the asymmetry in the plasma potential increases which

causes convective losses to further increase. If convection from ICRH causes the perpendicular confinement time to attempt to drop below the ionization source time,

$$\langle \tau_{\perp i} \rangle < \frac{L_p \sum n_i}{S_o}, \tag{4.7}$$

then particle balance cannot be maintained and a large portion of the plasma will be lost. The plasma density will decrease until a new equilibrium is reached based upon ionization of neutral gas by the hot electrons. Experimentally this model can be tested by measuring the perpendicular flux fraction ($F_\perp$) as a function of the applied ICRH voltage. The perpendicular flux fraction is found from

$$F_\perp = \frac{S_o - \sum \Gamma_{\|i}}{S_o} \tag{4.8}$$

and is of value because it normalizes out changes in the source function during ICRH. This model predicts $F_\perp$ should increase smoothly with antenna voltage and that the candle effect should occur when $F_\perp = 1$ is reached.

The measured perpendicular flux fraction as a function of antenna voltage is shown in Fig. 4-64 for a hydrogen plasma and in Fig. 4-65 for a helium plasma.[2] The measurement is at the plasma center for hydrogen and at the 6 cm radius flux surface for helium. The highest antenna voltage plotted is just below the candle effect boundary. This data generally supports the proposed candle effect model because ion radial transport increases with antenna voltage and the candle effect boundary occurs at the largest perpendicular flux fraction. However, the candle effect boundary occurs not at $F_\perp = 1$ as proposed, but instead at $F_\perp = 0.8$ for hydrogen and $F_\perp = 0.7$ for helium. The most likely explanation of this is that a small amount of parallel ion flux is needed out the ends of the mirror in order to neutralize the electron density in the mirror throat (see section 3.6). Thus, when the parallel flux fraction (*i.e.* $1 - F_\perp$) falls below a value of 0.2–0.3, the plasma can not longer satisfy both charge neutrality and particle balance and the candle effect occurs.

As mentioned earlier, the antenna voltage at which candle effect occurs is dependent upon the neutral pressure. Fig. 4-66 is a map of this boundary for a helium plasma for fixed ECRH power and magnetic field. The antenna voltage needed to

---

[2]The helium data was taken by Daniel Goodman.
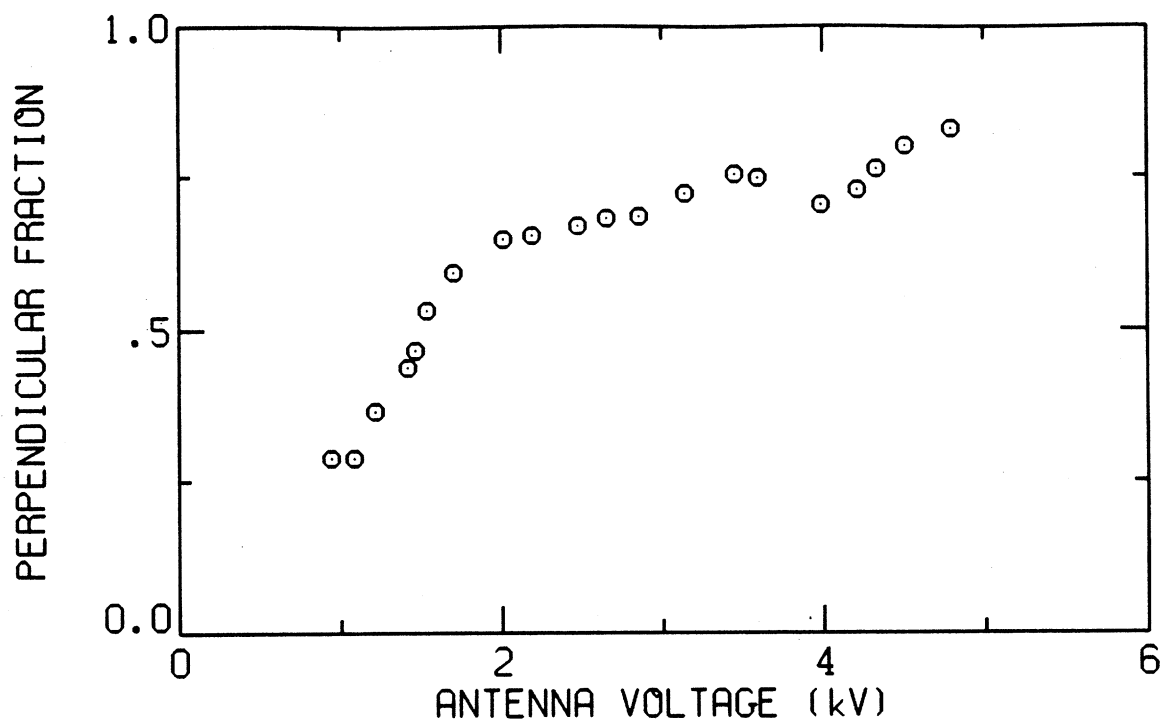
Figure 4-64: Measured perpendicular flux fraction as a function of ICRH antenna voltage for a hydrogen plasma.
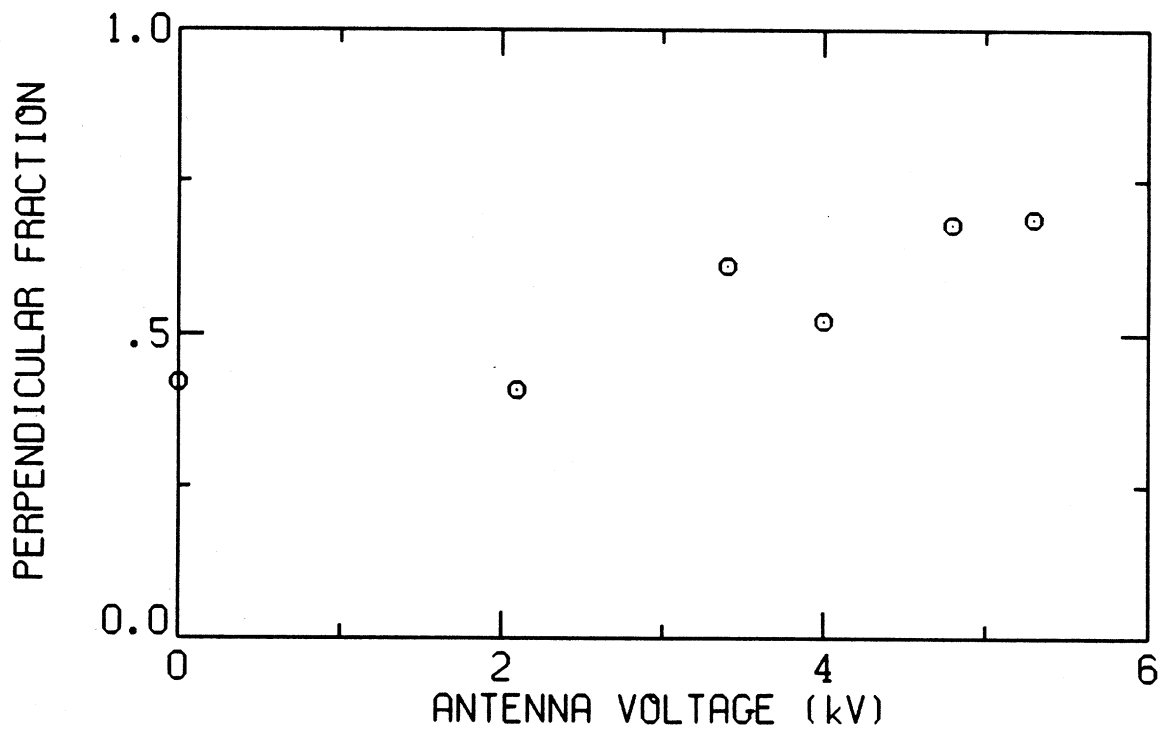
Figure 4-65: Measured perpendicular flux fraction as a function of ICRH antenna voltage for a helium plasma.
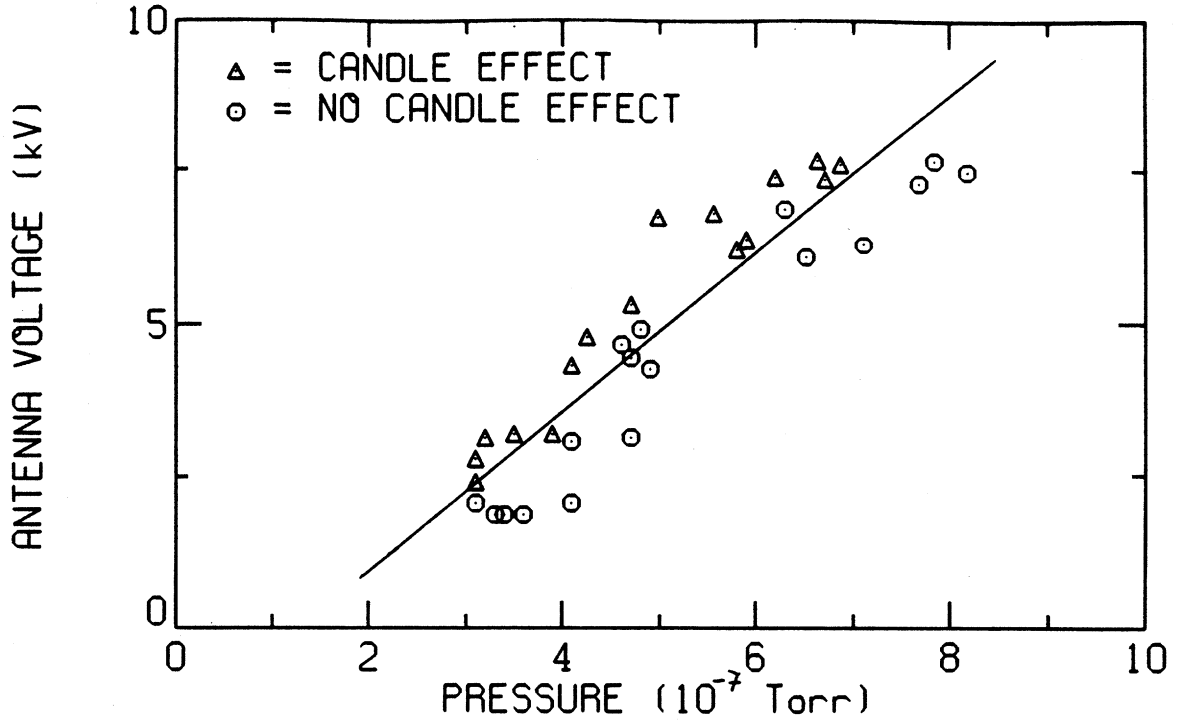
Figure 4-66: Candle effect boundary for a helium plasma with 2 kW ECRH and 3.5 kG midplane magnetic field.

cause candle effect increases linearly with neutral pressure. This can be explained using the proposed candle effect model. If the perpendicular diffusion coefficient before ICRH is D_o, then the perpendicular flux fraction during ICRH can be written as

$$F_\perp = \frac{L_p \sum n_i}{S_o} \frac{K_\perp}{a^2} \left(D_o + \frac{\Delta\phi}{K_\perp B} \right), \qquad (4.9)$$

where $\Delta\phi$ is the potential difference on opposite sides of the plasma surface and the candle effect boundary occurs at $F_{\perp m} = 0.7$–0.8. Assuming that $\Delta\phi/V_{rf} = $ constant $= \alpha$, where V_{rf} is the antenna voltage, and using $S_o \approx L_p n_e \langle \sigma v \rangle^{ion} n_o$ gives the following candle effect boundary:

$$V_{rf} = \left(\frac{a^2 B}{\alpha} \frac{n_e \langle \sigma v \rangle^{ion}}{\sum n_i} F_{\perp m} \right) n_o - \frac{B K_\perp D_o}{\alpha}. \qquad (4.10)$$

This formula has the same linear dependence of antenna voltage on neutral pressure as shown in Fig. 4-66.

Another possible explanation for the physical mechanism of candle effect is that ICRH modifies the axial plasma potential so that the potential dip is forcibly eliminated. This would make it impossible to maintain particle balance since the large

137

decrease in parallel confinement time could not fully be made up by an increase in the perpendicular confinement time. It is not possible to test this experimentally since the potential dip has not been physically measured. However, it is found that the potential dip *deduced* from theoretical confinement models actually increases during ICRH and therefore this explanation does not seem likely. Also the candle effect is not related to ion heating since the loss of plasma can occur even when the ions are not resonant with the launched rf frequency.

4.5   Gas mixing

In operating ECR ion sources, operators have found that by mixing a lighter gas with a heavier gas, the extracted currents for high charge states of the heavier gas increase over what they would be if the lighter gas was not present. In order to learn more about this phenomenon, a case of gas mixing is studied for Constance B. The ion densities and fluxes as a function of charge state are measured for the gas mixing case in order to determine the parallel ion confinement times. The electron densities, electron temperatures and ion temperatures are also measured for use in the ion model. After the experimental results are presented, the ion model is used to attempt to explain the gas mixing effect.

For this gas mixing experiment, the 3.4 kW, 1×10^{-6}Torr oxygen conditions are repeated (see section 4.1), except that a mixture of 55% oxygen and 45% helium (by gauge pressure) is used. This mixture gives approximately equal end-loss current densities of both elements. A comparison of the electron density, temperature and plasma beta between the pure oxygen and oxygen-helium plasmas is shown in Table 4.14. The gas mixing increases the hot electron density and temperature and decreases the cold density and temperature. The total electron density stays nearly the same.

The oxygen ion densities are shown in Fig. 4-67 for both the pure oxygen and oxygen-helium plasmas. The helium ion density during gas mixing is estimated from the amount of helium flux using the theoretical parallel confinement time of helium.

Table 4.14: Comparison of electron parameters between the pure oxygen and oxygen-helium plasmas.

Gas	100% O_2	55% O_2 + 45% He
ECRH power	3.4 kW	3.4 kW
Neutral pressure	1×10^{-6}Torr	1×10^{-6}Torr
Magnetic field	3.5 kG	3.5 kG
Hot electron density	4.3×10^{11}cm^{-3}	5.3×10^{11}cm^{-3}
Hot electron temperature	290 keV	310 keV
Plasma beta	0.25	0.32
Cold electron density	3.8×10^{11}cm^{-3}	2.6×10^{11}cm^{-3}
Cold electron temperature	230 eV	140 eV
Plasma potential	200 V	140 V
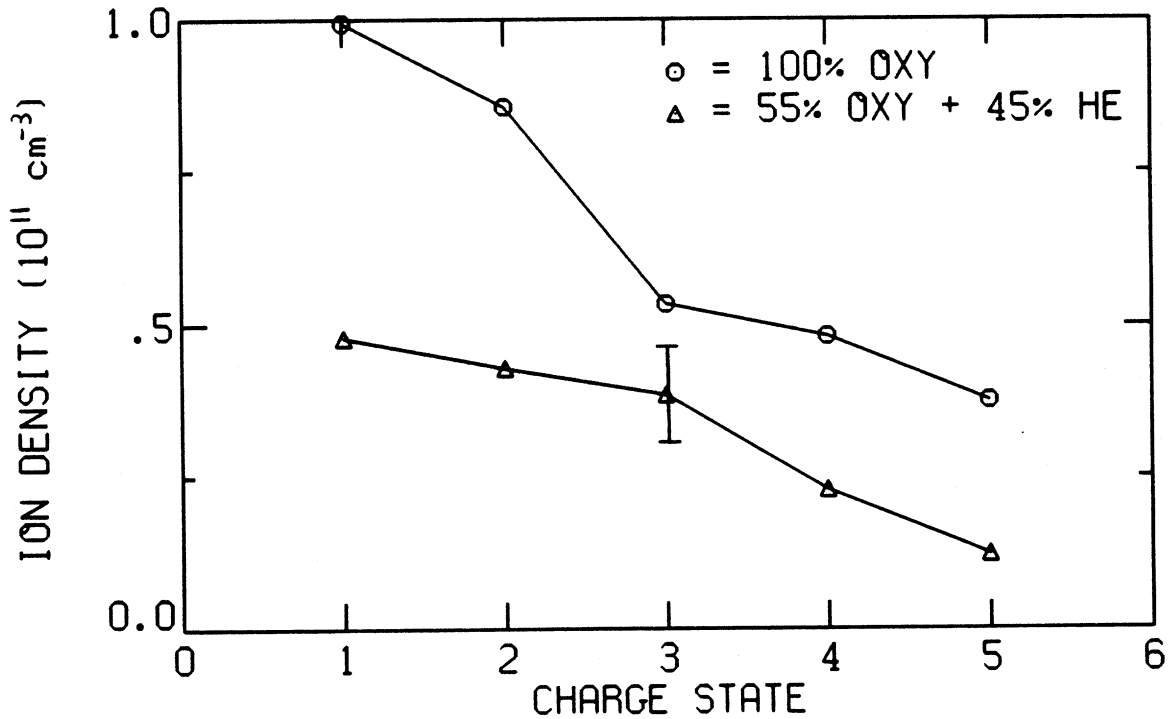
Figure 4-67: Ion densities in plasma center for pure oxygen and oxygen-helium plasmas.
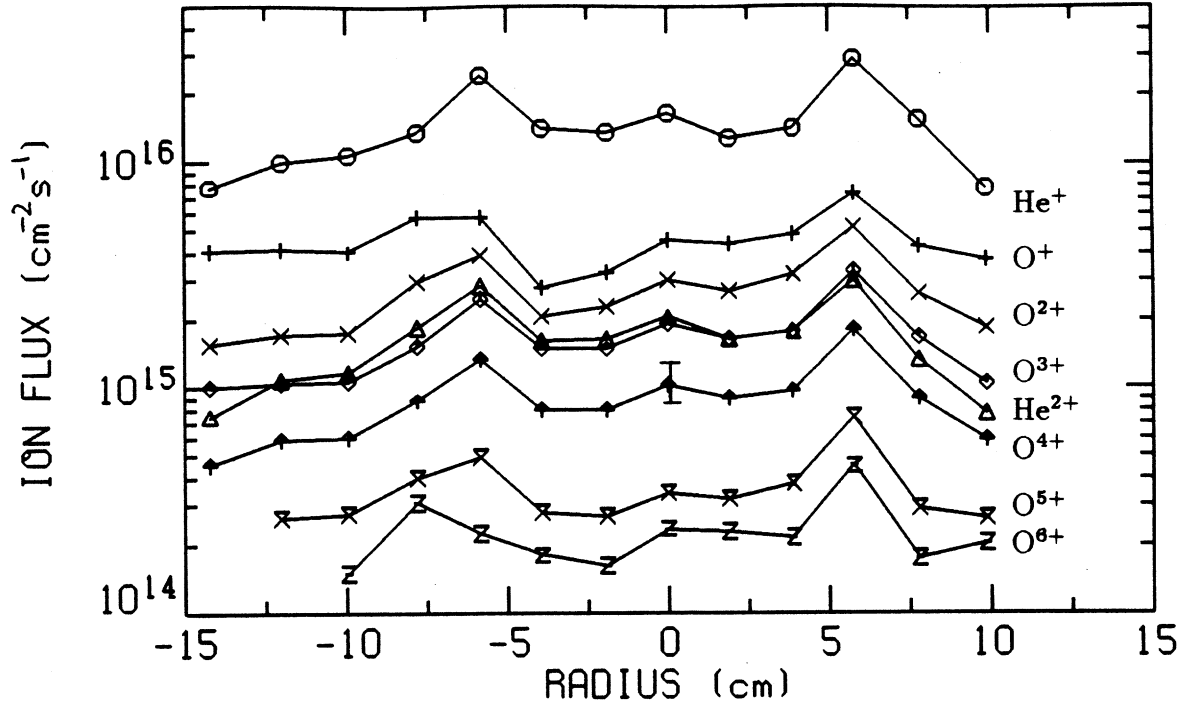
Figure 4-68: Ion fluxes mapped to the magnetic midplane for the oxygen-helium plasma.

The oxygen ion density for the oxygen-helium plasma is one-half that for the pure oxygen plasma. The ion fluxes for the oxygen-helium plasma are shown in Fig. 4-68. The fluxes in the plasma center for the pure oxygen and oxygen-helium plasmas are given in Table 4.15. The oxygen fluxes for the first five charge states of the oxygen-helium plasma are within 15% of the pure oxygen plasma, while the flux of O^{6+} increases by 80%. This increase in the O^{6+} end loss is the gas mixing effect.

Since the gas mixing case has one-half the oxygen ion density but the same oxygen flux as the pure oxygen case, the average parallel confinement time for the gas mixing

Table 4.15: Ion fluxes in the plasma center for the pure oxygen and oxygen-helium plasmas.

Gas	100% O_2	55% O_2 + 45% He
O^+	$4.1 \times 10^{15} cm^{-2} s^{-1}$	$4.6 \times 10^{15} cm^{-2} s^{-1}$
O^{2+}	$3.2 \times 10^{15} cm^{-2} s^{-1}$	$3.0 \times 10^{15} cm^{-2} s^{-1}$
O^{3+}	$2.0 \times 10^{15} cm^{-2} s^{-1}$	$2.0 \times 10^{15} cm^{-2} s^{-1}$
O^{4+}	$9.8 \times 10^{14} cm^{-2} s^{-1}$	$1.0 \times 10^{15} cm^{-2} s^{-1}$
O^{5+}	$3.9 \times 10^{14} cm^{-2} s^{-1}$	$3.4 \times 10^{14} cm^{-2} s^{-1}$
O^{6+}	$1.3 \times 10^{14} cm^{-2} s^{-1}$	$2.4 \times 10^{14} cm^{-2} s^{-1}$
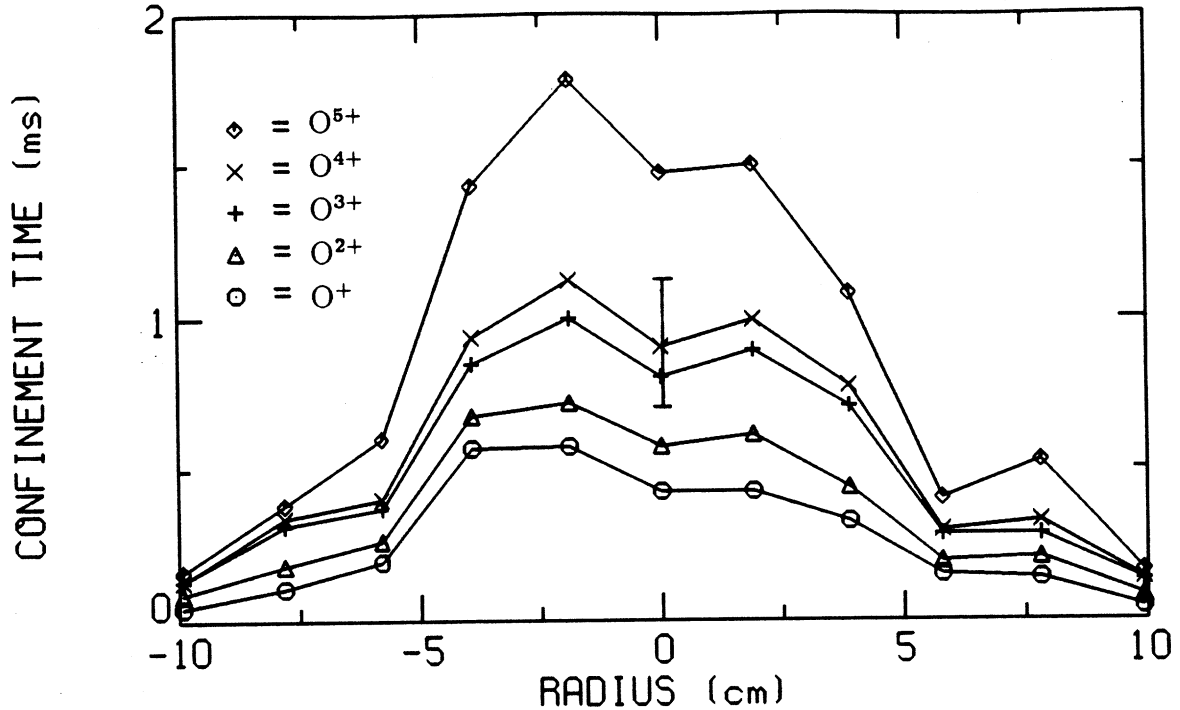
Figure 4-69: Parallel confinement times for oxygen ions in the oxygen-helium plasma.

Table 4.16: Comparison of ion confinement times for the pure oxygen and oxygen-helium plasmas.

Gas	100% O_2	55% O_2 + 45% He
S_o	$2.3 \times 10^{16} cm^{-2} s^{-1}$	$1.2 \times 10^{16} cm^{-2} s^{-1}$
$\langle \tau_{\parallel} \rangle$	1.2 ms	0.6 ms
$\langle \tau_{\perp} \rangle$	1.1 ms	4.8 ms

case must be one-half that of the pure oxygen case. The parallel confinement times for oxygen ions in the oxygen-helium plasma are shown in Fig. 4-69. There is a clear stepwise increase in parallel confinement time with ion charge state. The calculated oxygen source function and average parallel and perpendicular confinement times for the pure oxygen and oxygen-helium plasmas are given in Table 4.16. Since the electron density does not change much, the source function is proportional to the oxygen neutral pressure. The amount of ion radial transport appears to be considerably reduced for the gas mixing case. The reason why ion radial transport reduces is not known, but it may be due to a reduction in turbulent diffusion.

Fig. 4-70 shows the perpendicular ion temperatures measured by Doppler broadening for the pure oxygen and oxygen-helium plasmas. The parallel ion temperatures
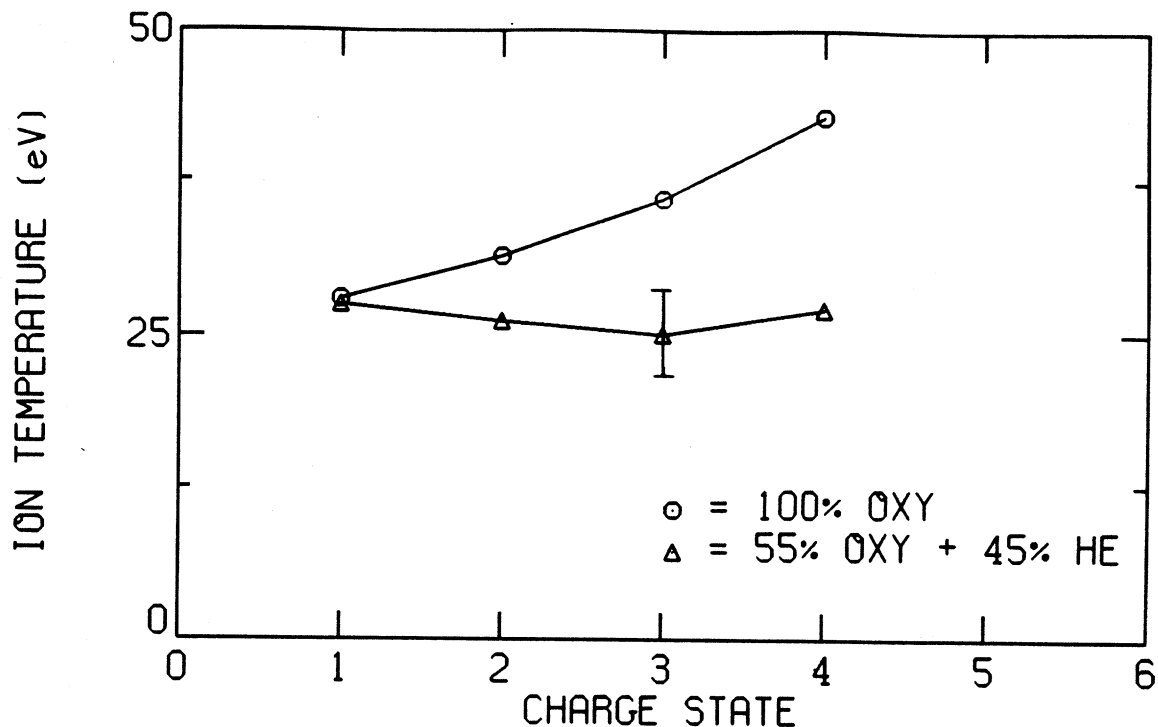
Figure 4-70: Ion temperatures perpendicular to the magnetic field measured by Doppler broadening for the pure oxygen and oxygen-helium plasmas.

agree with the perpendicular temperatures to within experimental error. The pure oxygen plasma has an increase in ion temperature with charge state, while the oxygen-helium plasma has about the same ion temperature for all charge states. The helium ion temperature measured by Doppler broadening is 9 eV.

In order to explain the gas mixing effect (the 80% increase in the O^{6+} flux), the changes in the plasma must be examined individually. There are five major changes in the plasma caused by gas mixing: (1) an increase in the ratio of hot-to-cold electrons, (2) a lowering of the cold electron temperature, (3) a lowering of the ion temperature, (4) a lowering of the average charge state of the confined ions and (5) a decrease in ion radial transport. Experimentally these changes cannot be isolated from one another, but by using the ion model the effect of each change on the ion flux can be studied independently.

The first effect to be studied is changes in the electron density. Although the total electron density stays nearly constant, the ratio of hot-to-cold electrons (α) increases from $\alpha = 1.1$ to $\alpha = 1.7$. Fig. 4-71 shows the fraction of O^{6+} in the end loss for
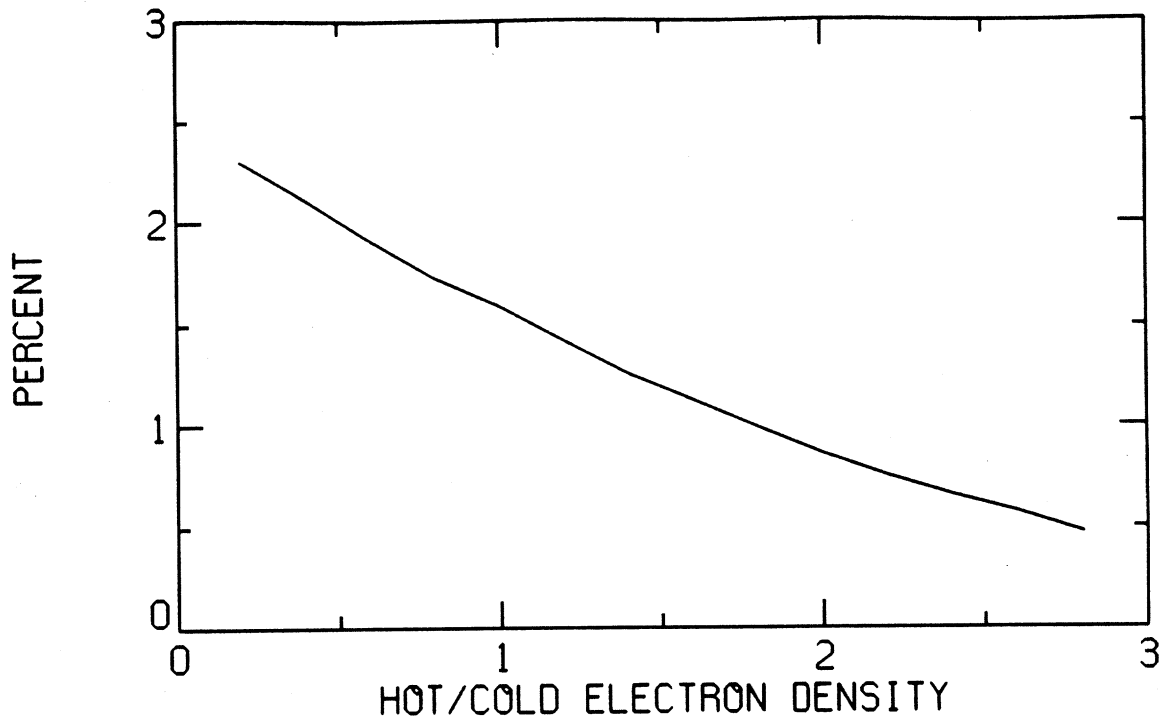
Figure 4-71: Fraction of O^{6+} in the end loss (in %) as a function of the ratio of hot-to-cold electrons.

various values of α, with all other plasma parameters held constant. The relative amount of O^{6+} flux is seen to increase as the fraction of cold electrons increases. This is because the ionization of oxygen ions is due primarily to the cold electrons, since the cold electron temperature is close to typical ionization potentials of oxygen ions. Thus, the increase in the ratio of hot-to-cold electrons does not explain the gas mixing effect.

Another change is that the cold electron temperature decreases during gas mixing from 230 eV to 140 eV. Fig. 4-72 shows the fraction of O^{6+} in the end loss as a function of the cold electron temperature. The model predicts that lowering the cold electron temperature decreases the flux of O^{6+} and therefore it does not explain the gas mixing effect. The main reason a higher temperature is better is because the ionization of O^{5+} to form O^{6+} peaks around $T_e = 1$ keV. Thus, increasing the cold electron temperature leads to a larger density of O^{6+}, which increases its end loss.

Next the effect of ion temperature is studied. Mixing helium with oxygen lowers the average ion temperature from 33 eV to 26 eV, with the largest cooling effect
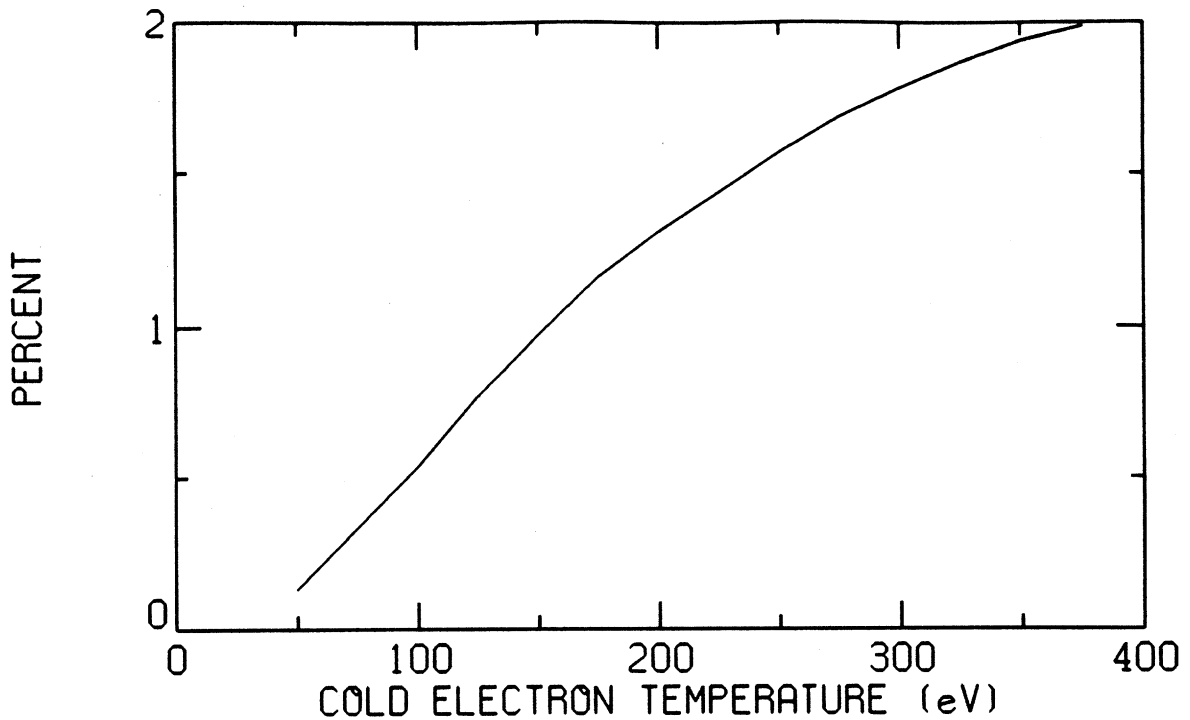
Figure 4-72: Fraction of O^{6+} in the end loss (in %) as a function of cold electron temperature.

occurring for the highest charge state. As previously seen in Fig. 4-29, the ion temperatures increase with ion mass. Since the helium ions in the oxygen-helium plasma are at 9 eV, the oxygen ions lose energy to them in collisions. Also since the collision frequency increases with ion charge state, the highest charge states show the largest amount of cooling. As seen in Fig. 4-73, both low and high ion temperatures can improve the O^{6+} flux. To explain this behavior, start at the high temperature end. All the ions in this case are in the Pastukhov-flow regime. By increasing the ion temperature in this regime, the ions are becoming relatively more mirror trapped and less electrostatically trapped. This increases the end loss of O^{6+} because it decreases its parallel confinement time. (Although the ion density of O^{6+} decreases with increasing temperature, the decrease in parallel confinement time is a larger effect.) As the ion temperature is decreased below 20 eV, O^{6+} becomes collisional enough to move from the Pastukhov-flow regime to the spatial diffusion regime. The parallel confinement time in this regime increases strongly as the ion temperature decreases and so the end loss of O^{6+} also quickly decreases with temperature. As the ion temperature contin-
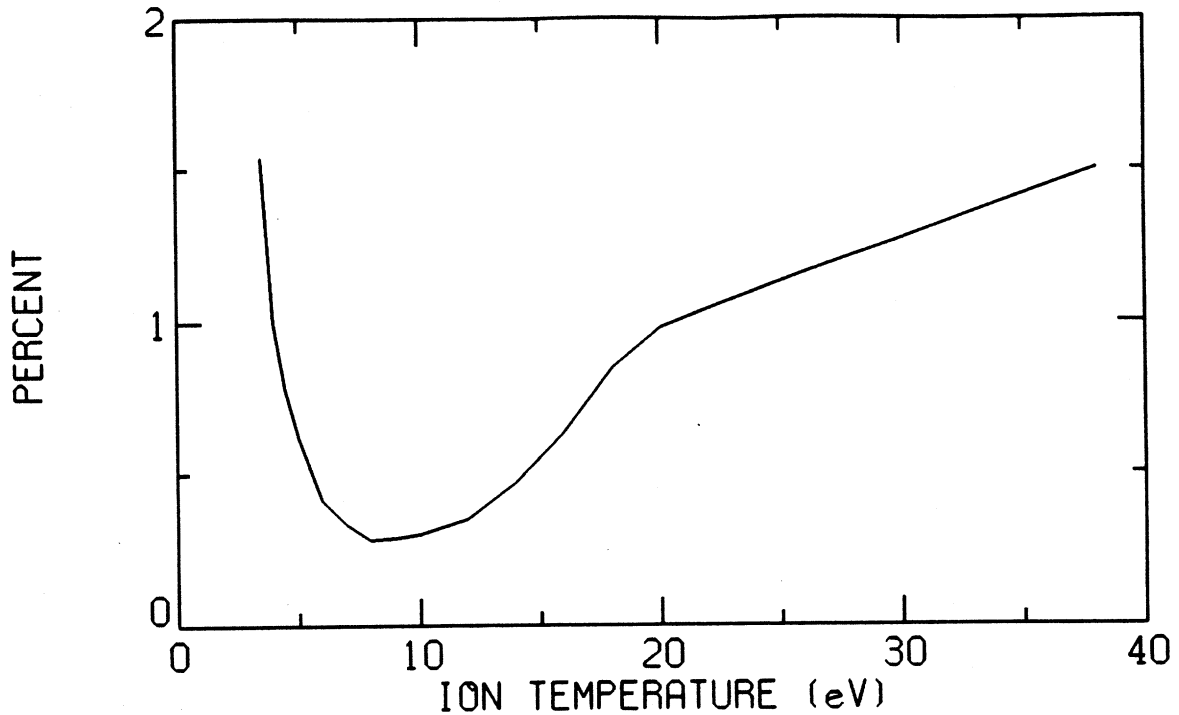
Figure 4-73: Fraction of O^{6+} in the end loss (in %) as a function of ion temperature.

ues to decrease, more and more ions enter the spatial diffusion regime. When most of the ions are collisionally confined (below $T_i = 8$ eV), the need for electrostatic confinement diminishes. As the potential dip falls to zero, the parallel confinement time of O^{6+} rapidly decreases, causing a rapid increase in its end loss. For Constance B where the ions are anomalously hot, decreasing the ion temperature hurts the end loss of O^{6+} and therefore does not explain the gas mixing effect.

Mixing helium with oxygen lowers the average charge state of the confined ions, which therefore increases the collision time of the oxygen ions. The average charge state of the plasma falls from $\langle z_p \rangle = 2.5$ for the pure oxygen plasma to $\langle z_p \rangle = 1.7$ for the oxygen-helium plasma. Increasing the collision time by lowering $\langle z_p \rangle$ is similar to increasing the collision time by raising the ion temperature. From Fig. 4-73, it can be seen that in the Pastukhov-flow regime, increasing the collision time does improve the end loss of O^{6+}, but the effect is too small to entirely explain the 80% increase.

The last effect to be studied is ion radial transport. The perpendicular flux fraction falls from $F_\perp = 0.51$ for the pure oxygen plasma to $F_\perp = 0.11$ for the oxygen-helium plasma. The effect of the perpendicular flux fraction on the end loss of O^{6+} is shown in

145
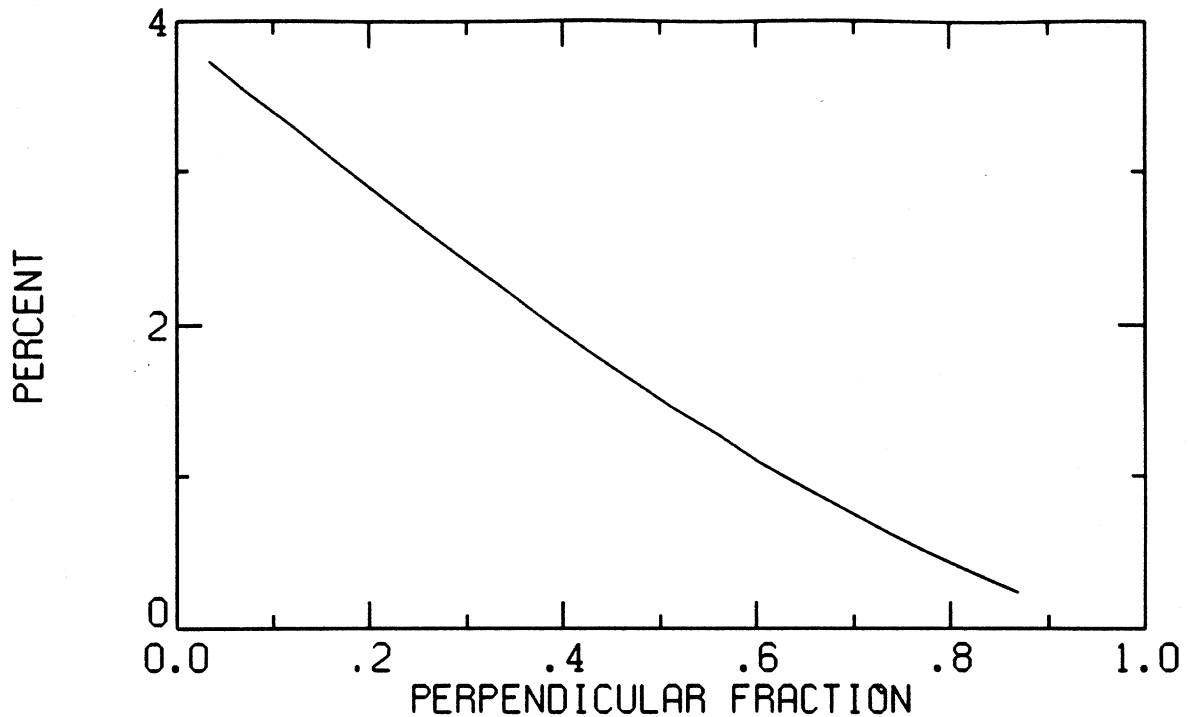
Figure 4-74: Fraction of O^{6+} in the end loss (in %) as a function of perpendicular flux fraction.

Fig. 4-74. The end loss of O^{6+} strongly increases as the amount of ion radial transport decreases. The amount of increase is so large, it can offset the "bad" changes in the ratio of hot-to-cold electrons, cold electron temperature and ion temperature to result in a net gain. In comparing runs of the ion model for pure oxygen and oxygen-helium plasmas, the model predicts that the changes in the fluxes for the first five charge states of oxygen are less than 20% while the flux of O^{6+} increases by 60%. These model results agree with experiment to within experimental error.

4.6 Electrons

In this section the theoretical confinement times and scaling laws from Chapter 3 for the hot and cold electrons are compared to experiment. The experimental confinement times are determined from the measured electron densities and fluxes. First the cold electron physics are studied. Fig. 4-75 shows the radial profile of the cold electron flux for an oxygen plasma. The end loss is strongly peaked at the edge of the ECR zone (6 cm radius). The parallel confinement time for the cold electrons as a function
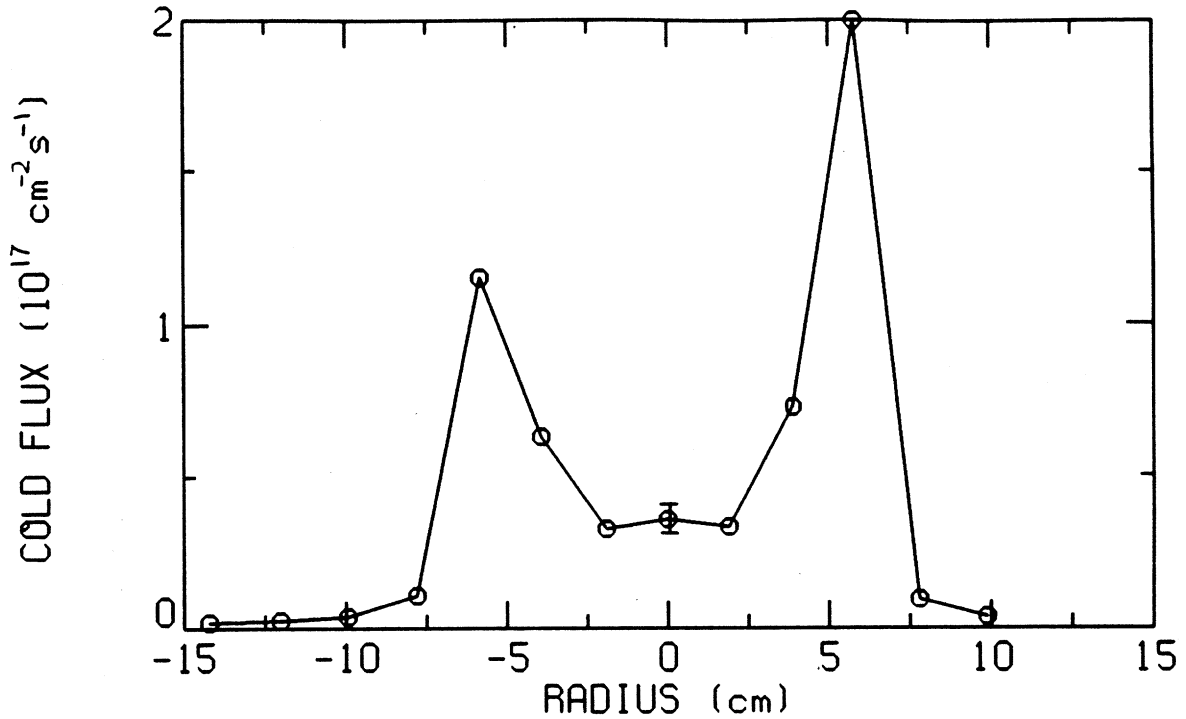
Figure 4-75: Cold electron flux mapped to the magnetic midplane for the 1 kW, 5×10^{-7} Torr oxygen plasma.

of radius is shown in Fig. 4-76 for the same oxygen plasma. The parallel confinement time is shortest at the edge of the ECR zone. Electrons at this radius have the strongest interaction with the microwaves because the electron stays in resonance for the longest period of time. In the plasma center, the cold electrons should obey the Pastukhov confinement time. For the oxygen plasma shown in Fig. 4-76, the maximum plasma potential is $\phi_p = 145$ V and the deduced potential dip is $\Delta\phi_i = 15$ V. Neglecting any potential in the mirror throat ($\phi_m = 0$), the ambipolar potential is therefore $\Delta\phi_e = 130$ V. Using this value in Eqn. 3.51 along with the measured cold electron density and temperature and the ion charge state distribution gives a Pastukhov confinement time of $\tau_p = 0.16$ ms. This is in fair agreement with the experimentally measured $\tau_{ec} = 0.13$ ms. In reality, the potential in the mirror throat will not be zero and so the actual ambipolar potential will be smaller than $\Delta\phi_e = 130$ V. This will improve agreement between experiment and theory.

The theoretical cold-electron absorption coefficient, given by Eqn. 3.60, for this oxygen plasma is $\eta_c = 4.3\%$. Experimentally, the cold electron absorption coefficient
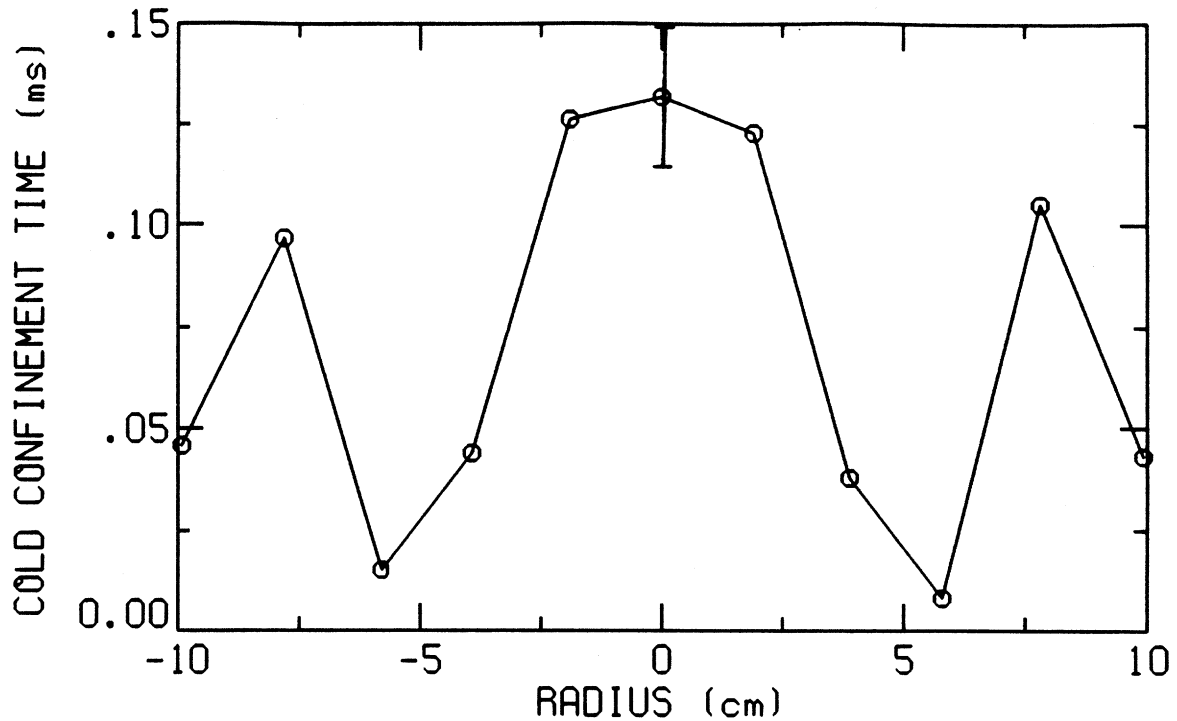
Figure 4-76: Parallel confinement time of the cold electrons for the 1 kW, 5×10^{-7} Torr oxygen plasma.

can be determined from Eqn. 3.64, which gives $\eta_c = 4.4\%$. The theoretical and experimental values therefore agree to well within experimental error.

Next the scaling laws for cold electron confinement and density (Eqns. 3.65 and 3.66) are compared to experiment. First the effect of ECRH power density is studied. The cold electron temperature enters the scaling laws only in the ionization rate parameter. Fig. 4-77 shows the cold electron temperature as a function of ECRH power for a helium plasma. The electron temperature does not vary much with ECRH power, therefore variation in the ionization rate parameter with ECRH power density will be neglected. For this case, Eqn. 3.65 predicts that the cold electron confinement time is independent of ECRH power density. Fig. 4-78 shows the parallel confinement time of cold electrons as a function of ECRH power for a helium plasma. The parallel confinement time does not vary significantly with ECRH power, in agreement with theory. Eqn. 3.66 predicts that the cold electron density will increase with the square-root of ECRH power density. The measured cold electron density as a function of ECRH power is shown in Fig. 4-79 for neon. The ECRH power density is also varied

Figure 4-77: Cold electron temperature as a function of ECRH power for a helium plasma.
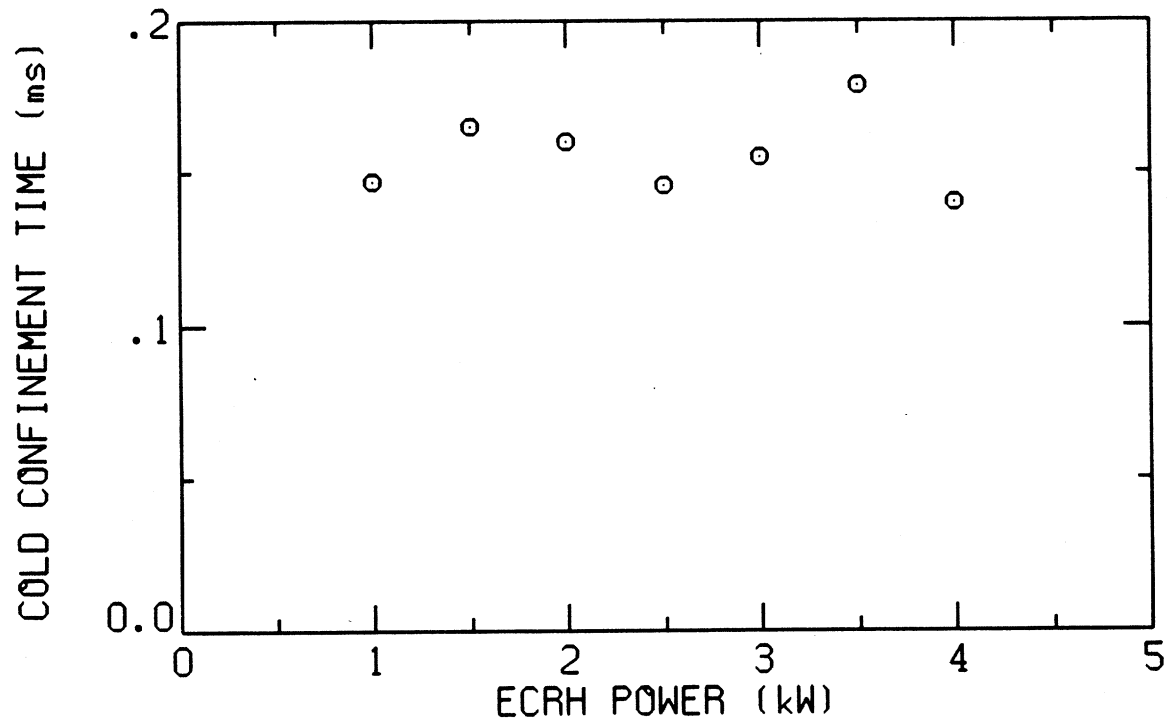
Figure 4-78: Parallel confinement time of cold electrons a function of ECRH power for a helium plasma.
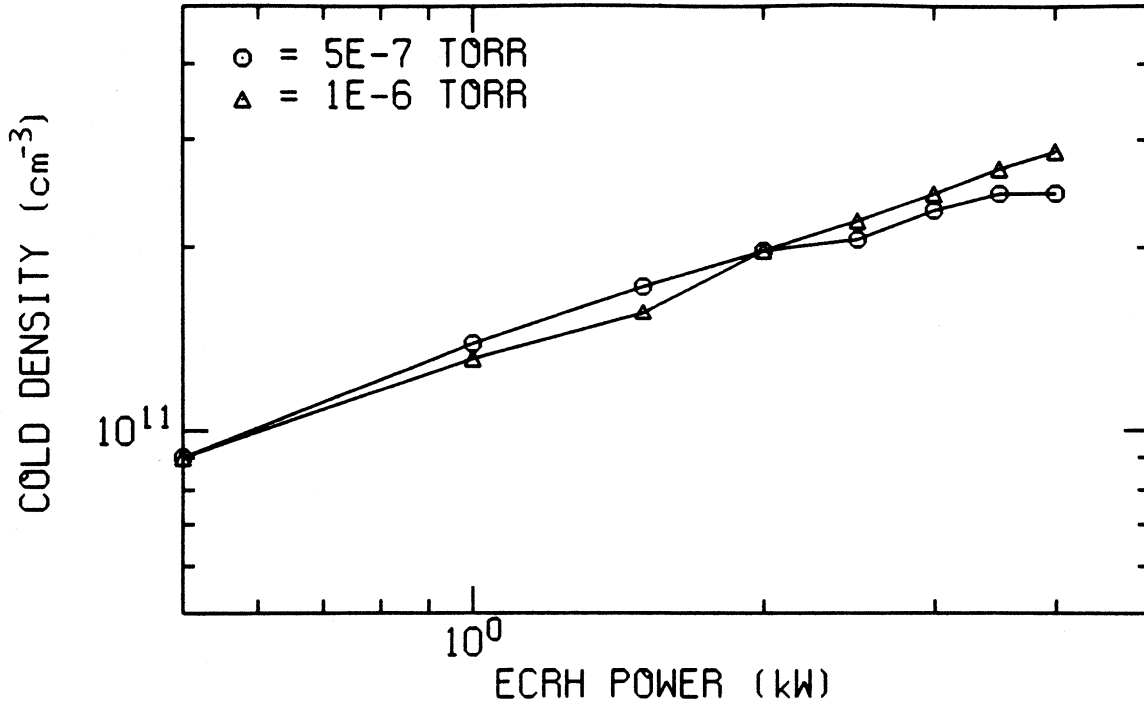
Figure 4-79: Cold electron density as a function of ECRH power for neon.

by changing the size of the plasma in other experiments. Both methods produced a scaling of cold electron density with ECRH power density of $n_{ec} \propto P_{ech}^{.52\pm.04}$, in good agreement with theory. This is also in agreement with previous measurements on Constance B for hydrogen plasmas [Hokin, 1987].

Eqn. 3.66 also predicts that the cold electron density should decrease with the square-root of neutral pressure. It can be seen from Fig. 4-79 that there is actually little change in the cold electron density with changing neutral pressure. This is probably because the cold electron temperature decreases with increasing neutral density[3] like $T_{ec} \propto n_o^{-.59}$. Thus, increasing the neutral pressure by a factor of two lowers the cold electron temperature by 50%. This causes a decrease in the ionization rate parameter which can offset the increase in the neutral pressure.

Next the hot electron physics are studied. Fig. 4-80 shows the radial profile of the hot electron flux for an oxygen plasma. The radial profile of the hot electrons is very similar to that of the cold electrons. The end loss is strongly peaked at the edge of the nonrelativistic ECR zone (6 cm radius). The parallel confinement time

---

[3]This data was taken by Daniel Goodman.

150
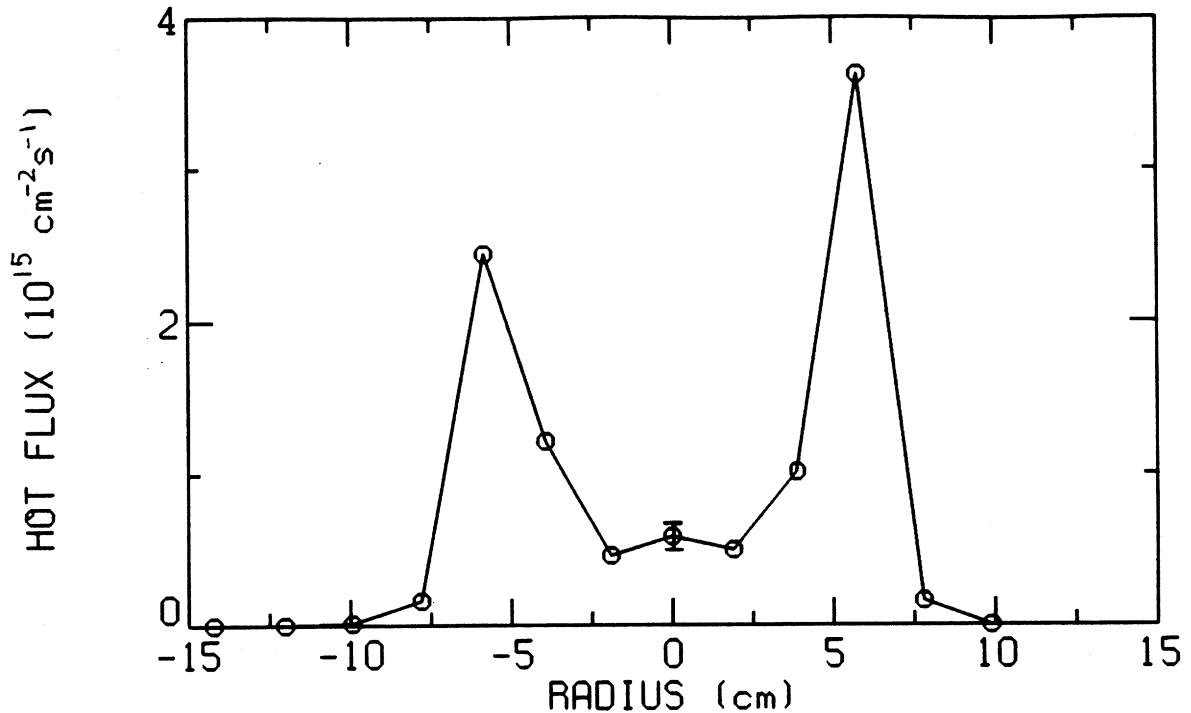
Figure 4-80: Hot electron flux mapped to the magnetic midplane for the 1 kW, 5×10^{-7} Torr oxygen plasma.

for the hot electrons as a function of radius is shown in Fig. 4-81 for the same oxygen plasma. The parallel confinement time is shortest at the edge of the nonrelativistic ECR zone. The measured end loss in this region is probably dominated by weakly relativistic electrons which are strongly rf diffused at this radius. The hot electron confinement time in the plasma center is about 20 ms. This is much shorter than the classical mirror confinement time, which is calculated for these plasma parameters to be 1.2 s. Previous work on Constance B has shown that this is due to rf diffusion of the hot electrons into the loss cone [Hokin, et al., 1989]. The global hot-electron confinement time determined from Eqn. 3.69 is 16 ms, in fair agreement with the value in the plasma center.

Next the scaling law for hot electron density, temperature and confinement time (Eqn. 3.68) is compared to experiment. The left hand side of this equation is broken up into two parts, n_{eh} times T_{eh}/τ_{eh}, for comparison with experiment. The measured hot electron density as a function of ECRH power is shown in Fig. 4-82 for neon. The ECRH power density is also varied by changing the size of the plasma in other
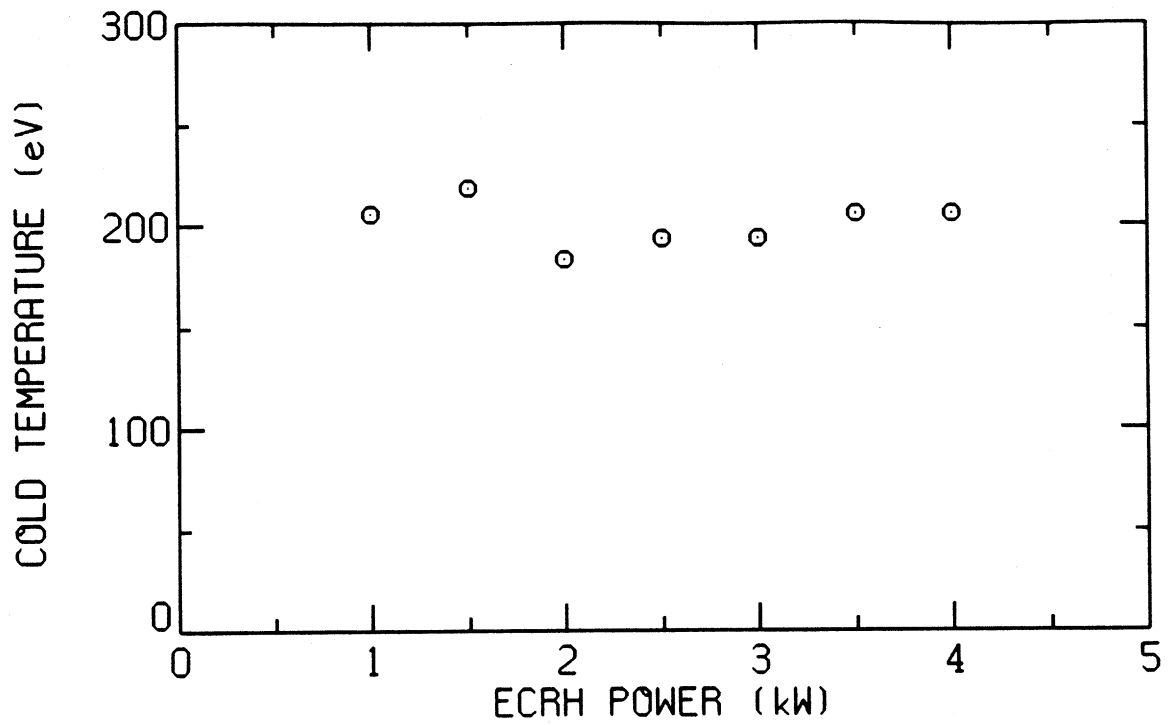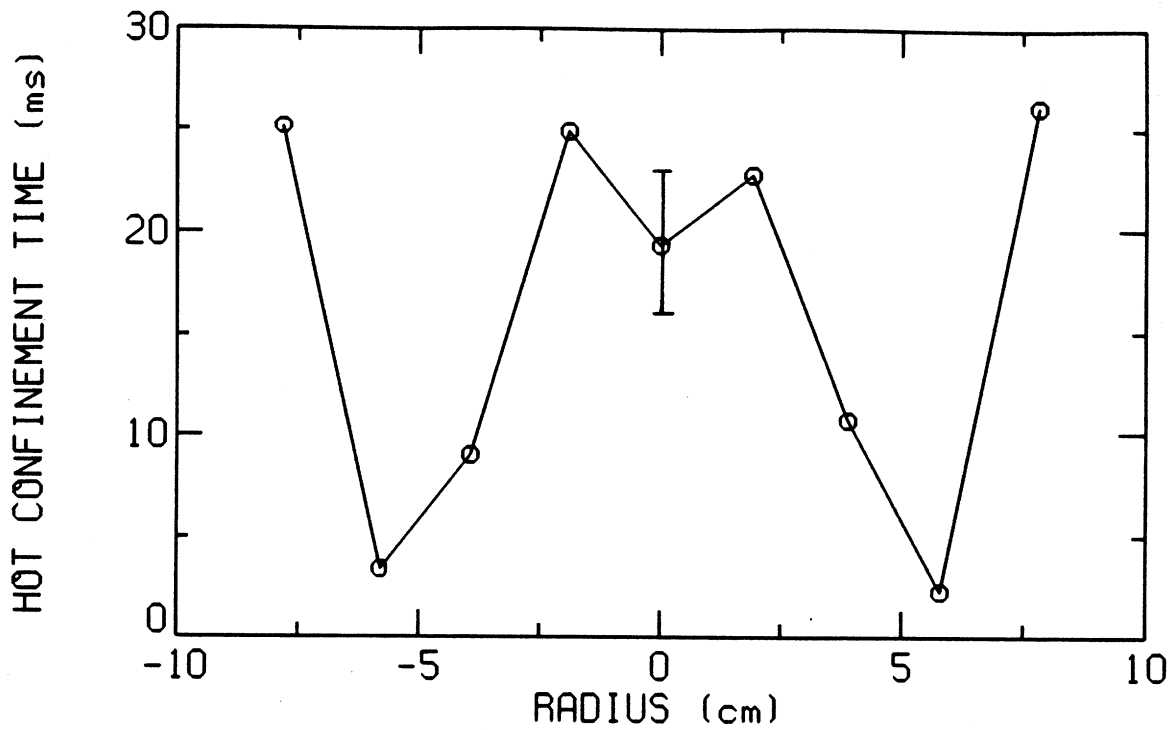
Figure 4-81: Parallel confinement time of the hot electrons for the 1 kW, 5×10^{-7} Torr oxygen plasma.
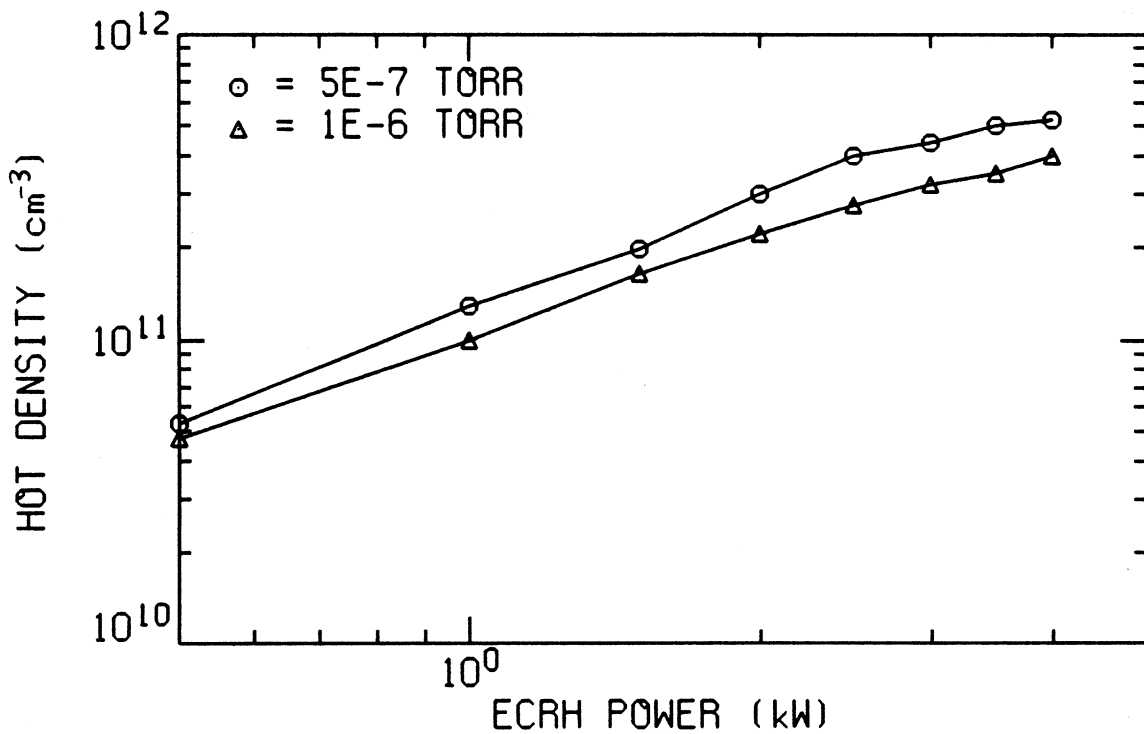
Figure 4-82: Hot electron density as a function of ECRH power for neon.
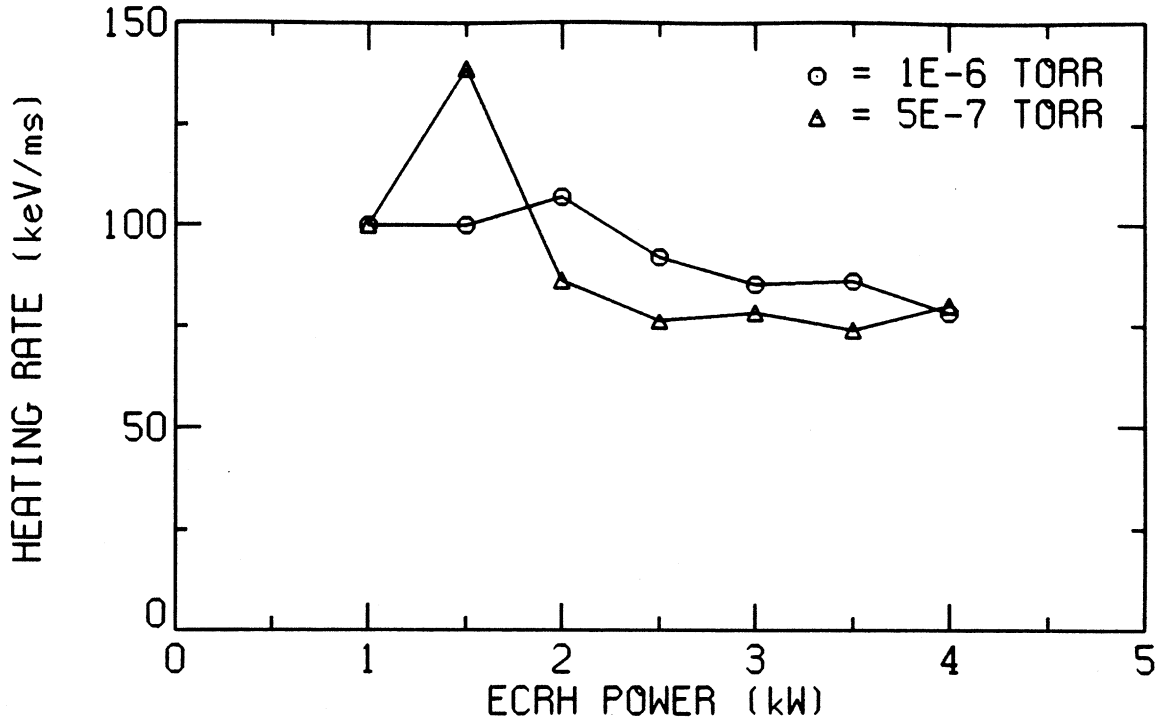
Figure 4-83: Heating rate (T_{eh}/τ_{eh}) of the hot electrons as a function of ECRH power for neon.

experiments. The two methods produced a scaling of hot electron density with ECRH power density of $n_{eh} \propto \mathcal{P}_{ech}^{.94\pm.23}$. The heating rate of the hot electrons (T_{eh}/τ_{eh}) as a function of ECRH power is shown in Fig. 4-83 for the same neon plasmas. The confinement time used in this figure is the particle confinement time in the plasma center. The heating rate is seen to be only a weak function of the ECRH power, with T_{eh}/τ_{eh} decreasing slowly with increasing ECRH power. The experimental results for ECRH power density scaling can be approximately summed up as $n_{eh} \sim \mathcal{P}_{ech}$ and $T_{eh}/\tau_{eh} \sim$ constant, which agrees with Eqn. 3.68.

Fig. 4-82 shows that the hot electron density decreases with neutral density like $n_{eh} \propto n_o^{-.41\pm.08}$. This is unexpected since there is no explicit neutral pressure dependence in the hot-electron particle-balance equation. A possible explanation of this effect is that the cold electron heating time increases with increasing neutral pressure. As mentioned earlier, the cold electron temperature decreases with increasing neutral pressure. This may increase the shielding effects of the cold electrons, lowering the rf field in the plasma. This in turn may increase the amount of time needed to heat

153

a cold electron up to a hot electron. As seen from Eqn. 3.61, increasing the cold electron heating time decreases the hot electron density.

Chapter 5

Conclusions

5.1 Summary of results

The main goal of this thesis is to measure the parallel ion confinement times as a function of ion charge state in an ECRH mirror plasma. To determine the parallel ion confinement times, the ion densities, end loss fluxes and temperatures are measured for oxygen and neon plasmas. The ion densities are determined from line brightnesses measured by a normal incidence VUV spectrometer. The density profile of each ion species is assumed to be the same as the electron density radial profile measured with a CCD camera and microwave interferometer. The cold electron temperature, needed to calculate the excitation rates, is measured using the singlet-triplet ratio of neutral helium (added as an impurity). The ion end-loss fluxes are measured with a time-of-flight analyzer, which was built for this thesis. The TOF analyzer fluxes are calibrated by the total ion current density measured by a gridded end-loss analyzer. The TOF analyzer also measures the ion temperatures, but they appear to be dominated by fluctuations in the plasma potential. Accurate perpendicular and parallel ion temperatures are found from Doppler broadening of visible ion emission lines.

The average charge state of the ions decreases with higher neutral pressure, probably because the ion confinement time decreases and charge exchange increases. The average charge state of the ions increases with higher ECRH power, probably because

the ionization time decreases due to a higher electron density. The radial profile of ion end loss is usually hollow due to large ion radial transport ($\tau_{\|i} \approx \tau_{\perp i}$), with the peak fluxes occurring at the edge of the ECR zone. The parallel ion confinement times increase with charge state and peak on axis, both strong indications of an ion-confining potential dip created by the hot electrons. The ion temperatures are found to increase with ion mass and are an order of magnitude larger than can be explained by electron drag heating.

An attempt is made to increase the flux of a selected ion species by "boiling" it out of the electrostatic trap using ICRH. The resonant ion temperatures increase by several hundred eV with 2 kW of ICRH, but all ion species show some heating due to drag off the resonant ions. The heating is primarily in the perpendicular direction. During ICRH, the end loss flux of resonant ions increases by 20% in cases when the radial transport induced by ICRH is not too severe. In cases when the induced transport is large, all ion fluxes decrease. The 20% increase that is achieved is much less than the factor of two to three that is predicted from ion modeling. The degraded performance is probably due to induced ion radial transport, increased charge exchange losses and non-resonant ion heating through dynamical friction.

It is found that a large antenna voltage can dump a large portion of the plasma. The "candle effect" is important because it limits the amount of ICRH power that can be applied to the plasma. Candle effect appears to be a consequence of the large ion radial transport that ICRH can induce through convection. Convective losses can occur due to asymmetries in the plasma potential caused by asymmetric cold-electron heating by the antenna geometry. When the perpendicular flux fraction exceeds 0.7–0.8, the plasma can probably no longer satisfy both charge neutrality and particle balance and equilibrium is lost. The threshold antenna voltage for candle effect increases linearly with neutral pressure in agreement with the above picture.

The effect of gas mixing is investigated by adding helium to an oxygen plasma. The flux of O^{6+} increases by 80% during gas mixing even though the total oxygen density decreases by half. This appears is due to decreased ion radial transport during gas mixing. A significant amount of oxygen ion cooling by helium is also observed.

An ion model is developed to predict the ion densities, end loss fluxes and confinement times in the plasma center. It uses the ion particle balance equations, the quasi-neutrality condition and theoretical confinement time formulas. The parallel confinement time is determined by both electrostatic and magnetic trapping. Low charge state ions have a parallel confinement time given by the Pastukhov-flow formula, while high charge state ions are confined by spatial diffusion. Radial transport of ions by classical and turbulent diffusion is also included. The ratio of parallel-to-perpendicular losses is calculated using the measured total ion flux. Other model inputs are the hot and cold electron density and temperature, the neutral pressure outside the plasma, the ion temperature and the magnetic geometry.

The ion model generally agrees with experimental data for oxygen and neon plasmas to within experimental error. However, for heavy gases such as krypton or xenon, the experimental data is strongly shifted to higher charge states compared to the ion model. The model follows the experimental data as neutral pressure and ECRH power change. Normally the transition from the Pastukhov-flow regime to the spatial diffusion regime occurs above $z_i = 5$, but for plasmas with small potential dips the transition appears to occur at $z_i = 4$; perhaps in these cases the axial plasma profiles are broader. The ion model also generally agrees with experimental data for plasmas heated with ICRH. An important exception is that the measured parallel confinement times of resonant ions in oxygen are much shorter than the theoretical values, probably due to rf diffusion of the ions into the loss cone.

5.2   Implications for ECR ion sources

In this section, results from experiments on Constance B and the ion model are applied to understanding important issues and phenomenon of ECR ion source operation.

Confinement time. It has been suggested that increasing the ion confinement time improves the extraction of the high charge states [Geller, 1979]. Neglecting external fluxes, the average ion confinement time from section 3.2 is

$$\tau_i \approx \frac{1 + \alpha}{z_p n_o \langle \sigma v \rangle^{ion,c}},$$

(5.1)

where α is the ratio of hot-to-cold electrons. Thus, the ion confinement time is inversely proportional to the neutral pressure and only weakly dependent upon other plasma parameters. Lowering the neutral pressure increases the density of high charge state ions because it reduces charge exchange losses and increases the ion confinement time (important for single step ionization). However, if the parallel confinement time becomes too long, then the ion end loss will decrease because the ions cannot get out. The end loss flux of ions is given by

$$\Gamma_{\|i} = \frac{L_p n_i}{\tau_{\|i}}, \tag{5.2}$$

therefore increasing the confinement time (by lowering the neutral pressure) benefits the extraction of an ion only if it increases its density more than it increases its parallel confinement time. The ion model predicts that the optimum neutral pressure decreases with increasing ion charge.

Electron density. It has also been suggested that increasing the electron density improves the extraction of the high charge states [Geller, 1979]. Normally raising the electron density increases the end loss of high charge state ions in two ways: (1) it increases the total flux of ions since $J_i \propto n_e$ and (2) it raises the average ion charge state in the plasma by decreasing the ionization time. However, since classical diffusion increases with density, increasing the electron density can also increase ion radial transport, which hurts extraction of high charge state ions. Thus, there is an optimal electron density for ECR ion source operation. However, the ion model predicts that this optimal density is large and may not normally be reached.

Hot vs. cold electrons. The electrons in an ECRH mirror plasma may be divided into "hot" and "cold" components according to their temperature. Ideally, the temperature of one group of electrons should be near the peak in the ionization rate curve for the desired charge state ion. For example, for O^{6+} the optimal temperature is around 1 keV, which for Constance B is best satisfied by the cold electrons. Since the cold electrons have the optimal temperature, the flux of O^{6+} will be largest for the smallest ratio of hot-to-cold electrons. For a higher charge state ion, however, the opposite may be true. For Ar^{18+}, the optimal electron temperature is about 50 keV.

This temperature is best satisfied by the hot electrons and therefore the flux of Ar^{18+} will be largest for the largest ratio of hot-to-cold electrons. In reality, a distribution consisting of only hot electrons cannot be achieved in an ECR ion source since electrons are born cold and are heated over a finite amount of time.

Magnetic field strength. Geller, *et al.*, (1987) suggest that raising the magnetic field increases the ion confinement time since $D_i \propto B^{-1}$ (Bohm) or $D_i \propto B^{-2}$ (classical). However, since the ion confinement time is determined by the need to balance creation and loss of particles (see Eqn. 5.1), it has no explicit dependence on magnetic field strength. In reality, any change in D_i due to a change in B will be offset by a modification in the potential dip to keep τ_i the same. Changing the magnetic field can change the ratio of parallel-to-perpendicular losses, however. Thus, raising the magnetic field can have the beneficial result of decreasing ion radial transport, which improves the high charge state performance of the ion source.

Changing the magnetic field strength while leaving the ECR frequency the same also affects the plasma volume. Experiments on Constance B show that the plasma approximately fills the non-relativistic ECR zone, which gives a scaling of $V \propto B^{-8.4}$. Decreasing the plasma volume increases the ECRH power density, which in turn increases the electron density since $n_{ec} \propto \sqrt{P_{ech}}$ and $n_{eh} \propto P_{ech}$ for Constance B. However, as the magnetic field is raised the plasma length shrinks like $L_p \propto B^{-2.7}$. Since the ion current density scales like $J_i \propto L_p n_e$, the actual increase in ion current with magnetic field is like $J_i \propto B^{1.5-5.7}$, depending upon the ratio of hot-to-cold electrons. Thus, raising the magnetic field strength can both increase the ion current and shift it to higher charge states.

Quiescient operation. Many ECR ion source groups have noted that quiescent operation (when the extracted ion currents are quasi-noiseless) is needed to produce the highest ion charge states. This phenomenon can be explained by the presence or absence of turbulent diffusion. In section 4.5, it was shown that ion radial transport greatly reduces the flux of high charge state ions. The reasons are twofold: (1) radial transport reduces the density of high charge state ions by decreasing their *total* confinement time and (2) the increase in the potential dip which accompanies

radial transport increases the *parallel* confinement time of the high charge states. In Constance B, ion radial transport is much greater than can be explained by classical and neoclassical diffusion and is probably due to plasma turbulence created by the electron microinstability. Thus, the observation that ECR ion sources work best when the plasma is quiescent is possibly due to a reduction of turbulent-driven ion radial transport. Perpendicular losses from classical and neoclassical diffusion should still be present. The ion temperature for quiescent operation may also be lower because there is less turbulent heating of ions.

Gas mixing. The gas mixing phenomenon, discussed in section 4.5, is re-examined for ECR ion sources. For Constance B, it is found that mixing helium with oxygen increases the O^{6+} flux by reducing ion radial transport, presumably by decreasing plasma turbulence. ECR ion sources see a decrease in the energy spread of extracted ions during gas mixing [Antaya, 1989] which may be due to a reduction of turbulence. A lower level of plasma turbulence allows the ECRH power to be increased until a new stability limit is reached, therefore increasing the electron density which improves the source performance.

Another explanation by Geller, *et al.*, (1987) is that gas mixing makes the hot electrons less collisional by lowering the average charge state of the plasma. This increases the energy confinement time, which allows a higher electron density and temperature to be achieved. This explanation is reasonable when hot electron losses are determined by collisions, but when hot electron losses are determined by rf diffusion, decreasing their collisionality has little effect on their confinement time. Also this explanation for the gas mixing effect leads to the result that hydrogen or helium should always be the best gas to mix with. In reality, the mass of the best mix gas is found to be 3–5 times lighter than the mass of the main gas [Geller, *et al.*, 1987].

In section 4.5, it is shown that ion cooling can also lead to an increase in the fluxes of high charge state ions. Ion cooling of oxygen by helium is observed experimentally in Constance B. For this case, the best mix gas is the one that cools the heavy ions the most [Antaya, 1989]. The cooling rate is given by

$$\frac{dT}{dt} = \frac{T_* - T}{\tau^{eq}},$$

(5.3)

160

where τ^{eq} is given by Eqn. 3.44. As shown in Fig. 4-29, the ion temperature increases linearly with ion mass (which explains why a light gas can cool a heavy gas), therefore $T_* - T \propto m_* - m$. In addition, if the temperature difference is not too large, then approximately $1/\tau^{eq} \propto \sqrt{m_* m}$ (ignoring differences in the average charge state). Thus, the mass dependence of the cooling rate is approximately

$$\frac{dT}{dt} \propto (m_* - m)\sqrt{m_* m}. \tag{5.4}$$

This scaling represents a trade off between lighter mixing gases which have a larger temperature differential and heavier mixing gases which have a shorter equilibration time. The strongest cooling rate (most negative) occurs at $m_* = m/3$, in good agreement with experimental results.

Two stage operation. Most ECR ion sources presently use two stages, in which the first stage runs at high neutral pressure to produce a low charge state plasma which is then fed into a second stage at low neutral pressure to produce a high charge state plasma. For a one stage ion source, such as Constance B, the neutral pressure is the source of particles and therefore must remain finite. However, for a two stage source, the first stage provides a source of particles for the second stage and therefore the neutral pressure in the second stage can be as low as possible. This reduces charge exchange losses and can increase the flux of high charge state ions by several times.

One-ended operation. Constance B has a symmetric magnetic well, with identical mirror ratios on both ends. Thus, half of the ion flux exits each end of the plasma. For an ion source which extracts from one end, this means that half of the ions are wasted. By raising the mirror ratio on one side of the plasma, most of these otherwise lost ions can be directed out the other end. This occurs because most ions are knocked into the loss cone by small angle scattering. Asymmetric mirror ratios can also double the effective length of the plasma, which can increase the flow confinement time by a factor of two and the spatial diffusion confinement time by a factor of four. In addition, ECR ion sources with one-ended operation can run stably at higher ECRH power and therefore higher electron density [Jacquot and Geller, 1987; Antaya, 1989].

An early ECR ion source to use asymmetric mirror ratios was Caprice [Jacquot

and Geller, 1987]. It used $R = 2.7$ on the injection side and $R = 1.7$ on the extraction side. The presence of a $\omega_{ce} = 2\omega_{ech}$ region in the magnetic well lead its operators to conclude that the improved performance was due to to reabsorption of plasma second harmonic emission at this layer, which would increase the energy confinement time. However, a series of experiments by Antaya (1989) showed that the extraction of high charge state ions improves gradually as the mirror ratios are made more asymmetric and no resonance-like effects were seen when the $\omega_{ce} = 2\omega_{ech}$ region was present.

Frequency scaling. The maximum electron density that can be achieved in an ECR ion source is determined by microwave cutoff. For example, for X-mode launch the density limit occurs at $\omega_{pe} = \sqrt{2}\omega_{ce}$. This density limit can be raised by increasing the ECR frequency like $n_e \propto \omega_{ce}^2$. To actually achieve this density increase requires that the ECRH power density be raised with frequency. For Constance B, this would mean $\mathcal{P}_{ech} \propto \omega_{ce}^{2-4}$, depending upon the ratio of hot-to-cold electrons. For super-adiabatic electrons which are classically mirror confined, the power scaling from Eqn. 3.73 is $\mathcal{P}_{ech} \propto \omega_{ce}^{60/19}$. The ECR ion source MINIMAFIOS experimentally shows a scaling of approximately $\mathcal{P}_{ech} \propto \omega_{ce}^2$ [Geller, et al., 1987]. This shows that to achieve the full advantage of frequency scaling requires a large increase in transmitter power.

Shifting to higher frequency can be beneficial even if the ECRH power cannot be raised. This is because the higher magnetic field strength can reduce radial transport of ions, which will increase the end loss of high charge state ions.

5.3   Suggestions for future work

Since complete measurements of ion densities, fluxes and temperatures were only done for the first five charge states of oxygen and neon, extending these measurements to higher charge states is the next logical step. This would be especially useful for fully exploring the spatial diffusion regime of parallel confinement. Since the charge state limit in this thesis is due to the VUV spectrometer wavelength range and sensitivity, changing to a grazing incident spectrometer with a high efficiency detector is recommended. The sensitivity of the TOF analyzer may also need to

be increased by improving the electrostatic lens so that higher charge states can be observed.

The one important parameter for ion confinement that was not measured is the potential dip. This measurement is needed to fully test the theoretical parallel confinement theories (this thesis only tested the scaling with ion charge state). The potential structure in the plasma cannot be measured with emissive or Langmuir probes because the hot electrons would destroy them. Thus, two non-contact diagnostics are proposed to measure the potential dip. The first method is to inject a singly-charged ion beam into the plasma parallel to the magnetic field and observe the transmitted beam with the TOF analyzer. A fraction of the beam ions will be ionized by electron impact in the plasma and these ions will gain an amount of energy equal to the plasma potential at the point they are ionized. Measuring the energy difference between the singly and doubly ionized ions will determine this potential. Knowing the peak potential from the plasma end loss allows the potential dip to be found. Since the beam trajectory is not changed by ionization, no spatial resolution would be possible. The potential dip can also be measured by sweeping the energy of the ion beam around the plasma potential. If the beam energy is greater than $\phi_p + \Delta\phi_i$, then both the singly and doubly ionized atoms will pass through the plasma. If the beam energy is between ϕ_p and $\phi_p + \Delta\phi_i$, then the singly ionized atoms will pass through but the doubly ionized atoms will be trapped, reducing their flux. If the beam energy is below ϕ_p, then no injected ions will be observed on the other side. A small cusp ECR ion source (2.45 GHz) was actually built for Constance B to measure the potential dip in this way. However, its extracted ion current was fairly small (5–10 mA) and the axial magnetic field at the source aperture was too weak (50 G) to magnetize the ions. The injected ion current was therefore too small to be used for this experiment.

A second method of determining the potential dip is to measure the time-of-flight of an injected electron beam along the magnetic field lines [Chang, *et al.*, 1988]. The TOF depends upon the electron velocity, which in turn depends upon the axial potential distribution. Modulating the beam amplitude allows the electron velocity

be determined from the beam phase by the relation

$$\theta = \omega \int \frac{ds}{v(s)}.$$

(5.5)

The beam phase can be measured at various points along the axial magnetic field by observing the neutral or ion emission lines the beam induces through electron excitation with a spectrometer of sufficient spatial resolution. This will allow the electron velocity as a function of axial potential to be determined, from which the axial potential distribution can be found using

$$\phi(s) = V_b - \frac{1}{e}\frac{m_e v^2(s)}{2},$$

(5.6)

where V_b is the beam voltage.

Since the experimental data for operating ECR ion sources is sparse (except for extracted ion currents), almost any measurement of electron or ion density, temperature or confinement time would be helpful. A microwave interferometer to measure electron density would be especially useful to see how close ECR ion sources operate to the density cutoff. Also of great interest would be to measure ion radial transport and the effect of plasma turbulence. Determining the ion temperature with and without gas mixing would be an important step to resolving that issue.

Bibliography

[Antaya, 1989]   T.A. Antaya, J. Physique **50**, C1-707 (1989).

[Antonsen and Manheimer, 1978]   T.M. Antonsen and W.M. Manheimer, Phys. Fluids **21**, 2295 (1978).

[Baldwin, 1980]   D.E. Baldwin, "Model for ion confinement in a hot-electron tandem mirror anchor," Lawrence Livermore Nat. Lab. rep. UCID-18802 (1980).

[Bernhardi and Wiesemann, 1982]   K. Bernhardi and K. Wiesemann, Plasma Physics **24**, 867 (1982).

[Brau, *et al.*, 1988]   K. Brau, J.H. Irby, E. Sevillano, D. Goodman, J.A. Casey, S.N. Golovato, S. Horne and R.S. Post, Nucl. Fusion **28**, 2093 (1988).

[Bliman and Chan-Tung, 1981]   S. Bliman and N. Chan-Tung, J. Physique **42**, 1247 (1981).

[Brown, 1966]   S.C. Brown, *Basic Data of Plasma Physics* (MIT Press, Cambridge, 1966).

[Chang, *et al.*, 1988]   C.P. Chang, M.A. Lieberman, H. Meuth and A.J. Lichtenberg, Phys. Fluids **31**, 123 (1988).

[Chen, 1974]   F.F. Chen, *Introduction to Plasma Physics* (Plenum Press, New York, 1974).

[Chen, 1988]   X. Chen, "Hot electron plasma equilibrium and stability in the Constance B mirror experiment," MIT Plasma Fusion Center rep. PFC/RR-88-6 (1988).

[Chen, *et al.*, 1989]   X. Chen, B.G. Lane, D.L. Smatlak, R.S. Post and S.A. Hokin, Phys. Fluids B **1**, 615 (1989).

[Cho, *et al.*, 1988]   T. Cho, M. Inutake, K. Ishii, I. Katanuma, Y. Kiwamoto, A. Mase, Y. Nakashima, T. Saito, N.

Yamaguchi, K. Yatsu, M. Hirata, T. Kondoh, H. Sugawara, J.H. Foote and S. Miyoshi, Nucl. Fusion **28**, 2187 (1988).

[Cohen, *et al.*, 1978]   R.H. Cohen, M.E. Rensink, T.A. Cutler and A.A. Mirin, Nucl. Fusion **18**, 1229 (1978).

[Cohen, 1979]   R.H. Cohen, Nucl. Fusion **19**, 1295 (1979).

[Dupree, 1967]   T.H. Dupree, Phys. Fluids **10**, 1049 (1967).

[Flügge, 1955]   S. Flügge, *Handbuch der Physik* (Springer, Berlin, 1955).

[Fredian and Stillerman, 1986]   T.W. Fredian and J.A. Stillerman, Rev. Sci. Instrum. **57**, 1907 (1986).

[Gabriel and Jordan, 1971]   A. Gabriel and C. Jordan, from *Case Studies in Atomic Collision Physics*, Eds. E. McDaniel and M. McDowell (North Holland, Amsterdam, 1971).

[Garner, 1986]   R.C. Garner, "Electron microinstabilities in an ECRH, mirror-confined plasma," MIT Plasma Fusion Center rep. PFC/RR-86-23 (1986).

[Garner, *et al.*, 1987]   R.C. Garner, M.E. Mauel, S.A. Hokin, R.S. Post and D.L. Smatlak, Phys. Rev. Lett. **58**, 1853 (1987).

[Geller, 1976]   R. Geller, IEEE Trans. Nucl. Sci. **NS-23**, 904 (1976).

[Geller, 1979]   R. Geller, IEEE Trans. Nucl. Sci. **NS-26**, 2120 (1979).

[Geller, *et al.*, 1987]   R. Geller, F. Bourg, P. Briand, J. Debernardi, M. Delaunay, B. Jacquot, P. Ludwig, R. Pauthenet, M. Pontonnier and P. Sortais, "The Grenoble ECRIS status 1987 and proposals for ECRIS scalings," Nat. Superconducting Cyclotron Lab. rep. MSUCP-47 (1987).

[Goodman, 1989]   D.L. Goodman, "Radial ion transport in a non-axisymmetric magnetic mirror," MIT Plasma Fusion Center rep. PFC/RR-89-2 (1989).

[Harting and Read, 1976]   E. Harting and F.H. Read, *Electrostatic Lenses* (Elsevier, New York, 1976).

[Haste, *et al.*, 1968]   G.R. Haste, J.L. Dunlap, N.H. Lazar, *et al.*, Oak Ridge Nat. Lab. reps. ORNL-TM-4401 (1968), ORNL-TM-4545 (1969) and ORNL-TM-4688 (1970).

[Hokin, 1987]   S.A. Hokin, "Electron velocity-space diffusion in a micro-unstable ECRH mirror plasma," MIT Plasma Fusion Center rep. PFC/RR-87-17 (1987).

[Hokin, *et al.*, 1989]   S.A. Hokin, R.S. Post and D.L. Smatlak, Phys. Fluids B **1**, 862 (1989).

[Hutchinson, 1987]   I.H. Hutchinson, *Principles of plasma diagnostics* (Cambridge University Press, New York, 1987).

[Itikawa, *et al.*, 1985]   Y. Itikawa, S. Hara, T. Kato, S. Nakazaki, M.S. Pindzola and D.H. Crandall, Atom. Data and Nucl. Data Tables **33**, 149 (1985).

[Jacob, 1989]   M. Jacob, J. Physique **50**, C1-505 (1989).

[Jacquot and Geller, 1987]   B. Jacquot and R. Geller, "Caprice 10 GHz—New $2\omega_{ce}$ radial B field," Nat. Superconducting Cyclotron Lab. rep. MSUCP-47 (1987).

[Jongen, 1980]   Y. Jongen, "Confinement and charge state distribution in ECR sources," Laboratorie du Cyclotron rep. LC-8001, Univ. Cath. De Louvain, Belgium (1980).

[Kennel and Engelmann, 1966]   C.F. Kennel and F. Engelmann, Phys. Fluids **9**, 2377 (1966).

[Köhler, *et al.*, 1987]   H. Köhler, M. Frank, B.A. Huber and K. Wiesemann, Nucl. Inst. B **23**, 186 (1987).

[Kuthi, *et al.*, 1988]   A. Kuthi, L. Olson, K.L. Lam, H. Zwi and A.Y. Wong, Phys. Fluids **31**, 1787 (1988).

[Lotz, 1968]   W. Lotz, Z. Physik **216**, 241 (1968).

[Lyneis, 1986]   C.M. Lyneis, *Proceedings of the 11th International Conference on Cyclotrons and Their Applications*, Tokyo, 707 (1986).

[Lyneis, 1987]   C.M. Lyneis, "Operating experience with the LBL ECR source," Nat. Superconducting Cyclotron rep. MSUCP-47 (1987).

[Mauel, 1985]   M.E. Mauel, unplublished work (1985).

[Meyer, 1986]   F.W. Meyer, "Operation of the ORNL ECR
                                  source," *Proceedings of the 7th ECR Ion Source
                                  Workshop*, Jülich, Ed. H. Beuscher (1986).

[Müller and Salzborn, 1977]   A. Müller and E. Salzborn, Phys. Letters **62A**,
                                  391 (1977).

[Müller, *et al.*, 1980]   A. Müller, E. Salzborn, R. Frodl, R. Becker, H.
                                  Klein and H. Winter, J. Phys. B: Atom. Molec.
                                  Phys. **13**, 1877 (1980).

[Najmabadi, *et al.*, 1984]   F. Najmabadi, R.W. Conn and R.H. Cohen, Nucl.
                                  Fusion **24**, 75 (1984).

[Pardo, *et al.*, 1989]   R.C. Pardo, P.J. Billquist and J.E. Dey, J.
                                  Physique **50**, C1-695 (1989).

[Parks, 1987]   P.B. Parks, Phys. Fluids **30**, 3212 (1987).

[Pastukhov, 1974]   V.P. Pastukhov, Nucl. Fusion **14**, 3 (1974).

[Petty, *et al.*, 1988]   C.C. Petty, D.K. Smith and D.L. Smatlak, Rev.
                                  Sci. Instrum. **59**, 601 (1988).

[Porkolab and Kino, 1968]   M. Porkolab and G.S. Kino, Phys. Fluids **11**, 346
                                  (1968).

[Post, 1987]   R.F. Post, Nucl. Fusion **27**, 1579 (1987).

[Press, *et al.*, 1986]   W.H. Press, B.P. Flannery, S.A. Teukolsky and
                                  W.T. Vetterling, *Numerical Recipes* (Cambridge
                                  University Press, Cambridge, 1986).

[Rognlien and Cutler, 1980]   T.D. Rognlien and T.A. Cutler, Nucl. Fusion **20**,
                                  1003 (1980).

[Sackett, 1978]   S.J. Sackett, "EFFI: A code for calculating the
                                  electromagnetic field force and inductance in coil
                                  systems of arbitrary geometry," Lawrence Liver-
                                  more Nat. Lab. rep. UCRL-52402 (1978).

[Smatlak, *et al.*, 1986]   D.L. Smatlak, X. Chen, R.C. Garner, D.L. Good-
                                  man, S.A. Hokin, J.H. Irby, B.G. Lane, D.K.
                                  Liu, R.S. Post, D.K. Smith and J. Trulsen, "Ex-
                                  perimental results from the Constance B mag-
                                  netic mirror," MIT Plasma Fusion Center rep.
                                  PFC/RR-86-15 (1986).

[Smith, 1980]   D.K. Smith, Ph.D. thesis, University of Wisconsin at Madison, Dept. of Electrical Engineering (1980).

[Smith and Petty, 1986] D.K. Smith and C.C. Petty, Bull. Am. Phy. Soc. **31** (9), 1511 (1986).

[Tamagawa, *et al.*, 1976] H. Tamagawa, I. Alexeff, C.M. Jones and P.D. Miller, IEEE Trans. Nucl. Sci. **NS-23**, 994 (1976).

[West, 1982]   H.I. West, Jr., "Calculation of ion charge-state distribution in ECR ion sources," Lawrence Livermore Nat. Lab. rep. UCRL-53391 (1982).